Integration of highly reflective back contacts in microstructured Cu(In, Ga)Se$_2$ solar cells

Dissertation

zur Erlangung des Doktorgrades der Naturwissenschaften
(Dr. rer. nat.)

der

Naturwissenschaftlichen Fakultät II
Chemie, Physik und Mathematik

der Martin-Luther-Universität
Halle-Wittenberg vorgelegt von

Herrn Thomas Schneider
geb. am 8. Juni 1988 in Halle (Saale)

Gutachter: Prof. Dr. Roland Scheer
                 Prof. Dr. Ralf B. Wehrspohn
                 Prof. Dr. Michael Powalla
Datum der Verteidigung: 07.06.2023

Contents

General introduction

More than 190 countries worldwide have declared to take actions for a limitation of the human-caused increase of global temperature to less than 2 °C compared to pre-industrial levels, during the Paris climate agreement of 2015 [1]. A significant reduction of the global emission of greenhouse gases is mandatory to reach this goal. The reduction of greenhouse gases requires a transition to technologies that do not rely on the emission of such gases, like the renewable energy technologies. The generation of electricity via photovoltaics (PV) can significantly contribute to this transition. This fact is mainly enabled through a strong decrease in the average module prices over time - a rapid development, which lead to the fact that the levelized cost of energy for PV systems has even surpassed the conventional technologies in large areas of the world [2]. This strong price decrease is caused by innovation and the cost reduction obtained due to up-scaling of the production processes.

The current work aims to research possible concepts to reduce the absorber layer thickness in $Cu(In, Ga)Se_2$ (CIGSe) based solar cells. Such a reduction could decrease the cost of CIGSe based solar cells not only due to a reduced material usage but also by an increased cell production throughput. The latter fact can be explained by the circumstance that the CIGSe absorber layer is grown on a substrate via evaporation. Hence a thicker absorber layer is equal to a longer processing time.

A reduction of the absorber layer thickness does however lead to an incomplete absorption of the light and therefore to a reduction of the current output of the solar cell. Furthermore, lower open circuit voltages (V_{OC}) are typically reported for solar cells employing ultrathin (< 500 nm) absorber layers [3]. Those V_{OC} losses are commonly attributed to an increased influence of the back contact recombination on the solar cell performance. Both effects result in a decreased power conversion efficiency.

Light management techniques can be used to decrease the required absorber layer thickness to obtain a complete photon absorption. The Mo back contact, which is employed in almost all CIGSe solar cells, turns out to be a major obstacle. The reflectivity of the CIGSe/Mo interface is rather low (~20%). Hence, a significant portion of the light will be lost by light absorption in the Mo, even when scattering elements are used [4]. One focus of this work was therefore the replacement of Mo by another highly reflective back contact .

A direct deposition of CIGSe is not possible on most metals, due to an interdiffusion of the metal and the CIGSe during the high temperature CIGSe deposition. A diffusion barrier between the back contact metal and the absorber layer was investigated in this thesis to resolve this issue. Transparent conductive oxides (TCO) were employed for this task. TCO layers provide sufficient conductivity enabling a charge carrier transport to the back contact metal while being mostly transparent.

The properties of the TCO/CIGSe interface at the back contact have consequently become an important topic of this work. TCO layers of n-type conductivity are usually employed for CIGSe solar cells on transparent back contacts. Working CIGSe solar cells on n-type TCO back contacts were already demonstrated by several authors [5, 6, 7, 8, 9, 10, 11]. This is interesting due to the resulting npn structure, which is expected to block any current flow through the device. The reason why an n-type TCO can be used as a back contact in such a configuration is still not resolved. A potential explanation will be discussed in this work. Rather poor electrical performances are commonly reported when a TCO back contact is employed as the back contact and high temperatures (~600 °C) are used for the CIGSe deposition [6, 5, 11]. The formation

of a thin Ga_2O_3 layer was found in several publications and identified as the probable reason for the poor performance. High deposition temperatures are however usually employed in the industry.

Highly reflective back contacts enable a reduction of the absorber thickness. However, the full potential is achieved only if additional scattering elements are introduced in the solar cell design. First results of solar cells which combine a highly reflective back contact metal with a structuring element will be presented in this work.

This thesis is divided into six chapters. Chapter 1 and 2 provide the basic knowledge to understand the rests of the thesis, as well as an overview of the literature status regarding the topic. Chapter 3 to 5 will present the scientific results of this thesis.

Chapter 3 shows the test results of different combinations of metal/TCO back contacts. The Al/ITO back contact, which has proven to be the most promising type of back contact is tested in more detail. The gain in the short circuit current due to such a back contact for an unstructured solar cell will be presented.

Chapter 4 analyzes the electrical properties of the Mo/CIGSe and ITO/CIGSe interface. The back contact recombination velocity is determined for an ITO/CIGSe interface using bifacial solar cells. Temperature dependent admittance and JV measurements are used for a further analysis of both back contact types. Based on the results, the impact of the back contact on the solar cell parameters is analyzed.

Chapter 5 presents the results of first Al/ITO-based prototypes of solar cells on structured back contacts. The growth behavior of the individual layers is analyzed. The absorption in the solar cells is calculated using 3D optical simulations and is compared with measured EQE curves.

The final chapter summarizes the thesis while suggesting paths for future research on the topic.

Chapter 1

Introduction

The general purpose of a solar cell is the conversion of the energy provided by the irradiance from the sun into electrical energy. A pn-junction is used in CIGSe based solar cells to separate the hole-electron pairs created by the sun light. Both carriers have to be collected by the electrical contacts on both ends of the solar cells before they are subjected to recombination processes. Recombination processes are therefore an important subject of solar cells and will be discussed first.

1.1 Generation and recombination

The generation of charge carrier describes the process of the creation of an electron-hole pair. This process requires additional energy, which can be provided to the system by the absorption of photons or thermal energy. The opposite process, called recombination, is the assimilation of an electron-hole pair. The energy has to be transferred to another energy form in this case. Under equilibrium conditions, both processes will happen at the same rate in a semiconductor resulting in an equilibrium electron density n and hole density p.

If the light is absorbed by the semiconductor, an excess of electrons and holes is created compared to the equilibrium carrier densities, which is denoted as Δn. As soon as the illumination is removed the net recombination will be higher than the net generation bringing the system back into the equilibrium state. The time it takes to reach the equilibrium is connected to the charge carrier lifetime τ_n (for electrons) and τ_p (for holes), which is an important parameter for solar cell absorber layers. The charge carrier lifetime is defined by the time in which a given excess carrier density is reduced to 1/e of the initial value through the recombination process. Multiple types of recombination processes can be found in the bulk of a semiconductor: namely Shockley-reed hall recombination, radiative recombination, and Auger recombination. The various recombination processes will be explained in the following.

1.1.1 Band to band radiative recombination

Figure 1.1 a) shows the process of the radiative band to band recombination. An electron from the conduction band recombines with a hole from the valence band. The lost chemical energy is used to create a photon. In the case of an indirect semiconductor, an additional phonon is
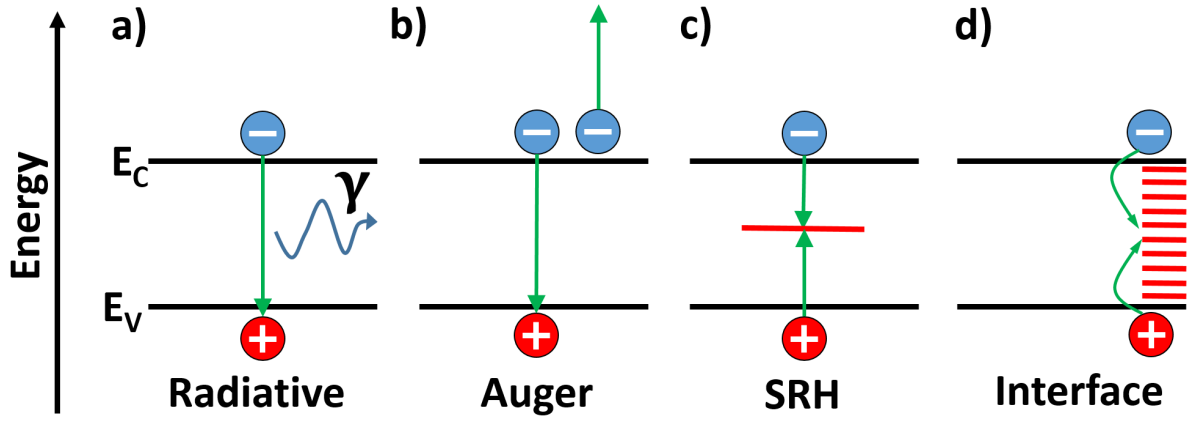
Figure 1.1: Overview of the different recombination paths found in semiconductors. a) radiative recombination b) Auger recombination, c) Shockley-Read-Hall recombination, d) interface recombination.

required if the process is not happening via the direct band gap. This recombination process is important for the operation of the solar cell. It is the inverse process to the charge carrier generation. This recombination rate cannot be avoided; a complete suppression would also lead to a suppression of the carrier generation via light absorption. The recombination rate R_r associated with band to band recombination is proportional to the amount of both charge carriers as reflected by the corresponding equation

$$R_r = B_r np, \tag{1.1}$$

where B_r is a material specific quantity.

1.1.2   Auger recombination process

Figure 1.1 b) shows the Auger recombination process. The released energy, due to the recombination of a hole, and an electron is transferred to another electron. The additional energy given to the electron will quickly be transferred to the lattice of the semiconductor. Hence phonons are created and consequently heat. This process requires the presence of three particles (two electrons and one hole). It is typically only of importance if the generation rate is very high, which translates to a high illumination intensity. The rate R_a of this process is given by:

$$R_a = B_a n^2 p, \tag{1.2}$$

with B_a beeing a material specific quantity.

Note that this recombination can take place also between two holes and one electron. A hole is excited in this case and R_a is given by

$$R_a = B_a n p^2. \tag{1.3}$$

1.1.3 Shockley-Read-Hall recombination

The Shockley-Read-Hall (SRH) recombination process is shown in Figure 1.1 c). It requires the presence of states within the band gap of the semiconductor. The recombination process is in this case facilitated through the states in the band gap, which are called trap states in the following. The trap state can interact with both, the valence and the conduction band of the semiconductor. An electron can either be captured into the trap state from the conduction band or emitted in the opposite direction. Additionally, a hole can either be captured into the trap state from the valence band or emitted in the opposite direction. Hence, an electron can recombine with a hole in a two-step process. The SRH recombination process is often the dominating bulk recombination process. An absorber layer with a low SRH recombination rate (in the context of the absorber layer material) is said to have a high electrical quality. The recombination rate R_{SRH} is given by

$$R_{SRH} = \frac{np - n_i^2}{\tau_{SRH,p}(n + n^*) + \tau_{SRH,n}(p + p^*)},\tag{1.4}$$

with $\tau_{SRH,p}$ and $\tau_{SRH,n}$ being the minimal lifetime of the holes and electrons. The two quantities n^* and p^* are given by $n^* = N_C exp(\frac{E_c - E_T}{kT})$, and $p^* = N_V exp(\frac{E_T - E_V}{kT})$, where N_C is the effective electron density in the conduction band, N_V is the effective hole density in the valence band, and E_V, E_C, E_T being the energetic levels of the valence band, conduction band and the energetic position of the trap state, respectively. It can be shown that this recombination rate is highest, when the defect is situated in the middle of the band gap.

1.1.4 Interface recombination velocity

A high density of defects can often be found at the interface between semiconductors. Figure 1.1 d) shows an example with a continuous defect density in the band gap at the interface between two semiconductors. Atoms near the interface can be missing a bonding partner, which can lead to the creation of trap states inside the band gap. Often these trap states are assumed to be of continuous nature. The surface recombination rate R_{it} is given by

$$R_{it} = (n_S p_S - n_i^2) \int_{E_V}^{E_C} \frac{v_{th} D_{it}(E)}{\frac{n_s + n^*(E)}{\sigma_p} + \frac{p_s + p^*(E)}{\sigma_n}} dE,\tag{1.5}$$

where n_s and p_s are the concentrations of the electrons and holes at the surface, σ_n and σ_p are the capture cross sections of both carriers, with the thermal velocity v_{th}, the surface defect density D_{it}. It can be shown that he contribution of the defect density is highest for energy levels in the middle of the band gap. The recombination at interfaces are however typically characterized by an interface recombination velocity S_n for electrons and S_p for holes. Both can be connected to the recombination currents at the contacts of the solar cells. The recombination currents of the electrons $j_{n,it}$ and holes $j_{p,it}$ at a Schottky contact are given by

$$j_{n,it} = qS_n(n - n_{eq}) \text{ and } j_{p,it} = qS_p(p - p_{eq}).\tag{1.6}$$

Where n_{eq} and p_{eq} are given by
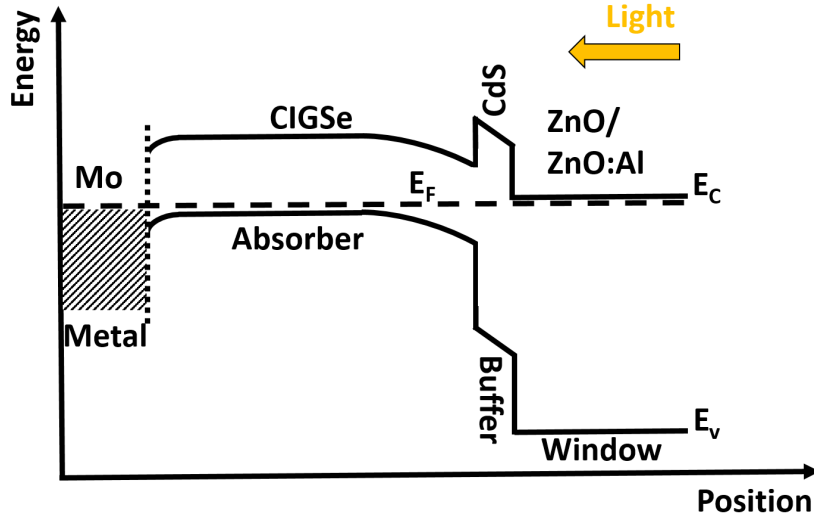
Figure 1.2: Schematic band diagram of a CIGSe solar cell.

$$n_{eq} = N_C \frac{q(\phi - \chi)}{kT} \text{ and } p_{eq} = N_V \frac{E_g - q(\phi - \chi)}{kT}, \tag{1.7}$$

with the band gap E_g, the electron affinity χ and the metal work function ϕ. The interfaces between metals and semiconductors are often rather defective. Both S_n and S_p have an upper limit given by the thermal velocity, which is usually assumed to be 10^7 cm/s. The recombination process is in this case only limited by the diffusion to the interface. Good passivation layers can archive surface recombination velocities below 10 cm/s [12]. The surface recombination velocity of an interface can be estimated from measurements of the charge carrier lifetimes [13]. Another approach is modeling of EQE curves, especially for bifacial solar cells. Bifacial solar cells have a transparent back contact which allows an illumination through the rear side of the solar cell [7, 9]. The EQE is stronger influenced by back contact recombination in this case.

1.2 The pn-junction

The pn-junction is formed for CIGSe based solar cells between the p-type CIGSe absorber layer and the n-type buffer (usually Cd), and the n-type window layer (usually a bilayer of ZnO/ZnO:Al), as visible in the band diagram in Figure 1.2. The doping density of the buffer layer usually assumed to be significant higher doped than the CIGSe layer. The space charge region is therefore much wider in the CIGSe absorber layer than on the n-type side. The functional dependence of the electrical current J of an ideal diode is given by the ideal diode equation

$$J = J_0(exp(qVA/kT) - 1), \tag{1.8}$$

with the dark saturation current J_0, the elementary charge q, and the applied voltage V [14]. The resulting JV curve in the dark is shown in Figure 1.3 a).

Upon illumination, excess charge carriers are generated in the semiconductor. The electric field induced by the pn-junction forces electrons to the p-side and holes to the n-side. Those minority carriers can then recombine at the metallic contacts creating a current in reverse direction. This
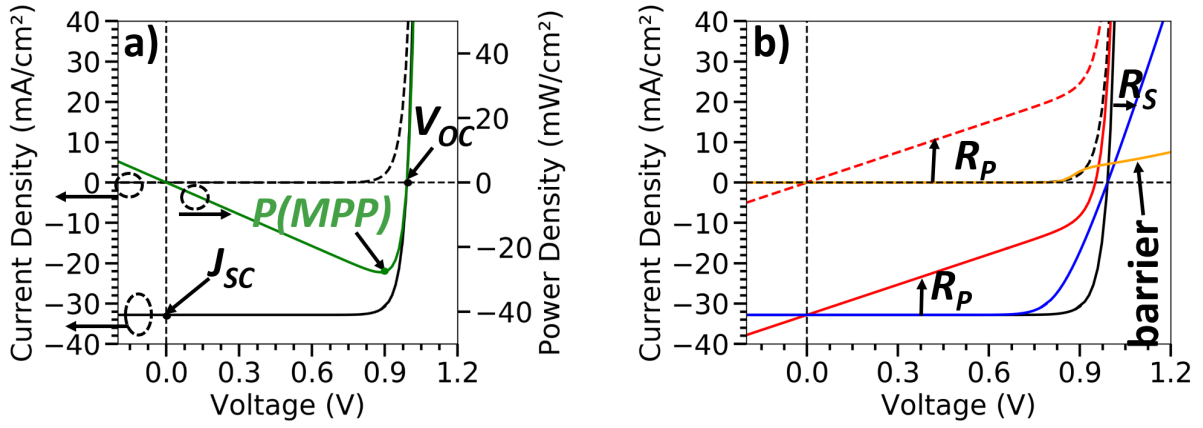
Figure 1.3: a) A typical JV curve under illumination (black full line) together with the open circuit voltage V_{OC} and short circuit density J_{SC}. The dashed black line represents the JV curve without illumination. The green line gives the output power of the illuminated solar cell with the marked maximum power point. b) The same JV curves as in picture a) together with a JV curve affected by a series resistance (blue) together with the two JV curves affected by a low parallel resistance (red). The orange curve shows a JV curve of a solar cell with a large back contact barrier measured in the dark.

current, which is commonly referred to as photocurrent. The resulting JV curve under illumination is therefore given by the dark current of the diode offset by the photocurrent $J_{photon}(V)$:

$$J = J_0(exp(qVA/kT) - 1) + J_{photon}(V) \tag{1.9}$$

The illuminated JV-curve is in the ideal case given by the dark JV-curve offset by the photocurrent, when the collection of photogenerated carriers is not affected by the applied voltage. Deviations can be caused by a voltage dependence of the photocurrent or a modification of the forward current because the system is altered through the illumination. The dark and illuminated curves can cross each other under forward bias, a phenomenon commonly referred to as a cross-over.

The performance of a solar cell can be characterized by a set of 4 parameters derived from JV curves. The standard conditions for the characterization of solar cells are a sample temperature of 25 °C with an illumination resembling AM1.5G conditions. Figure 1.3 a) shows an example for an illuminated JV curve together with the output power of the solar cell. The four parameters are:

- The short circuit current density J_{SC} is given by current density at 0 V. It is a measure for the the absorbed photon density within the absorber layer of the solar cell, reduced by portion of the carriers, which is lost due to recombination.

- The open circuit voltage V_{OC} is defined by the voltage, where the output current of the illuminated solar cell is 0 A. The open circuit voltage is propotional to the band gap of the absorber layer. It can theoretical reach a value of 877 mV for a CIGSe solar with a band gap of 1.12 eV [15]. The V_{OC} values of real CIGSe solar cells are however limited to lower values mainly due to losses through non-radiative recombination processes.

11

- The filling factor FF of a solar cell is defined by $FF = V_{OC} \cdot J_{SC}/(V_{mpp} \cdot J_{mpp})$, where V_{mpp} and J_{mpp} are given by the voltage and current density of the solar cell where the highest power output is obtained (See Figure 1.3). The FF is typically limited by recombination and collection losses as well as trough the series and the parallel resistance of the solar cell.

- The power conversion efficiency PCE is defined by the fraction $PCE = P_{mpp}/P_{in}$, where P_{mpp} is given by the maximum power output found in the JV-curve and P_{in} is the incident power of the light. The PCE can be calculated from the other parameters by $PCE = J_{SC} \cdot V_{OC} \cdot FF/P_{in}$

The performance of a solar cell can be furthermore characterized by its series resistance R_S and its resistance in parallel R_P. The influence of R_S and R_P can be seen in 1.3 b). An impact of R_S can mainly be seen under sufficient forward bias. The differential resistance of a diode decreases exponentially with increasing forward bias. Hence, the series resistor, which is independent of the applied voltage, will dominate the total resistance of the device at a certain voltage. A significant portion of the applied voltage will drop over the resistor rather than over the diode. The influence of R_S does in most cases only affect the filling factor (and hence the PCE).

The parallel resistance of the solar cell should be as high as possible. The influence of the parallel resistance can be seen most clearly without illumination and under reverse bias (see Figure 1.3 a)). An ideal diode is blocking the current flow in this case, while some current will flow through the parallel resistor for a sufficiently low value of R_P. A low value of R_P mainly affects the filling factor. However, a serious shunting of the solar cell will also lead to a reduced V_{OC} value (the PCE is of cause also affected by the reduction of those two quantities).

Barriers in the solar cell can furthermore affect the measured JV-curve. A barrier at the back contact can typically be found at the Mo/CIGSe interface as visible in Figure 1.2. This barrier can be seen as a counter diode to the pn-junction. This counter diode will be biased in the reverse direction if a foward bias is applied. This can lead to a so-called roll-over effect as visible in Figure 1.3, where the exponentially growth of the dark JV curve stops at a certain voltage in forward direction, leading to a kink in the JV curve. However, the conductivity at the Mo/CIGSe interface is usually much higher than the conductivity of the pn-junction at room temperature. Such distortion are therefore only visible at low temperatures for typical CIGSe solar cells.

1.3 The CIGSe solar cell architecture

Figure 1.4 a) depicts a standard architecture used for CIGSe solar cells. The individual layers and their purpose will be discussed in the following.

A soda-lime glass (SLG) is typically used as the substrate of CIGSe solar cells. It provides the mechanical stability for the solar cell stack. SLG is usually the preferred substrate, not only due to the well-suited thermal expansion coefficient, but also because it provides a source of Na during the absorber preparation. Na has various beneficial effects on the absorber layer including an increase of the doping density [17]. Another advantage of glass-based substrates is the low roughness of the surface which otherwise can cause problems given the small layer thicknesses of the CIGSe absorber layer.
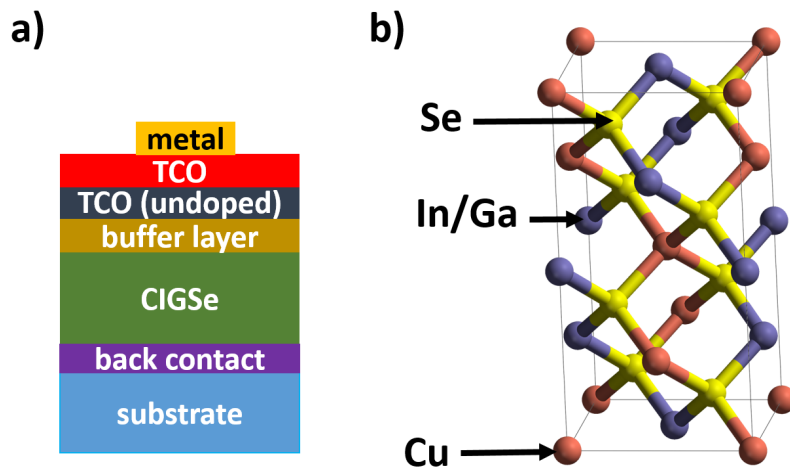
Figure 1.4: a) Typical layer structure of a CIGSe solar cell. b) Unit cell of the CIGSe chalcopyrite structure (picture from [16]).
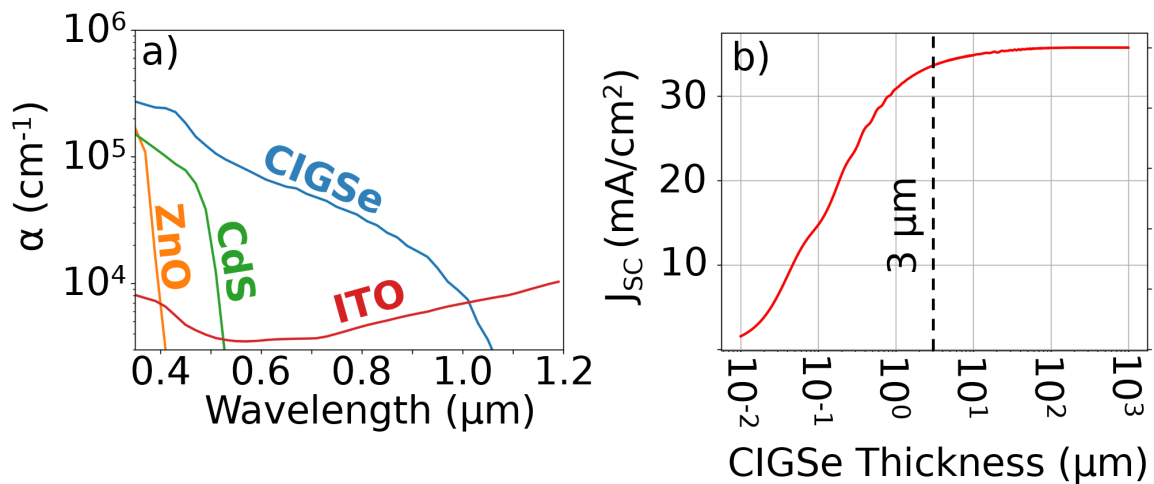
Figure 1.5: a) Absorption coefficients of various layers present in a CIGSe solar cell. b) Obtainable J_{SC} values of a CIGSe solar cell under the assumption of no electrical losses for different absorber thicknesses calculated via the TMM. The layer stack used in the calculation is (Mo/CIGSe/CdS(45 nm)/ZnO(200 nm)/ITO(200 nm)).

By far the most common used back contact material for a CIGSe solar cell is Mo. The reactivity with Se is sufficiently low in order to directly deposit the CIGSe on top of Mo. Only a thin layer of MoSe$_2$ is formed at the CIGSe/Mo interface. Most other metals are less suited due to the formation of thicker compounds of the metal and selenium. Furthermore, no Mo is diffusing in the absorber layer during the absorber layer deposition.

Cu(In, Ga)Se$_2$ is a semiconductor material based on a tetragonal chalcopyrite structure. A schematic of the unit cell is given in Figure 1.4 b). In and Ga share the same position in the unit cells. The fraction between In/Ga can be varied between 0 and 1. The band gap of pure CuInSe$_2$ is 1.02 eV and the band gap of pure CuGaSe$_2$ is 1.68 eV. The band gap can therefore be adjusted to the application purpose through the In/Ga ratio. The amount of Cu can also be adjusted to a certain degree, meaning that the chalcopyrite structure is in principle not altered for slightly Cu poor absorbers. The following two fractions are commonly used when discussing CIGSe based solar cells:

$$CGI = Cu/(Ga + In), \tag{1.10}$$

$$GGI = Ga/(Ga + In). \tag{1.11}$$

Typically targeted values for the CIGSe absorber are a CGI of 0.9 and a GGI of 0.3. The GGI is however in most cases only an averaged value given the fact that the GGI is usually depth-dependent. Stoichiometric CIGSe possesses a p-type doping, which is typically adjusted by the introduction of alkali metals. The most common deposition techniques rely on a thermal evaporation of the materials inside a vacuum chamber. A detailed explanation of the three-stage process employed in this work will be given in Section 2.1.1. The grain size of CIGSe absorber is influenced by various effects like the GGI of the absorber, the Na content and the deposition temperature [18, 19, 20, 21]. Rather small CIGSe grains (<100 nm) are typically obtained for low deposition temperatures around 500°C, while the CIGSe grains can be a few μm large at temperatures over 600°C (considering a GGI of 0.3)[18, 20]. The grain size of the CIGSe can have an impact on the electrical properties of the CIGSe due to increase or decrease of grain boundary interface area. However, it can also affect the optical properties of the solar cell. The roughness of the CIGSe surface will be transposed to some degree on the subsequent layers. The optical properties at the interfaces are effectively an average between the optical properties of the interface materials, if the roughness is significantly smaller than the wavelength of the light. The reflectivity at the CIGSe/buffer interface and all interfaces above is reduced due to the more gradual change of the refractive indices, which does increase the total absorption in the CIGSe absorber as a result [21]. Optical interference effects will also be reduced for rougher layers due to the random scattering at the interfaces [21].

CIGSe solar cells are usually prepared with a buffer layer between the CIGSe absorber layer and the front side TCO. The most commonly used material is CdS deposited by chemical bath deposition. CdS is a semiconductor with a band gap of 2.4 eV possessing an n-type conductivity. It is therefore part of the n-side of the pn-junction. One purpose of the CdS is the passivation of the front interface.

The window layer has to provide electrical conductivity to the front contact, while being as transparent as possible. It usually consists of a stack of two TCO layers. An undoped ZnO layer is commonly deposited on top of the buffer layer. This layer can avoid some local shunting in

the solar cells. While it is commonly used, it is not strictly required to obtain properly working solar cells.

After this, a TCO with a higher conductivity is deposited on top of the undoped ZnO, which is in most cases ZnO:Al. This layer completes the n-side of the pn-junction of the solar cell and provides the required lateral conductivity at the front contact. The thickness of the TCO is usually a balance between its parasitic absorbance and its electrical conductivity in lateral direction.

A thin metallic grid is often deposited on top of the window layers. It reduces the series resistance of the solar cell by providing an additional lateral conductivity, which is superior to the TCO conductivity. However, the metal blocks also a portion of the incoming light.

The absorption coefficients α of the materials used in the CIGSe solar cell stack are plotted in Figure 1.5 a). They were calculated using $\alpha = k \cdot 4\pi/\lambda$ from the extinction coefficients k taken from the literature for ZnO([22]), CdS([22]) and for CIGSe([23]) with a GGI of 0.33. The k values of the ITO are extracted from UV-VIS measurements as later explained in Section 3.4. The absorption coefficient of the ZnO is relatively high for wavelength up to 400 nm resulting typically in a complete absorption of the incoming light up to this wavelength. The CdS absorb light up to a wavelength of about 500 nm. The ITO posses on the other hand a lower absorption coefficient, which however extends over the whole regarded wavelength region. The CIGSe has a relatively high absorption coefficient as typical for direct bandgap absorber materials.

Figure 1.5 b) shows the calculated J_{SC} values for a complete CIGSe solar cell with a varying absorber thickness under the assumption that all generated charge carriers are collected. The J_{SC} values are calculated from TMM calculation for a layer stack consisting of a Mo/CIGSe/CdS(45 nm)/ZnO(200 nm)/ITO(200 nm) layer stack. An almost linear increase of J_{SC} can be seen in the semi-log plot up to a thickness of 1 µm, with some visible humps caused by interference effects in layer stack. CIGSe solar cells employ usually absorber thickness above 1 µm. A CIGSe solar cells with an absorber thickness of 3 µm and the standard Mo back contact reaches about 94% of the J_{SC} value limit obtained with very thick CIGSe absorber layers.

1.4   Relevant background knowledge

The following section gives an overview of relevant publications for this thesis. Generally, there are two major problems discussed for ultrathin CIGSe solar cells. Such solar cells often show increased electrical losses, which are often displayed as a reduced V_{OC} value besides the reduced short circuit current due to incomplete absorption. The poor electrical performance is typically explained by a higher impact of the back contact recombination for ultrathin absorber layers. The standard Mo contact is generally attributed having a high surface recombination velocity, while also having a rather low optical reflectivity at the CIGSe interface [3, 14, 24]. This low reflectivity leads to inevitable losses of photons by parasitic absorption, even when additional nanostructures are employed. The majority of research is therefore focused on either covering the Mo with a passivation layer or to replace the Mo entirely. Different strategies found in the literature will be given in the following.

1.4.1 Dielectric layers with local openings

One strategy to tackle the problem of parasitic absorption and recombination at the back contact is to cover the Mo with a dielectric layer. Layers of Al_2O_3 were studied extensively for Si solar cells as a surface passivation layer [25, 26, 27, 28] as well as for CIGSe solar cells [3, 24, 29, 30, 31, 32]. While dielectric materials can have excellent surface passivation properties, they lack of conductivity. Therefore, local openings have to be applied to the dielectric layer to enable charge carrier transport to the conductive part of the back contact. However, the diffusion length differ a lot between CIGSe and monocrystalline Si. Hence, the distance between the openings has to be much closer, due to the shorter diffusion lengths. The distance between the different openings is typically several 100 nm. Such structures have been shown in the literature, using several preparation techniques. These include the patterning of a thin oxidized Al film using e-beam lithography [33], the employment of nanoimprint [34], the deposition of Mo particles [29], and an approach based on particle rich CdS layers to create the local openings in an Al_2O_3 layer [35].

- Vermang et al. investigated Al_2O_3 passivation layers between the Mo back contact and absorber layer in several publications [24, 29, 30, 31]. In [35] Vermang et al. prepared nano sized openings with the help of CdS nano particles in an MgF/Al_2O_3 layer deposited on the Mo back contact. The average J_{SC} value was increased from 23.2 mA/cm^2 to 31.1 mA/cm^2 for a solar cell with a 400 nm absorber layer. The average V_{OC} value was at the same time increased from 576 mV to 633 mV.

- Jarzembowski et al. produced periodic openings in a SiO_2 layer using a laser interference lithography strategy, on Mo coated samples [36]. The J_{SC} value was increased from 18.4 mA/cm^2 to 23.7 mA/cm^2 for a solar cell with a 190 nm thick absorber layer. The V_{OC} value of the structured solar cell was with 597 mV higher than for the Mo reference with 569 mV.

- Van Lare et al. deposited a periodic array of SiO_2 nano particles on a Mo-covered sample using conformal imprint lithography [34]. The J_{SC} value was increased from 28.2 mA/cm^2 to 30.5 mA/cm^2 compared to the unstructured Mo-based solar cell for a 460 nm thick absorber layer. A similar V_{OC} value was measured for the patterned solar cell (592 mV) as for the unstructured solar cell (583 mV).

A summary of even more results of dielectric layers used for this purpose can be found in [3]. The beneficial influence of a dielectric layers was shown experimentally by numerous authors. A major obstacle for the industrial implementation of this structures is likely the preparation of hole openings in the dielectric layers. However, Vermang et al. showed already paths, which may allow the processing on industrial scales [30]. A limitation of the overall concept is the presence of Mo. The obtainable increase of J_{SC} is limited by the parasitic absorption in the Mo.

1.4.2 Highly reflective metals

The different strategies to include highly reflective metals (e.g. Ag, Au, Cu, Al), can roughly be divided into three approaches. A superstrate instead of the common substrate configuration can be used. The superstrate configuration has the inverse deposition sequence of the solar cell layers, e.g. starting with the deposition of the front contact [37]. Hence, the back contact

metal is deposited last, avoiding the exposure to the high-temperature process involved in the CIGSe deposition step. The second approach is the usage of a TCO back contact. The metal back contact can then be applied to the rear side of the glass substrate, after the full solar cell is finished. The lateral conductivity at the back contact in this case is only provided by the TCO, which usually has a much lower conductivity than a metal back contact. A third option is to cover the metal with a TCO layer, which acts as a diffusion barrier between the absorber layer and the metal back contact, while still providing an electrical connection between the metal back contact and the absorber layer.

- Bissig et al. investigated a back contact stack of Mo/Al/InZnO [38]. The goal of this study was to investigate the additional gain in J_{SC} through an increased reflection of the back contact for a 2 μm thick CIGSe solar cells. The solar cells exhibited a barrier-like behavior in the JV curves, leading to a decreased overall performance in respect to the Mo reference sample. This problem was absent for an additional sample prepared in the same run, which possessed a thin layer of MoSe$_2$ on top of the InZnO. Overall, an J_{SC} increase by 1.4 mA/cm^2 was observed in the experiment compared to the Mo reference, while the FF and the V_{OC} were on a similar level. Furthermore, a high-efficiency solar cell was prepared using a RbF post-deposition treatment (PDT) together with an MgF$_2$ anti-reflective coating (ARC) and a CIGSe absorber of 3 μm. The sample with the alternative back contact reached an efficiency of 19.9%, which is 0.4% absolute higher than the efficiency of the corresponding Mo reference. This gain was mainly archieved by the increased absorption in the portion of the absorber layer, having the minimum GGI and hence the minimum band gap.

- Gouillart et al. investigated Ag-based back contacts [10, 11]. A ZnO:Al/Ag/ZnO:Al/ITO /Al$_2$O$_3$ was successfully employed in CIGSe solar cells for deposition temperatures up to 550°C. The ZnO:Al layers did successfully block the diffusion of Ag, while the Al$_2$O$_3$ layer did create smother Ga$_2$O$_3$ layers at back contact. The efficiency of a CIGSe solar cell with an absorber thickness of 500 nm at a deposition temperature of 500°C was improved to 13.5% compared to the efficiency of the Mo-based reference cell with 12.5%. This gain was mainly attributed to an increase of J_{SC} from 26.2 mA/cm^2 to 28.9 mA/cm^2. The ITO samples exhibited poor performances for a deposition temperature of 550°C when they were tested without the Al$_2$O$_3$ layer.

- Sim et al. successfully prepared CIGSe solar cells using a Cu foil covered with a layer of graphene as the back contact [39]. An increase of J_{SC} of roughly 0.6 mA/cm^2 was archived for a CIGSe solar cell with a 1 μm absorber layer, comparing a sample with the Cu/graphene back contact with a sample based on a Mo covered foil. The overall efficiencies were low (9.9 % for the Cu/graphene back contact, 7.8% for the Mo-based back contact), which is however maybe related to a rather low absorber quality. The CIGSe layer was formed by sputtering of a CuGa and In target, followed by a selenization process.

- Yin et al. deposited a periodic array of SiO$_2$ nanoparticle on an ITO-based back contact using substrate conformal imprint lithography [40]. The J_{SC} value was increased from 25.7 mA/cm^2 to 30.5 mA/cm^2 compared to the flat ITO-based sample with a 390 nm thick absorber layer. A 200 nm thick Ag layer was additionally deposited at the rear of the solar cell, leading to a J_{SC} value of 32.4 mA/cm^2. The efficiency of the solar cell with the unstructured ITO was with 6.8% relatively low due to low V_{OC} (518 mV) and FF (50.7%) values. A barrier at the back contact, which was concluded from temperature dependent, JV measurements, was used to explain those low values. Both values improved

by the SiO_2 nanostructure together with the Ag reflector to a V_{OC} value of 558 mV and a FF value of 55.2%, which was explained through a reduced barrier at the back contact, induced by the structuring. Finally, a sample was produced, combining the Ag reflector, the SiO_2 nanostructure and an anti reflective coating. This sample reached an impressive J_{SC} value of 34.0 mA/cm^2 with an absorber thickness of 390 nm.

- Mollica et al. prepared bifacial solar cells based on ZnO:Al and SnO_2:F back contacts [7]. The 450 nm thick absorber layer was deposited using a single-stage process with a substrate temperature ranging between 500 °C and 550 °C with a NaF post deposition treatment. The bifacial solar cells have been measured with a black surface underneath the solar cell, as well as on a Cu surface. The samples placed on the Cu surface exhibited an increased J_{SC} value compared to the samples placed on the black surface (25.5 mA instead of 22.3 mA for the ZnO:Al back contact, and 25.9 mA/cm^2 instead of 22.3 mA/cm^2 for the SnO_2:F back contact). Higher J_{SC} values were obtained in all cases compared to the Mo reference sample with 21.3 mA/cm^2. Lower V_{OC} values were obtained for the ZnO:Al-based sample (623 mV) and for the SnO_2:F-based sample (630 mV) than for the Mo reference (651 mV). The ZnO:Al-based sample exhibited with 58% a lower FF than the Mo reference (74%) and the SnO_2:F-based sample (72%). Lower J_{SC} values were obtained for illumination through the rear, with -5.3 mA/cm^2 for the ZnO:Al-based sample and -10.6 mA/cm^2 for the SnO_2:F-based sample in respect to the results under front illumination. The back contact recombination velocity was determined, by calculating rear measured EQE curves for different back contact recombination velocity values from an analytical model, which was then compared to the measured EQE curves. The back contact recombination velocity was determined to be in the 10^7 cm/s range for the SnO_2:F-based sample and 10^5 cm/s range for the ZnO:Al-based sample.

The successful implementation of highly reflective metal reflector in CIGSe solar cells was demonstrated in the literature. A common problem is the presence of a TCO/CIGSe interface. This interface acts as the n side of the pn-junction in case of the superstrate configuration. One of the major challenges of this concept is the lower quality of this interface compared to solar cells prepared in the more common substrate configuration, which results in lower efficiencies [41]. This is likely the reason why currents works on this topic do not use this approach. The other two options offer configuration, were most CIGSe research on the implementation of highly reflective back contacts is based on. The literature results highlight the difficulties of obtaining good electrical properties for the TCO/CIGSe interface at the back contact. This problem is even more pronounced for increasing temperatures. It was shown that this problem can be tackled using additional layers like a $MoSe_2$ layer [38], which unfortunately increase the overall preparation complexity. The literature is however missing an implementation of those highly reflective metallic back contact combined with an additional scattering element. Such a configuration could enable a significant reduction of the CIGSe thickness, without a reduction of J_{SC} and ideally with no higher series resistance compared to solar cells with the more common Mo back contact. The implementation of this concept was investigated in this thesis. The approach is the implementation of a scattering element through the structuring of the substrate on which the full CIGSe solar cell layer stack is then deposited on.

1.4.3 Bifacial solar cells

A selection of further results regarding bifacial CIGSe solar cells is given in the following.

- Nakada et al. tested several TCO materials (SnO$_2$:F, ITO, ZnO:Al) as the back contact material for CIGSe solar cells deposited at varying temperatures [5]. The highest *PCE* (15.2%) was achieved with an ITO back contact and a deposition temperature of 520 °C, for an absorber thickness of 2 μm. The *PCE* decreased for the ITO-based back contact at deposition temperatures above 520 °C was mainly caused by a reduction of the *FF*. The formation of a thin layer of Ga$_2$O$_3$ layer was observed at the ITO/CIGSe interface and brought forward as the likely cause. In the case of the SnO$_2$:F back contact a steep reduction of the *PCE* was found for deposition temperatures above 500 °C. The resistivity of the SnO$_2$:F back contact layer increased rapidly above a temperature of 500 °C due to a loss of the dopant fluorine.

- Keller et al. investigated hydrogen-doped In$_2$O$_3$ (IOH) layers as the electrical back contact for CIGSe solar cells, with an absorber thickness of 650 nm [8, 9]. In [9], Keller et al. compared the solar cell performance of bifacial solar cells for different thicknesses of the IOH layer. Additionally, all IOH layers and the Mo references were tested for three different sample treatments before the absorber deposition (no treatment, NaF deposition, NaF deposition + an Al$_2$O$_3$ layer). The highest efficiency (11%) for the different IOH layer configurations was obtained for the thinnest IOH layer (210 nm) with the NaF PDT. Similar V_{OC} values (680 mV) and J_{SC} values (24.9 mA/cm^2) have been obtained compared to the Mo reference sample (V_{OC} = 697 mV, J_{SC} = 24.6 mA/cm^2). While the *FF* was lower for the IOH-based sample (64.9%) than for the Mo reference (76.7%). Bifacial measurements showed strongly reduced EQE values for measurements through the rear TCO. The lowest losses (-6 mA/cm^2), comparing the results for front and rear illumination, have been obtained for the sample with a 340 nm IOH layer and with an Al$_2$O$_3$ layer and NaF deposition. Keller et al. furthermore tried to assess the back contact recombination velocity from rear EQE measurements in combination with optoelectrical simulations. A detailed analysis showed, however, that such an evaluation is not applicable, since the influence of the diffusion length is rather similar to the influence of the back contact recombination velocity.

1.4.4 Optical simulations

Following publications discuss the potential gain in J_{SC} (under the assumption of no electrical losses) based entirely on 3D optical calculations.

- Krc et al. performed in [4] optical simulations, to investigate the potential short circuit increase through the optimization of various properties of CIGSe solar cells. The potential gain in J_{SC} through the implementation of a scattering element at the various interface was analyzed for a solar cell with an ideal reflector at the back contact. The largest gains were obtained for an introduction at the CdS/CIGSe (+17.8%) and CIGSe/back contact interface (+17.4%) for a solar cell with a 300 nm absorber layer. 3D simulations were furthermore conducted for a nanostructured CIGSe solar cell (300 nm absorber) with a semi-ellipsoidal shape and an ideal reflector. The encapsulation and the front side glass were also included in the simulations. The highest gains were obtained for a pitch of 400 nm - 600 nm with a structure height of 300 nm and for a pitch between 500 nm - 900 nm with a structure height of 600 nm. The simulations show that current densities over 33 mA/cm^2 should be possible for such solar cells.

- Kovacic et al. investigated in [42] the impact of various scattering structures on the potential short circuit density in CIGSe solar cells, through 3D optical simulations. All structures were calculated for a standard $Mo/MoSe_2$ back contact as well as with an Ag/Al_2O_3 back contact. The simulations included three back contact structures (a sine-like, a u-like, and a negative u-like) as well as a light-trapping structure at the front interface of the solar cell. Two of the back contact structures (sine-like, u-like) and the front interface light-trapping structure archived potential J_{SC} values above 34 mA/cm^2 for an absorber thickness of 500 nm. These values exceeded the J_{SC} value of the unstructured solar cell (33 mA/cm^2) with the standard Mo back contact and an absorber thickness of 1800 nm.

Chapter 2

Methods

2.1 Experimental methods

2.1.1 Preparation of CIGSe solar cells

Figure 2.1 shows a picture of the evaporation chamber used for the CIGSe deposition. A diffusion pump is connected to the chamber which evacuates the chamber to a pressure of about 10^{-7} mbar prior to the sample preparation.

The samples are mounted upside down on a rotary disk in the upper part of the chamber. The samples are constantly rotated during the deposition process to improve the homogeneity of the deposited CIGSe layers. A thermal heater is situated above the sample holder to heat the samples to the desired temperature. This temperature is controlled by a PID controller, using a thermocouple resting on top of the sample back during the deposition. The heater temperature is furthermore monitored by a thermocouple resting on the heater itself.

The evaporation of the materials is done using thermal evaporation sources, with one evaporation source for each material evaporated. Furthermore, a laser light scattering system is installed. Two lasers with different wavelengths (650 nm and 1550 nm) are directed onto the sample. The scattered light is then measured by a detector situated at the opposite side of the chamber.

A so-called three-stage process was employed to prepare the CIGSe layers with will be explained in the following. The process consists of three different deposition steps, which are shown in Figure 2.2 for the deposition of an ultrathin absorber layer. In the first step, a precursor layer of $(In, Ga)_2Se_3$ is deposited. In, Ga, and Se are evaporated during this step, whereas the sample is heated to a temperature of 450 °C. During this step oscillations of the scattered laser-light signal can be measured which are connected to the layer growth by thin-film Fabry-Perot interferences. The determination of the layer thickness allows an adjustment of the deposition time to take into account the different growth rates typically experienced between different CIGSe deposition runs. A complete oscillation corresponds to a thickness increase of roughly 180 nm of the final CIGSe layer (GGI = 0.3) with the employed wavelength of 650 nm for the laser light. The control of the layer thickness using this method is challenging when the targeted layer thickness is lower than 500 nm due to the low number of oscillations. A fixed time, calculated from the growth rate of thicker absorber layers was therefore used in such a case. The final thickness of the layers was then measured using using SEM cross sections.
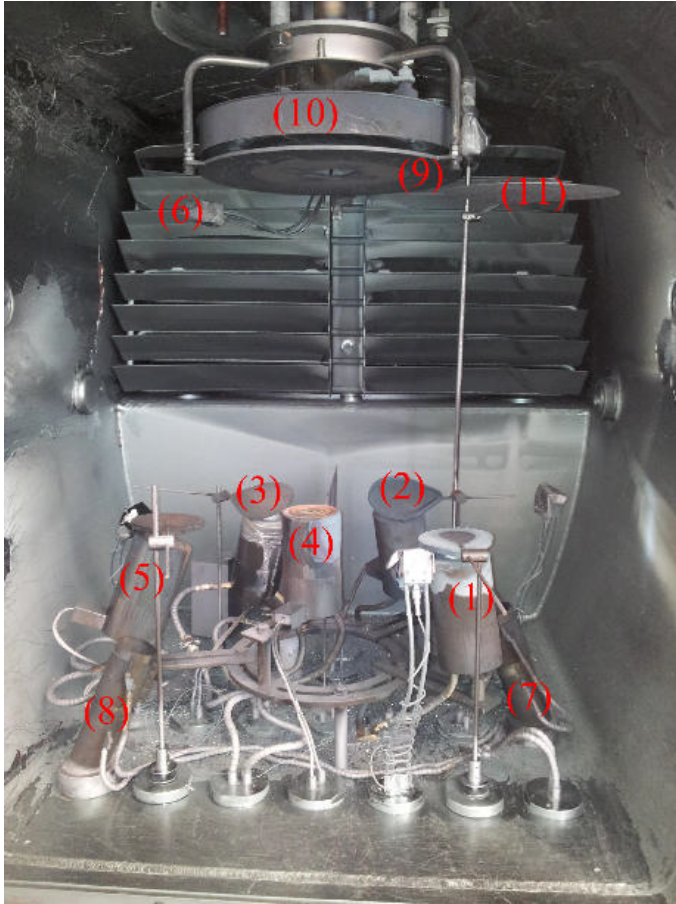
Figure 2.1: Picture of the inside of the vacuum chamber employed for the CIGSe deposition. The number represent:
(1) Cu source,
(2) Ga source,
(3) In source,
(4) Se source,
(5) NaF source,
(6) quartz crystal microbalance,
(7) laser light source,
(8) laser light detector,
(9) sample holder,
(10) sample heater,
(11) substrate shutter.

Only Cu and Se are evaporated in the second deposition step. The sample temperature is increased to a higher temperature at this step (between 480 °C and 600 °C in this work). This temperature is kept up to the end of the third step. During the second stage, the CIGSe is formed. The time where the CIGSe reaches a stoichiometric Cu content can usually be detected using two signals. Both are related to the fact that a layer of $CuSe_2$ will grow on top of the CIGSe, as soon as sufficient Cu is present to form a stoichiometric CIGSe layer. First of all, a steeper increase of the laser-light signal can be seen due to the increased roughness of the substrate caused by the formation of $CuSe_2$. This signal was routinely visible for the deposition of regular thick absorber layer (2.8 μm) but not observed when ultrathin absorber layers were deposited, supposedly due to a too low intensity. The roughness increase does however also cause an increase of the emissivity of the sample, which can be detected because the sample heater has to adjust to a higher power output to ensure a constant sample temperature. A temperature increase is therefore measured on the thermocouple which is resting on the heater itself (see the first cross in Figure 2.2). The Cu evaporation rate can be calculated from the time span required to reach the stoichiometric point, under the assumption that the Cu evaporation rate is constant throughout this stage. This fact is used to adjust the time of the second stage to the point where the CGI reaches a value of 1.09. After this, the evaporation of Cu is stopped and the same materials as in the first step are evaporated again.

The Cu content is reduced in the third deposition phase again until the desired CGI is reached, which is typically a value around 0.9. The point where the sample is stoichiometric again can be detected through a kink in the laser light signal (see the second cross in Figure 2.2) as the $CuSe_2$ is incorporated into the sample.

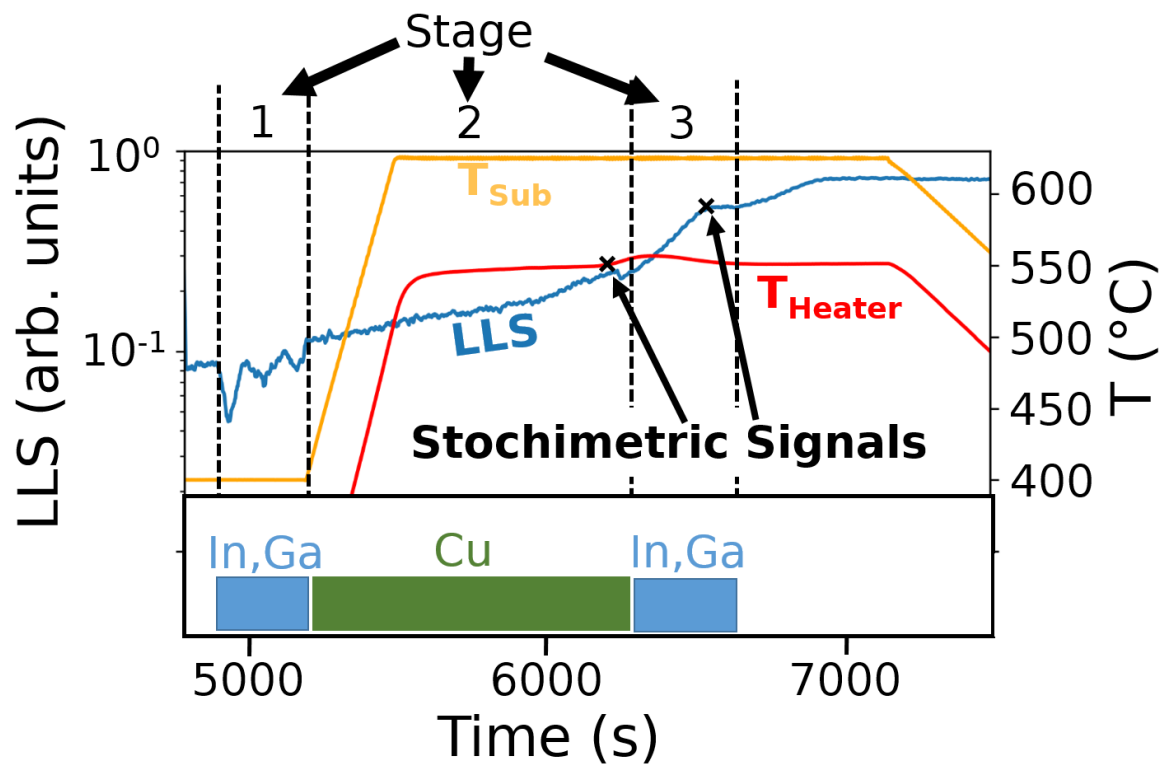Figure 2.2: Laser light signal (LLS) during the deposition of an ultrathin CIGSe solar using a three-stage process, together with the temperature of the substrate T_{Sub} and the temperature measured at the heater T_{Heater}. The two crosses mark the position, where a signal origination from the first and second stoichiometric point is visible, in the T_{Heater} and laser light signal respectively.
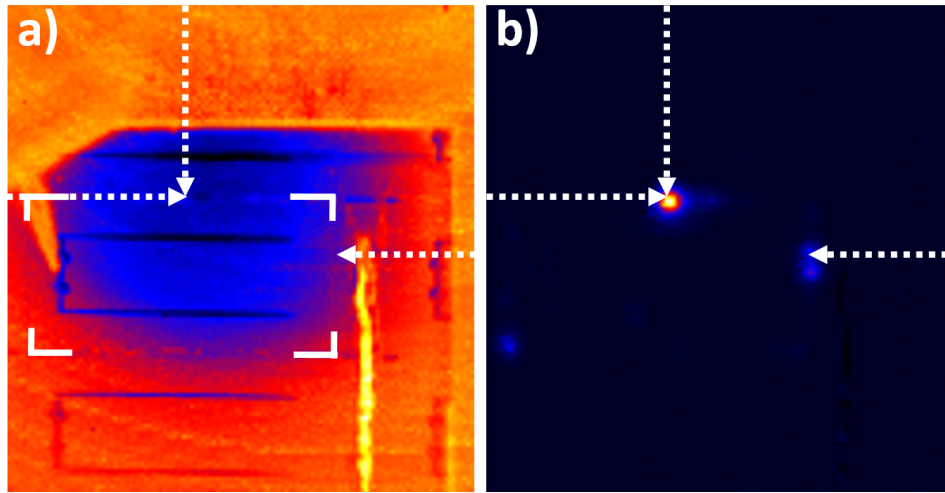
Figure 2.3: Lock-in thermography images of a CIGSe solar cell with an Al/ITO back contact, which was defined by mechanical scribing. a) Absolute temperature signal of the sample surface as seen from the lock-in thermography camera. The white rectangle shows the circumference of a solar cell. The dotted lines are plotted as a visual aid. b) Lock-in thermography signal at the same position as in a). The dotted lines are at the same position as in a).

A NaF post-deposition treatment (PDT) was performed on all samples in this work. The sample temperature is reduced to 450 °C directly after the CIGSe deposition. NaF is then deposited on top of the sample, while Se is still being evaporated over the whole time. The NaF is diffusing in the CIGSe layer due to the elevated temperature.

CdS was deposited after the absorber layer preparation using a chemical bath deposition process. The thickness of this layer was estimated to be around 40 nm from the characteristic dent in the EQE curves caused by the parasitic absorption of the CdS layer. The samples are loaded into a sputtering deposition chamber afterwards. First, a layer of ZnO is deposited with a typical thickness of 120 nm. The deposition is performed at a pressure of $6 \cdot 10^{-3}$ mbar in Ar atmosphere at room temperature. The ITO layer with a typical thickness of 240 nm is then deposited at a pressure of $1 \cdot 10^{-3}$ mbar in Ar atmosphere, also at room temperature. Finally, the front metalization is applied using e-gun evaporation in the same chamber. A Ni/Al/Ni layer stack is deposited through a shadow mask. The samples are rotating in the chamber during the TCO and front metalization deposition to ensure homogeneous results.

The completed layer stacks were divided into several solar cells with an average area of 45 mm^2. Commonly this is done by a mechanical separation using a blade, locally removing all layers above the back contact. However, solar cells based on alternative back contacts separated this way suffered from a strong shunting of the solar cell.

Lock-in thermography images revealed the existence of local shunts at the scribe positions as can be seen in Figure 2.3. A possible explanation for this can be seen in the SEM picture of Figure 2.4 a). The scratch position of the blade can be clearly seen in this figure. The solar cell stack was not properly removed at this position, a portion of the stack was lifted from the surface instead. This lifted portion can create an electrical connection between the front and rear contact and therefore shunt the sample.

Therefore, another cell separation was developed and employed, which can be seen in Figure 2.4 b). HCl was applied to the front surface of the solar cell using a very fine paintbrush. The HCl removes all layers above the CIGSe layer by etching. A removal of the CIGSe layer is not
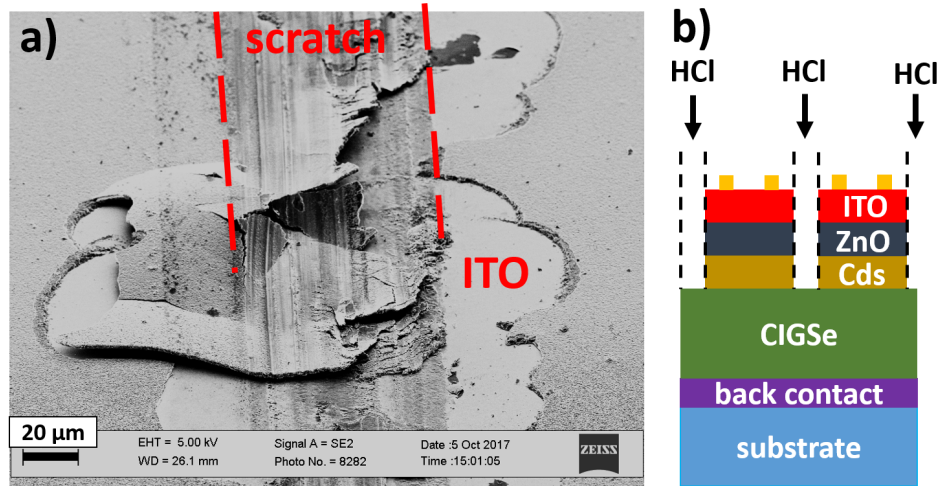
Figure 2.4: a) SEM picture of the surface of a CIGSe solar cell with an Al/ITO back contact along a mechanical scribe. b) Sketch of the employed cell definition method based on chemical etching of the window layers using HCl.

necessary to separate the solar cells. The diffusion length in the CIGSe absorber layer is much shorter than the dimensions of the solar cells, hence charge carrier created in the area outside the TCO covered area cannot contribute to the JV curves.

2.1.2 Preparation of nanostructured back contacts

Structured back contacts were prepared by laser interference lithography (LIL). Figure 2.5 shows a schematic of the created solar cell structures. A SiO_2 layer with circular opening was prepared on a Mo-covered substrate. Those holes are located on a hexagonal pattern. The full solar cell stack is then deposited on top of this structure, creating a nanostructured solar cell.

The process to create the SiO_2 structures involves the preparation of an array of photoresist pillars. These sacrificial pillars fulfill the purpose of a shadow mask for the SiO_2 deposition. An overview of all the involved process steps will be given to the reader. Afterwards details about the processing steps will be discussed. Figure 2.6 shows the separate steps to prepare the SiO_2 nanostructures. Those steps are (see Table 2.1):
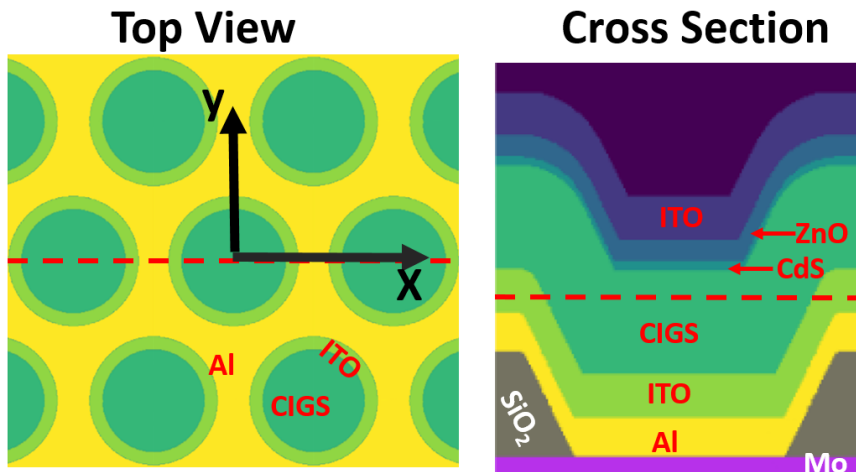
Figure 2.5: Schematic representation of the prepared nanostured solar cells. The left picture gives a top view, while the right picture is viewed from the side. The dashed lines in the left picture defines the cross section from which the right picture is situated. The dashed line in the right picture does the same for the left picture.
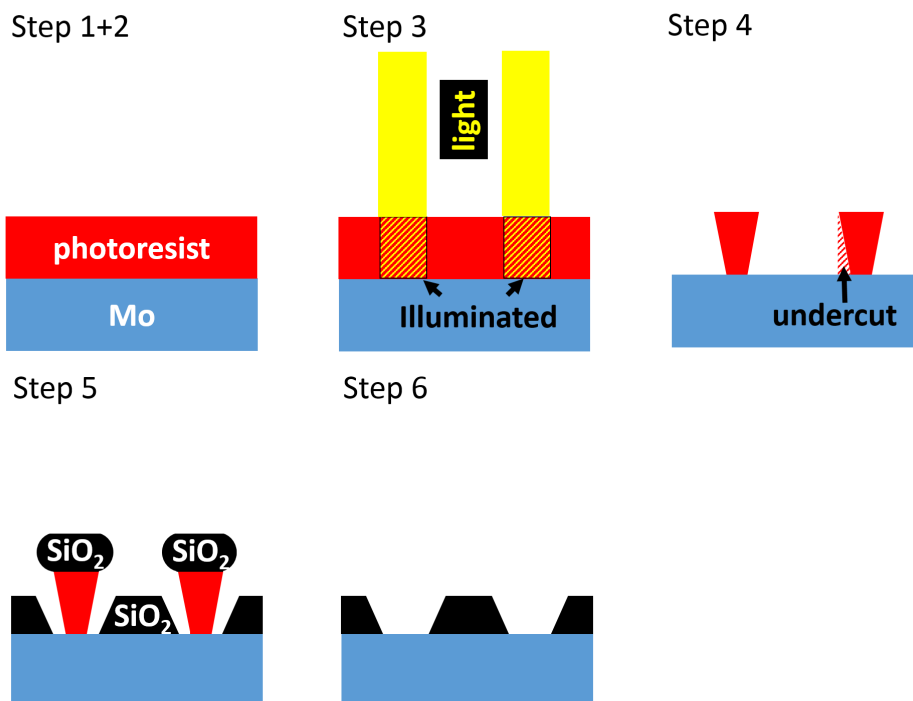

Figure 2.6: Sketch of the separate steps involved in the preparation of the SiO_2 nanostructures.
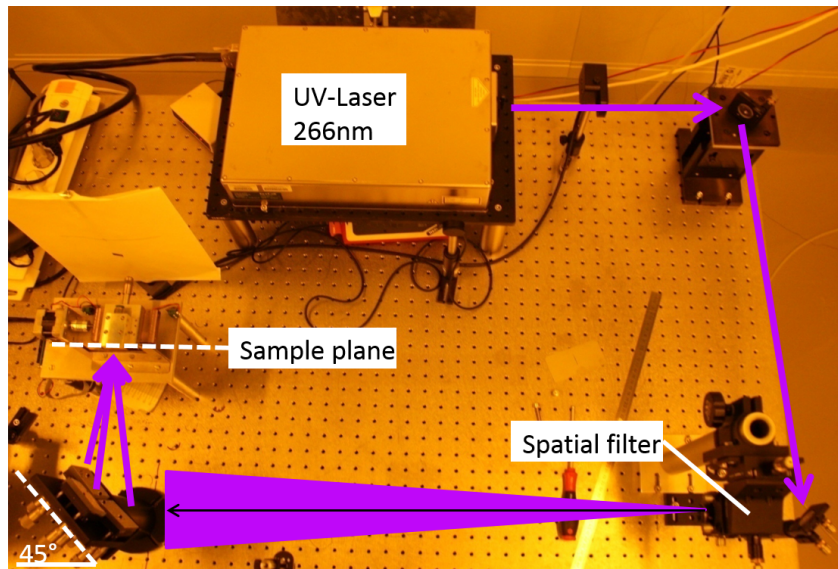
Figure 2.7: Picture of the LIL setup used. The purple arrows display the path of the UV laser beam.

Table 2.1: Overview on the employed steps to prepare SiO_2 nanostructures.

Step	
1	Deposition of an adhesion promoter (AR 300:80) via spin coating followed by an annealing step at 180 °C for 3 min on a heat plate.
2	Deposition of a negative photoresist (ARN 4240), with a thickness of approximately 700 nm via spin coating. Afterwards an annealing step at 90 °C for 20 min is conducted on a heat plate.
3	Illumination of the sample using LIL to illuminate a hexagonal array of circle-shaped areas. A post exposure bake is performed afterwards by annealing of the samples at 85 °C for 5 min on a heat plate.
4	Dipping of the samples into a photoresist developer (AR 300-475) to remove the areas of the photoresist which did not receive sufficient illumination in step 3.
5	SiO_2 is deposited using e-beam evaporation.
6	The remaining photoresist is removed using acetone at 50 °C for 30 min using an ultrasonic bath.

In the following, the steps are explained in more detail.

Step 1: The adhesion promoter in step 1 is used to improve the wetting behavior and adhesion of the photoresist. The heating steps after the deposition of the adhesion promoter and photoresist improve the layer quality and helps with the desorption of water.

Step 2: The thickness of the photoresist was optimized for the process by adjusting the spin rate of the spin coater together with the amount of thinner added to the solution. A general rule is that the photoresist thickness needs to be thicker than the SiO_2 thickness. Otherwise, the SiO_2 deposited on top of the photo resist pillar will merge with the SiO_2 deposited on the Mo surface (see Figure 2.6 step 5). Such a merging could hinder the lift-off completely.

Step 3: The employed LIL setup can be seen in Figure 2.7. An UV-laser emits a beam with a wavelength of 266 nm, which is then redirected by two mirrors. Afterwards, the light passes a
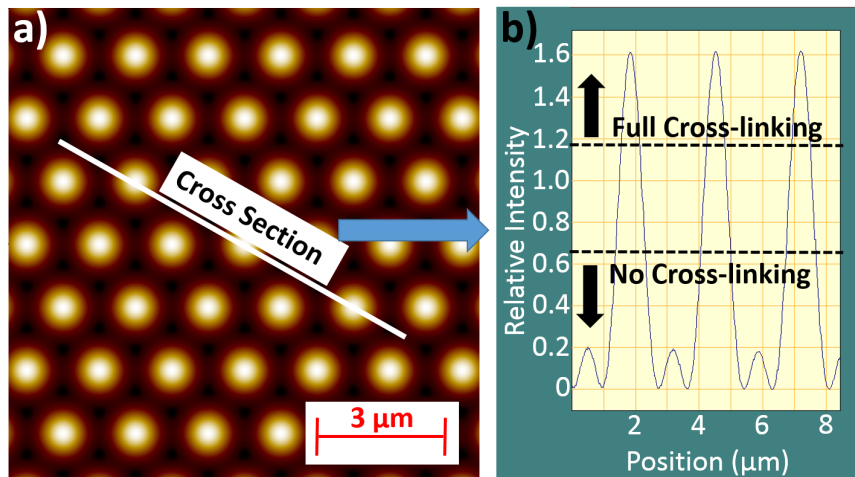
Figure 2.8: Calculated intensity profile of the LIL setup as viewed from above the sample surface (left), together with the intensity profile alongside the cross section (right). The two lines define two special intensity levels for the given photoresist and exposure duration. A complete cross-linking of the photoresist happens in regions, where the intensity surpasses the upper line. the second line represents the intensity, where not even the surface of the photoresist reaches enough intensity to cross-link.

spatial filter. The spatial filter creates a wider divergent beam with a "clean" intensity profile. The divergent beam is hitting a set of three mirrors, which redirect the light on the sample. The interference of the three reflected beams creates an interference pattern on the sample surface location as visible in Figure 2.8. The LIL method allows an adjustment of the pitch of the structure through an alignment of the three mirrors. The tilting of the mirrors is adjusted using three micrometer screws located on the back of each mirror. The resulting interference pattern were calculated using a computer program.

An important quantity in this context is the light dose, which is defined by the power density of the light source multiplied by the exposure time. A chemical reaction called cross-linking does occur within the photoresist during the post exposure annealing, but only in regions that received a sufficient light dose. This cross-linking process decreases significantly the solubility of the material in the developer solution (see Step 4).

To understand the resulting structure after the application of the photoresist developer, it is important to understand the light intensity profile, which the sample receives in Step 3. Figure 2.8 a) shows a calculation of the light intensity distribution, created by the LIL setup at the surface of the photoresist. Figure 2.8 b) gives furthermore the intensity profile alongside a dedicated line along the surface. The intensity profiles has major peaks with along smaller peaks in between having approximately 1/8 of the intensity of the major peaks.

Figure 2.8 b) only represents the light intensity at the surface of the photoresist. The light intensity in deeper layers of the photo resist will be reduced, due to an absorption of the light in the photoresist (note that this fact is not strictly true due to the occurrence of interference phenomena). Hence in some parts of the photoresist, only the upper part of the photoresist will receive the sufficient light dose to cross-link. Two lines are marked in Figure 2.8 b). The upper line denotes the required intensity for a certain exposure time, at which the photo resist receives sufficient light to cross-link over its full thickness. A second line denotes the intensity, where for the given exposure time no cross-linking occurs at all. For an intensity in between

these two lines, only the photoresist closer to the surface will receive the sufficient light dose to cross-link. This helps to understand the phenomena of the so-called undercut, a reduction of the pillar width closer to the substrate (see Figure 2.6 step 4). This undercut is essential for the whole structuring process.

Step 5: The SiO_2 deposition source is kept as close as possible to the normal direction of the sample surface to avoid any deposition of SiO_2 on the sidewalls of the photoresist pillars. The photoresist pillars are sacrificial structures which act practically as a shadow mask for the SiO_2 deposition on the Mo surface.

The SiO_2 on top of the pillars is not only growing in the normal direction to the surface but also in the lateral direction (see Figure 2.6 step 5). This is equal to a widening of the top part of the pillars, and hence to a widening of the "shadow mask". This effect leads eventually to a sloping of the sidewalls of the SiO_2 located on the Mo.

Step 6: During step 6, the photoresist pillars are removed together with the SiO_2 resting on top. This step is called the lift-off step. The solution needs to be able to access the photoresist pillars to remove the photoresist pillars. For this purpose, the aforementioned undercut is of importance. No SiO_2 will grow on the sidewalls of the photoresist pillars due to the sloping of the photoresist pillar base, as long as the SiO_2 deposition source is positioned with no tilting against the surface normal.

The failure rate of the lift-off step does increase if the undercut is only small. The obtainable structures are limited by the lateral growth of SiO_2 on top of the pillars. The probability of a successful lift-off does decrease when the SiO_2 on top of the pillars does merge between the different pillars.

2.2   Characterization methods

2.2.1   Glow discharge optical emission spectroscopy (GDOES)

GDOES measurements were used to characterize the depth dependence elemental distribution of CIGSe absorber layers. A sputtering processes is used to remove the sample material. The plasma used for the sputtering process is created in a small volume, which is connected to the sample surface on a circular area with a diameter of about 2 mm. The sample is pushed against a rubber ring resting on top of the sputtering chamber to create an airtight connection between the sample surface and the sputtering chamber. This chamber was evacuated and then filled with Ar gas until a pressure of 4.2 hPa was reached. The sample surface is then removed via a sputtering process at a rate of about 20 nm/s. The particles removed from the sample diffuse to the plasma and there the electrons of those atoms get lifted to an excited state by the energy of the plasma. The emitted light after the relaxation of those electrons, which is characteristic for a specific element, is analyzed using a spectrometer. The light is diffracted on a holographic grating and then measured by a combination of detectors based on photomultiplier tubes and charge-coupled devices (CCD). The intensity of the measured spectra can then be translated into a molar density, by measuring several samples of known composition, but with different relative concentrations of the involved elements. A GDA 750 of Spectruma Analytik was used for the GDOES measurements. All materials of interest (Cu, In, Ga, Se, Na, Zn, Al) were calibrated by the manufacturer.

2.2.2   Ultraviolet-visible spectroscopy (UV-VIS)

UV-VIS measurements were used to measure the transmittance and reflectance of TCO layers. An UV-VIS-IR spectrometer (Lambda 900 from PerkinElmer) was used. No integration sphere was used during the measurements. However, the results of one of the glass/ITO samples were cross-checked using another setup with an integration sphere. The differences in transmission and reflection were found to be very low (deviation <1% absolute), which means that the diffuse scattering is sufficiently low.

2.2.3   Solar cell characterization

All prepared solar cells have been analyzed using a home-built sun simulator. The samples are resting on a copper plate during the measurements, which is cooled by a Peltier element to 25 °C to ensure that the solar cells are in the right working condition. The current-voltage curves (JV curves) are measured using a four-wire connection with needles placed on the samples. A Keithley 2400 source-measure-unit was used to measure the JV curves. Illuminated JV curves were conducted using a halogen light source. The intensity of the light source was calibrated to AM1.5G like conditions using a calibrated Si solar cell with a known short circuit density under AM1.5G conditions. A shadow mask with an area of 0.307 cm^2 was employed to define the total illumination area on prepared solar cells. The mask was not used for solar cells with a smaller total area as the shadow mask.

CIGSe solar cells show typically metastable properties, which change when the sample is being illuminated and typically revert back again after the illumination is removed [14]. This creates a difficulty with the exact characterization of the solar cells. The V_{OC} value typically increased after several minutes of illumination. The degree of the changes can be different from sample to sample. Small differences in the solar cell parameters can therefore be created simply by the fact that a sample was subjected to illumination for a longer time. All samples presented in this work were illuminated for at least for one hour to avoid that the solar cell parameters are affected by the measurement time of a sample, which would be difficult to control. Tests showed that only very small changes of the parameters occurred after this time span.

The external quantum efficiency (EQE) was measured using a commercial system. The expected short circuit current density was usually calculated from the EQE curves under AM1.5G condition. This value is not affected by the spectra of the halogen light in contrast to the JV measurements. A halogen light has compared to the sun a higher portion of its intensity at longer wavelengths. Hence losses in this region will be over-represented with a halogen lamp. Furthermore, the determination of the cell area can cause an additional error. While both the area error and the spectra error are avoided for the determination of the J_{SC} value via EQE measurements, it must be noted that the J_{SC} value from EQE does not include the reduction of the J_{SC} value by the shadowing from the metal contacts.

Temperature-dependent JV curves and admittance measurements were performed inside a chamber with a connected cryostat. The compared samples (Mo vs ITO back contact), were measured always simultaneously. Samples were glued to a metallic sample holder for this purpose. The connections to the sample were established using bonding contacts in four-wire configuration. The temperature was measured directly at the sample surface of each sample individually. JV curves were measured also with a Keithley 2400 source-measure-unit. The illuminated JV measurements were performed using a xenon-arc lamp, with the illumination calibrated to AM1.5G conditions, in the same manner as the other JV measurements.

2.2.4 Scanning electron microscopy (SEM) & energy-dispersive X-ray spectroscopy (EDX)

SEM measurements have been performed using a SUPRA 40VP from Zeiss. The composition of the samples was determined using EDX measurements. All EDX measurements were conducted with an acceleration voltage of 15 kV.

2.2.5 Admittance spectroscopy

The admittance Y of a sample is given by the inverse of the impedance Z of the sample:

$$Y = \frac{1}{Z} \tag{2.1}$$

An impedance analyzer can be used to measure both the absolute value of the impedance Z, as well as the corresponding phase shift ϕ between the current and the voltage. It is rather common for analysis purposes not to use the impedance (or admittance) of the sample, but instead to employ an equivalent circuit formed by a capacitance with a parallel resistor, which represents the sample. The admittance in complex notation of such a circuit is given by

$$Y = G + i\omega C \tag{2.2}$$

with the measurement frequency $\omega = 2\pi f$. The conductivity G and capacitance C can therefore be calculated by

$$G = \mathrm{Re}(Y) \tag{2.3}$$

and

$$C = \mathrm{Im}(Y)/\omega. \tag{2.4}$$

Note that the determined capacitance C is only representing the capacitance of the device correctly if the equivalent circuit is applicable to the sample. A series resistance will always be present in the sample due to the electrical connections. The admittance of a capacitor with a parallel resistor and a resistor in series to both is given by

$$Y = \frac{G + R_s G^2 + R\omega^2 C^2 + i\omega C}{1 + 2R_s G + R_s^2 G^2 + R_s^2 \omega^2 C^2}, \tag{2.5}$$

with the series resistance R_S. The computation of $\mathrm{Im}(Y)/\omega$ will therefore yield for this circuit

$$\mathrm{Im}(Y)/\omega = \frac{C}{1 + 2R_s G + R_s^2 G^2 + R_s^2 \omega^2 C^2}. \tag{2.6}$$

The computation of $\text{Im}(Y)/\omega$ will therefore only yield the capacitance of the device if both the conditions $R_S G \ll 1$ and $R_s^2 \omega^2 C^2 \ll 1$ are met. The first condition is usually fulfilled for a non shunted device, while the second condition will often not be fulfilled for high measurement frequencies around 1 Mhz. This can lead to an apparent drop of the determined capacitance at higher frequencies. The total capacitance of a sample is proportional to the measured area of the sample. The second condition can therefore still be fulfilled at higher frequencies if the area of the sample is reduced.

The admittance of a sample will be modified by several properties of the sample including defect states, the doping density, and the presence of barriers. The effect on the admittance of those various effects can be however quite similar. For example, a defect signal can be mistaken for a transport barrier and vice versa. The interpretation of admittance measurements is therefore rather challenging.

Admittance measurements were conducted using an Agilent E4980A LCR meter. Those measurements were performed in the same cryostate chamber as the JV(T) measurements.

2.2.6 Lock-in thermography

Lock-in thermography measurements were used to investigate completed solar cells for local shunts. Heat will be generated in a solar cell if a voltage is applied to it. The additional heat generation in the solar cell through the applied voltage is given by $P = JV$. This heat generation would be homogeneous over the whole area of the solar cell in the case of a shunt-free solar cell (assuming homogeneous layers). Local shunts increase the current flow at the position of the shunt. Hence, an increased amount of heat will be generated at shunt positions. The temperature of the sample is measured using an infrared camera with a CCD sensor, which can provide a spatial image of the sample. The voltage applied to the sample is not constant, but it is instead modulated by the voltage source. The voltage modulation will cause a modulation of the temperature. Through the lock-in technique, both the voltage modulation and temperature modulation can be correlated to measure very small temperature changes of only a few mK. Shunts in the solar cell are visible as brighter spots in the thermography image. The measurements were conducted using a home-built system.

2.3 Simulation methods

2.3.1 Transfer-matrix-method (TMM)

The transfer-matrix method is a commonly used method to calculate the propagation of light in 1D layer stacks systems. The light in each layer is represented by a plane wave propagating in forward direction plus a plane wave propagating in the opposite direction. A layer stack with N layers will be considered in the following (see Figure 2.9). In the layer n, the amplitude of the electric field in forward direction will be denoted as v_n, while the amplitude of the electric field in reverse direction will be denoted as w_n. It can be shown that both v_n, and w_n of a particular layer can be connected with v_{n+1}, and w_{n+1} from a neighboring layer using a matrix in the form

$$\begin{pmatrix} v_n \\ w_n \end{pmatrix} = M_n \begin{pmatrix} v_{n+1} \\ w_{n+1} \end{pmatrix}, \tag{2.7}$$
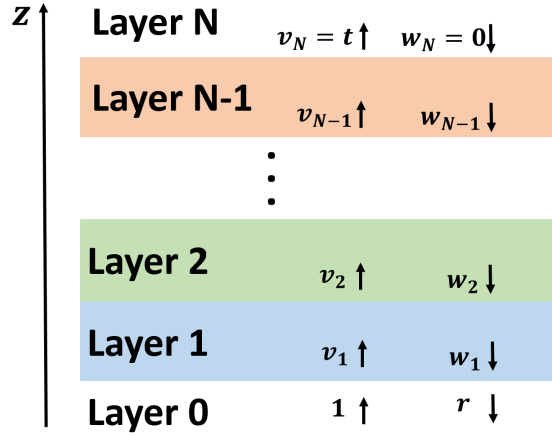
Figure 2.9: Schematic image to explain the TMM for a layer stack system with N layers.

with M_n being the so-called transfer-matrix [43]. The expression for M_n can be derived from the boundary conditions at each interface similar to the Fresnel equations. Expression 2.7 can be expanded to describe the relationship of the amplitudes of the electric fields, between arbitrary layers of the layer stack. If the amplitude of the incoming light is set to 1 the following expression can be derived connecting the first layer with the last layer:

$$\begin{pmatrix} 1 \\ r \end{pmatrix} = \hat{M} \begin{pmatrix} t \\ 0 \end{pmatrix}, \tag{2.8}$$

with r the amplitude of the reflected light at the first layer, t the amplitude of the transmitted light through the stack and $\hat{M}$ the transfer-matrix connecting the first with the last layer of the stack. This equation can be solved to obtain both r and t. Afterwards Equation 2.7 can be used to derive the solutions of all subsequent layers.

A python-based implementation of the transfer-matrix method was used in this work [43]. This implementation can be used to calculate the absorption in each layer for a layer stack with an arbitrary number of layers. It also includes the possibility to treat the light in certain layers of the system as incoherent.

All CIGSe layers prepared in this work possess a GGI gradient. Hence, the optical properties will change depth-wise. Yin et al. determined the optical constant of ungraded CIGSe layers, having different GGI values in [23]. The optical properties for a CIGSe layer having an arbitrary GGI were determined here by calculating the weighted average of the optical parameter from the closest tabulated adjacent GGI values, using the optical data from [23]. The GGI gradient is then implemented by dividing the CIGSe absorber into more than 100 sublayers, assigning each of the sublayers the desired GGI. Only the optical constants of the ITO layers were determined from measurements. The references for the other layers are: Mo([22]), ZnO([22]), CdS([22]), Ag([44]), and Al([44]).

2.3.2 Finite-difference time-domain method (FDTD method)

The FDTD method is used to solve the propagation of light in a media by solving the Maxwell equations. It can also be applied to 3D systems in contrast to the TMM. The FDTD method
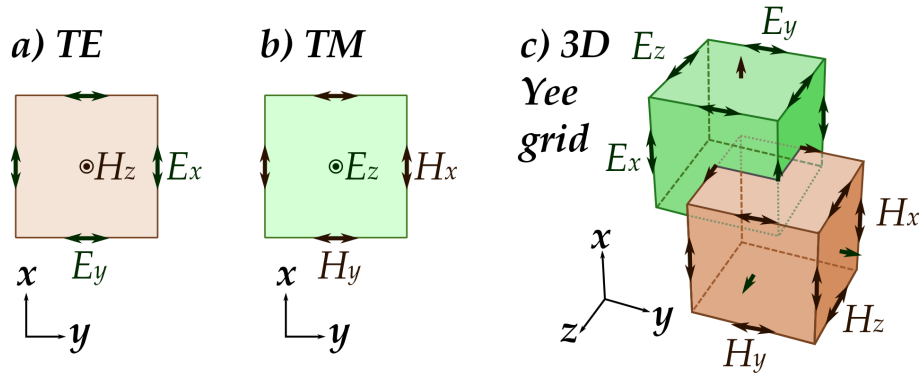
Figure 2.10: Schematic representation of the Yee lattice as commonly used in FDTD calculations. a) The transversal electric (TE) field in the x-y plane. b) The transversal magnetic (TM) field in the x-y plane. c) 3D representation showing how the lattice points of the E-field and H-field are positioned in respect to each other. (Picture taken from [45])

calculates the electromagnetic field on a grid using a finite difference method. The evolution of the electromagnetic field is calculated in a leapfrog manner, meaning that the electric field E at a given time is calculated from the magnetic field H at a time step prior and vice versa. The grid points for the E- and H-field are positioned in a staggered way as visible in Figure 2.10. This so-called Yee grid offers several advantages, including a straightforward implementation of the curl operator on a grid [46]. The absorption in each layer of the solar cell can be calculated from the electromagnetic field in steady-state condition. A source for an electromagnetic field is placed in front of the sample to create a plane wave. The evolution of the electromagnetic field is then calculated until a steady state of the system is reached. The absorption in the various layers of the solar cell can be calculated using several approaches, which in its core rely on the continuity equation. The local absorption P_{abs} at each grid point can be calculated using

$$P_{abs} = -0.5\omega|E|^2 imag(\varepsilon),$$ (2.9)

with the angular frequency ω of the light, $|E|^2$ the absolute square of the complex electric field and $imag(\varepsilon)$ the imaginary part of the complex dielectric function.

The total absorption in each material of the solar cell can then be calculated by summing up the local absorption values. The software package MEEP was used to calculate the absorption in 3D structured solar cells [47]. It allows for the implementation of periodic boundary conditions to implement the prepared nanostructures.

2.3.3 Electrical simulations

The software package AFORS-HET was used to calculate JV curves for varying layer properties [48]. This software solves the one dimensional semiconductor equations for steady state conditions and for small sinusoidal ac-perturbations. An arbitrary sequence of semiconductor layers can be modelled with this software. The depth-dependent carrier generation rate was imported from TMM calculations for the illuminated JV curves. AC calculations were also calculated using AFORS-HET, to obtain CV and Cω curves.

Electrical simulations have been furthermore conducted using the software wxAMPS, which implements a method to calculate the tunneling current at heavily doped pn-junctions [49]. It

was consequently used to discuss the possible presence of a tunneling contact at the CIGSe/ITO interface.

Chapter 3

TCO based diffusion barriers integrated in solar cells

3.1   Introduction

The following chapter analyzes the utilization of metal/TCO back contacts for CIGSe solar cells. The goal is to find a highly reflective back contact for CIGSe solar cells, which is compatible with the typical temperatures used during the CIGSe deposition.

This chapter is organized in the following: Section 3.2 directly compares different metal/ITO-based back contacts. A concise summary of the experimental results using further metal/TCO-based back contacts is then given in Section 3.3. Those results show overall, why the Al/ITO back contact was chosen as the main focus inside this thesis. Afterwards, experiments testing the required ITO thickness (Section 3.4) and maximum applicable deposition temperature (Section 3.5) are presented. A general discussion of the observed shunting problems observed in the experiments is made in Section 3.6. Afterwards, a comparison of the overall performance of solar cells with the alternative back contacts compared with solar cells employing the standard Mo back contact will be given (Section 3.7). Finally, the potential reduction of the absorber layer thickness by the alternative back contact will be analyzed (Section 3.8).

> Note that the results of this chapter are partly published in:
>
> - Schneider T, Scheer R. 2019 Aluminum Based Back Reflectors for Ultrathin Cu(In,Ga)Se$_2$ Solar Cells with ITO Diffusion Barrier. *36th European Photovoltaic Solar Energy Conference and Exhibition* 684-688 (doi:10.4229/EUPVSEC20192019-3BV.1.44)

3.2   Evaluation of metal/ITO back contacts

The TCO used on top of the back contact metal has to fulfill the role of a diffusion barrier, while enabling a current transport between the absorber layer and the metallic back contact. Furthermore, the parasitic absorption within the TCO has to be kept as low as possible to enable the full potential of the back contact. ITO is a promising candidate for this purpose, given the

Figure 3.1: Sketch of the different back contact types employed in the experiment.
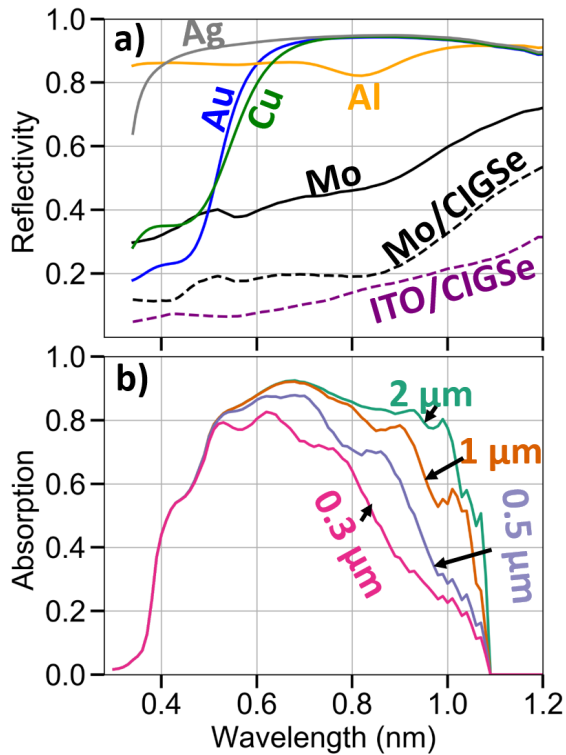

Figure 3.2: a) Calculated reflectivity for different metal/ITO interfaces (solid lines), and at the Mo/CIGSe and the ITO/CIGSe interfaces (dashed lines) b) Calculated absorption within the CIGSe layer of complete CIGSe solar cells with different absorber layer thicknesses. A Mo back contact was used for this calculations.

fact that relatively good results have been obtained on ITO-based bifacial solar cells (see Section 1.4.3). ITO is also known to provide relatively good diffusion barrier properties [50].

Four different metals were chosen for testing in this experiment, namely Al, Ag, Au, and Cu. A sketch of the employed back contacts is given with Figure 3.1. The basis for all back contacts was a commercial deposited Mo layer with a thickness of 500 nm, on a 3 mm SLG, with a 200 nm SiO_xN_y layer in-between. The SiO_xN_y layer acts as an alkali diffusion barrier, and was employed to avoid that a different Na concentration will be present in the absorber layers of the different sample types. The other metals were then deposited on top of this type of back contact. A thin layer (~4 nm) of Cr was deposited before the Au deposition in the same chamber without a vacuum break. Prior Au-based samples without the Cr layer peeled off the substrate after the ITO deposition, likely caused by an insufficient adhesion of the Au layer. The stress induced by the ITO layer was apparently sufficient to remove the Au from the Mo surface.

The ITO layer was deposited simultaneously on all back contact types. The usage of the same base substrate (the Mo-based sample), has the advantage that the same sodium diffusion barrier, and the identical glass is used. Furthermore, the emissivity on the back of the sample is the same.

The four investigated metals are typically considered for highly reflective back contacts as
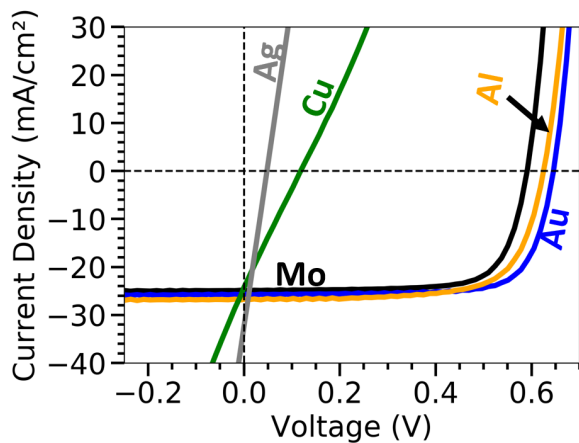
Figure 3.3: Representative illuminated JV curves from sample batch 3. Ag, Cu, Au, and Al stand representative for the corresponding back contact types containing the metal as found in Figure 3.1.

can be motivated with Figure 3.2. Figure 3.2 a) shows the reflectivity at the ITO/metal interfaces calculated with the Fresnel equations. Additionally, the reflectivity at the Mo/CIGSe and ITO/CIGSe interface are given for a CIGSe layer having a GGI of 0.33. Figure 3.2 b) shows further the calculated absorption in the CIGSe layer of a (Mo/CIGSe/CdS (40 nm)/ZnO (200 nm)/ ITO (200 nm)) solar cell. The direct comparison of both graphs helps to understand, which range of the reflection spectra is of importance, for a certain CIGSe thickness.

The three metals Ag, Au, and Cu show basically the same reflectivity for wavelengths above 700 nm (~ 94%). The reflectivity drops sharply for sufficiently low wavelengths (corresponding to frequencies above the plasma frequencies of the metals). This drop occurs at roughly 600 nm for the Cu and Au interfaces, while the reflectivity at the Ag interface stays high down to 400 nm. Note that this drop would occur for Al at even lower wavelengths, which are outside the displayed range. The Al/ITO interface exhibits on the other hand a lower reflectivity below a wavelength of about 1 μm, with a reflectivity between 82% and 86%. Differences in the reflectivity of these metals matter only in wavelength regions where some light intensity reaches the back contact at all. A comparison with calculated absorption shows clearly, that the differences between the reflectivity of the Ag, Au and Cu interfaces matter only in a very limited wavelength region (~550 nm - 650 nm), even for absorber layers thickness of only 300 nm. The Mo/ITO back contact has a reflectivity between 40% and 60%. The Ag, Cu, Au, and Al interface with ITO possess all a considerably higher reflectivity than the Mo/CIGSe interface. The reflectivity of the Mo/CIGSe interface is only 20% below a wavelength of 800 nm and goes up to 50% at a wavelength of 1.2 μm. Note that typically a thin layer of $MoSe_2$ is forming at this interface during the deposition of CIGSe [51, 52, 53, 54, 55]. This layer decreases the reflectivity even further [4].

The reflectivity at the ITO/CIGSe interface does increase almost linearly from about 6% at 400 nm to about 31% at 1200 nm. The effective reflectivity of both interfaces (the metal/ITO and ITO/CIGSe) combined will differ in reality slightly from the results of the Fresnel equation, due to interference phenomena.

Three batches of solar cells with an absorber thickness of 500 nm were prepared. The maximum deposition temperature during the CIGSe deposition was 480°C. A 2 nm layer of NaF was deposited during the PDT. Representative JV curves are shown in Figure 3.3. All measured solar cells based on an Ag or Cu reflector exhibited heavy shunting. This problem did not occur
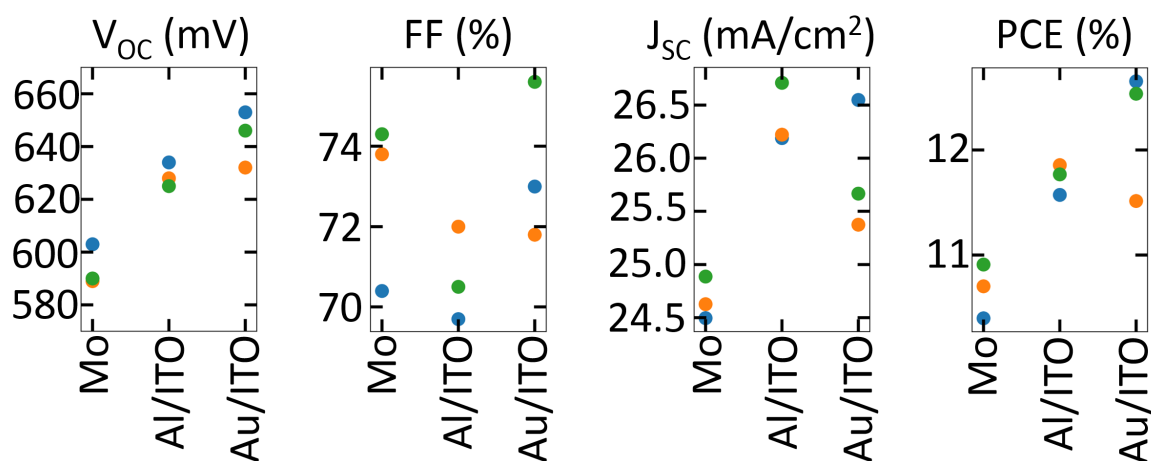
Figure 3.4: Solar cell parameters of the solar cells with the highest *PCE* for all three batches (blue = batch 1, orange = batch 2, green = batch 3)

for the other back contact types. The corresponding determined solar cell parameters of the highest *PCE* solar cells for all batches are shown in Figure 3.4. The results from the Ag and Cu back contacts were excluded due to the excessive shunting.

The open circuit voltage for all Mo-based solar cell types is between ~590 - 600 mV. Both ITO-based solar cell types exhibit higher V_{OC} values, with ~ 630 mV for the Al-based samples and around 630 mV - 650 mV for the Au-based sample. The *FF* results are less systematic. Values between 70% - 75% were obtained, with no systematic difference between the different back contact types. The short circuit current densities for the Mo-based samples are between 24.5 - 24.8 mA/cm^2. The Al/ITO-based samples have J_{SC} values between 26.1 - 26.7 mA/cm^2, and the Au/ITO-based samples have J_{SC} values between 25.4 - 26.5 mA/cm^2. The J_{SC} values obtained with the Au/ITO back contact show a larger variation between the different batches. The Al/ITO-based samples displayed higher J_{SC} values for two of the batches. The highest *PCE* values for each back contact type are 11.0% for the Mo-based sample, 11.9% for the Al/ITO-based sample, and 12.9% for the Au/ITO-based sample.

An increase of V_{OC} through the ITO-based back contact was unexpected. Likely explanations include a decreased negative effect of the back contact recombination on V_{OC} as well as a difference in the bulk quality of the absorber layer, induced by the different back contact. Similar V_{OC} differences between samples grown on Mo or an ITO-based back contact were also found in further experiments of this thesis. A detailed discussion of this phenomena will be given in Section 4.10 in combination with simulation results.

The measured EQE curves for batch 1 and batch 3 can be seen in Figure 3.5. The results on the Cu- and Ag-based back contacts are omitted due to the high shunting. The EQE curves of the Mo-based samples are lower over almost the whole spectral region above 500 nm. Both the Au/ITO- and the Al/ITO-based samples show additional peaks compared to the Mo-based samples. This is especially visible for batch 1, where a clear peak can be seen at about 1 μm. An additional peak can be seen at 900 nm for batch 1. The peak structures are less pronounced for batch 3. A higher EQE value is visible for the alternative back contact especially close to wavelengths corresponding to the band gap of the CIGSe. The Al/ITO-based sample shows for wavelengths around 700 nm higher EQE values than the Au/ITO-based sample, while it is vice versa for batch 1.

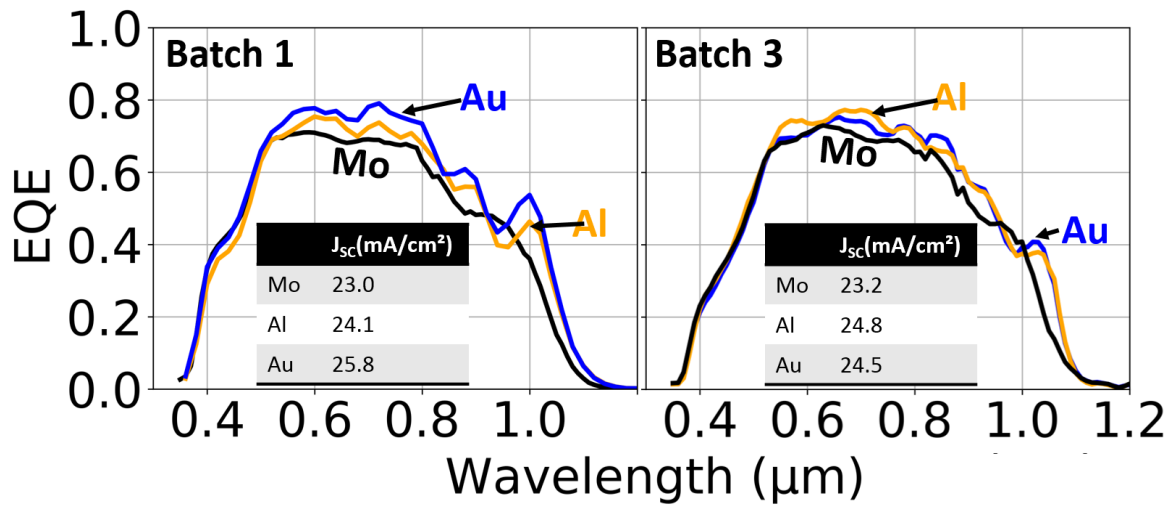Figure 3.5: EQE curves measured on solar cells with the highest *PCE* for batch 1 and batch 3. The calculated short circuit current density from EQE is given in the tables.
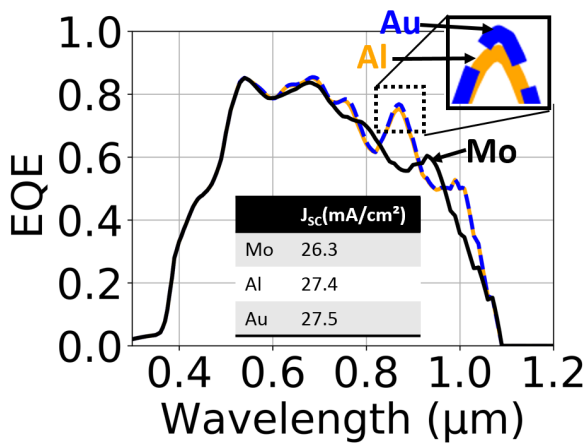

Figure 3.6: Calculated absorption within the CIGSe layer for the layer thickness found in batch 3. The calculated J_{SC} value under an assumed complete collection of all generated charge carriers, is given in the table.

Figure 3.6 shows the calculated absorption within the CIGSe layer according to TMM calculations. The calculated absorption is higher than the measured EQE curves over almost the whole wavelength region. This is also reflected in the higher calculated short circuit current, which are about 2-3 mA/cm^2 higher than in the experiment. The general shape of the measured EQE is however comparable with the calculated absorption. The absorption peaks are generally less pronounced in the EQE curves. Both ITO/metal-based samples show an increased absorption for wavelengths above 1 μm as seen in the EQE curves. For wavelengths below 700 nm no differences can be seen between the different back contact types in contrast to the EQE results. The difference of the calculated absorption between the Au/ITO- and the Al/ITO-based samples are overall rather minimal, which can be explained by the fact that the parasitic absorption within the Al is already rather low for the given CIGSe layer thickness.

The TMM calculations show that between the two ITO-based samples no differences in the EQE values around 700 nm is to be expected. The differences in the EQE can have several reasons. The window layers might be different despite the simultaneous deposition, leading to a variation of the transparency of the window layers. The surface roughness might differ between the samples. Some roughness of the surfaces causes a reduction of the reflectivity through the creation of smoother transitions of the refractive index at the air/ITO interface. However, an increased roughness should also lead to a reduced height of interference related phenomena due to scattering together with the associated thickness fluctuations. The samples with the overall highest EQE level in Figure 3.5 show rather more pronounced peak structures, which is in contrast to an assumed higher roughness. Hence, differences in the roughness appear to be unlikely the reason for the different EQE values at around 600 nm.

The differences at lower wavelengths could also be based on recombination losses. The different V_{OC} values obtained for the Mo-based and metal/ITO-based samples can also hint to an increased recombination rate in the Mo-based samples. However, these differences where only found in this experiments, while similar experiments in this thesis do not exhibit large variations for this wavelength region, despite the fact that the V_{OC} differences between the Al/ITO- and Mo-based samples are comparable.

Overall, the variations between the transparency of the window layers appear to be the likely cause for the observed differences at around 600 nm in the Au/ITO vs Al/ITO comparison experiment. The TMM calculations predict that no significant differences in the CIGSe absorption should be visible between these two back contact types. A higher J_{SC} value was obtained with Au in one sample set, while the samples with Al yielded higher J_{SC} values in the other sample sets. This suggests that those differences are rather caused by a random scattering between the samples.

The experiment shows that both the Au/ITO and the Al/ITO back contacts are suitable to increase the reflectivity at the back contact, without a decrease of the FF or V_{OC} of the solar cell. It is however unrealistic that Au would be used in commercial solar cells due to its high associated material costs. The next section will give a concise overview on the experimental results obtained with other metal/TCO combinations. The rest of the thesis will then analyze the Al/ITO back contact, given the fact that this back contact has shown the most promising results (excluding Au).

3.3   Testing of further metal/TCO combinations

The following section is meant to give a condensed overview of further results obtained for various metal/TCO combinations.

Cu/ITO:

Additional experiments were conducted on Cu/ITO-based solar cells. The Cu was deposited via e-gun evaporation on Mo-based back contacts. The first test have been conducted using a 200 nm ITO layer deposited via sputtering at the Catalonian Institute for Energy Research (IREC).

A large quantity of $CuSe_2$ formed on the sample after an attempted deposition of CIGSe, indicating that a large amount of Cu has diffused from the back contact to the absorber layer. The same result was obtained with an ITO layer deposited at the MLU with the same sputtering parameters and in the same chamber as used for the front side ITO.
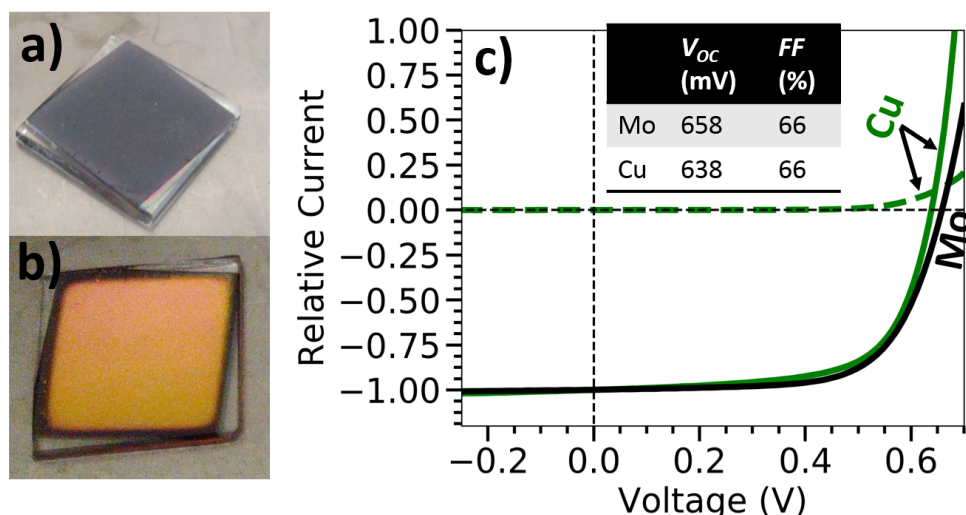
Figure 3.7: Appearance of Cu/ITO back contacts after a thermal annealing at 480°C for 30 min in a muffle oven. The back contact in a) was deposited with the same sputtering conditions as for the window layer deposition, while the sputtering pressure in b) was reduced to $8 \cdot 10^{-4}$ mbar. c) JV curves of the solar cell with a Cu/ITO back contact having the highest obtained FF compared to the Mo reference under illumination (full lines). A dark JV curve is additional given for the sample with a a Cu/ITO back contact (dashed lines). The relative current denotes the current divided by the short circuit current of each solar cell under illumination.

Different sputtering parameters were tested to optimize the barrier properties of the ITO layer against Cu diffusion. The testing was performed using a muffle oven, and visual inspection. A significant diffusion of Cu through the ITO can be detected after the annealing due to the formation of a black layer as visible in Figure 3.7 a). This sample was annealed for 30 minutes at 480°C. The ITO deposition of this sample was performed with the same sputtering parameters as the front ITO layer.

A deposition of ITO layers with different sputtering powers ranging from 80 W to 160 W resulted in ITO layers with the same problems. A variation of the sputtering pressure revealed

that ITO layers deposited with higher process pressures did also not stop the diffusion of Cu, while a lower pressure of $8 \cdot 10^{-4}$ mbar lead to a significant reduction of Cu diffusion. A black layer was only visible at the rim of the sample for ITO layers deposited at such low pressures as can be seen in Figure 3.7 b). This black border is caused by the rims of the sample which are not covered by ITO due to the shadowing by the sample holder during the ITO deposition.

The lowest usable process pressure, at which the plasma is still stable was tested for the ITO deposition. An ITO layer deposited using this pressure ($4 \cdot 10^{-4}$ mbar), showed a similar result as Figure 3.7 b), even when the sample was annealed for 60 min at 600°C. Note that this ITO deposition process was used for all Al/ITO back contacts in this thesis.

Several solar cells prepared at a substrate temperature of 480°C showed all an excessive shunting of the prepared solar cells. However, it could be shown that solar cells with no apparent shunting characteristics could be prepared on smaller areas (~1 mm^2). Figure 3.7 c) shows the highest obtained FF using a solar cell with a Cu/ITO back contact. The ~1.1 μm thick absorber layer was deposited with a maximum process temperature of 480°C. Note that no absolute values for the current density can be given, due to the fact that the active area of this solar cell was not determined. A FF of 66% was obtained, which is similar to the one obtained using the Mo reference sample.

A lock-in thermography image of a regular sized solar cell with a Cu/ITO back contact can be seen in Figure 3.8. Several spots can be seen, which are apparently shunted.
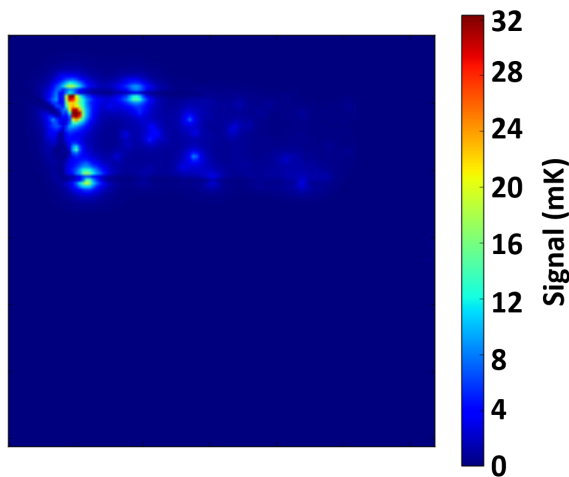
Figure 3.8: Lock-in thermography image of a solar cell with a Cu/ITO back contact.

Cu/ZnO:

CIGSe solar cells were prepared for deposition temperatures up to 600°C on Cu/ZnO substrates. The Cu was also deposited using e-Gun evaporation on Mo substrates. ZnO was sputtered on the Cu, using the same deposition parameters as used for the window layer preparation. CIGSe solar cells were prepared with an absorber thickness of ~1.1 μm.

The CGI values of the resulting CIGSe layers deposited on the Mo reference were compared to absorber layers prepared on the Cu/ZnO back contact. A similar CGI was measured by both EDX and GDOES measurements for both back contact types for deposition temperatures up to 600°C. This indicates that no significant diffusion of Cu from the back contact took place
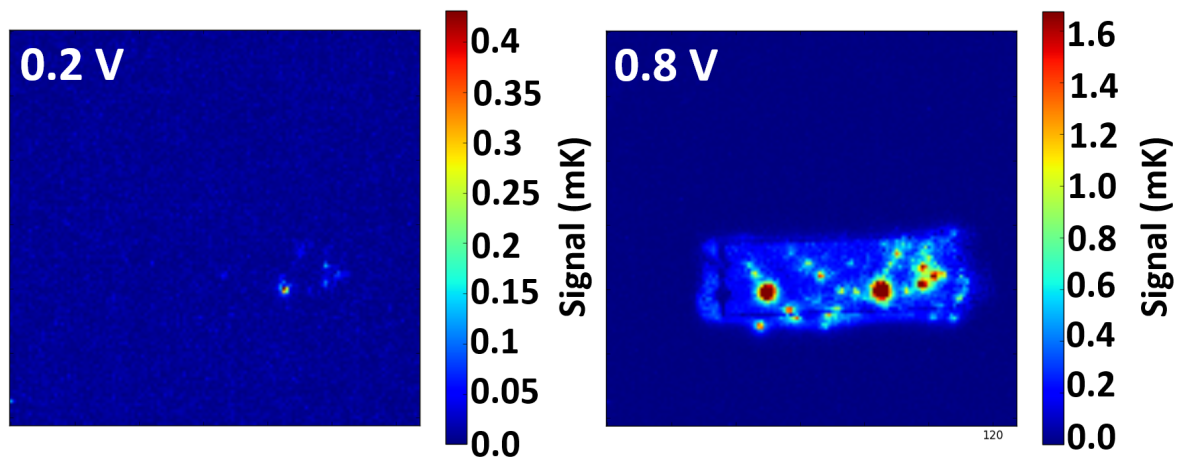
Figure 3.9: Lock-in thermography images of a Cu/ZnO/ZnO:Al-based solar cell for two different applied voltages.

during the deposition of the CIGSe. However, a large number of local shunts was found via lock-in thermography, similar to the results on Cu/ITO back contacts as visible in Figure 3.9.

The thermal stability of different ZnO layers was tested using a simple annealing experiment. The compared ZnO layers were:

- Two layers of ZnO:Al with a thickness of 100 nm and 500 nm, deposited via sputtering using the same sputtering parameters as used for the window layer ITO.

- An undoped ZnO layer (100 nm) deposited with the same sputtering conditions as used for the ZnO in the ZnO/ITO window layer.

- A combination of the undoped ZnO layer (100 nm) and the ZnO:Al layer (200 nm)

- The latter combination of layers, but deposited at an external institute.

These samples were annealed in a Se atmosphere, at a temperature of 480°C for 1 h to replicate the CIGSe absorber deposition conditions. Two of the samples showed a blackish appearance, namely the ZnO:Al layer with a thickness of 100 nm and the layer system deposited at an external institute (see Figure 3.10 a). This indicates that an excessive amount of Cu has diffused to the surface.

The other samples kept their metallic appearance after the treatment, indicating that the Cu diffusion was blocked and that the Cu was protected from the Se atmosphere. Shunt free solar cells were demonstrated on small area solar cells (~1 mm^2). Figure 3.10 b) shows the solar cell with the highest obtained FF, which has the ZnO(100 nm)/Al:ZnO(200 nm) diffusion barrier. The ~1.1 μm CIGSe layer was deposited with a maximum temperature of 480°C. The absolute value of the current density does increase for negative voltages for the alternative back contact, despite the fact that the dark JV curve appears to be shunt free. The short circuit current is reduced compared to the Mo-based solar cell. This effect is likely caused by a barrier at the CIGSe/ZnO interface. The overall distortion of the illuminated JV curve leads to a reduced FF of only 50%. The V_{OC} value is with 624 mV about 40 mV lower than the V_{OC} value of the Mo reference cell.
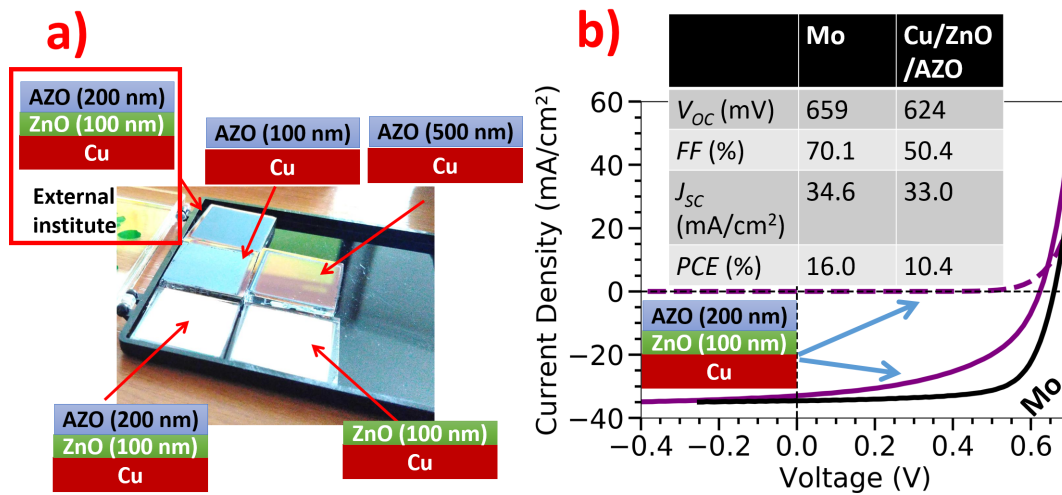
Figure 3.10: a) Appearance of different combination of ZnO based layers deposited on a Cu based back contact, after an annealing at 480°C for 30 min in a Se atmosphere. b) Highest *PCE* solar cell obtained on a Cu/ZnO/ZnO:Al back contact in comparison to the Mo reference curve. The JV curves with a solid line were measured under illumination, while the JV curve with a dashed line was measured in the dark. The sample area was about 1 mm^2.

Cu/SnO:

A limited amount of Cu/SnO back contacts were tested. The Cu was deposited via thermal evaporation on Mo-based samples. The SnO was deposited using sputtering. A Cu rich layer was visible after the deposition of the CIGSe layer through the appearance of thick copper selenide layer using a maximum deposition temperature of 480°C, which indicated a complete failure of the SnO layer as a Cu diffusion barrier.

Cu/graphene:

Cu foils covered with graphene were tested as a back contact. Literature results show that even monolayers of graphene can block Cu diffusion up to at least 700°C [56]. However, a large amount of Cu diffused into the CIGSe after the deposition of CIGSe with a deposition temperature of 480°C, resulting in the formation of copper selenide followed by a partial delamination of the layer structure.

3.4 Analysis of the minimum barrier ITO thickness

The ITO diffusion barrier was further tested for a variation of the ITO diffusion barrier thickness on top of the Al-based back contact. The sample structure is otherwise identical to the samples shown in Section 3.2. CIGSe solar cells with an absorber thickness of approximately 500 nm were prepared with a maximum deposition temperature of 480°C, and a NaF PDT having a targeted thickness of 2 nm. Four different ITO thicknesses (50 nm, 100 nm, 200 nm, 400 nm) were deposited onto Al-based back contacts.

Figure 3.11a) shows the illuminated JV curves for all sample types. The corresponding solar cell parameters are given in Table 3.1. All samples using the Al/ITO back contact exhibit higher V_{OC} and J_{SC} values compared to the Mo reference cell. The only exception is the sample with

Table 3.1: Extracted solar cell parameters for the JV curves shown in Figure 3.11 a).

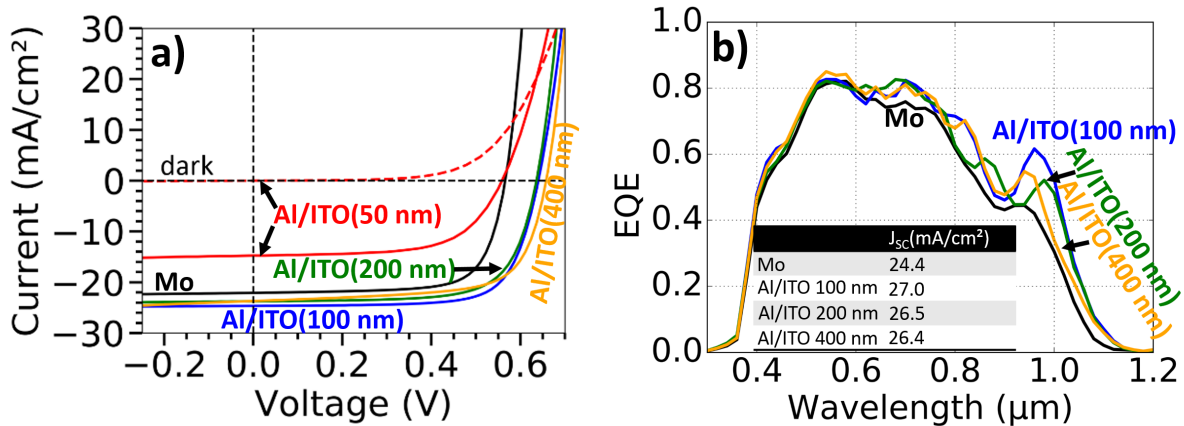| back contact	V_{OC} (mV)	FF (%)	J_{SC} (mA/cm^2)	PCE (%)
Mo	566	72.4	22.1	9.1
Al/ITO (50 nm)	556	62.6	17.6	6.2
Al/ITO (100 nm)	640	72.8	24.7	11.5
Al/ITO (200 nm)	636	70.8	23.7	10.8
Al/ITO (400 nm)	658	68.8	23.7	10.7

Figure 3.11: a) JV curves of the best performing solar cells with the Al/ITO back contact with varying ITO thickness in comparison to the Mo reference sample, under illumination. A dark JV curve is additionally given for the Al/ITO sample with an 50 nm ITO layer. b) Corresponding EQE curves.

the thinnest ITO layer. The 50 nm ITO-based sample has furthermore a noticeably reduced FF. The dark JV curve is given for this sample to show that the decreased V_{OC} and FF values are not caused by a shunting of the sample. The most notable effect is however the very low J_{SC} value of this sample. Note that this effect was reproduced for further samples with the same sample configuration.

An Al signal could not be detected in the CIGSe layer in any of the samples via GDOES.

Figure 3.11b) shows the corresponding EQE measurements. The EQE reaches a maximum value of 0.8 and decreases for wavelengths above 800 nm. EQE peaks at different positions can be seen for the various Al/ITO-based sample. The integrated short circuit density is increasing for the Al/ITO-based solar cells with decreasing ITO thickness (except for the 50 nm layer). Compared to the Mo reference a gain of up to 2.6 mA/cm^2 is reached. The overall efficiency is increased from 9.1% to 11.5%, when comparing the Mo reference with the Al/ITO (100 nm) sample.

The peak structure in the EQE curves can be understood with the help of Figure 3.2. The absorption within the CIGSe of a 500 nm CIGSe layer is high enough for wavelengths up to ~700 nm to absorb almost all light, even with the Mo back contact. Because no light is even reaching the back contact, it can be concluded that interference phenomena in this wavelength region have to be related to the thicknesses and optical properties of the window layers. The absorber layer and the diffusion barrier both are a part of the interference phenomena at longer wavelengths in contrast. This can be seen in Figure 3.13, where the position of the interference peaks for wavelengths above 700 nm does change with the thickness of the ITO.
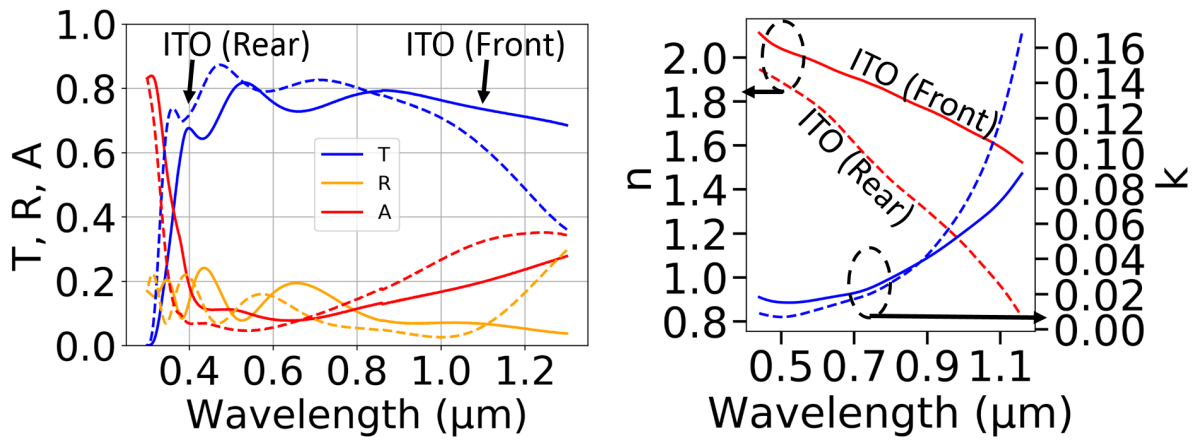
Figure 3.12: a) Measured transmittance T and reflection R from UV-VIS measurements together with the calculated absorption A. Two glass/ITO samples have been used, one using the same deposition properties as the front ITO in the solar cell (full lines), the other is similar to the back ITO of the solar cell (dashed lines). b) Determined refractive index n and extinction coefficient k from the measurements shown in a).

UV-VIS measurements were conducted on ITO layers to understand the parasitic losses in those layers. The two ITO layers differ in two ways. First of all, a lower sputtering pressure is employed for the ITO diffusion barrier layer ($4 \cdot 10^{-4}$ mbar instead of $1 \cdot 10^{-3}$ mbar). Furthermore, while both layers are deposited at room temperature, the ITO diffusion barrier layer will receive an additional annealing during the CIGSe deposition. Two layers of the same thickness (250 nm) were deposited on SLG substrates using the same sputtering parameters as used in the solar cells. The back ITO was additionally annealed for 1 h at 480°C in vacuum using the same chamber as used for the CIGSe deposition to simulate the thermal treatment.

Some differences can be seen in the transparency of both ITO-layers (Figure 3.12 a)). The transparency drops to zero at wavelengths below 300 nm, due to a strong increase of the absorption of the ITO. The ITO diffusion barrier layer remains transparent for shorter wavelengths. The location of the reflectance peaks differs between the two ITO layers. A steady increase of the absorption can be seen for both layers at longer wavelengths. The absorption of the ITO diffusion barrier layer is however significantly higher.

The UV-VIS results were further used to extract the optical properties (refractive index *n* and extinction coefficient *k*) for both layers. The results can be seen in Figure 3.12. A detailed explanation on how this data is derived of the UV-VIS measurements is given in the Appendix A. The derived refractive indices differ, which explains why the reflection peaks from interference are shifted, despite the fact that both layers have the same thickness. The determined value of n falls below 1 for the ITO diffusion barrier layer for wavelengths above 1100 nm. The extinction coefficient for the ITO diffusion barrier layer start with a lower value but it rises faster with increasing wavelength.

The strong increase of the absorption below a certain wavelength is linked to the band gap of the ITO. It can therefore be concluded that the ITO used as diffusion barrier has a larger band gap than the front side ITO. The higher extinction coefficient *k* of the rear ITO is likely related to a stronger absorption by free carriers. This corresponds well to the the fact that the refractive index falls below 1 in the visible light spectra indicating that the plasma frequency of the diffusion barrier ITO is situated at higher frequencies than in the front ITO case.

The absorption in the individual layers was analyzed using TMM calculations as visible in
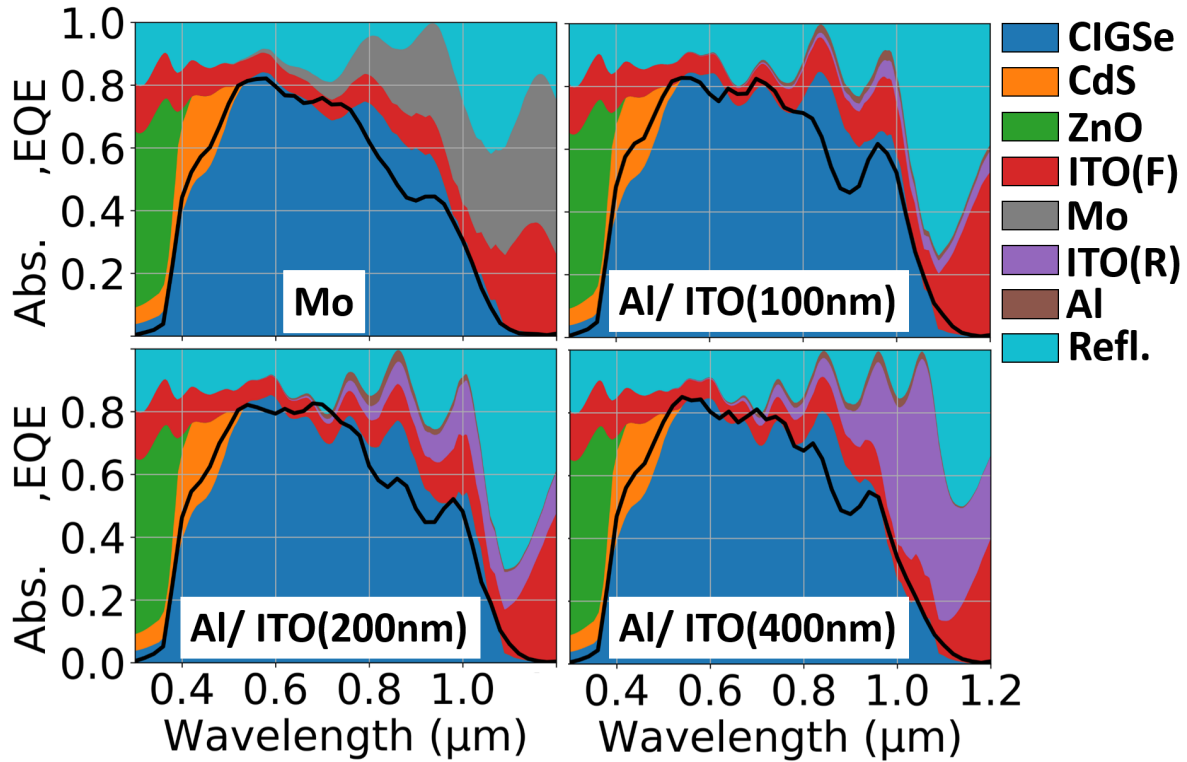
Figure 3.13: Via TMM calculated absorption in the separate solar cell layers in comparison to the measured EQE for the Mo reference (a), and the Al/ITO back contact sample with an ITO layer of 100 nm (b), 200 nm (c), 400 nm (d).

Table 3.2: Calculated J_{SC} values from the simulations depicted in Figure 3.13 under AM1.5G conditions integrated in the range of 0.3 μm to 1.2 μm, with the assumption of complete carrier collection. The value for the other layers than CIGSe denotes the potential lost J_{SC} values by parasitic absorption.

all in mA/cm^2	Mo	Al/ITO (100 nm)	Al/ITO (200 nm)	Al/ITO (400 nm)
CIGSe	26.3	28.7	27.9	27.0
CdS	1.38	1.38	1.38	1.38
ZnO	0.59	0.59	0.59	0.59
ITO (Front)	4.93	5.25	5.08	4.65
Mo	6.3	X	X	X
ITO (Rear)	X	0.77	2.3	5.84
Al	X	0.56	0.63	0.55
Refl.	6.9	9.1	8.48	6.34

Figure 3.13. The calculated J_{SC} values from the TMM calculations are given in Table 3.2 together with the potential lost J_{SC} through absorption in the other layers. The comparison of the EQE curves with the calculated CIGSe absorption shows that all features of the EQE are also visible for the TMM calculations. In case of the Mo back contact samples a significant part of the absorption is happening in the Mo back contact. The calculations do not include a thin $MoSe_2$ layer which is typically observed for CIGSe solar cells on Mo back contacts. However, the influence of this layer is most likely small due to its small expected thickness for the given CIGSe deposition temperature. The absorption in the ITO diffusion barrier layer does increase with the thickness of the layer. The TMM calculations predict that the obtainable J_{SC} value of the 400 nm ITO layer is 1.7 mA/cm^2 lower than for the sample with the 100 nm ITO layer. It is therefore on a similar level as the differences observed via EQE (1.4 mA/cm^2).

The peaks in the EQE spectra of all samples, were reproduced in the TMM calculations at very similar positions. This indicates that the thicknesses of the used layers in the TMM calculations are largely correct. The heights of the peaks were however less pronounced in the EQE curves than in the TMM calculations. This is to some extent expected. The layers of the solar cell will have some roughness, which should decrease the interference phenomena. Electrical losses might also reduce the interference phenomena further, especially at longer wavelengths, where a meaningful portion of the light will be absorber further away from the junction. A 2D simulation to estimate the influence of the surface roughness on J_{SC} can be found in the Appendix C.

It can be concluded that ITO thicknesses below 200 nm should be targeted to minimize losses due to parasitic absorption. However, other electrical losses may appear upon such a reduction ad the 50 nm ITO barrier sample shows.

3.5   Thermal stability of the Al/ITO back contact

The thermal stability of the Al/ITO back contact was tested for deposition temperatures ranging from 480°C to 600°C. Samples with glass/SiO_xN_y/Mo and glass/SiO_xN_y/Mo/Al/ITO back contacts were processed simultaneously. Additionally, a sample using a glass/ITO back contact was tested for the highest processing temperature of 600°C. Note that no Na diffusion barrier was present for this sample. A 2 nm NaF PDT was also used in this experiment.

Figure 3.14 shows the solar cell parameter as a function of the process temperature. The V_{OC} value of the Al/ITO-based samples decreases with increasing deposition temperature. The V_{OC} value of the Al/ITO-based samples is about 40 mV higher than for the Mo reference sample at 480°C, while the V_{OC} values at the highest deposition temperatures are quite similar. Interestingly, a relatively high V_{OC} value of 650 mV is found for the ITO sample prepared at 600°C, which is similar to the V_{OC} value of the Al/ITO-based samples at lower temperatures. In case of the Mo reference samples, a minimum of the V_{OC} values is obtained at 540°C followed by a continuous increase of for lower and higher temperatures. The trend of the FF appears to be less clear. For most samples a FF above 70 % was obtained. The FF of the Al/ITO samples is at average lower compared to the Mo-based samples. The FF of the ITO-only back contact is lower than the FF of the other back contact types. The change of J_{SC} with temperature appears to be not of systematic nature. The J_{SC} of the Al/ITO-based samples is at average 2 mA/cm^2 higher compared to the respective Mo-references.

The PCE is at average about 1% absolute higher for the Al/ITO-based solar cells. This difference is mainly caused by the increased J_{SC} values, but also by the increased V_{OC} values at
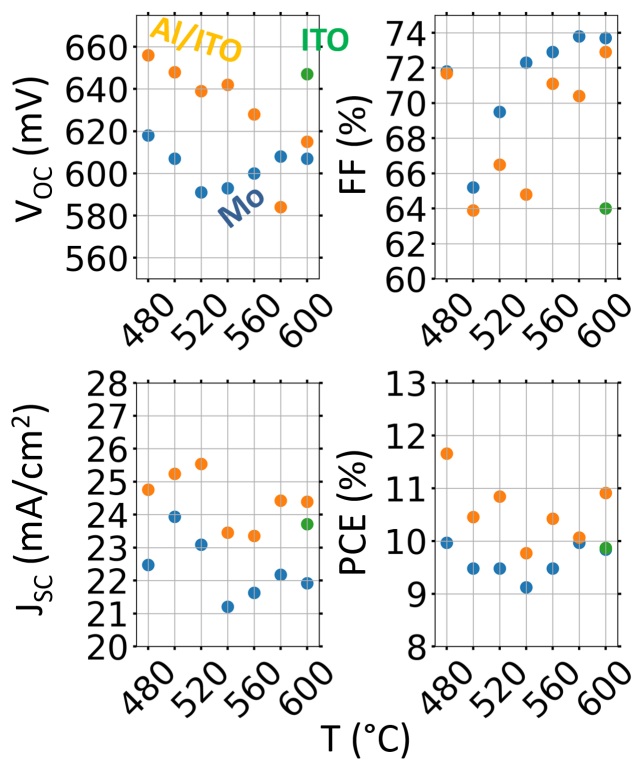
Figure 3.14: Determined PV parameters of the highest *PCE* solar cells using a Mo back contact (blue), and an Al/ITO back contact (orange), with deposition temperatures ranging from 480°C to 600°C. The ITO thickness was 200 nm for all Al/ITO samples. A sample with the same ITO but without the Al layer is also given for the 600°C sample (green).
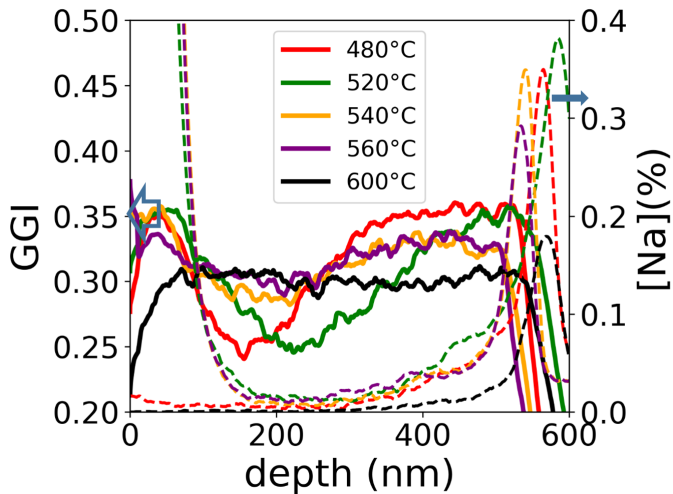
Figure 3.15: GGI gradient from GDOES measurements of samples with a Mo back contact at different deposition temperature ranging from 480°C to 600°C. The determined Na part is also given (dashed lines).

the lower end of the processing temperatures. The higher V_{OC} and J_{SC} values of the ITO-only sample compared to the Mo reference are completely offset by the lower FF values leading to similar PCE values.

Overall, no positive effect on the PCE was observed due to an increase of the deposition temperature in this experiment. Such an increase could be anticipated due to the increased average crystal size of the CIGSe layer. Larger CIGSe crystals result in a reduced amount of grain boundaries and therefore likely in a reduced impact of grain boundary recombination. A decrease of the FF for the ITO-based samples with increasing deposition temperatures was also not observed, which is in contrast to the experimental findings by Nakada et al. [5].

GDOES measurements were performed on further characterization samples with a Mo back contact (Figure 3.15). The GGI notch is most pronounced for the 480°C sample. The notch is less and less pronounced with increasing processing temperature and does completely disappear at 600°C. A reduction of the gradient with increasing processing temperature is anticipated. The GGI gradient is produced in the second and third phase of the three stage process due to the different mobilities of the Ga and In atoms. An increase of the temperature increases the diffusion rate and therefore reduces the time until both elements are uniformly distributed over the sample. The mol concentration of Na is also plotted in Figure 3.15. An aggregation of Na can be seen close to the position of the back contact. This concentration is lowest for the sample deposited at the highest employed temperature. The lower density of Na for the highest deposition temperature could be related to the larger grain size of the CIGSe, which results in less grain boundaries. Such grain boundaries can enhance the overall diffusion of the Na.

TEM measurements were performed on three different samples. The first two samples were part of the deposition temperature series shown in Section 3.5. Namely a solar cell processed at 480°C with a Mo/Al/ITO-back contact and a solar cell processed at 600°C with a Mo/ITO-back contact. Note that the Al is missing by accident in the latter mentioned sample. The third sample is the Al/ITO (50 nm) solar cell from Section 3.4. Corresponding EDX line scans can be seen in Figure 3.17.

All layers of the solar cells are properly separated. This demonstrates the good diffusion barrier properties of the ITO. A thin Ga-rich layer can be seen for the sample processed at 600°C.
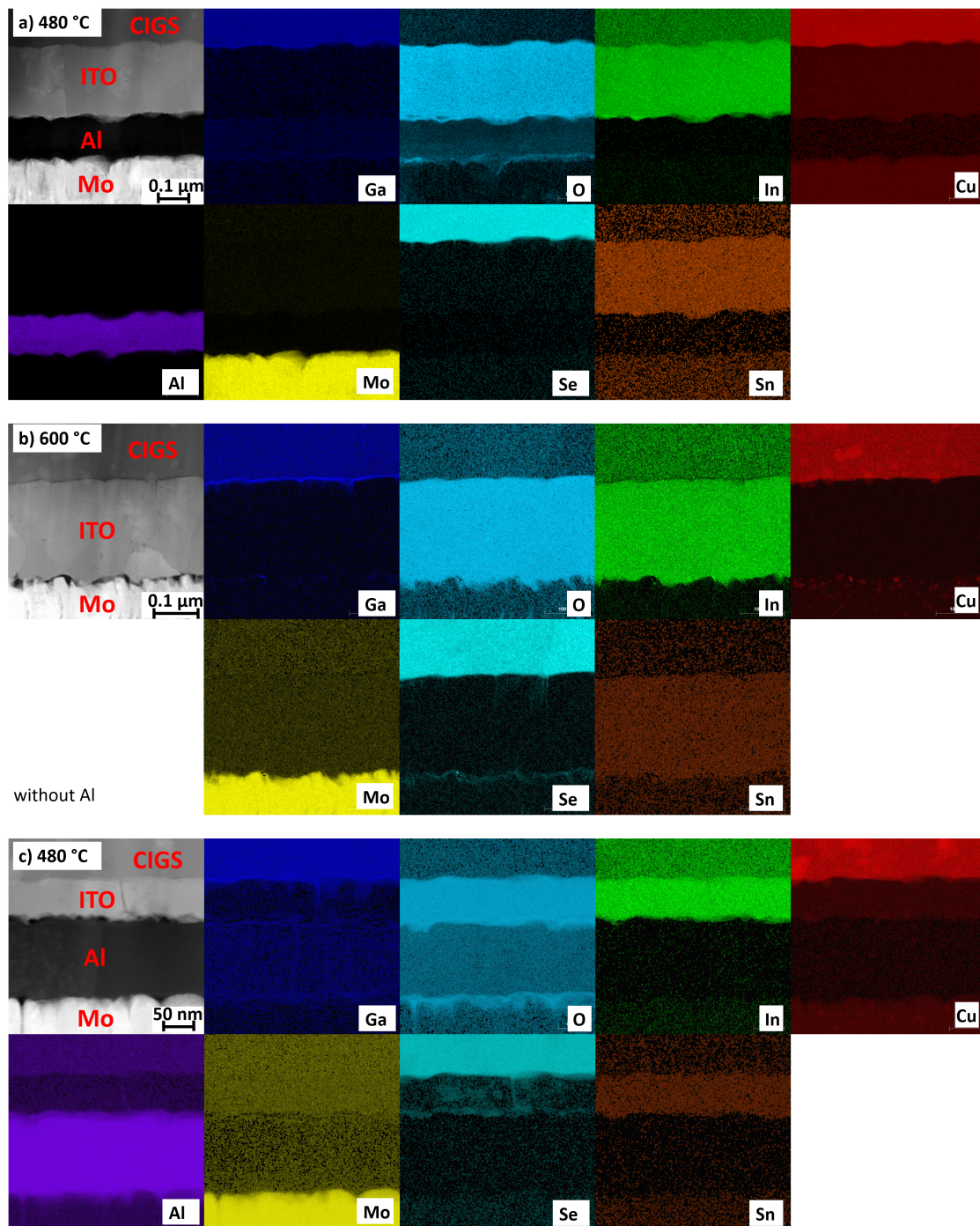
Figure 3.16: TEM images with an intensity plot of the EDX lines of various elements of a) A solar cell with an Al/ITO back contact deposited at 480°C b) A solar cell with a Mo/ITO back contact deposited at 600°C c) A solar cell with an Al/ITO back contact deposited at 480°C.
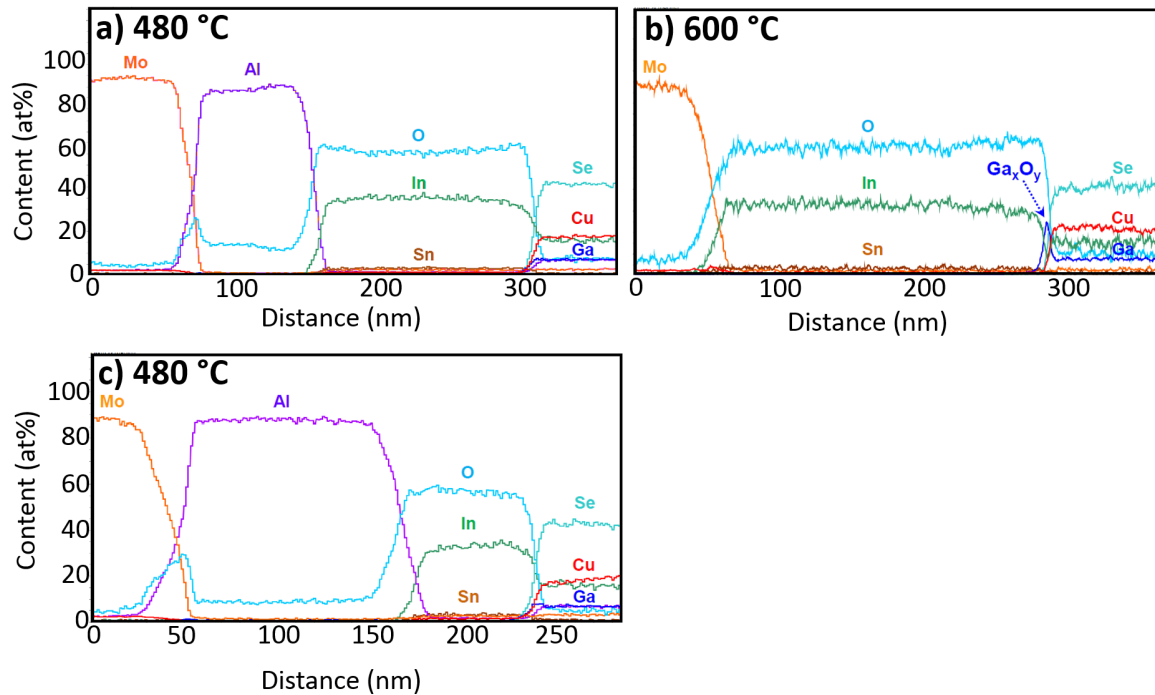
Figure 3.17: EDX line scans in normal direction to substrate plane of a) A solar cell with an Al/ITO back contact deposited at 480°C b) A solar cell with a Mo/ITO back contact deposited at 600°C c) A solar cell with an Al/ITO back contact deposited at 480°C.

The EDX line scan reveals that a thin layer ($\sim$ 5 nm) of Ga_2O_3 is present for this sample. It is therefore below the typical spacial resolution obtained in GDOES measurements. A presence of a Ga_2O_3-layer was in contrast not detectable for the other two samples. The absence of a thick Ga_2O_3-layer even for temperatures as high as 600 °C is unexpected. It likely explains why relatively good results were obtained with the Al/ITO-based samples at such high temperatures. The low thickness of the Ga_2O_3-layer could be a result of a high thermal stability of the employed ITO layers or it could be due to the absence of Na during the CIGSe layer. The absence thick layer of Ga_2O_3 might also explain why no increase in the FF was observed in this sample set at higher process temperatures in contrast to the results of Nakada et al. [5].

3.6   Failure of the TCO barrier layers

The results show that an ITO barrier layer can be used successfully in combination with an Al reflector for processes temperatures as high as 600°C. Al could not be detected in any of the absorber layers in any of the experiments. Au has also proven to be a suited metal to be employed in metal/TCO back contacts. Ag and Cu on the other hand appear to be more challenging to implement, due to the occurrences of shunting problems.

The reason for the occurrence of shunting problems is not completely clear. The results presented for Cu/ZnO- and Cu/ITO-based samples suggest that the problem is not a complete inability of those two TCO layers to block the diffusion of Cu, but the problem appears to be rather a local failure of the barriers. Working solar cells were demonstrated with Cu as the reflecting metal on small areas as shown in Section 3.3. A local failure of the barrier layer could lead to an increased CGI and therefore to a locally enhanced formation of $CuSe_2$. The $CuSe_2$,

which is typically formed in the second stage of the three-stage-process is usually disappearing in the third stage of the process. However, a too high CGI in the second stage might lead to a formation of an amount of CuSe$_2$, which is not completely transformed into CIGSe in the third stage.

The sputtering parameters during the TCO deposition are important for the diffusion barrier properties of the TCO as shown in Section 3.3. This was visible both for the variation of the ITO deposition pressure, as well as for the different ZnO-based diffusion barriers, where the same TCO layer stack (100 nm ZnO with 200 nm ZnO:Al) either failed or worked depending on the deposition conditions. A lower sputtering pressure during the layer deposition does lead to a larger average velocity of the particles arriving at the sample surface, due to the longer mean free path. Therefore, a more compact layer might be formed, which could explain why the ITO layers deposited at lower pressures appear to be more suited as Cu diffusion barriers.

Dirt particles, which can be trapped between the layers, because of surface contamination in-between the separate deposition steps might be the reason for the local failure of the diffusion barriers. Such a contamination can only be avoided to a certain degree when the samples are not prepared in a cleanroom atmosphere. The different expansion coefficients of the layers of the back contact lead to mechanical stress, which can lead to a local delamination of layers or a cracking of layers. Trapped particles might enhance such problems.

While the absence of shunts in the case of the Al/ITO is suggesting that such local failures were not present for this back contact type, it must be noted that it is unclear if a local failure of the ITO in case of an Al or Au back contact, would necessarily lead to the same shunting as in the case of Cu. Small local phases containing these metals might better dissolve during the third stage. However, this theory is highly speculative and the fact that no Al could be detected via GDOES is also rather opposing this theory.

The usage of Graphene as the diffusion barrier is also an interesting alternative, to be employed in combination with Cu. Especially given the fact that Cu foils are commonly used to create monolayers of graphene. Although this barrier failed in the presented work, it was shown by Sim et al. that a solar cell based on a (Cu foil)/graphene back contact can be prepared successfully [39].

Gouillart et al. demonstrated that an Ag back contact can be implemented directly in a CIGSe solar cell. A bilayer consisting of ZnO/ITO was used to block the diffusion of Ag from an Ag back reflector into the absorber layer. Solar cells without apparent shunting problems were prepared for a CIGSe deposition temperature of 550°C [11]. Hence, bilayers of TCO materials are also interesting and might enable the usage of further metals like Cu the reflective metal in CIGSe solar cells.

A further optimization of the parameters for the TCO deposition and the cleaning process might enable further metal/TCO combinations, which did not prove successful in this thesis. However, due to its stable performance and due to cost aspects the focus of this thesis was set to the Al/ITO-back contact

3.7   PV performance

An increased short circuit current density could be demonstrated both for the Au/ITO and Al/ITO-based samples. The increased reflectivity of those back contacts was visible through peaks in the EQE spectra, which are related to interference phenomena.

Similar results regarding the FF were obtained comparing the Mo-based with the ITO-based samples. This indicates that the ITO/CIGSe interface does not increase the series resistance compared to the standard Mo contact (in most cases). Interestingly, this seems to be the case, even for a relative high deposition temperature of 600°C. This is in contrast to the results obtained by Nakada et al. where the FF was decreasing with increasing deposition temperature [5]. This decrease was attributed to an increased formation of Ga_2O_3 near the ITO/CIGSe interface. Similar results were reported in various publications [8, 11].

No Ga_2O_3 could be found in the TEM measurements for both samples deposited with a maximum deposition temperature of 480°C. A thin layer of Ga_2O_3 was visible for the sample prepared at a deposition temperature of 600°C. Due to the relatively high FF obtained for the Al/ITO-based sample deposited at 600°C, two conclusions appear to be reasonable. Either the Ga_2O_3 layer is not responsible for the low FF obtained in the literature or the Ga_2O_3 layer is still too thin to cause serious problems. Given the fact that several authors reported poor FF in correlation with increased Ga_2O_3 formation, the latter mentioned explanation appears to be more reasonable.

The testing of the Cu/ITO and Cu/ZnO back contact revealed that the sputtering conditions during the TCO deposition influence the blocking behavior against Cu diffusion of both oxides. Hence the chemical stability of the ITO is possibly influenced by the sputtering conditions. The absence of a systematic reduction of the FF with increasing temperature as observed by Nakada et al. might be therefore related to a higher stability of the ITO in this thesis. Another factor might be a different thermal budget used, depending on the total deposition time required for the CIGSe deposition. The actual substrate temperature might differ to some extent. Another factor is the presence of Na. Gouillart et al. discussed that Na does likely lead to an increased formation of Ga_2O_3[11]. The usage of an alkali diffusion barrier might therefore help to limit the formation of Ga_2O_3, in contrast to the other works in the literature. However, the fact that the ITO only sample, without any alkali barrier, had a reasonable FF of 64% does rather contradict this theory.

The FF for the ZnO-based solar cells was in contrast rather low and the shape of the JV curve indicates a problem with the current collection (Figure 3.10). Therefore more formation of Ga_2O_3 might have occurred for this back contact. However, it must be noted that the charge carrier transfer mechanism between the CIGSe and the n-type TCO at the back contact is still not finally resolved. Hence the problems with the carrier collection might be directly related to the ZnO/CIGSe interface.

The low J_{SC} value obtained using the 50 nm Al/ITO back contact is likely also related to a problem with the carrier collection. A possible model for the carrier extraction of the ITO/CIGSe interface will later be given in Section 4.9, together with possible explanations for the observed carrier collection problems.

Regarding the samples using a ~500 nm absorber, almost all ITO-based solar cell exhibited higher V_{OC} values than their Mo-references. The V_{OC} values of the Mo-based solar cells are generally lower than the typically obtained value of ~650 mV, for standard solar cells (absorber thickness=2.8 µm, GGI=0.3, deposition temperature=625°C) prepared in the same laboratory. The V_{OC} differences decrease with increasing deposition temperature, with the exception of the ITO-only sample which possesses a V_{OC} value of ~650 mV, even at a deposition temperature of 600°C. The V_{OC} difference could originate from several causes. A possible reason could be a difference in the back contact recombination velocity of the two different interfaces at the back contact. It is furthermore unclear if the CIGSe growth is completely identical on the different substrates, hence the bulk recombination rate might differ.

The actual substrate temperature might also differ between the different back contact types. This is probably more of an issue for the ITO only back contact because the other substrates had all Mo at the glass/back contact interface. The ITO only back contact has furthermore a different glass thickness and no diffusion barrier against Na diffusion from the glass substrate. Hence the substrate temperature and Na supply of this sample might differ from the rest of the samples explaining why higher V_{OC} values were found for this sample than for the Al/ITO back contact. An analysis of the likely cause for the V_{OC} differences between the two back contact types will be given later in Section 4.10, after further information on the back contact are established in Chapter 4.

The results show overall that an increase of the short circuit density can be achieved with the alternative back contacts as aimed for. The predicted J_{SC} gains from TMM calculations have been close to the actual measured J_{SC} gains. This shows that the additional J_{SC} values can be justified by optical gains. Additionally, higher V_{OC} values were obtained. TCO based back contacts with similar FF can be obtained as with the standard Mo back contact, indicating that high efficiency solar cells should be possible with the proposed back contact concept. This is supported by the results of Bissig et al. where a sample using an Al/InZnO/MoSe$_2$ back contact reached an efficiency of 19.9% [38]. The results here could be obtained without the usage of an intermediate layer like MoSe$_2$ between the CIGSe and the TCO layer (as employed by various authors [38, 57, 55]). They show therefore that such a layer is likely not necessary with ITO as the back contact TCO layer.

The next section will discuss the potential gain in J_{SC}, which can be obtained for a flat back contact due to the usage of the alternative back contacts.

3.8 Potential CIGSe thickness reduction by metal/ITO back contacts

This section will explore to which extent the CIGSe absorber thickness can be reduced when a metal/ITO back contact is used in an unstructured solar cell. The reflectivity of the back contact can significantly be improved by the metal/ITO back contacts as shown in Figure 3.2. However, the potential gain is also limited by the parasitic absorption of the ITO used as the diffusion barrier.

ITO layers are commonly highly doped, hence a degenerated semiconductor can often be assumed [58]. Differences in the optical constant of ITO layers used at the back contact and at the front contact have been revealed by UV-VIS measurements. A negative value for n was determined at longer wavelengths in case of the ITO diffusion barrier layer. Negative values for n are typical for metals. Hence, a degeneracy can be assumed at least for the ITO diffusion barrier layer. This can also explain why the reflectivity is increasing noticeably for this layer type for wavelengths over 1 μm. The increased absorption at longer wavelengths found in both ITO layers is likely related to free carrier absorption. The free carrier absorption is usually proportional to the doping of the TCO [58]. A reduction of the ITO doping density could therefore possibly reduce the impact of the parasitic absorption. A high conductivity of the ITO is not necessary in terms of series resistance, because the lateral conductivity is provided by the back contact metal. A reduction of the doping might however also affect the carrier extraction mechanism.

Another effect visible in Figure 3.12 is a shifting of the absorption edge to shorter wavelengths for the ITO diffusion barrier layer. This indicated that the band gap of the ITO is larger. In most
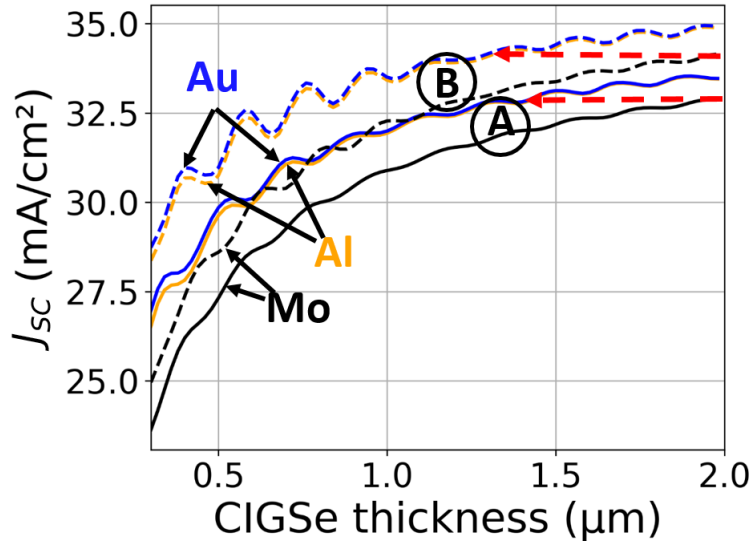
Figure 3.18: Calculated J_{SC} values for a complete collection of all created electron-hole pairs for CIGSe solar cells with varrying absorber layer thickness. The full lines correspond to configuration A, while the dashed lines correspond to samples with configuration B. Al and Au correspond to Al/ITO and Au/ITO back contacts, respectively. The red arrows show the possible CIGSe thickness reduction from a solar cell using a 2 μm absorber layer, when the back contact is changed from a Mo back contact to the metal/ITO back contact, were the same J_{SC} value is reached.

cases this is irrelevant for the total absorption within the absorber layer, due to the absorption in the other layers of the window layers. The different band gap might however affect the carrier extraction at the back contact.

The minimum required ITO thickness appears to be somewhere around 100 nm, despite the fact that no Al diffusion was found for the thinnest barrier thickness. The reason for the poor performance of the 50 nm ITO barrier sample is unknown. The EQE measurements in combination with the TMM calculations show however, that the absorption in the rear ITO is already reasonably reduced for a thickness of 100 nm. The front ITO does also absorb a significant part of the incoming light. Hence an optimization of the transparency or thickness of the ITO could enable larger J_{SC} gains. However, it must be noted that the absorption in the front ITO visible in Figure 3.13 does not only include the absorption of light prior to the passing of the absorber, but also the absorption of light reflected at the back contact, which is mostly lost after the second pass of the absorber layer anyways.

The potential absorber thickness reduction, without losses in J_{SC}, will be discussed in the following. Figure 3.18 shows the dependence of the maximum possible J_{SC} values (all created electron-hole pairs are collected) on the thickness of the absorber. Two different configurations of the involved ITO layers are considered. A layer thickness of 100 nm for both ITO layers in configuration A and a thickness of 200 nm for both ITO layers in configuration B. The J_{SC} values were calculated for solar cells with an Al/ITO, an Au/ITO, and a Mo-based back contact.

Solar cells with the Au/ITO back contact show only slightly higher values for J_{SC} than the Al/ITO-based samples, while the biggest differences can be seen for the thinnest absorber thickness. Solar cells with both metal/ITO-based back contacts perform considerably better than the Mo-based back contact for all thicknesses but especially for thinner absorber layers. An oscillation of the J_{SC} values with the absorber thickness can be seen, especially for the metal/ITO-

based solar cells. These oscillations are caused by interference phenomena; the reflected light at the back contact is superimposed with the light entering the solar cell from the front. The electric field is locally enhanced and locally weakened as a result. The number of regions with an increased or decreased electric field strength (and hence the amount of local absorption) does change with the thickness of the absorber layer. This leads to a relative increase or decrease of J_{SC} compared to a hypothetical system without any interference phenomena.

Two red arrows indicate in Figure 3.18 the possible thickness reduction of the corresponding solar cell computed with a standard solar cell with a 2 μm absorber layer and a Mo back contact, for which the same J_{SC} value is obtained. For Configuration A the thickness can be reduced to 1.4 μm (-30%) and for Configuration B a reduction to 1.3 μm (-35%) is possible under the premise of reaching the same J_{SC} value. The additional reflection at the back contact can however also be used to increase the efficiency of regular thick absorber solar cells. When the Mo back contact is replaced with the metal/ITO back contact for the 2 μm solar cell, the J_{SC} value can be increased by 0.5 mA/cm^2 (+1.8%) for configuration A and 0.7 mA/cm^2 (+2.2%) for configuration B.

It can be seen in summary that the Al/ITO back contact does lead to a similar improvement of J_{SC} as the three other regarded metals, despite its lower reflectivity. The potential thickness reduction through the new back contacts is about 35% for a solar cell with a 2 μm absorber layer as a reference. A further reduction requires an additional scattering element which can for example be obtained by a structuring of the back contact. A prototype structure combining the Al/ITO back contact with a structured substrate will later be presented in Chapter 5.

3.9 Conclusion of Chapter 3

Several metal/TCO back contact combinations for CIGSe solar cells were tested. A major challenge is the occurrence of shunts. Such shunts were present in solar cells, even when no significant diffusion of the back contact metal could be observed after the CIGSe deposition. The capabilities of the TCO layers to block the diffusion of the tested metals appears to be dependent on the sputter deposition parameters. Working solar cells could be demonstrated for both the Cu/ITO and Cu/ZnO back contact on very small areas. The local shunting might originate in particle contamination or local inhomogenities of the diffusion barriers. An optimization of the deposition parameters or the cleaning/handling of the samples could possibly reduce this issues, and therefore enable further metal/TCO combinations.

Both the Au/ITO and the Al/ITO back contact proved to work well as back contacts for CIGSe solar cells. However, Au back contacts are not of interest for industrial application due to the high associated costs.

The minimum thickness for the ITO barrier in Al/ITO-based solar cells was found to be ~ 100 nm for a process temperature of 480°C. A solar cell with a thinner ITO layer showed a significant reduction of J_{SC}. This reduction is unexpected given the fact that no Al could be detected in the CIGSe in all these experiments. It is likely related to the carrier extraction at the ITO/CIGSe interface as will be discussed in Section 4.9.

Relatively high FF (~72%) were demonstrated for samples with an Al/ITO back contact, even at a deposition temperature of 600°C. This is in contrast to literature results, where poor FF are often reported at higher deposition temperatures, due to the excessive formation of Ga_2O_3.

This difference might be explainable by the absence of Na during the process and/or because of a higher stability of the employed ITO layers. TEM images revealed that no formation of Ga_2O_3 was detectable for a deposition temperature of 480°C, while some Ga_2O_3 was visible for a deposition temperature of 600°C. Interestingly, no beneficial effect of high process temperatures was found even for the Mo-based samples. Such an effect was to some extent anticipated because higher process temperatures result in an increased average crystal sizes of the absorber layer and therefore likely too less grain boundary recombination. Note however that high process temperatures are likely required in industrial processes, where the deposition time is of importance to increase the throughput. A higher process temperature allows for a reduction of the process temperature to obtain the same thermal budget.

The potential decrease of the CIGSe absorber thickness due to the usage of the alternative back contacts was discussed. A reduction of the layer thickness up to 35% appears to be reasonable (taking an absorber thickness of 2 µm as reference). No significant difference in the potential J_{SC} was found in the TMM calculations for the Al back contact compared to the Au back contact, both metals are therefore similar suited to increase the reflectivity at the back contact with the investigated concept. The Al/ITO back contact has superior optical properties compared to the standard Mo back contact, while providing similar, if not better electrical properties. The results suggest further that a thin intermediate layer between the ITO and CIGSe layer is likely not necessary to obtain high efficiency solar cells on TCO-based back contacts.

The reason for the improved V_{OC} values found for ITO-based samples compared to their Mo reference samples is unclear at this point. Furthermore, the carrier extraction mechanism is unknown for n-type TCO/CIGSe back contacts. Chapter 4 is meant to improve the understanding of both the ITO/CIGSe and Mo/CIGSe interfaces. Both aforementioned issues will be discussed with the help of the presented experimental results.

Chapter 4

Electrical characterization of the back contact

4.1   Introduction

Chapter 3 demonstrated that Al/ITO-based back contacts can provide an improved reflection at the back contact while providing similar if not better electrical properties. The following chapter tries to assess the electrical properties of both the Mo/CIGSe interface and the ITO/CIGSe interface. Solar cells with three different CIGSe thicknesses (300 nm, 550 nm, 1020 nm) were prepared. Samples with an ITO back contact were prepared simultaneously with Mo reference samples. A sketch of the used back contact types is given in Figure 4.1. The layer stack for the ITO-based solar cell is SiO_xN_y(110 nm)/ITO(260 nm)/CIGSe/CdS(50 nm)/ZnO(140 nm)/ITO(210) and the layer stack of the Mo-based sample is SiN_x(200 nm)/Mo(500 nm)/CIGSe/CdS(50 nm)/ZnO(140 nm)/ITO(210 nm). An ITO back contact without Al was used in this experiments to allow bifacial measurements. It is assumed, that the CIGSe/ITO interface is comparable for both sample types (with and without Al). Note that a thickness of the rear ITO above 200 nm is not optimal in terms of the amount of parasitic absorption as shown in Section 3.4. An ITO thickness in this range was used in this and the following experiments to ensure the comparability of the experimental results with previous findings nevertheless.

First the chemical composition (Section 4.2) and performance of the prepared solar cells (Section .4.3) will be shown. Those results will then be used in combination with simulations to estimate the back contact recombination velocity at the ITO/CIGSe interface (Section 4.4). Afterwards the results of temperature dependent JV measurements and AC measurements (Section

Figure 4.1: Sketch of the different back contact types employed in this chapter.

Table 4.1: GGI and CGI from EDX measurements measured on samples with a Mo back contact.

Absorber layer thickness (nm)	300	550	1020
CGI	0.8	0.78	0.79
GGI	0.37	0.32	0.33

4.5 to Section 4.7) will be shown of samples from the very same batch. The obtained results will then be used to discuss the presence of a back contact barrier for the two interfaces (Section 4.8) the carrier extraction at the CIGSe/ITO interface (Section 4.9), and an estimation of the influence of the electrical properties of the back contact on the solar cell parameters (Section 4.10).

4.2 Chemical composition

The GGI and CGI values obtained from EDX measurements are given in Table 4.1. It must be noted that the Mo back contact was visible in the EDX measurements for absorber thicknesses below 1.1 μm. Therefore, a higher error is expected for thinner absorber layers.

Corresponding GGI profiles from GDOES measurements are given in Figure 4.2 for all thicknesses together with the Na profiles. A GGI notch is observable in all samples, except for the 300 nm absorber sample with the Mo back contact. The position of the GGI notch is further away from the front contact, with increasing absorber thickness.

The notch is furthermore more pronounced with increasing absorber thickness. The Na profile has its minimum located at the notch position of the GGI, and is increasing exponentially from there on in both directions for the ITO-based samples. The Mo-based samples show in contrast a plateau of the Na content which increases close to the front and back contact. The Na signal is increasing at average with decreasing absorber layer thickness.

The slight differences in the composition profiles between the two sample types might be related to the fact that the actual temperature of the substrate is likely different between the two sample types. The GGI notch is generally more pronounced at lower process temperatures as shown in Section 3.5. The real substrate temperature will differ from the targeted temperatures even for the Mo-based samples for which the temperature was measured during the process, due to the fact that the thermocouple is resting on the glass side. Hence, the actual process temperature is generally lower because the temperature gradient alongside the thickness of the sample will
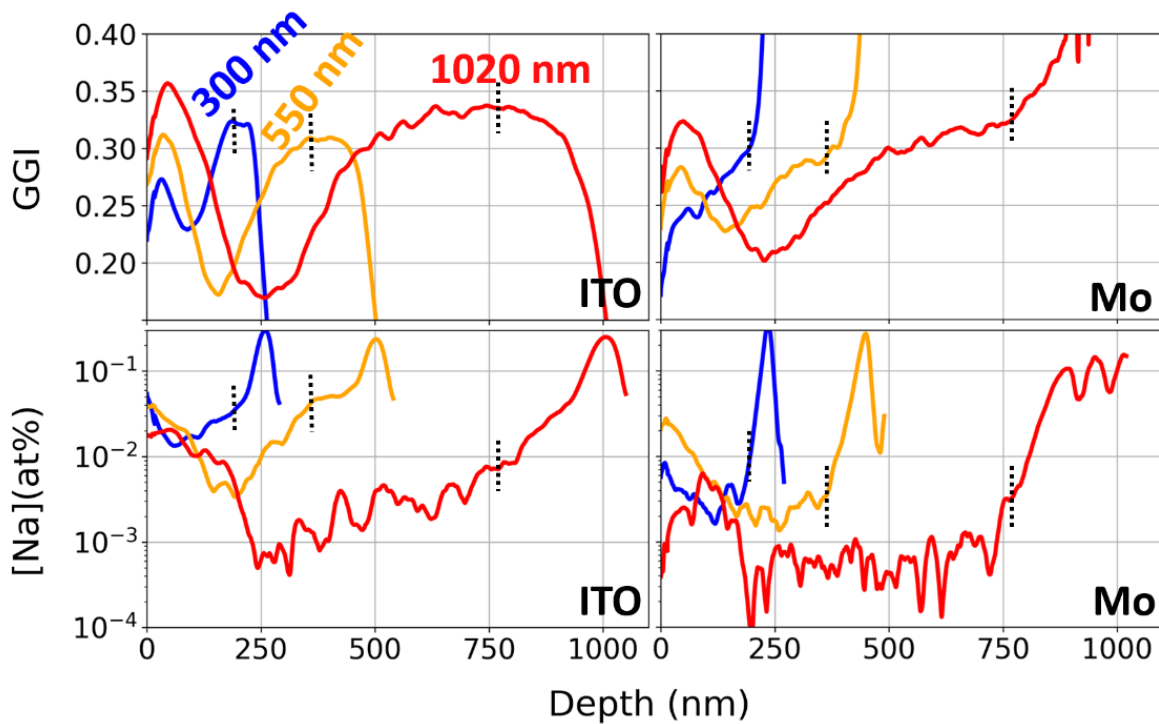
Figure 4.2: GDOES data for the different CIGSe absorber layer thicknesses on ITO back contacts (left column) and on Mo back contacts (right column). The upper row shows the GGI, while the lower row shows the Na content in atomic percent. The dashed lines mark the positions, where the Mo signal reaches 1 at% for the Mo-based samples as an estimation of the border location to the back contact.
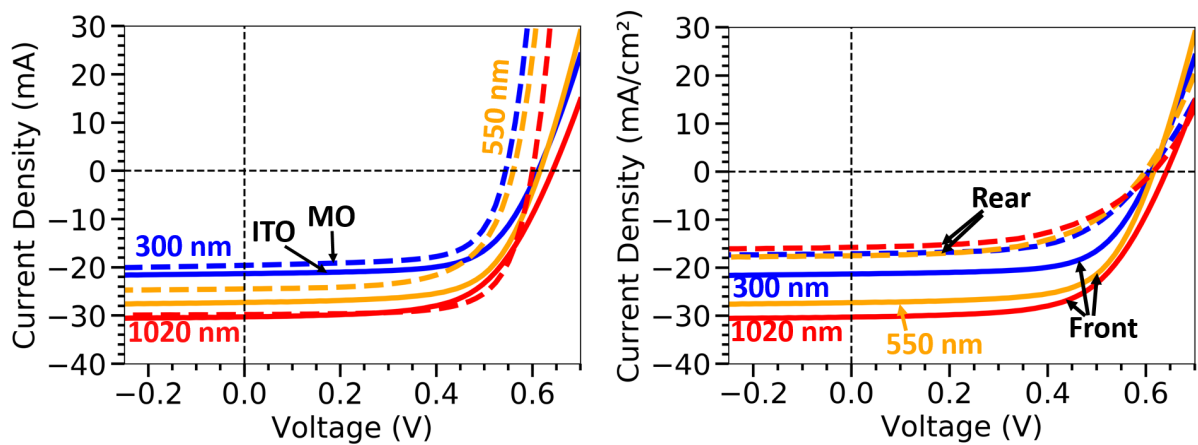
Figure 4.3: a) JV curves of the highest *PCE* solar cells using a Mo back contact (dotted lines) and ITO back contact (full lines), with different absorber thicknesses (blue for 300 nm, orange for 550 nm, red for 1020 nm). b) Comparison of the ITO samples shown in a) with the illumination both from the front (full lines) as well as from the rear (dashed lines).

lead to a reduced temperature. The sample temperature depends on a balance of the direct heat transfer from the heater to the sample and the emissivity of the sample. The heat transfer will differ, given the fact that the glass of the ITO-based samples is slightly thinner with 2.1 mm instead of 3 mm. Furthermore, the emissivity of the ITO will differ from the emissivity of the Mo. It is difficult to assess the resulting difference in temperature. However, the shape of the GGI profile suggests strongly, that the ITO-samples experienced a lower process temperature. This inconsistency will affect the prepared layers grown on the two sample types. It should however not alter the samples fundamentally.

4.3 Solar cell characterization

Figure 4.3 a) shows JV curves of all samples involved in this experiment. A comparison of the JV curves measured from the front and back contact is given in Figure 4.3 b) for the ITO-based samples. Note that the rear surface was covered with an absorptive material in the case of the ITO samples, to limit an unwanted reflection back into the sample. The extracted solar cell parameters are given in Table 4.2, together with the determined values of the parallel and series resistance.

The results under front illumination are first discussed. The V_{OC} values decrease with decreasing absorber thickness for all sample types. However, the effect is much more pronounced for the Mo-based samples. The ITO-based samples exhibit for all thicknesses larger V_{OC} values than their corresponding Mo references, with a difference of ~70 mV for the thinnest absorber layer. The FF of the sample with the thickest absorber layer is noticeably higher for the Mo reference sample. The series resistance of the ITO-based samples is considerably larger, while the relative difference of the parallel resistance is in contrast not that significant. Higher J_{SC} values were obtained with the ITO-based samples. The highest efficiency of 13% is obtained for the Mo-based 1020 nm absorber layer sample.

The ITO-based samples show generally lower solar cell parameters when they are measured with back illumination. The relative losses decrease with decreasing absorber thickness. The short circuit current exhibits the largest losses, with a loss of almost 50% of the current in the

Table 4.2: Solar cell parameters for the different back contact types and absorber layer thicknesses. In case of the ITO-based samples, the parameters are given for illumination through the front and through the rear. The J_{SC} values are determined using EQE measurements, while the other parameters are extracted from JV curves.

Back contact	Illum. side	V_{OC} (mV)	FF (%)	J_{SC} (mA/cm^2)	PCE (%)	R_s (Ωcm^2)	R_P (kΩcm^2)
d(CIGSe) = 300 nm							
Mo	Front	544	68.9	19.6	7.3	0.52	3.47
ITO	Front	611	65.5	21.3	8.5	3.27	2.23
ITO	Rear	606	59.2	17.1	6.1	5.68	1.95
d(CIGSe) = 550 nm							
Mo	Front	560	63.9	24.5	8.7	0.57	3.25
ITO	Front	616	65	27.3	10.9	2.63	2.48
ITO	Rear	598	54.7	17.5	5.7	4.24	2.41
d(CIGSe) = 1020 nm							
Mo	Front	605	72	29.8	13	0.51	3.32
ITO	Front	642	61.3	30.3	11.9	3.75	2.48
ITO	Rear	615	52.6	15.8	5.1	5.35	2.45

case of the 1020 nm absorber layer solar cell. The loss of the FF is also substantial. It is about ~9-10% absolute for the 550 nm and 1020 nm sample and about 6% absolute for the thinnest absorber layer.

The GGI measurements presented in Section 4.2 were used to calculate the absorption within the CIGSe layer. This way, the differences in the composition profiles between the ITO and Mo-based samples are included in the calculations. Figure 4.4 a) shows the measured EQE from the front side for all sample types. The corresponding calculated absorption in the CIGSe layer is presented in Figure 4.4 b).

The TMM calculations show that the absorption is mainly reduced above a wavelength of 700 nm, when comparing the 550 nm absorber layer samples with the 1020 nm absorber layer samples. The TMM measurements show further, that a reduction of the absorption is expected for the 300 nm absorber layer sample, for wavelengths above 500 nm compared to the other two absorber thicknesses. A comparison with the measured EQE shows that especially the 300 nm absorber layer samples exhibited a reduced EQE at a wavelength of 500 nm compared to the other samples, in contrast to the TMM calculations.

The EQE values of the Mo-based samples are overall slightly lower than the EQE values of the ITO-based samples. These differences are not visible in the TMM calculations. Also, lower EQE values are measured at longer wavelengths (> 900 nm) for the Mo-based samples which are not entirely justified by the calculated absorption.

Figure 4.5 shows a direct comparison of the calculated absorption and measured EQE for the ITO-based samples measured for both illumination cases. All absorption peaks can be found in the EQE curves; the peaks are however less pronounced in the EQE curves. The EQE curves are considerably lower than the calculated absorption for the rear illuminated case. The EQE is increasing with decreasing absorber thickness in the rear illuminated case. It behaves therefore opposite to the front illuminated case.

The results give an indication that the higher V_{OC} values with the ITO-based samples, which were also obtained in the other experiments, might be only observable for thin enough absorber

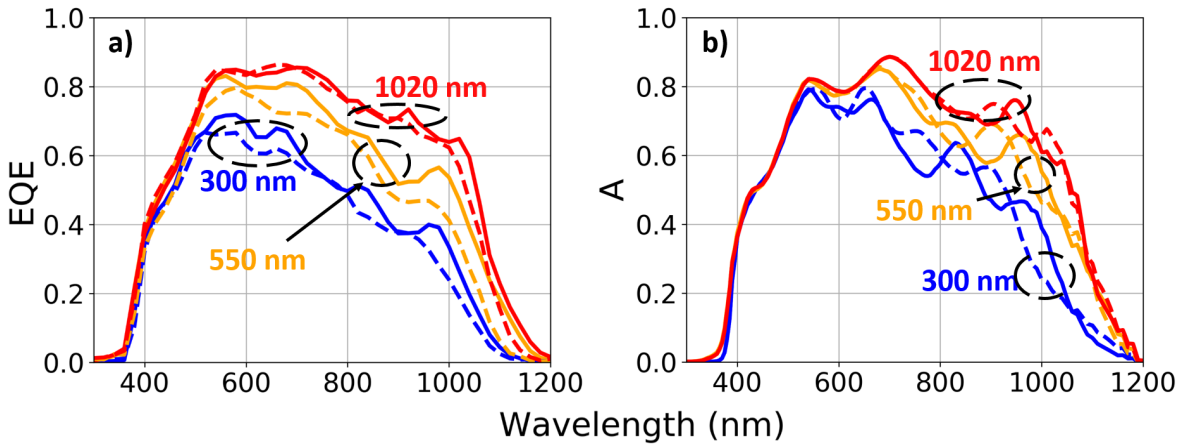Figure 4.4: a) Comparison of the measured EQE of samples with an Mo back contact (dotted lines) and ITO sample (full lines) measured from the front. b) Corresponding, calculated absorption within the CIGSe absorber layer.
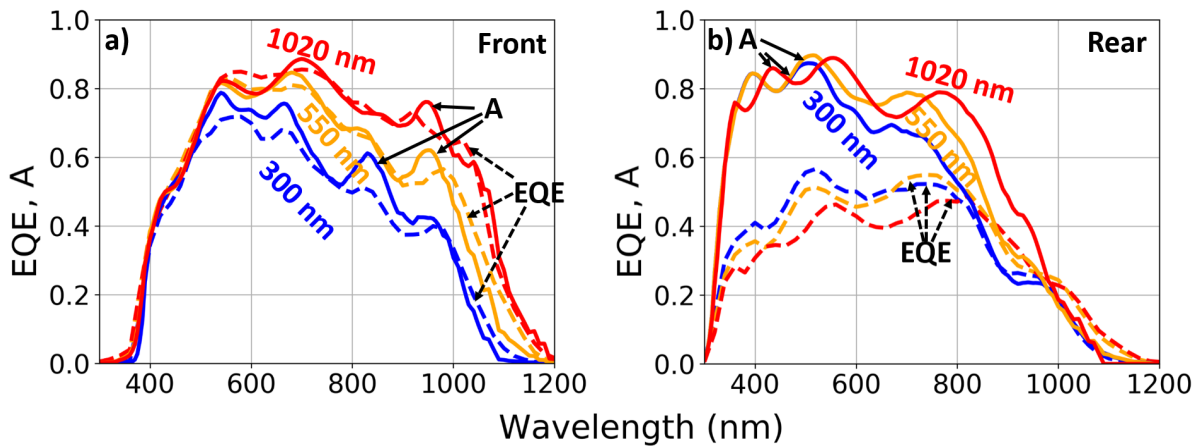

Figure 4.5: EQE of samples with an ITO back contact (dotted lines) and the corresponding calculated absorption inside the CIGSe absorber (full lines) measured/calculated from the front (a) and rear (b).

layers. A detailed analysis about the most likely cause for the observed differences in V_{OC} will be provided in Section 4.10, together with additional electrical simulations.

The comparison of the EQE curves with the TMM calculations shows that the decrease of J_{SC} with decreasing absorber layer thickness is not entirely justified through the optical losses. The lower J_{SC} values of the Mo-based samples are therefore likely also caused by higher electrical losses. The lower V_{OC} values of the Mo-based samples fit well to higher electrical losses. Higher series resistances were determined for the ITO-based samples than for the corresponding Mo-references. The difference is large enough to justify several percent of FF losses. The higher series resistance could originate from a higher sheet resistance of the back contact or it could originate from a higher contact resistance at the ITO/CIGSe interface. Given the fact that FF values above 70% were obtained for the Al/ITO samples presented in the prior chapter, it seems more likely that the limited conductivity of the ITO is causing the higher series resistance. The sheet resistance was determined to be around 7 Ω/sq from four-point analysis. The CIGSe layer was removed from a completed solar cell using a blade before this measurement. An unprocessed substrate from the same batch had a sheet resistance of 20 Ω/sq. The thermal treatment during the CIGSe deposition appears to increase the conductivity of the ITO.

The bifacial measurements show that the EQE values are increasing, instead of decreasing with the decreasing absorber layer thickness when the illumination is conducted through the rear side. A significant portion of the charge carriers will be generated in the vicinity of the back contact in this case. The minority carriers have to diffuse a longer distance to be collected as a result. They are therefore stronger subjected both to back contact recombination as well as to bulk recombination. The observed behavior can be understood by the fact that the collection losses increase faster with the absorber thickness, than the gains through the additional absorption. Rather strong differences are found between the calculated absorption and the EQE curves around 400 nm. The collection function is therefore very low close to the back contact.

The obtained rear EQE curves can be compared to the results of Keller et al. who measured the rear EQE on IOH based bifacial solar cells with an absorber layer thickness of 650 nm [9]. The obtained EQE curves for the 550 nm absorber sample in this work is comparable to the EQE obtained by Keller et al. for a sample employing an Al_2O_3 passivation layer. It can however not be concluded from this observation that both interfaces have a similar back contact recombination rate, due to the influence of the bulk recombination rate.

4.4 Determination of the back contact recombination velocity

The measurements shown in the prior section will be used in the following to estimate a value for the back contact recombination velocity of the electrons at the ITO/CIGSe interface. Difficulties arise from the inaccessibility of certain parameters, which are important for the simulations.

Most notably a large uncertainty concerns the electron mobility. Values used by other authors in the literature range typically from 2 cm^2/(Vs) to 100 cm^2/(Vs) [59, 60]. This uncertainty stems from the fact that only a very limited amount of experimental determinations of the carrier mobilities exists, which is furthermore mostly focused on the hole mobility [61, 62, 63, 64, 65]. The measured carrier mobilities differ from 0.01 cm^2/(Vs) to 100 cm^2/(Vs). However, the effect of the back contact recombination velocity on the cell parameters will differ depending on the electron mobility within the CIGSe layer.
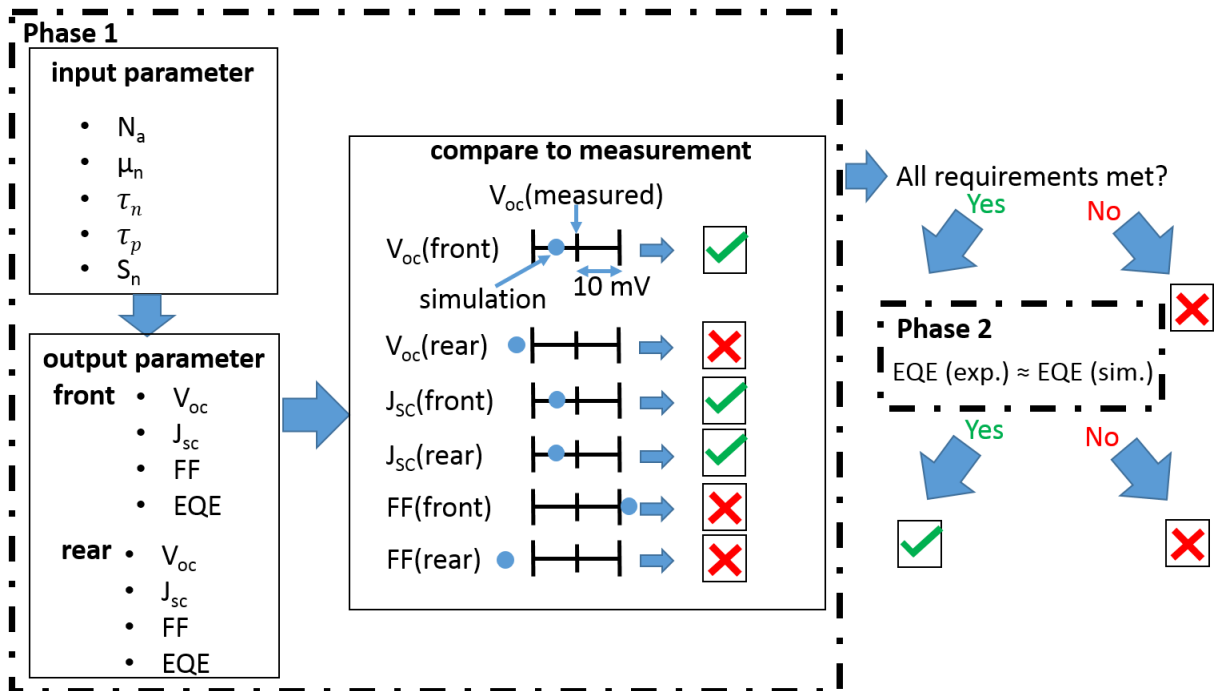
Figure 4.6: Flow chart explaining the condition used to determine if a specific set of input parameters is considered correctly representing the measured data of a specific solar cell.

Figure 4.7: Simplified example using only two input parameters, to explain how the range of valid parameters for the simulations is determined. A fixed set of values for the input parameters is defined and each possible combination of the input parameter is calculated.
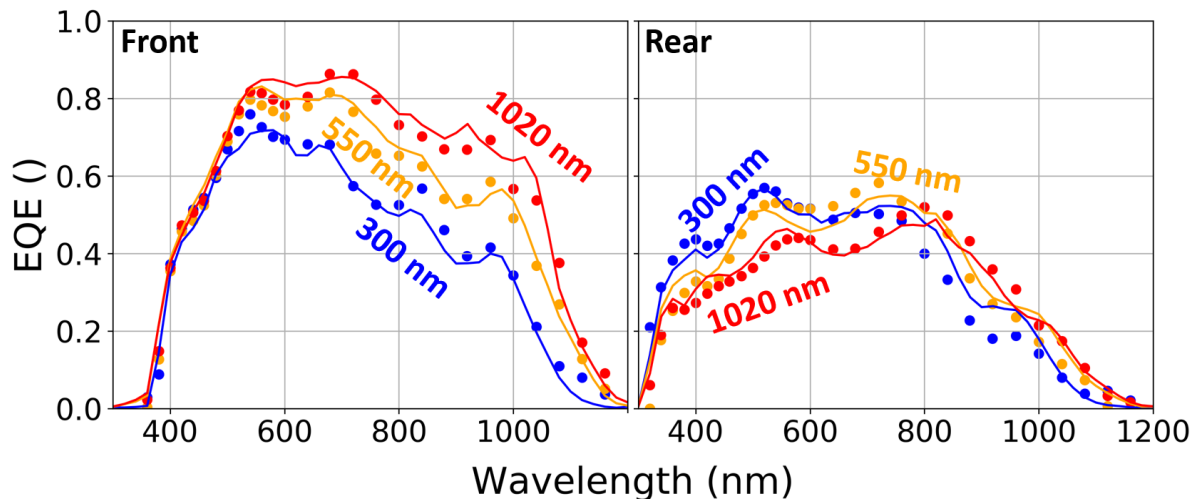
Figure 4.8: EQE values calculated from the electrical simulations (points) with EQE measurements (lines). The parameter set for the simulations was picked randomly from the available parameter sets, which fullfills all defined solar cell parameters targets.

Table 4.3: Overview of the used model parameter for each solar cell layer.

	ITO (Front)	ZnO	CdS	CIGSe
ε ()	9	9	10	13.6
χ (eV)	4.1	4.1	4	varied
E_g (eV)	4	3.3	2.4	varied
N_C (cm^{-3})	$2.2 \cdot 10^{18}$	$2.2 \cdot 10^{18}$	$2.2 \cdot 10^{18}$	$2.2 \cdot 10^{18}$
N_V (cm^{-3})	$1.8 \cdot 10^{19}$	$1.8 \cdot 10^{19}$	$1.8 \cdot 10^{19}$	$1.8 \cdot 10^{19}$
μ_n (cm^2/(Vs))	100	100	100	varied
μ_p (cm^2/(Vs))	100	100	100	10
N_a (cm^{-3})	0	0	0	varied
N_d (cm^{-3})	10^{19}	10^{18}	10^{17}	0
v_e (cm/s)	10^7	10^7	10^7	10^7
v_h (cm/s)	10^7	10^7	10^7	10^7
Defect				
Type	acceptor	-	-	donor
E_d-E_v (eV)	1.7	-	-	midgap
Density (cm^{-3})	10^{14}	-	-	10^{13}
c_n (cm^2)	10^{-14}	-	-	varied
c_p (cm^2)	10^{-14}	-	-	varied

Table 4.4: Determined valid parameter range in which at least one possible combination of the input parameters is found, correctly describing the experiment.

Absorber thickness (nm)	300	550	1020
N_a (cm^{-3})	$(3.4...4.6) \cdot 10^{16}$	$(1.0) \cdot 10^{16}$	$(3.4...4.6) \cdot 10^{15}$
S_n (cm/s)	$(5...7) \cdot 10^4$	$1 \cdot 10^4 ... 1 \cdot 10^5$	$1 \cdot 10^4 ... 5 \cdot 10^5$
μ_n (cm^2/(Vs))	20...40	5...30	20...70
τ_n (ns)	0.2...1	5...10	1...20
τ_p (ns)	0.1...0.2	0.1...10	10...100

This highlights the general complexity of the problem. The solution space for one parameter does change with the assumed value for another parameter in the simulations. To accommodate to this problem, a strategy was chosen, which does rely on as few as possible assumptions. Bifacial measurements enable the analysis of the cell parameters for two distinct carrier generation profiles. The back contact recombination rate will generally have a larger effect on cell parameters, if the illumination is happening through the rear side. The combination of the EQE and JV measurements from both illumination directions will be used to reduce the possible range of the inaccessible quantities in the following. This is possible through the asymmetric effect of the simulation input parameters on the cell parameters. E.g. the back contact recombination velocity has generally a much stronger effect on J_{SC} when the illumination is performed through the rear side. The doping density will affect in contrast V_{OC} for both illumination conditions with a similar sensitivity.

The JV and EQE results were simulated for each ITO-based sample using AFORS-HET. A summary of the used model parameter and layer systems is given in Table 4.3. The GGI given in Figure 4.1 was also included in the electrical simulations. The back contact is implemented at the CIGSe/ITO interface using a metal-semiconductor-Schottky-contact with no band bending at this interface.

A total of five different modeling parameters was systematically varied through the simulations. Those parameters, which will be referred in the following as **input parameters** are:

- The electron recombination velocity at the back contact S_n.

- The bulk recombination was modeled by a singular donator defect located in the middle of the band gap of the absorber. The defect density of this defect was set to a fixed value of 10^{13} cm^{-3}. The bulk recombination is varied through the electron capture cross section σ_n and hole capture cross section σ_p of this defect level. This way the bulk lifetime of both charge carriers is varied.

- The doping density of the acceptors N_A inside the CIGSe absorber.

- The electron mobility μ_n in the CIGSe absorber.

The hole mobility was also included in former versions of the simulations. However, those results revealed that the impact of the hole mobility was very limited, when it was varied between 1 cm^2/(Vs) and 100 cm^2/(Vs). Hence it was set to a fixed value of 10 cm^2/(Vs) to reduce the total amount of simulations.

A methodology was developed to evaluate the solution space in which combinations of the five input parameters can be found, which appropriately describe the experimental data. A flow chart of the employed methodology is given in Figure 4.6. Each sample is characterized by a total of six solar cell parameters being: the V_{OC}, the FF, and the J_{SC} values; each for both front and rear illumination. Each set of the five input parameters calculation model is validated through two validation phases.

In the first phase, it is checked if the simulated JV parameters are equal to the measured ones. A confidence interval is defined for each solar cell parameter. The accepted maximal deviation from the experimental values are namely 10 mV for V_{OC}, 4% absolute for the FF, and 0.5 mA/cm^2 for J_{SC}. A set of parameters passes the first validation phase only if all 6 solar cell parameters fall in this range simultaneously.

The second phase takes the shape of the rear EQE into account. Simulations showed that the back contact recombination velocity will mainly affect the carrier collection in the short wavelength region, when illumination is performed is through the rear. The calculated EQE value at a wavelength of 400 nm is compared to the experimental one. If the relative difference is less than 5%, then the input parameter set will pass the second phase and is hence considered to correctly describing the experiment. A comparison at only a singular wavelength has proven to be sufficient, due to the fact that the J_{SC} value is already tested in the first phase. Consequently, the rest of the calculated EQE curves is following the measured EQE, as can be seen for both illumination conditions in Figure 4.8. The input parameters sets for this figure were picked randomly from all sets passing both validation phases. An overall good match is visible between the experimental and calculated EQE as can be seen in this figure.

A challenge of this method is the large number of input parameters. The solution space for each input parameter will depend on the regarded value ranges of the other 4 input parameters. A fixed set of different values is defined for each input parameter e.g. $S_n = (10^3, ... 10^7)$ cm/s. Each possible combination of the input parameters is then tested. This ensures that the solution space of one parameter is not artificial narrowed down by another parameter. The large number of possible combinations means however that more than 10^6 simulations have to be performed.

Only a fraction of the parameter sets passes both phases. The strategy is to find out in which range for each parameter at least one solution is found. A simplified example using only two input parameters is given with Figure 4.7. The back contact recombination velocity in the given example has to be between 10^3 cm/s and 10^5 cm/s. Other parameter ranges e. g. the doping density come out as a by-product. Hence, a range in which the back surface recombination velocity is situated can be given at the end.

The resulting parameter ranges found through simulations can be seen in Table 4.4. The doping density decreases with increasing layer thickness according to the simulations. The back contact recombination velocity was determined to be somewhere between $5 \cdot 10^4$ cm/s to $5 \cdot 10^5$ cm/s. The electron mobility ranges between 5 and 70 cm²/s. The average and maximum value for the acceptable range for both τ_n and τ_p is increasing with the absorber layer thickness.

The determination of the back contact recombination rate highlights how difficult it is to obtain a reliable value for this quantity. The same analysis as shown, performed using only the rear EQE as experimental information gave the result that an almost arbitrary value for S_n could be used to describe the curves. A similar result was obtained by Keller et al., who showed that the rear EQE of the measured bifacial solar cell can be modeled using different values of S_n depending on the chosen value for the diffusion length L_n [9].

The main issue is the large number of unknown quantities. TRPL (Time-Resolved Photoluminescence) measurements could be used to extract the minority carrier lifetime. However, the extraction of the minority carrier lifetime is unfortunately also not trivial. The decay of the TRPL signal might be manipulated by other processes than the charge recombination process [59].

The methodology was developed to accommodate to these issues. It is however only applicable to bifacial solar cells. The value for S_n was determined to be somewhere around 10^4 cm/s and 10^5 cm/s. This value is larger than a typical value aimed for by a passivation layer ($10^2 - 10^3$ cm/s), but lower than the thermal velocity of 10^7 cm/s. The relevance of this parameter on cell parameters will later be discussed in Section 4.10.

Mollica et al. determined a value for S_n for CIGSe solar cells with two different TCO back contacts from rear EQE measurements. A value of 10^5 cm/s was determined at a ZnO:Al/CIGSe

interface and a value of 10^7 cm/s for a SnO_2:F/CIGSe interface [7]. However, this value was obtained for an assumed value for τ_n and μ_n, which is problematic as can be seen in the work of Keller et al. and the current work [9]. Most publications assume a value between $S_n = 10^4$ cm/s and $S_n = 10^7$ cm/s for the Mo/CIGSe interface [29]. However, values as low as $S_n = 10^2$ cm/s were reported for this interface [13]. Hence, some uncertainty is present even for the most common interface at the back contact - the Mo/CIGSe interface.

4.5   Temperature-dependent JV measurements

The solar cells used in the preceding sections were further characterized using temperature dependent JV and admittance measurements. The area of the solar cells was reduced to about 20 mm^2 for this purpose. Those samples with a reduced area are also used for admittance measurements. Smaller sample areas are advantageous for admittance measurements due to the reduced impact of the series resistance on admittance results. Note that the samples were brought in the relaxed state prior to the dark JV measurements, which was done by leaving the sample overnight in the chamber. CIGSe solar cells are known to possess some metastable properties, which change upon illumination of the solar cells and typically revert back if the sample is left without illumination [14]. The sample is therefore brought into a controlled state when it is brought into the relaxed state. Further details on the measurement setup are given in Section 2.2.5.

Figure 4.9 shows JV curves with and without illumination measured at temperatures ranging from 80 K to 330 K in 10 K steps. The dark JV and illuminated JV measurements were performed on separate days. The current in this figure is adjusted to the calculated J_{SC} values from the EQE measurements at room temperature. Several distortions of the JV curves can be seen for the illuminated JV curves. A kink can be seen for all Mo-based samples at temperatures below roughly 150 K in forward bias direction (I quadrant). This kink is least visible for the sample with the thinnest absorber layer. A different distortion can be seen for the 550 nm and 1020 nm ITO-based solar cells. The J_{SC} values are decreasing with decreasing temperature. The JV curves are also not parallel to the voltage axis around 0 V. A pronounced crossover can be seen for all samples. It is however generally more pronounced for the Mo-based samples.

$V_{OC}(T)$ curves can be used to determine the activation energy of diodes. It can be shown that for an ideal diode the extrapolation of a V_{OC} vs. T graph to 0 K should yield the activation energy of the diode [14]. This activation energy does correspond to the band gap of the absorber layer minus 75 meV [14].

A linear dependence of the $V_{OC}(T)$ curves is however only found for the ITO-based samples as can be seen in Figure 4.10. A change of the slope can be seen at lower temperatures in case of the Mo-based samples. Another linear slope appears to be entered roughly at 150 K. The presence of a back contact barrier was often found for CIGSe solar cells [53, 66, 67]. Such a barrier acts as a counter diode to the main junction. The conductivity of the back diode is usually assumed to be much higher than the conductivity of the main diode at room temperature [68]. No significant influence on the JV curve is expected through the back diode under this assumption because both diodes are connected in series, and the much lower resistance of the back diode can be neglected. The resistance of the back diode will however increase with decreasing temperature. Therefore, some voltage drop will occur at the back diode at sufficiently low temperatures, reducing the voltage drop across the main junction.
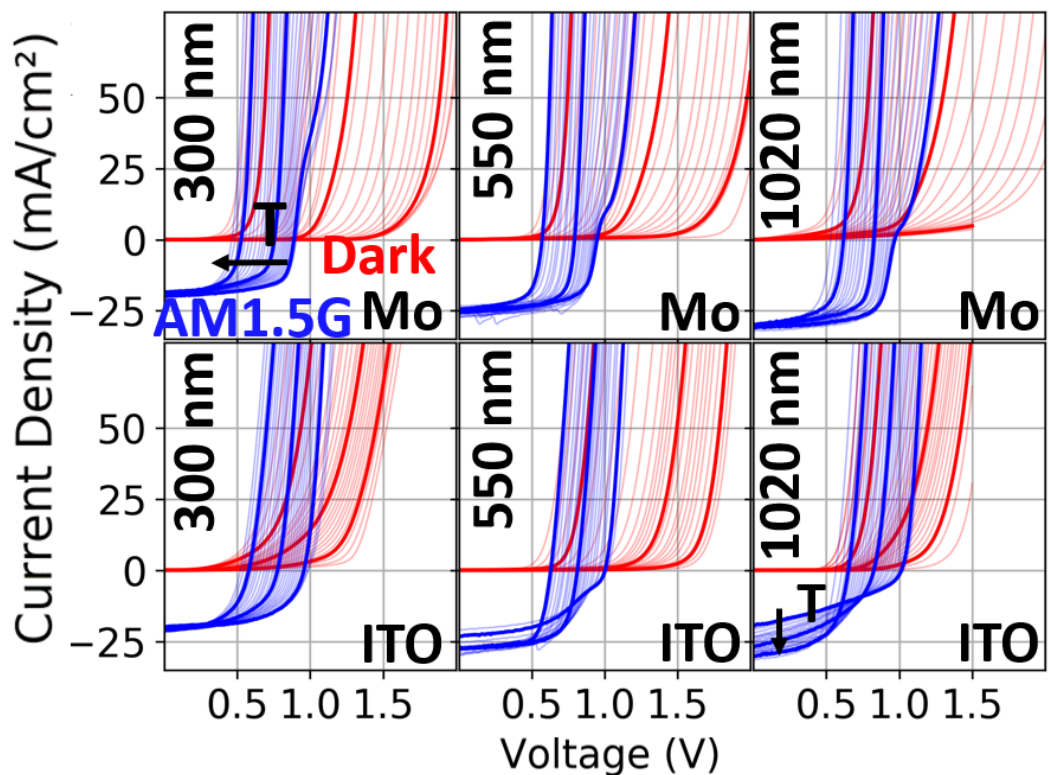
Figure 4.9: Temperature-dependent JV curves measured in dark (red) and under illumination (blue) for the different absorber layer thicknesses and back contact types. The curves are plotted with thick lines for 100 K, 200 K, and 300 K. The black arrows show the relative shifting direction of the JV curves with increasing temperature. The temperature ranges between 80 K and 330 K in 10 K steps.
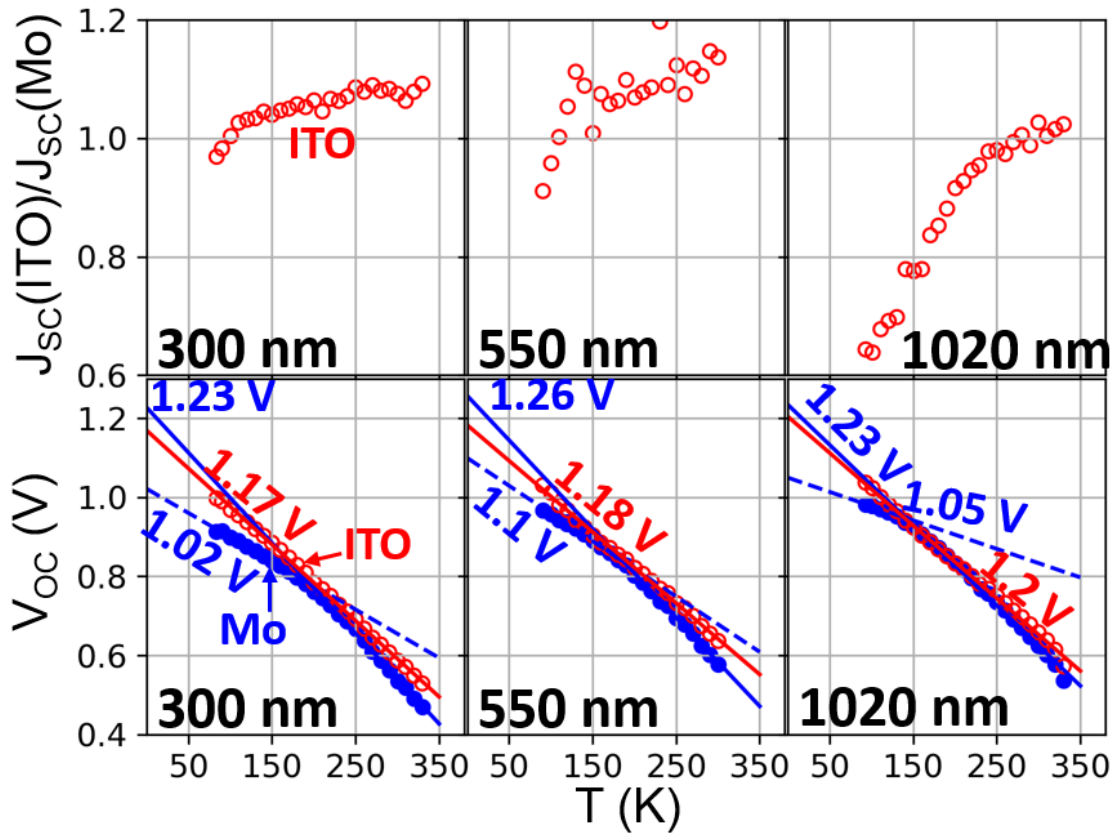
Figure 4.10: upper row: Temperature dependence of the relative J_{SC} values. The J_{SC} values of the ITO-based samples are referenced to the J_{SC} values of the Mo-based samples, the latter thus serving as an approximate measure of the variation of the light intensity. lower row: Temperature dependence of the V_{OC} values. The lines correspond to linear fits of the V_{OC} curves at low temperatures (dashed lines) and at higher temperatures (full lines) respectively. In case of the ITO-based samples, the whole V_{OC} measurement range was used for the linear fit. The voltage labels give the V_{OC} extrapolated to 0 K.

Ott et al. studied the functional dependence of $V_{OC}(T)$ in the framework of a phototransistor model [69]. The mathematical derivation showed that two linear slopes are expected for $V_{OC}(T)$ curves, one for sufficient high temperatures and another linear slope at low temperatures. According to this theory, a linear extrapolation of $V_{OC}(T)$ to 0 K is yielding the same result as an ideal diode without a back contact barrier. This value is lowered by the back contact barrier height when the linear regime at lower temperatures is employed for the extrapolation. Hence, the differences of the two extrapolated values should be equal to the back contact barrier height.

Corresponding linear fits are also shown in Figure 4.10. The determined activation energy is about 1.23 eV for the Mo-based back samples, while it is about 50 meV lower for the ITO-based samples. The determined barrier heights for the Mo-based samples are in increasing absorber thickness order 210 meV, 160 meV, and 180 meV.

Another feature found in the JV curves is the presence of a kink in case of the Mo-based sample. The presence of a kink was reported in several publications. A large cliff at the buffer/window interface can explain a blocking of the diode current under larger forward bias [70]. Alternatively, the kink might be related to a rollover. A rollover can be expected at sufficient low
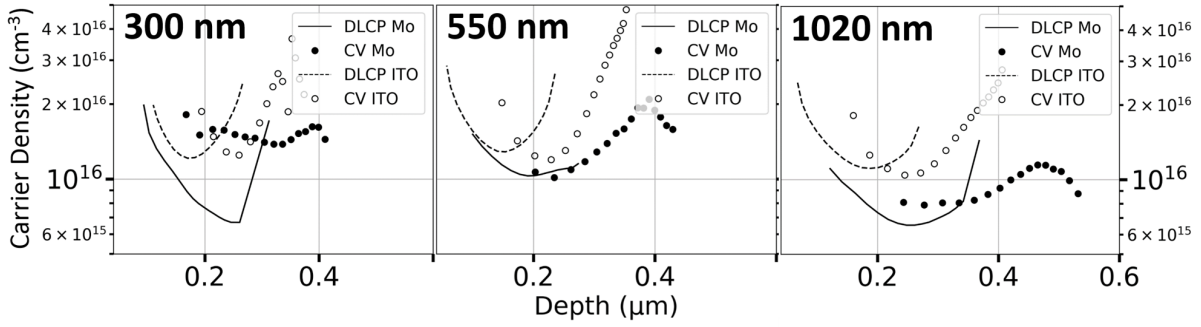
Figure 4.11: Charge carrier density profiles extracted from CV (circle) and DLCP (line) measurements.

temperatures if a back contact is present. This will be discussed in Section 4.8.

The last effect visible in the $JV(T)$ curves is the reduction of the short circuit current under decreasing temperatures. Figure 4.10 shows the relative change of J_{SC} with the sample temperature for the ITO-based samples. The J_{SC} values have been divided by the J_{SC} values for the corresponding Mo-based samples to mitigate a scattering of the current values caused by the instability of the sun simulator. The J_{SC} values appear to decline linearly with the sample temperature. However, the amplitude is much more pronounced for the 1020 nm sample. In the case of the 550 nm absorber a stronger decrease of J_{SC} appears to happen roughly below 130 K. This indicates a problem with the charge carrier collection for this kind of back contact. It could be therefore directly related to a problem at the CIGSe/ITO interface. This effect will be discussed in Section 4.9, when a proposed model for the CIGSe/ITO interface will be presented.

4.6 Charge carrier density

Both DLCP and CV measurement were used to determine the charge carrier density inside the absorber layers for two different measurement frequencies. Figure 4.11 shows the determined values for a measurement frequency of 5 kHz (a figure with a further measurement frequency can be found in the Appendix D).

A typical U-shape of the values can be seen for almost all curves. Relative similar results are obtained for both measurement techniques. The overall shapes of the CV measurements look similar to the DLCP measurements but appear to be slightly shifted. The determined values of the average charge carrier density are around 10^{16} cm^{-3}. Only a small increase of the carrier density is visible for decreasing layer thickness, for the charge carrier densities determined from CV measurements. The values of the ITO- and Mo-based samples appear to be very similar.

The observed U-shape of the determined charge carrier profiles from both the CV and the DLCP measurements is commonly reported. Several explanations were proposed for this observation by the literature.

One possible explanation for the increasing carrier density in reverse bias (largest depth) is the charging of deep defect states [71]. Eisenbarth et al. proposed the back contact barrier as a possible reason for the apparent increase of the charge carrier density in forward direction [68]. Because this increase was also observed for the ITO-based back contact, this explanation
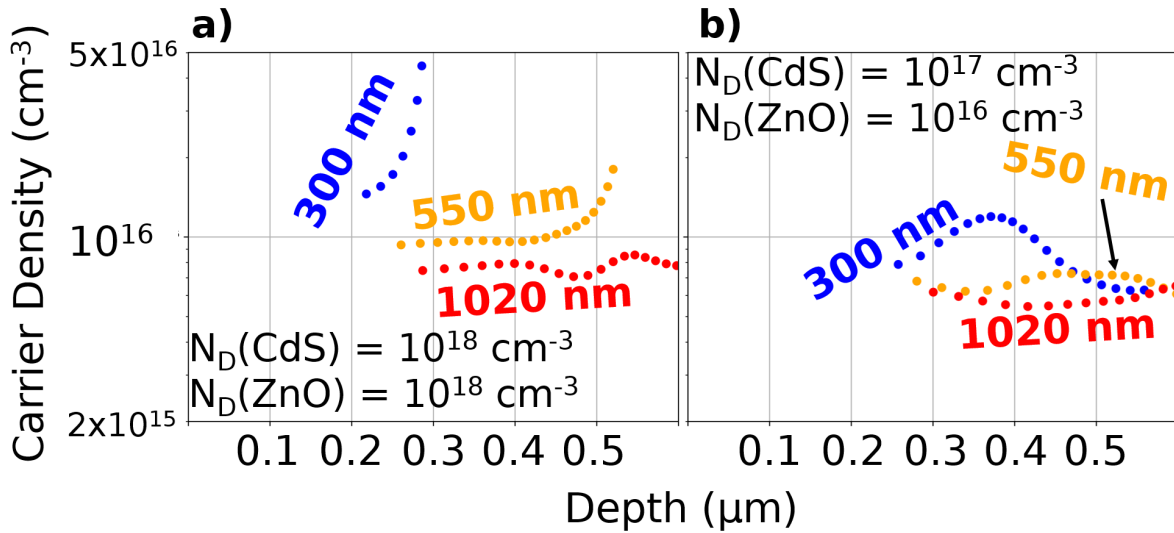
Figure 4.12: Determined charge carrier density from simulated CV curves for CIGSe solar cells with different absorber layer thickness. The doping density of the CIGSe layer in ascending absorber thickness order are $0.8\cdot10^{16}$ cm^{-3}, $1\cdot10^{16}$ cm^{-3} and $1.5\cdot10^{16}$ cm^{-3}. The extraction of the doping density was performed in the same manner from the calculated CV curves as used in the experiment. a) The doping density of the CdS and ZnO layers was set to 10^{18} cm^{-3}. b) The doping density of the CdS layer was set to 10^{17} cm^{-3}, while it was set for the ZnO layer to 10^{16} cm-3.

would require the presence of a barrier for both back contact types. As will be discussed later in Section 4.8, no such barrier is assumed to be present for the ITO/CIGSe interface.

Sozzi et al. investigated the influence of different properties of the CdS layer on the determined charge carrier density profiles for CIGSe solar cells through simulations [72]. Furthermore, the doping density of the undoped ZnO layer was varied. Generally, one side of the pn-junction has to be assumed much higher doped than the other side of the pn-junction to apply the formula used for both CV and DLCP calculations. Sozzi et al. showed that the U-shape is explainable by an insufficient doping of the CdS or ZnO layer. It was found that the determined value approaches the real doping density of the absorber layer under large forward or reverse bias, while a lower value was found in-between.

Another thing to remark is that the CV measurements yield values at positions larger than the absorber thickness. Electrical simulations were conducted to improve the understanding on this topic. CV curves were calculated using AFORS-HET and the same procedure as used for the experiment was employed to determine the charge carrier density with the same absorber thicknesses as used in the experiment. The results are shown in Figure 4.12 for two cases. In the first case visible in 4.12 a), both the CdS and ZnO layers are highly doped (both with $N_D=10^{18}$ cm^{-3}). The used doping densities in the CIGSe layer in ascending absorber thickness order are $0.8\cdot10^{16}$ cm^{-3}, $1\cdot10^{16}$ cm^{-3} and $1.5\cdot10^{16}$ cm^{-3}. A very strong increase of the apparent carrier density can be seen in case of the 300 nm and 550 nm absorber layer solar cells, roughly at the position where the absorber is ending. This is caused by a saturation of the capacity because the full absorber layer is depleted. A CIGSe doping density in the $1.5\cdot10^{16}$ cm^{-3} range leads to this effect already at a small reverse bias in the case of the 300 nm absorber layer sample. The determined carrier densities before this increase are very close to the doping densities used in the model. The doping densities of both the CdS and ZnO layers were reduced in the second case (N_D(CdS)=10^{17} cm^{-3} and N_D(ZnO)=10^{16} cm^{-3}). The calculated carrier densities

yield carrier densities at a further distance than the absorber layer thickness in this case. The calculated carrier densities are furthermore lower than the doping densities used in the models. The calculation of the charge carriers densities relies on the assumption that one side of the pn-junction is significantly higher doped than the other side, which results in a expansion of space charge region mainly in the lower doped side of the pn-junction. The doping densities used in the second case are insufficient for this assumption. A change of the applied voltage will therefore change also the space charge width on the n-side of the junction. The fact that charge carrier densities beyond the sample thickness were found for the sample with the 300 nm absorber layer could therefore give a hint that the CdS and ZnO layers are possibly not sufficiently doped to extract the real doping densities of the CIGSe absorber layers. The calculated charge carrier densities would be systematically reduced compared to the absorber layer doping in this case. A determination of the doping density of the ZnO and CdS would be required for a further clarification.

Another estimation of the doping density was obtained from the determination of the back contact recombination. A much clearer increase of the doping density was found with decreasing absorber thickness in this case. An increase of the doping density is to some extend expected for these samples. All samples received the same NaF post deposition treatment. Therefore, the same amount of Na was distributed over less CIGSe material for the thinner absorber layers. This can also be seen through the increased Na signal found via GDOES for the thinner absorber layers. The fact that the charge carrier density is not only given by a singular value but rather a distribution makes a comparison of the doping densities obtained from the two methods difficult. A similar value to the one acquired from the bifacial analysis is obtained for the 550 nm absorber in the minima of the charge carrier density curves. The value obtained from the bifacial analysis is twice as high as the minimal value from CV measurements in case of the thinnest absorber layer. For the thickest absorber layer sample it is half of the determined value from CV measurements. This discrepancy could be explained to some extent by an insufficient doping of the window layer.

What the CV and DLPC measurements however show clearly, is that the CIGSe doping density of the ITO-based samples appears to differ not much from the corresponding Mo reference samples.

It is furthermore interesting that a Na distribution profile was found, despite the fact that the Na was applied after the absorber growth. The Na near the back contact has therefore to originate from a Na diffusion to the back contact. The gradient towards the back can be explained either by a reduced Na diffusivity at the CIGSe/back contact interface leading to a pile-up or by an enhanced density of grain boundaries close to the back contact since Na is typically found at the grain boundaries of CIGSe [73]. It however unclear, if a Na distribution can also lead to an inhomogeneous doping distribution.

4.7 Admittance spectroscopy

Frequency-dependent capacitance measurements were performed at different bias voltages and temperatures. The sample were brought into the relaxed state prior to the measurements. Figure 4.13 shows the results of the $C\omega$-curves of the two samples with a 550 nm absorber without a bias voltage. A complete overview about all obtained $C\omega$-curves is given in Figure 4.14 showing all included samples and bias voltages.
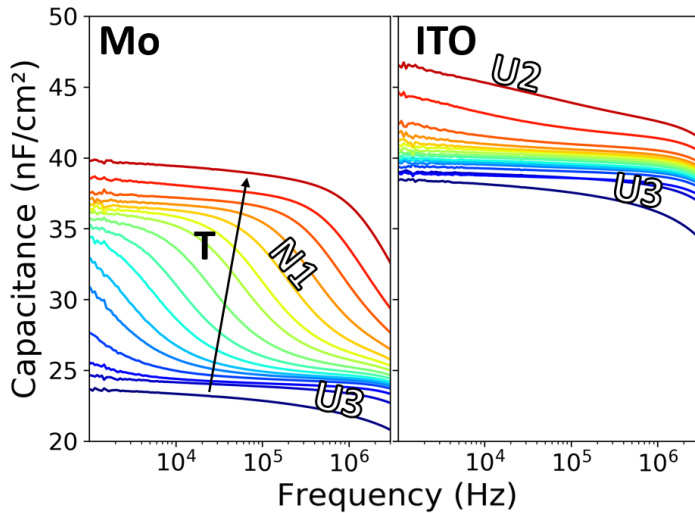
Figure 4.13: Frequency-dependent capacitance measurements at zero bias voltage of solar cells with 550 nm thick absorber layers and Mo and ITO back contacts, respectively. The temperature ranges between 80 K and 250 K in 10 K steps.

A major capacitance step can be seen for the Mo-based sample in Figure 4.13. This step will later be identified as the N1 signal, a signal found for almost all CIGSe solar cells. This feature is visible for all Mo-based samples as visible in Figure 4.14, but for none of the ITO-based samples. In case of the Mo-based samples it is also not visible for the sample having a 300 nm absorber layer, if not additionally a forward bias is applied.

Another feature clearly visible in Figure 4.13 for the ITO-based samples is a small capacitance drop, which is happening over the full frequency range at high temperatures. This feature will be denoted as U2 the following. Both samples of Figure 4.13 show a decrease of the capacity at low temperatures in the high frequency region. This signal will be called U3 in the following.

The last visible feature is the apparent drop of the capacitance near the maximum measured frequency.

The characteristics of the admittance signals can be further analyzed using color plots of $-\omega\frac{dC}{d\omega}$ as a function of temperature and angular frequency. This presentations helps to track the influence of an applied voltage on the position of the signal. Depending on the source of the signal, a different influence of the bias voltage is to be expected. Hence, more information are available to analyze the cause of the signal. Figure 4.15 shows the color plots for all samples and bias voltages. Note that the color scale was adjusted for each subplot individually to ensure that the signals can clearly be seen. The following observations can be made from this figure:

- N1. This signal is present in all of the Mo-based samples but is absent in all of the ITO-based ones. Its position in the ω-T diagram is virtually independent of the applied bias voltage. It shifts to higher temperatures with decreasing absorber thickness. However, the signal disappears in case of the Mo-based sample with the thinnest absorber layer at zero and reverse bias voltage.

- U1. This feature is clearly visible only for the sample with the Mo back contact and a 300 nm absorber layer thickness for zero and reverse bias.
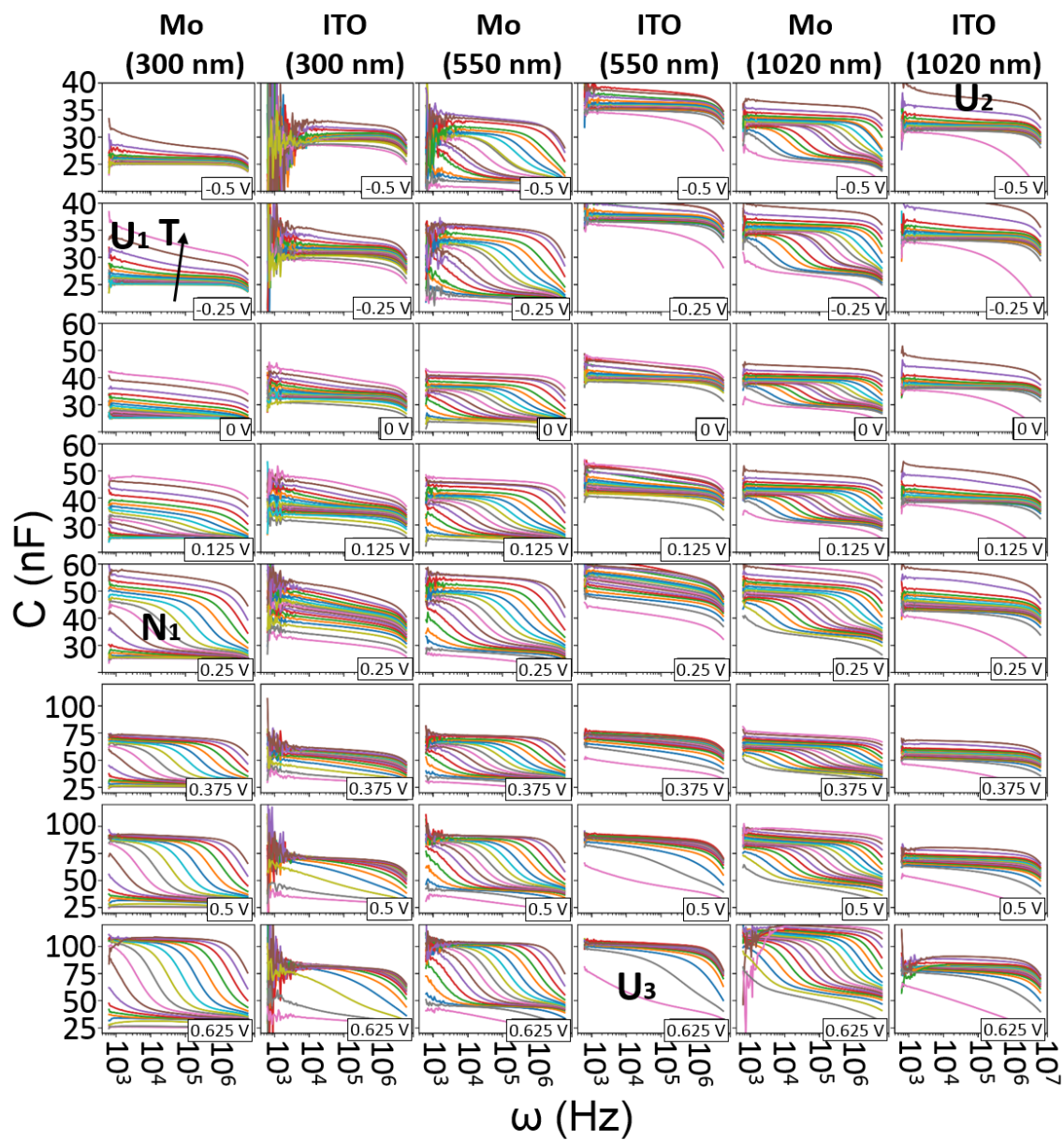
78

Figure 4.14: Frequency dependent capacitance measurements at different temperatures and bias voltages, for all samples included in the experiment.
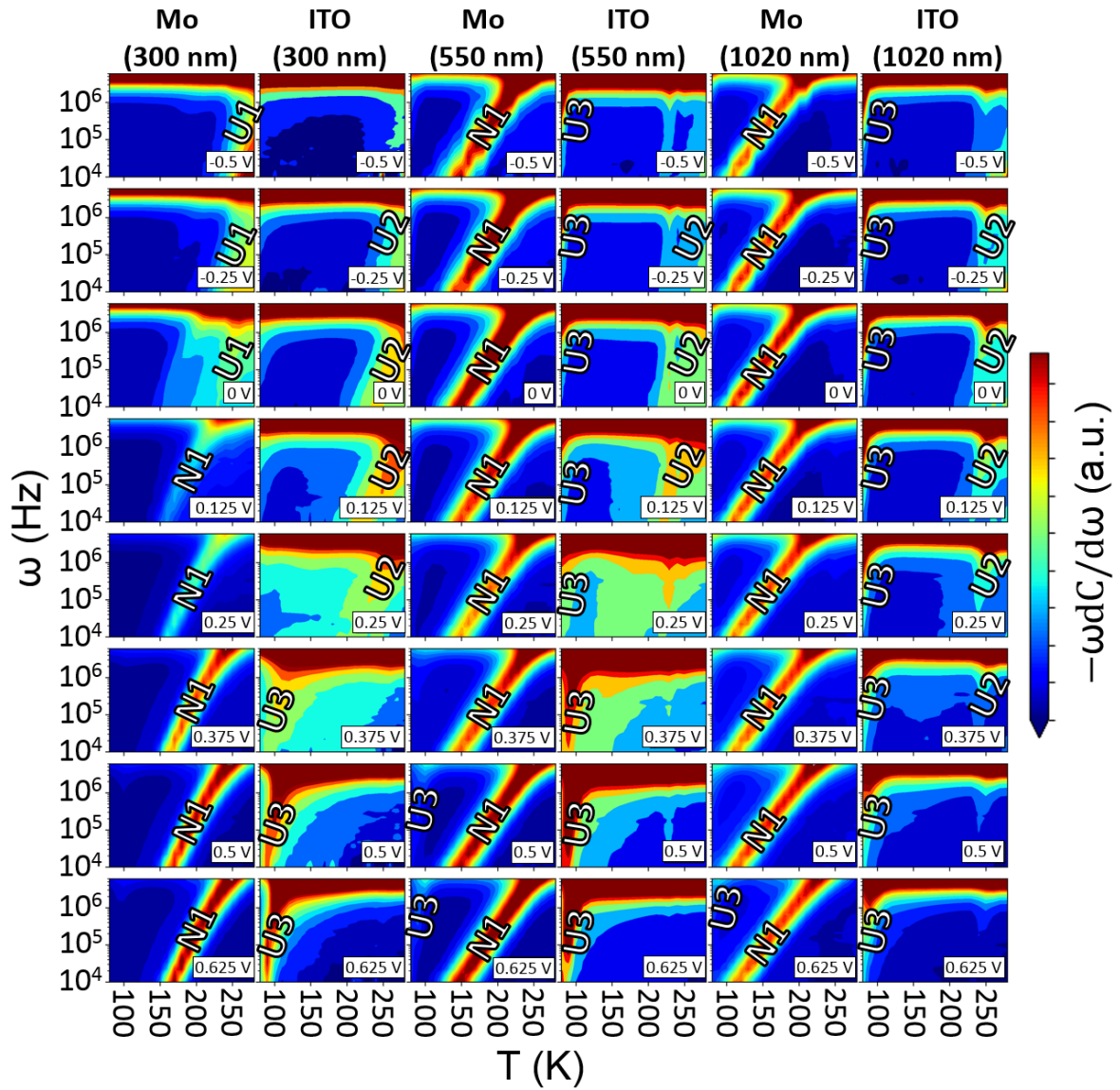
Figure 4.15: Color plot of -ωdC/dω as a function of temperature and angular frequency for the six samples at different bias voltages. Note that each plot has its own relative color scale.
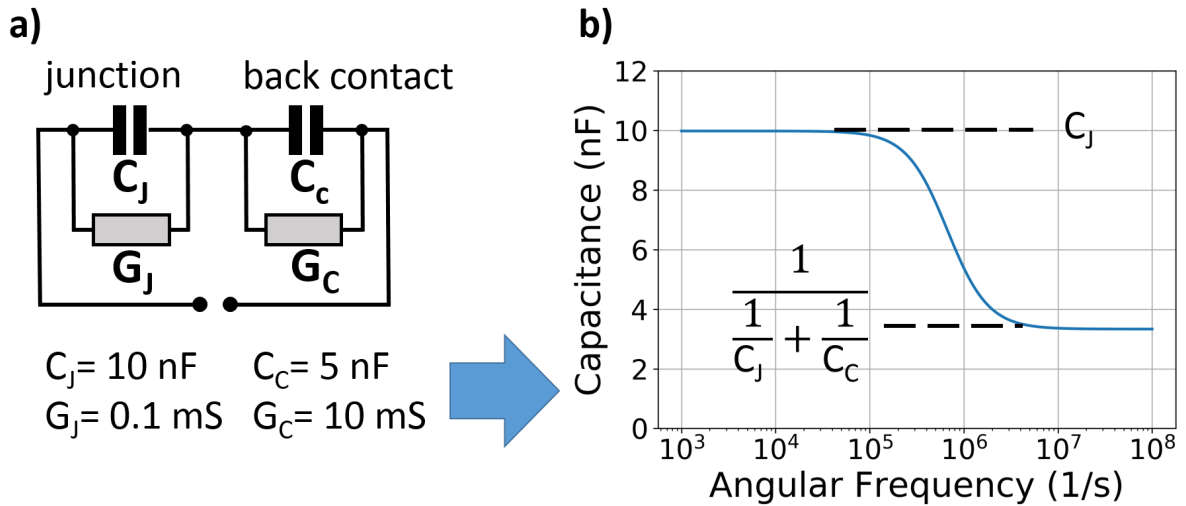
Figure 4.16: a) Equivalent circuit describing the pn-junction and back contact in series. b) Calculated total capacitance of the circuit given in a), which would occur in admittance measurements, when an equivalent circuit consisting of a singular capacitance with an parallel resistor is used for the evaluation of the capacitance.

- U2. This signal is only present in the samples with ITO back contact and disappears under larger forward bias. The position shifts to higher temperatures under reverse bias. Because of the similar position, this signal may be of the same origin as U1.

- U3. This admittance signature occurs at low temperatures. However, it is generally better visible for the ITO-based samples and under forward bias.

The interpretation of admittance spectra is generally quite challenging. Due to similar effects on the spectra, transport barriers can be mistaken as defects and vice versa. Interestingly, admittance measurements on Cu(In,Ga)Se$_2$ (CIGSe) based solar cells basically always show at least one capacitance-frequency step, which is commonly referenced as the so-called N1 signal. Despite 30 years of research, there is still an ongoing debate on its origin [68, 74].

One of the first interpretations of this signal was a shallow defect positioned around 50 to 150 meV away from one of the band edges [75, 76]. The location of this defect was often assumed to be at the CIGSe/CdS interface, after it was found that the position of the N1 signal can shift after an annealing in air atmosphere. A bulk defect was proposed by Heath et al. in contrast, according to new results from DLCP measurements [77]. Igalson et al. concluded a highly p-doped layer close to the window layer and that the N1 signal is originating from a combination of deep acceptor states in the CIGSe/CdS interface and bulk defects [78].

Eisenbarth et al. discussed a back contact barrier as the possible origin for the N1 signal [68]. A back contact barrier can create a counter diode to the main diode. These two diodes are in series connection and possess both a capacitance. The associated equivalent circuit consisting of two capacities in series, both possessing a parallel resistor can be seen in Figure 4.16 a). The conductivity of the counter diode is assumed to be very high at room temperature (otherwise a barrier should occur in the JV measurements, even at room temperature). The frequency dependence of the total capacitance of the equivalent circuit for different frequencies is calculated in Figure 4.16 b) for the exemplary values shown in the same figure.

A major capacitance step was found only for the Mo-based samples. Due to its universal appearance in the literature, this signal is assumed to be the N1 signal.
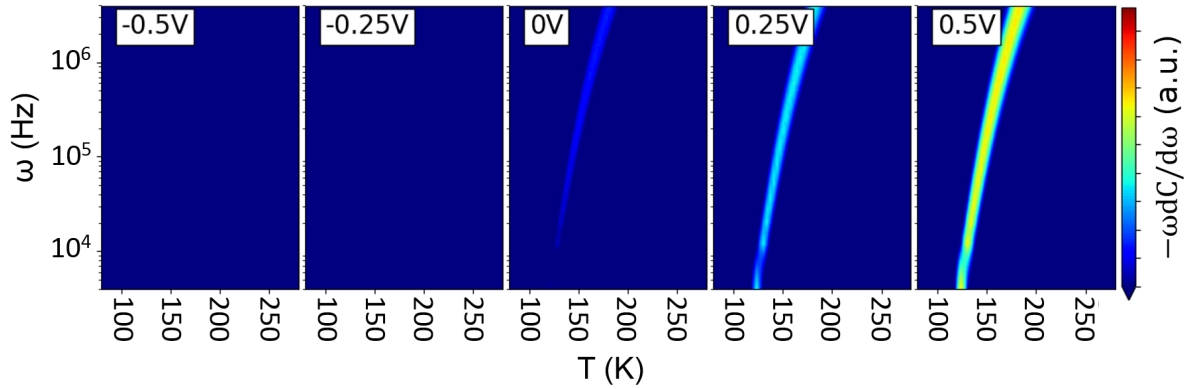
Figure 4.17: Simulated admittance spectra of a CIGSe solar cell with a 300 nm thick absorber layer and a hole extraction barrier of 250 meV at the back contact.

Following observations have been made for the N1 signal:

- It is only visible for the Mo-based samples.

- The position of the N1 signal does not shift in the $-\omega\frac{dC}{d\omega}$-diagram, when a bias voltage is applied.

- The signal was not observed for the thinnest absorber thickness, as long as not an additional reverse bias is applied.

The non-shifting of the N1 signal was also reported in the literature [75, 79]. It had led to the conclusion that in the case of an interface defect as the origin for the N1-signal, Fermi level pinning has to be assumed; otherwise a shifting of the signal should occur [75].

When the N1 signal would originate from a defect at the front interface, it could be concluded that the this defect is absent in case of the ITO back contact sample. This means that the ITO back contact has to alter the front interface compared to the samples with the Mo back contact. While a different layer growth of the CIGSe could be caused by the different substrate, it appears to be rather unlikely that this change is so profound that the signal is disappearing. Especially, when considering that the signal was found in many laboratories and different deposition conditions [68, 80, 81, 82, 83].

Contrary to this, the disappearance of the N1 signal could be explained in a rather straightforward manner, when a back contact barrier is used as an explanation for the N1 signal. The lack of any shifting of the position of the N1 signal in the ωT plots is furthermore expected.

The disappearance of the N1 signal for the thinnest absorber layer on Mo can also be explained via a back contact barrier. Figure 4.17 shows a similar color plot to Figure 4.15, obtained from CV curves, which were calculated using AFORS-HET. A back contact barrier of 250 meV was used in the calculations. The used modeling parameters can be found in the Appendix F. Similar to the experimental results a disappearance of the signal is observed under reverse bias. Also, no shifting of the signal with the applied bias voltage is visible.

These phenomena can be understood in the following manner. The expected thickness of the space charge region (at 0 V) exceeds the thickness of the absorber layer due to the low thickness of the absorber layer. The space charge regions of the main junction and the reverse diode are
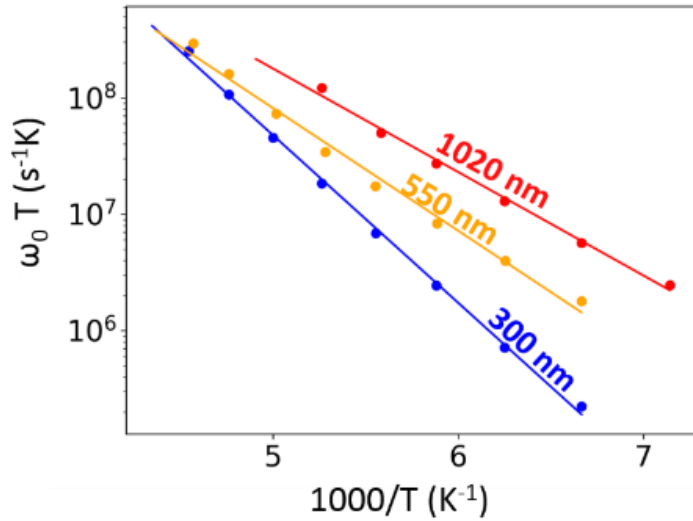
Figure 4.18: Arrhenius plots of admittance critical frequencies and temperatures to obtain the barrier height at the back contact for all three Mo-based samples with different absorber layer thicknesses. A bias voltage of 0.5 V was applied for all samples.

therefore overlapping. Hence the equivalent circuit in Figure 4.16 is not valid anymore. The width of the space charge region does however decrease with increasing bias voltage in forward direction. This leads again to a separation of the two diodes and therefore the transition between the two capacitance regions is possible again.

An extraction of the back contact barrier height is possible from admittance measurements under the assumption that the N1 signal is caused by the back contact barrier. The evaluation of the activation energy is quite similar to the evaluation of the activation energy originating from defects, despite its different origin. Walter et al. showed in [79] how the energetic position of a defect can be extracted from admittance measurements. The so called critical frequency ω_0 has to be determined for measurements at different temperatures for this purpose. This is done by finding the maximum value of a $-\omega dC/d\omega$ vs. ω plot. Afterwards an Arrhenius plot using a $\ln(\omega_0 T^2)$ vs $1/T$ plot can be used to extract the activation energy. Eisenbarth et al. showed that almost the same procedure can be used to extract the barrier height of a back contact barrier. The only difference is that a $\ln(\omega T^{1.5})$ vs $1/T$ plot has to be used for the Arrhenius calculation.

An own mathematical derivation yielded a different result. As given in the Appendix B a $\ln(\omega/T^{1.5})$ vs $1/T$ was obtained for an assumed temperature of $T^{-1.5}$ for the carrier mobilities limited by acoustic deformation potential scattering. The validity of this approach is confirmed by simulations (also given in the appendix).

The N1 signal was evaluated using this factor, with the fitting curves given in Figure 4.18. The determined activation energies are in increasing absorber thickness order: 285 meV, 210 meV, and 175 meV.

The further observed signals will be discussed in the following. Both the U1 and U2 signal are only found at high temperatures. The similar position in the color plot suggests that both signals might be of the same origin. A possible explanation for this effect could be a bulk defect. The determination of the activation energy is however not possible, because not enough inflection points can be extracted from the measurement data. A similar feature was also reported by Hölscher et al. in [83] and discussed as a bulk defect.

The decrease of the capacitance at very low temperatures denoted as U3 is most likely caused by a freeze out of the majority carrier response. In this case, the capacity should drop to the geometrical capacitance density of the absorber layer $C/A = \varepsilon/d$ with ε being the dielectric constant, A the cell area, and d the layer thickness. The calculated value is 40 nF/cm^2 for the 300 nm thick absorber layer. The measured capacitance is approximately 25 nF/cm^2 for the ITO-based and even lower for the Mo-based sample. The effect is better visible at forward bias because the difference between the space charge region capacitance and the geometrical capacitance is larger in this case. It is more pronounced for the ITO-based samples due to the absence of the N1 signal, which does otherwise reduce the capacitance already at lower frequencies. A possible explanation for the discrepancy between calculated and geometrical capacitance is that the geometrical capacitance at low temperatures is formed by the CIGSe, the CdS, and the i-ZnO layers with a total thickness of 480 nm. This explanation would require that the doping density in both the CdS and ZnO layers is not much higher than the doping density of the CIGSe layer. A fact that would be in agreement with the observations made with the charge carrier density determined.

The last feature to discuss is the apparent reduction of the capacitance for the largest measured frequency found mostly for the ITO-based samples. This is an expected feature, caused by the finite series resistance of the sample. The equivalent circuit used to calculate the capacitance from the impedance is only consisting of a capacitor with a parallel resistor. A disregard of a series resistor generally leads to an underestimation of the actual capacitance at high frequencies [84]. The lower conductivity of the ITO back contact compared to the Mo back contact can explain why this feature is seen more clearly for the ITO-based samples. Furthermore, the capacitance is higher for the ITO-based samples in this region due to the absence of the N1 signal, which should increase the effect.

4.8   Back contact barrier

Several results were found that suggest a presence of Schottky barrier at the Mo/CIGSe interface, which might be absent for the samples with an ITO back contact:

- A change of the slope in a V_{OC} vs. T plot, which is completely absent for the ITO-based samples.

- The N1 signal was not found for any of the ITO-based samples, but in all Mo-based samples. (Note that two additional measurements on ITO-based samples are given in the Appendix E; those measurements confirm the absence of the N1 signal in further ITO-based samples).

- The N1 signal was absent for the Mo-based solar cell with the thinnest absorber layer, without any bias voltage. It appeared again under forward bias. This behavior was confirmed by the simulations.

Slightly different activation energies were found from the determination of the barrier height from V_{OC} vs T measurements and the admittance measurements. These differences could be related to a slightly different treatment of the samples during those two measurements. The sample treatment can have an impact on the determined activation energy from admittance measurements as shown by Eisenbarth et al. [80]. For instance, there the sample exhibited an

N1 signal with an activation energy changing from about 160 meV in the relaxed (or reverse bias) state to about 40 meV in the white light soaked (or forward biased) state. The samples shown here were brought into the relaxed state only for admittance and dark JV measurements but were in the white light soaked state for the $V_{OC}(T)$ measurement. Hence the slightly lower activation energies found in the V_{OC} vs. T measurements could be caused by a different sample state.

The back contact barrier in the case of the Mo-based samples is related to a mismatch between the work function of the back contact and the Fermi energy of the absorber layer, i. e. a Schottky contact is forming at the interface. A thin layer of MoSe$_2$ is forming furthermore during the evaporation of CIGSe on top of the Mo back contact [51, 52, 54, 53, 85], which can impact the properties of this interface.

The impact of Na incorporation on the contact resistance between CIGSe and Mo was studied by Yoon et al. by performing transmission line measurements on samples with different Na supplies [53]. Samples without Na exhibited an approximately four times higher contact resistance compared to samples grown with Na incorporation. Similar results were obtained by Wada et al. [51]. Assuming that the barrier height is directly connected to the Na concentration near the back contact, one could speculate if the changes of the activation energy of the N1 signal upon sample treatment are related to a diffusion of Na. Na is known to be quite mobile in CIGSe [86]. Illumination leads to a diffusion of Na to the front and rear contact [86]. Upon relaxation, the Na will diffuse back to form a more even distribution in the absorber.

The presence of a kink in low temperature JV measurements instead of a complete rollover, could be related to the MoSe$_2$. Abou-Ras et al. investigated the thickness of MoSe$_2$ layers after the selenization of Mo covered substrates [55]. Only a very thin MoSe$_2$ layer was reported for process temperatures below 550 °C. Furthermore, Na is reported to enhance the formation of MoSe$_2$ [85]. Due to the low process temperature and the complete absence of Na during the layer growth, a rather thin MoSe$_2$ layer can be expected. Assuming that the kink is caused by a breakdown of a counter diode at the back contact, this may be facilitated by the very low MoSe$_2$ thickness (alternatively a tunneling between the absorber and the Mo might be facilitated).

A highly p-doped layer might be present close to the ITO interface as will be discussed in the next section. Such a highly doped layer can decrease the width of the space charge region at the back contact and hence increase the associated capacitance. The capacitance step will therefore decrease as can be understood with Figure 4.16. AFORS-HET was used for this figure to calculate frequency dependent capacitance curves of CIGSe solar cells with an absorber thickness of 1 μm for an absolute sample temperature of 150K and a back contact barrier height of 250 meV. The doping density of the CIGSe was set to 10^{16} cm^{-3} except for a 10 nm thick CIGSe layer at the back contact interface. The doping density of this thin layer was varied between 10^{16} cm^{-3} and 10^{20} cm^{-3} as visible in Figure 4.19. The capacitance step is greatly reduced for doping densities of 10^{19} cm^{-3} and almost not visible anymore for a doping density of 10^{20} cm^{-3}. An alternative explanation for the absence of a N1 signal in case of the ITO-based solar cells could therefore be the presence of highly p doped layer close to the ITO layer. The N1 capacitance step could be absent in this case even in the presence of a hole extraction barrier, but only for doping densities of at least 10^{20} cm^{-3} in this region.
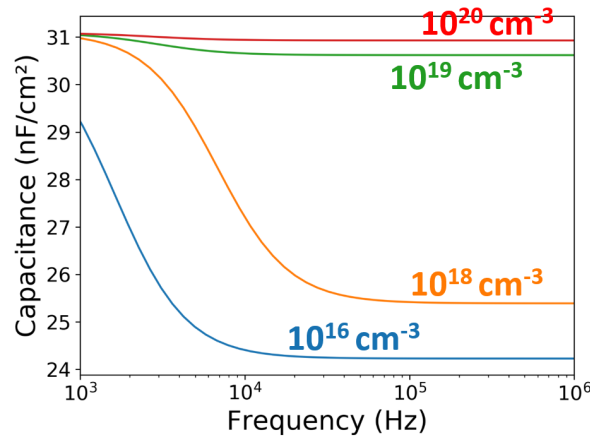
Figure 4.19: Calculated capacitance at difference frequencies of a CIGSe solar cells with a doping density of 10^{16} cm^{-3} except or a 10 nm thick CIGSe layer at the ITO interface, which has a doping density ranging from 10^{16} cm^{-3} to 10^{20} cm^{-3}.

4.9 Carrier extraction at the CIGSe/ITO interface

The carrier extraction in the case of the ITO back contact is not fully understood. For an n+ layer as back contact of a p-type solar cell, a counter diode hindering the current transport is expected, as can be seen in [57] for an AZO back contact. In contrast, often an ohmic contact is reported for CIGSe/TCO interfaces [5, 6, 7].

Such a counter diode should also affect the determination of the charge carrier density from admittance measurements in the case of ultrathin absorber solar cells. A complete depletion of the absorber layer is expected for doping densities around 10^{16} cm^{-3} of ultrathin absorber layers, due to the combined extension of both space charge regions. Contrary to this rather similar charge carrier densities were measured when comparing the Mo with the ITO-based solar cells even for absorber thicknesses of only 300 nm. This could hint to the presence of a higher doped p-region close to the CIGSe/ITO interface, which reduces the extension of the rear space charge region. The presence of acceptor defects could also explain the charge transport mechanism between the CIGSe and the rear ITO layer.

The carrier transport might occur due to trap assisted tunneling as displayed in Figure 4.20 a). A large density of defects at the ITO/CIGSe interface could allow the tunneling of electrons from the ITO into trap states within the CIGSe. These electrons could then recombine with holes from the absorber layer. A second possibility is the occurrence of band-to-band tunneling between the conduction band of the ITO and the valence band of the CIGSe as can be seen in Figure 4.20 b). This mechanism would require a high doping of both sides of the pn-junction. A very high doping can at least be assumed for the ITO layer, which is typically a degenerated semiconductor.

Simulations were performed to investigate the possibility of those charge transport mechanisms. A 1 μm thick CIGSe solar cell with a doping density of 10^{16} cm^{-3} and an ITO back contact was simulated. Acceptor like defects with a Gaussian distribution were placed 300 meV above the valence band in a 1 nm thick layer of CIGSe directly above the ITO. Further simulation details can be found in Appendix F. AFORS-HET does include the mathematical model according to Hurkx to describe the tunneling over trap states [48, 87]. The calculated JV curves for different integrated defect densities within the 1 nm CIGSe layer can be seen in the solid lines of Figure

Table 4.5: Solar cell parameters for different integrated defect densities of a Gauss like defect positioned 0.3 eV above the valence band inside a 1 nm thick CIGSe layer close to the rear ITO. Three simulation have been conducted in AFORS-HET with trap assisted tunneling enabled. One of the simulation was conducted in wxAMPS with band-to-band tunneling enabled.

Defect density (cm^{-3})	Tunnel mechanism	V_{OC} (mV)	FF (%)	J_{SC} (mA/cm^2)	PCE (%)
10^{20}	Trap assisted tunneling	441	70.0	33.3	10.0
$3 \cdot 10^{20}$	Trap assisted tunneling	689	73.5	33.1	16.7
10^{21}	Trap assisted tunneling	692	54.3	33.4	12.6
10^{21}	Band-to-band tunneling	708	78.6	33.4	18.6

4.21. The corresponding solar cell parameters are given in Table 4.5. The photogenerated carriers are extracted for a defect density of 10^{20} cm^{-3}. However the solar cell parameters are overall rather poor. An increase of the the defect density to $3 \cdot 10^{20}$ cm^{-3} increases the efficiency from 10.0% to 16.7%. A further increase of the defect density does degrade the solar cell parameters, especially the FF. This decrease is caused by a barrier like behavior of the JV curves in forward direction. The conduction band of the ITO is pushed below valence band of the CIGSe at a certain forward bias voltage in the simulation. The defect levels in the CIGSe are therefore above the occupied states of the ITO, which disables the tunneling process. A band-to-band tunneling process can occur in this circumstance. This process is however not implemented in AFORS-HET.

The simulation software wxAMPS does implement band-to-band tunneling and was therefore used to investigate the possibility of band-to-band tunneling [88]. Trap assisted tunneling is however not implemented in wxAMPS. The same modeling parameters as used in AFORS-HET were used in wxAMPS. A tunnel transport between the ITO and the CIGSe was observed for a defect density of 10^{21} cm^{-3}. This resulted in an JV curve with an efficiency of 20.6% as can be seen in the dashed line in Figure 4.21. The tunneling current for lower defect densities was much lower, resulting in a J_{SC} value below 1 mA/cm^3 for a defect density of $8 \cdot 10^{20}$cm^{-3}. The barrier like behavior at increasing defect densities (and hence trapped charges) found in AFORS-HET is hence likely an artifact due to the absence of band-to-band tunneling. A model encompassing both mechanism would likely transition between both carrier transport mechanism with an increase of the density of acceptor like defect.

The simulations prove that a n-type TCO can be used successfully as a back contact for a CIGSe solar cell, when a sufficient density of acceptor like defects is present to allow for trap assisted tunneling. A possible candidate to increase the p-type doping is Na. A large amount of Na is typically found at the back contact of CIGSe solar cells [73]. However, it would be expected in this case that a high doping density should also be present for the Mo based solar cells. This high doping density would significantly increase the capacitance of the rear junction, which should decrease the capacitance step of the N1 signal as shown in Figure 4.19. A large p-type doping could also be caused by the compensation of selenium vacancies (donors) by oxygen, which is available in the vicinity of a TCO-based back contact [89]. This could also explain why various n-type TCO work as a back contact for CIGSe.

The formation of Ga_2O_3 was reported by several authors, as the cause for a poor device performance of CIGSe solar cells with TCO back contacts[6, 8, 9]. Keller et al. observed the presence of a kink in the JV curves for a sample with an Al_2O_3 passivation layer and with a layer of NaF deposited prior to the CIGSe deposition. A relatively thick Ga_2O_3 layer (~50 nm) was found for this sample using TEM-EDX measurements. It is interesting that photo generated carriers
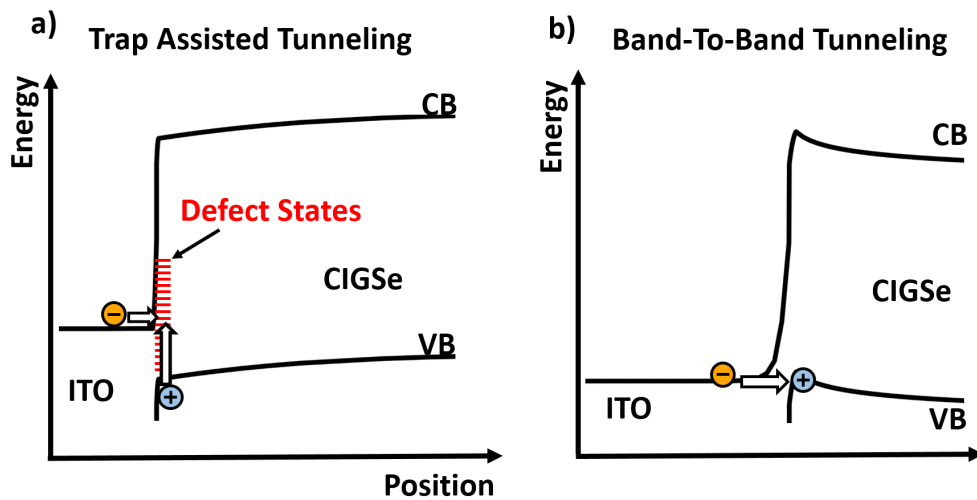
Figure 4.20: Possible band diagrams at the CIGSe/ITO interface for two different charge carrier transport mechanism between the ITO and CIGSe layer. (a) A highly p-doped layer is present in the CIGSe at the ITO/CIGSe interface. Electrons of the ITO can recombine with holes in the CIGSe via band-to-band tunneling. (b) A highly defective layer is present at the ITO/CIGSe interface. Electrons of the ITO tunnel in those defects, where they can subsequently recombine with holes from the CIGSe layer.
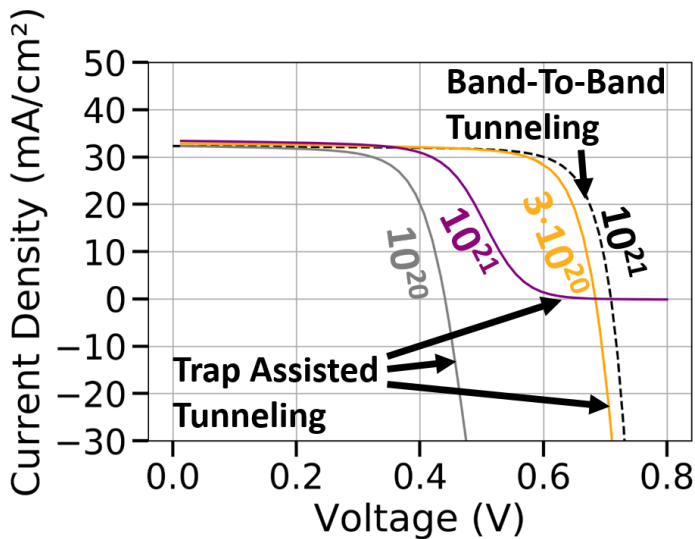
Figure 4.21: Calculated JV-curves of CIGSe solar cells with an ITO back contact for solar cells with the charge carrier transport to the ITO realized by band-to-band recombination (dashed line) or trap assisted tunneling (full lines). The displayed numbers are the integrated defect densities within a 1 nm thick CIGSe layer at the ITO interface in unis of cm^{-3}.

could be extracted from this sample at all. Assuming that the Ga_2O_3 layer is continuous, the charge carrier transport has to be possible on both the Ga_2O_3/ITO and Ga_2O_3/CIGSe interface, because no direct tunneling between the ITO and CIGSe should be possible at such a thickness anymore. Hence the formation of Ga_2O_3 could play a part for the carrier extraction at this interface. However, no Ga_2O_3 layer could be identified for the sample prepared at 480 °C in the TEM measurements provided in Section 3.5.

Two samples showed pronounced problems with the carrier collection. The sample with a 50 nm ITO diffusion barrier from Section 3.4 as well as the sample with a 1020 nm absorber layer from the current chapter (only when the sample temperature was reduced). A possible explanation for the reason, why the temperature dependence of J_{SC} was higher for the thickest absorber layer sample could lie in the longer processing time during the absorber deposition. The higher thermal budget could enhance the growth of Ga_2O_3, which could be responsible for the problem. However, basically no Ga_2O_3 was detectable for the sample with the 50 nm ITO diffusion barrier. Hence, an explanation of the carrier extraction issues using a thicker Ga_2O_3 layer can only be valid, if the problems of the two aforementioned samples are caused by different effects.

The structural and electrical properties of the ITO can change with the layer thickness of the ITO. The deposition of thinner layer thicknesses can result for example in a reduction of the grain size of the ITO crystals [90]. The electrical properties of the 50 nm ITO might be different from the other ITO layers, namely a change in the density of free charge carries and the work function of the ITO could shift the position of the ITO conduction band in relation to the valence band of the CIGSe. Such a shift can affect the carrier extraction mechanism negatively. However, the simulations results suggest that mainly the V_{OC} and the FF are negatively affected by such an effect and not J_{SC} as experienced in the experiment. An impact on J_{SC} could be explained by a lateral inhomogeneity of the sample. The carrier extraction might be blocked only in some areas of the solar cell, which would have a similar effect as a reduction of the active solar cell area. A potential cause for such local fluctuations are contamination at the ITO surface, which can be introduced to the interface prior to the deposition of the CIGSe layer. Contamination are known to affect interface properties like the work function of a material [91]. Hence, a combination of non ideal electrical properties of the 50 nm ITO layer, with an additional local fluctuation of the interface properties might explain the reduced current. A similar explanation could also be used to explain the reduction of J_{SC} with a reduction of the temperature as experienced for the sample with the 1020 nm absorber layer. It is however difficult to assess the impact of the temperature on the ITO/CIGSe interface, given the fact that multiple properties like the Fermi energy position and recombination rate will be affected by the temperature simultaneously. Further research is needed to clearly understand the carrier extraction mechanism in the ITO-based samples and the band diagram in the vicinity of the back contact.

4.10 Influence of the back contact on solar cell parameters

Low V_{OC} values are frequently reported for solar cells with ultrathin CIGSe absorber layers. Figure 4.22 shows the open circuit deficit $V_{OC,def}$ found in several publications, which can be calculated by $V_{OC,def}=E_{gap}(CIGSe)/q-V_{OC}$. A plot of the open-circuit voltage deficit was chosen to account for the different band gaps of the CIGSe layers employed in these publications. All publications used in this figure compare solar cells with a bare Mo layer (blue makers) with corresponding samples possessing a passivation layer between the absorber layer and the Mo

Table 4.6: Overview of the used model parameter for each solar cell layer for the calculation of the JV curves shown in Figure 4.21.

	ITO (Front)	ZnO	CdS	CIGSe
ε ()	9	9	10	13.6
χ (eV)	4.1	4.1	4	4.122
E_g (eV)	4	3.3	2.4	1.218
N_C (cm^{-3})	$2.2 \cdot 10^{18}$	$2.2 \cdot 10^{18}$	$2.2 \cdot 10^{18}$	$2.2 \cdot 10^{18}$
N_V (cm^{-3})	$1.8 \cdot 10^{19}$	$1.8 \cdot 10^{19}$	$1.8 \cdot 10^{19}$	$1.8 \cdot 10^{19}$
μ_n (cm^2/(Vs))	100	100	100	40
μ_p (cm^2/(Vs))	100	100	100	10
N_a (cm^{-3})	0	0	0	$5 \cdot 10^{15}/1 \cdot 10^{16}/2 \cdot 10^{16}$
N_d (cm^{-3})	10^{19}	10^{18}	10^{17}	0
v_e (cm/s)	10^7	10^7	10^7	10^7
v_h (cm/s)	10^7	10^7	10^7	10^7
Defect				
Type	acceptor	-	-	donor
E_d-E_v (eV)	1.7	-	-	midgap
Density (cm^{-3})	10^{14}	-	-	10^{13}
c_n (cm^2)	10^{-14}	-	-	$5 \cdot 10^{-12}/5 \cdot 10^{-13}/5 \cdot 10^{-14}$
c_p (cm^2)	10^{-14}	-	-	$5 \cdot 10^{-12}/5 \cdot 10^{-13}/5 \cdot 10^{-14}$
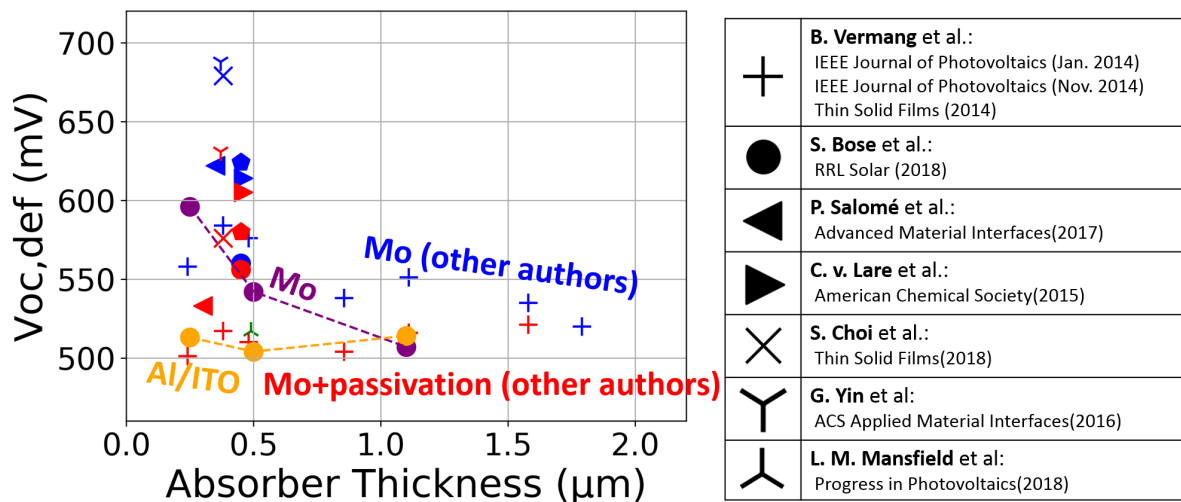
Figure 4.22: Overview of the obtained V_{OC} deficit values extracted from several publications, which tested solar cells with (blue marker) and without (red marker) an additional passivation layer deposited underneath the CIGSe layer. The V_{OC} deficit for a sample with a GGI back gradient is also inserted (green marker). The V_{OC} deficit values obtained in a layer thickness variation in this work are given additionally. The references corresponding to the legend are: Vermang et al.[24, 30], Bose et al. [92], Salomé et al. [33], Lare et al. [93], Choi et al. [94], Yin et al. [95], Mansfield et al. [96].

(red makers). The only exception is the work of Mansfield et al., which investigated GGI gradients for passivation purposes (green maker) [96]. The $V_{OC,def}$ values of the best solar cells obtained using the Al/ITO back contact are also given with their corresponding Mo references. Details about these solar cells are given in the Appendix J.

The figure shows that generally larger $V_{OC,def}$ values are obtained for ultrathin absorber layers. The samples with an additional passivation layer show lower $V_{OC,def}$ values. As a result $V_{OC,def}$ values similar to the one of solar cells with regular thick absorber layers are obtained for solar cells using an ultrathin absorber. The difference between the Al/ITO and Mo-based samples suggests that the ITO layers may have a similar effect as the other oxides presented in the literature. A much more pronounced decrease of the V_{OC} values was also observed for the Mo reference samples in the samples used for the determination of the back contact recombination velocity.

Three possible factors will be presented in the following, which could explain the reduced V_{OC} values for thinner absorber layers. Afterwards, simulations and literature results will be used to make an estimation about the relevance of these three factors.

The most common explanation found in the recent literature is the influence of the back contact recombination. Secondly, it must be questioned if the absorber quality does not change upon the thickness reduction. Lastly, a so-called punch-through effect could occur, which is an effect primarily known from CdTe solar cells [97]. It becomes relevant as soon as the expected width of the space charge region exceeds the absorber layer thickness. The classical diode equation is not applicable anymore due to the absence of a quasi neutral region, which is used for the derivation of the ideal diode equation. Especially an influence on V_{OC} by a back contact barrier is reported [97].

AFORS-HET was used to simulate JV curves for varying absorber thicknesses and barrier heights. The employed simulation parameters are oriented on the simulation results of Section 4.4. The minority carrier lifetime was set to 2 ns in this simulation, which corresponds to a diffusion length L_n= 0.45 µm. The other simulation parameter are given in Table 4.6. Figure 4.23 shows color plots of the calculated V_{OC} values, as a function of the barrier height and absorber thickness, for different absorber layer doping densities and back contact recombination velocities.

All graphs are roughly divided into three areas. For thick enough absorber layers, the V_{OC} values are almost independent of the barrier height (called region 1 in the following). The V_{OC} values in this region are basically constant regarding changes in the layer thickness, with only a very small decrease of V_{OC} (~2 mV) when the absorber thickness is increased from 1 µm to 2 µm. The V_{OC} values for thin enough absorber thicknesses are influenced by both the absorber thickness and the barrier height. A decrease of the V_{OC} values can be seen with decreasing absorber thickness for a sufficiently high barrier (region 2). The opposite relation is true for small barrier heights (region 3). In-between region 2 and region 3 almost no influence of the absorber thickness on V_{OC} is found. The barrier height for which the transition between this two regions is happening shifts to higher barrier heights for lower values of the back contact recombination velocity. An increase of the doping density expands the region 1 in which V_{OC} is basically unaffected by the barrier height to thinner absorber layers. The overall V_{OC} level does furthermore increase with the doping density.

The simulations show consequently that V_{OC} can both increase or decrease upon a reduction of the absorber layer thickness. The width of the space charge region is an important quantity to consider for ultrathin absorber layers. The space charge width is about 600 nm for $N_A = 5 \cdot 10^{16}$
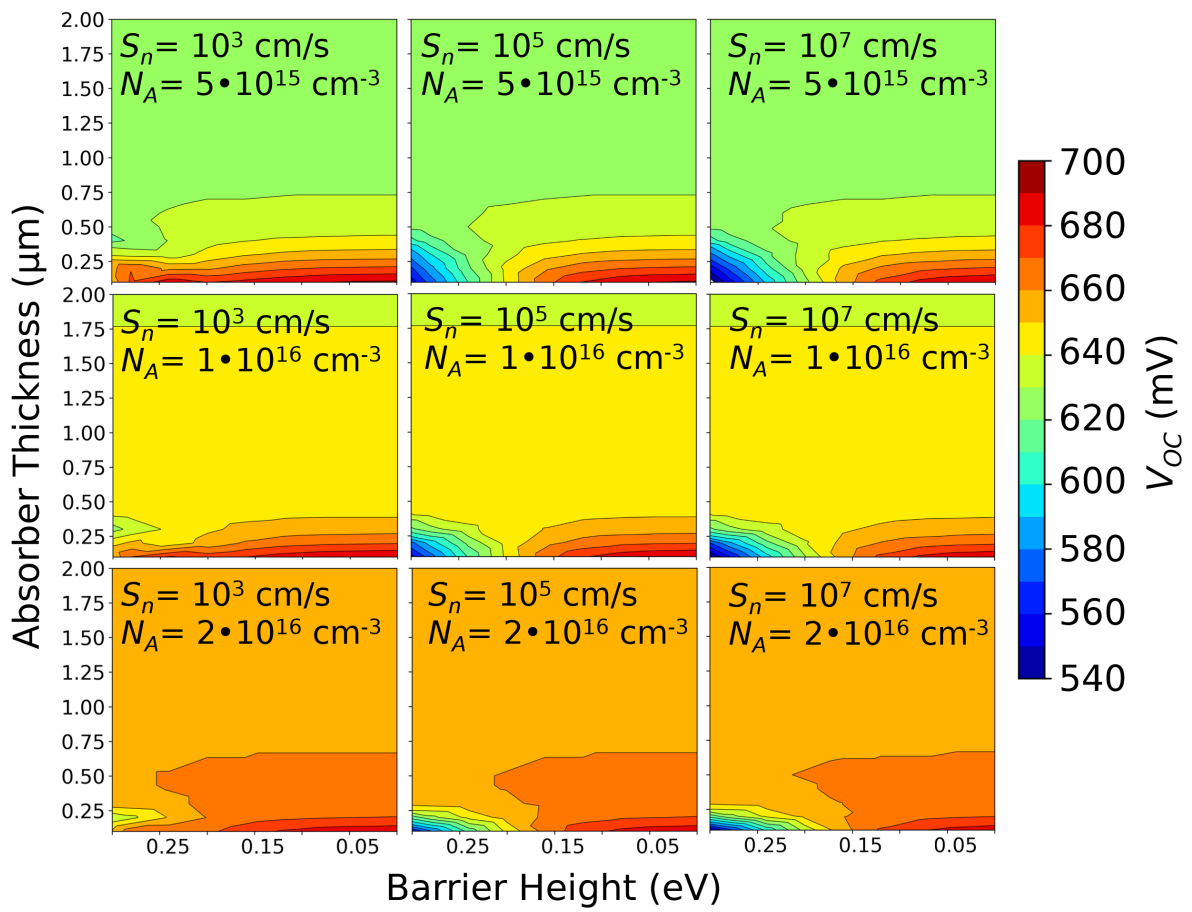
Figure 4.23: Color plots displaying V_{OC} as a function of the absorber thickness and barrier height at the back contact for different doping densities and back contact recombination velocities.
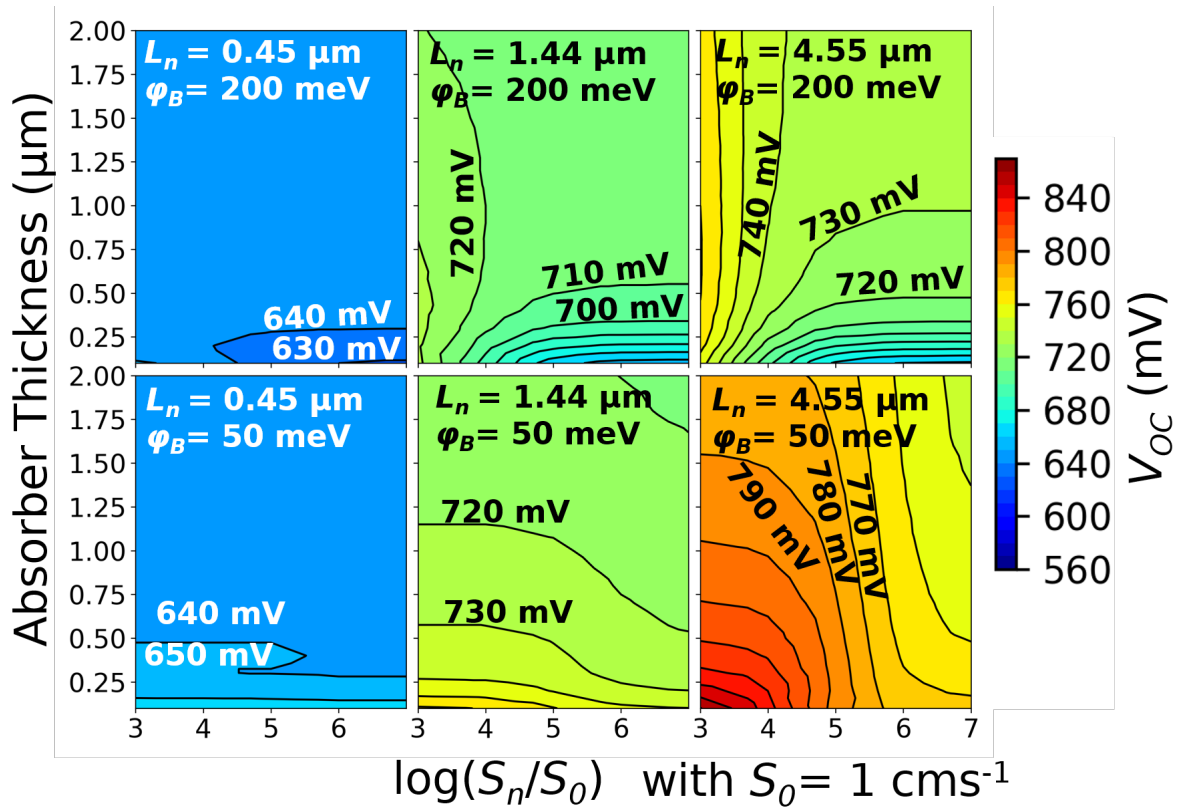
Figure 4.24: Color plots displaying V_{OC} as a function of the absorber thickness and back contact recombination velocity, for different minority carrier diffusion lengths and two different barrier heights at the back contact.

cm^{-3}, 400 nm for $N_A = 1 \cdot 10^{17}$cm^{-3} and 230 nm for $N_A = 2 \cdot 10^{17}$cm^{-3}. This means that the back contact properties do only affect V_{OC} if the expected space charge region is larger than the thickness of the absorber layer for the employed simulation parameters.

Further simulations were conducted to understand how the influence of S_n on the V_{OC} changes for different charge carrier lifetimes in the absorber layer. The minority carrier lifetime was chosen to be equal to the majority carrier lifetime to simplify the simulations. Three different carrier lifetimes were investigate (2 ns, 20 ns, 200 ns) which corresponds to minority carrier diffusion lengths of 0.45 µm, 1.4 µm and 4.5 µm. A doping density of 10^{16} cm^{-3} was chosen for this simulations, while the other simulation parameters were identically to the one used for Figure 4.23. Figure 4.24 shows color plots of V_{OC} as a function of S_n and the absorber layer thicknesses for three different charge minority carrier diffusion lengths and two different back contact barrier heights.

No significant influence on V_{OC} can be seen for the shortest diffusion length if the absorber thicknesses is above 500 nm. A decrease of V_{OC} can be seen for the case with $\varphi_B = 200$ meV for thinner absorber layer thicknesses if the recombination velocity is above 10^4 cm/s. The case with $\varphi_B = 50$ meV shows in contrast an increase of V_{OC} with decreasing absorber thickness in this region.

The overall V_{OC} level does increase with the diffusion length. Two distinct features are visible for the two longer diffusion lengths in the case $\varphi_B = 200$ meV. A decrease of V_{OC} can be seen with decreasing absorber layer thicker for back contact recombination velocities above 10^4 cm/s. The onset of the V_{OC} reduction does occur at thicker absorber layer thicknesses for longer

93

diffusion lengths. A loss of V_{OC} can therefore be seen also for absorber thicknesses thicker than the space charge region (~400 nm). The second feature visible is an increase of V_{OC} with a decreasing recombination velocity. The intensity of this effect does increase with the diffusion length. This effect is interestingly also visible for non ultrathin absorber layer thicknesses. The effect is only dependent on the back contact recombination velocity above a thickness of 500 nm for the longest diffusion length.

An increase of V_{OC} can be seen with a decreasing absorber layer thicknesses in all graphs with $\varphi_B = 50$ meV, for all surface recombination velocities. The effect is however much more pronounced for low surface recombination velocities, especially for the case with the longest regarded diffusion length.

An impact on V_{OC} can be seen for non completely depleted absorber layers for the two longer diffusion lengths. The impact of S_n on V_{OC} is however rather low for moderate diffusion lengths ($L_n \approx 1$ μm) in this case. A band bending at the back contact is absent for $\varphi_B = 195$ meV for an absorber doping density of $N_A = 10^{16}$ cm^{-3} (for a non depleted absorber layer). Lower values for φ_B result in an upward bending at the back contact, while higher values result in a downward bending. The minority carrier density is therefore reduced at the back contact for $\varphi_B = 50$ meV, through a back surface field. Hence, the impact of the back contact recombination is slightly increased for $\varphi_B = 200$ meV and decreased for $\varphi_B = 50$ meV, which can explain the higher V_{OC} values reached with the latter mentioned back contact barrier. Note that the longest regarded diffusion length is likely not obtainable in real CIGSe absorber layers.

Next the effect of different values for φ_B on the band diagram in the case of a completely depleted absorber layer, will be discussed. Figure 4.25 a) shows the band diagram of the CIGSe absorber for different values of φ_B. The overall band bending is reduced when the φ_B is increased. This has a similar effect as a reduction of the build in voltage. The current density of dark JV curves for different barrier heights and recombination velocities can be seen in Figure 4.25 b). The dark current does increase faster with the applied voltage when the back contact barrier is increased. This can be understood from the decreased built in voltage. It can explain, why the open circuit voltage is reached at lower voltages. The phenomenon is greatly reduced for a decreased recombination velocity, as also presented in the same figure. The reduced V_{OC} values for the lowest regarded diffusion length are therefore likely related to this effect, given that an impact of the back contact parameters on V_{OC} can only be seen for layer thicknesses below the width of the space charge region.

Jehl et al. simulated the evolution of solar cell parameters for different absorber thicknesses [98]. The employed diffusion length was $L_n = 1.7$ μm. A reduction of V_{OC} was mainly found in the simulations only when the absorber layer was completely depleted.

Vermang et al. simulated also the cell parameters for different absorber thicknesses and recombination velocities. A diffusion length of $L_n = 1.7$ μm was also used in this case with a rather low doping density ($4 \cdot 10^{15}$ cm^{-3}). A reduction of V_{OC} from ~630 mV to ~610 mV was found for a solar cell with $S_n = 10^7$ cm/s, when the layer thickness was reduced from 2 μm to 0.3 μm. For $S_n = 10^2$ cm/s, the same layer thickness reduction led, in contrast, to an increase of V_{OC} from ~630 mV to ~690 mV. Therefore, a rather moderate decrease of V_{OC} was also found in those simulations, when the absorber thickness is reduced and the back contact recombination velocity is high.

For most of the samples prepared in this work, a doping density in the range of 10^{16} cm^{-3} can be assumed. Hence, an influence of the back contact recombination velocity on V_{OC} can only be expected for the samples with an absorber thickness of around 300 nm from those simulation
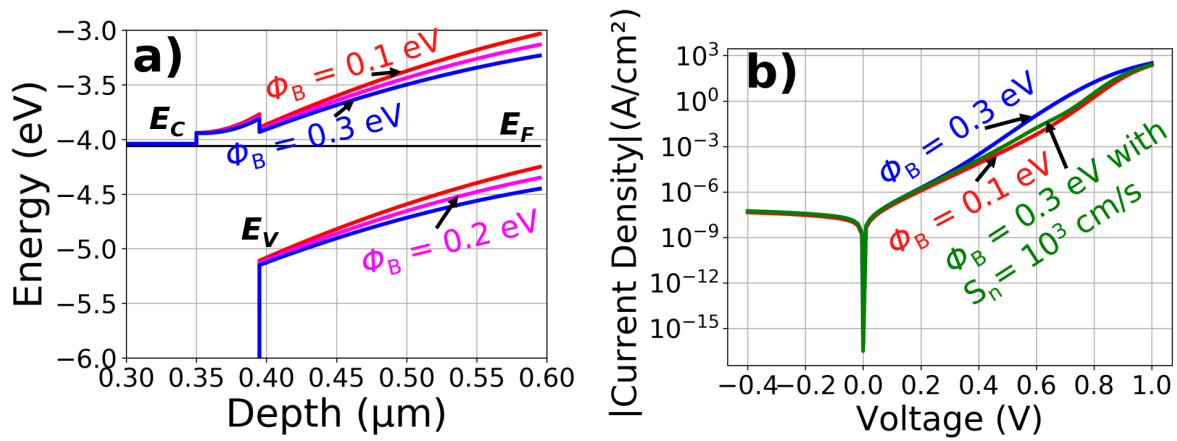
Figure 4.25: a) Band diagram of a CIGSe solar cell with a fully depleted absorber layer for three different back contact barrier heights. b) Dark JV curves corresponding to the solar cells given in a) for a $s_n = 10^7$ cm/s together with one example with an barrier height of 300 meV with $s_n = 10^3$ cm/s.

results. But even in this case, the determined back contact recombination rate in the range of 10^4-10^5 cm/s for the ITO back contact, together with back contact barrier height around 200 meV for the Mo back contact can not really justify the large differences for V_{OC} found for those samples. They can only partly explain the observed differences for the solar cells, and only for the solar cells with the thinnest absorber layers. In case of the solar cells with an absorber thickness of around 500 nm, no meaningful influence of the back contact on V_{OC} is expected from the simulations. Generally, very low V_{OC} values (< 600 mV) are not found in the simulations. To reach such low values, a reduction of the charge carrier lifetimes is necessary.

This raises the question of whether the observed differences in V_{OC}, found between the ITO-based and Mo-based solar cells, are related to the back contact or differences in the absorber layer. While the absorber layers were always deposited in the same chamber, it is unknown if the absorber layers grown on the different substrates are really identically. It is experimentally difficult to distinguish between the impact of the back contact on the cell parameters and the impact of a different bulk recombination rate. While an absorber thickness variation can theoretically solve this problem, this kind of variation does suffer from the fact that the grown absorber layer will typically differ to some extent between different deposition runs. The overall quality of the absorber might be also at average lower for thinner absorber layers.

Jehl et al. performed etching experiments, which can potentially solve some of these experimental problems [98, 99, 100]. A 2 μm thick absorber layer was deposited on Mo coated SLG substrate, which was then separated into multiple smaller samples. The absorber layers of those samples were then etched down to different absorber layer thicknesses using a bromine based solution. Consequently, solar cells with the same absorber layer, but different absorber thicknesses are available (assuming that the absorber properties are homogeneous in depth). The solar cells were then completed and characterized using JV measurements.

A small increase of V_{OC} was measured when the absorber thickness was reduced down to 500 nm. This increase was explained by a change of the band gap, caused by a slight GGI gradient. Only the J_{SC} value decreased for the 500 nm compared to the 2000 nm absorber layer sample. All parameters decreased for thinner absorber layer samples. The sample with the thinnest absorber layer (~ 200 nm) was completely shunted. Hence, it is unclear if the reduction of V_{OC}, below 500 nm was related to back contact recombination or a shunting of the solar cells. The low FF suggests rather a partial shunting of the solar cells.

The experiment was repeated, but this time the Mo back contact was removed and replaced by an Au back contact for some of the samples [100]. No decrease of V_{OC} was found when the absorber thickness was reduced to 400 nm. For the 300 nm absorber layer sample, the V_{OC} decreased dramatically (~ -240 mV) for the Mo-based samples. Interestingly, only a small decrease of V_{OC} (-10 mV) was reported for the sample with the Au back contact at the same thickness. The evolution of the FF was similar (-10% for both back contacts) suggesting that this V_{OC} difference is not explainable by a different shunting of the solar cells.

Overall, these experiments appear to fit well to the simulation results shown in Figure 4.23. No significant change of V_{OC} was found, up to the point, where the expected space charge region width is comparable to the absorber thickness. While the possible shunting problems make an evaluation for even thinner absorber layers difficult, the different results obtained with the Au and Mo back contact do suggest that the thinner samples might have been deteriorated by the reach through effect. The strong difference between the Au and Mo back contact could be related to a different back contact barrier height (and maybe a different back contact recombination rate).

Given the fact that no meaningful influence of the back contact is expected from the simulation results, as long as the absorber is not similar in thickness to the space charge region width, several questions arise. Why did multiple experiments in this work show a different V_{OC} value, comparing samples with an ITO with a Mo-based back contact? Why are low V_{OC} values often reported for CIGSe solar cells with ultrathin absorber layers [24, 30, 33, 92, 93, 94, 101]? Why do passivation layers often help to improve the V_{OC} values [24, 30, 33, 92, 93, 94, 101]?

A possible answer to those questions might be that it is more difficult to obtain absorber layers with long diffusion length for very thin absorber layers. Furthermore, the absorber quality might be affected by the substrate it is grown onto. This theory would explain, why in some experiments similar gains in V_{OC} are reported through the usage of a passivation layer, when comparing solar cells with relatively thin and relatively thick absorber layers. Ledinek et al. prepared CIGSe solar cells with absorber layer thicknesses ranging from 600 nm to 1.45 μm, with and without an Al_2O_3 passivation layer [102]. Despite the strong difference in the absorber layer thickness, similar V_{OC} gains through the passivation layers were found for the thinnest and thickest absorber layer. This is not expected, if this V_{OC} difference is directly connected to the back contact recombination rate, but it could be explained by a different bulk recombination rate induced by the different substrate types.

It is furthermore not clear if the Na supply is the same if different substrate types are used. A Na diffusion barrier is usually not employed when comparing different substrate types. This can potential lead to a different growth of the CIGSe and/or a different doping density.

An indication, that the CIGSe absorber layers might not be entirely identical between the CIGSe layers grown on different substrates can be seen in XRD measurements. Figure 4.26 shows Θ-2Θ measurements on Mo and Mo/Al/ITO-based solar cells, which were presented in Section 3.5, for two different deposition temperatures. It can be seen that the CIGSe (220/204) peak is much more pronounced for the Mo-based samples, while on the other hand the CIGSe (112) peak is much more pronounced for the samples with an ITO/CIGSe interface. While differences in the absorber quality cannot be deduced from this fact, the result still shows that the layer growth of the CIGSe is not entirely the same.

So far the discussion was solely focused on the impact on V_{OC}. Figure 4.27 a) shows the influence of the back contact on the FF based on the same simulations as used in Figure 4.24. The FF shows a minimum at a thickness of about 300 nm, which vanishes when the back
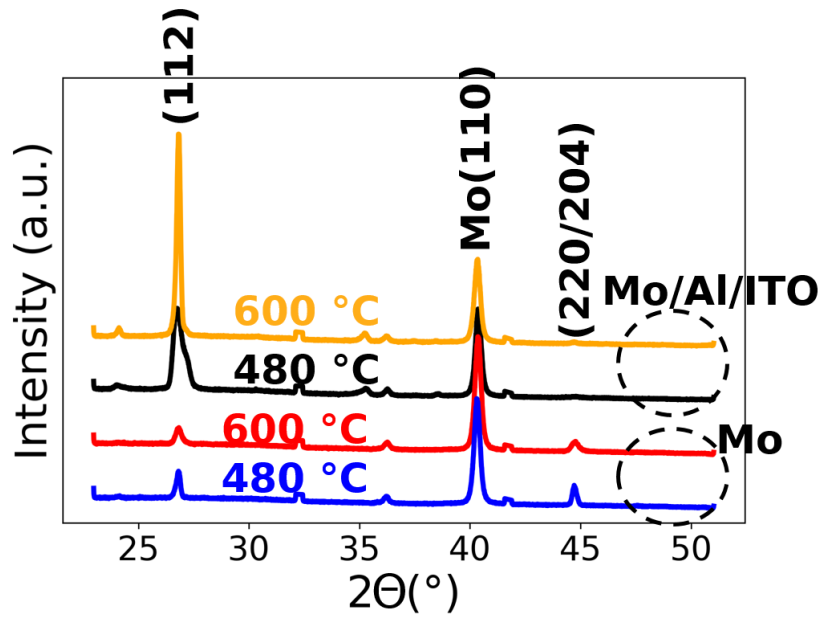
Figure 4.26: Θ-2Θ scans of samples deposited with an Mo/Al/ITO or Mo back contact for CIGSe absorber deposition temperatures of 480 °C and 600 °C.

contact recombination velocity is low enough, in the case of a 200 meV barrier. This minimum was also found in simulations by Jehl et al. in [98]. The simulation by Jehl highlighted that this behavior can be understood from the back contact recombination current. The back contact recombination current is increasing with a decreasing absorber layer thickness [98]. It was found to be however greatly reduced at a certain thickness, which was explained by the fact that the strong band bending caused by the pn-junction will drive all carriers to the front interface before they can recombine at the back contact. The forward bias does however reduce the band bending caused by the pn-junction resulting in an increased back contact recombination current. The minimum in Figure 4.27 a) is therefore likely related to the thickness were the back contact recombination current is only significant under forward bias but not at the J_{SC} point. This effect does vanish for even thinner absorber layers because then even at forward bias the pn-junction can drive the carriers to the front contact before they can recombine at the back contact.

Figure 4.27 b) shows the impact of the back contact on J_{SC}. All graphs show a reduction of J_{SC} with the layer thickness as expected due to the reduced absorption. The obtainable short circuit density is increasing for a carrier lifetime of 20 ns instead of 2 ns. The back contact recombination velocity has only a small influence on J_{SC} for the sample with $\varphi_B = 50$ meV. For the sample with the 200 meV barrier, S_n affects the short circuit density even for 1 µm absorber layer samples, especially for longer carrier lifetimes.

The impact of S_n on the absolute values of J_{SC} becomes very low for layer thicknesses below 500 nm. A similar result can also be seen in the simulations of Vermang et al. [31]. This low impact for low absorber thicknesses is likely due to the fact that most of the carriers are generated directly in the space charge region, where typically almost all carriers are collected.

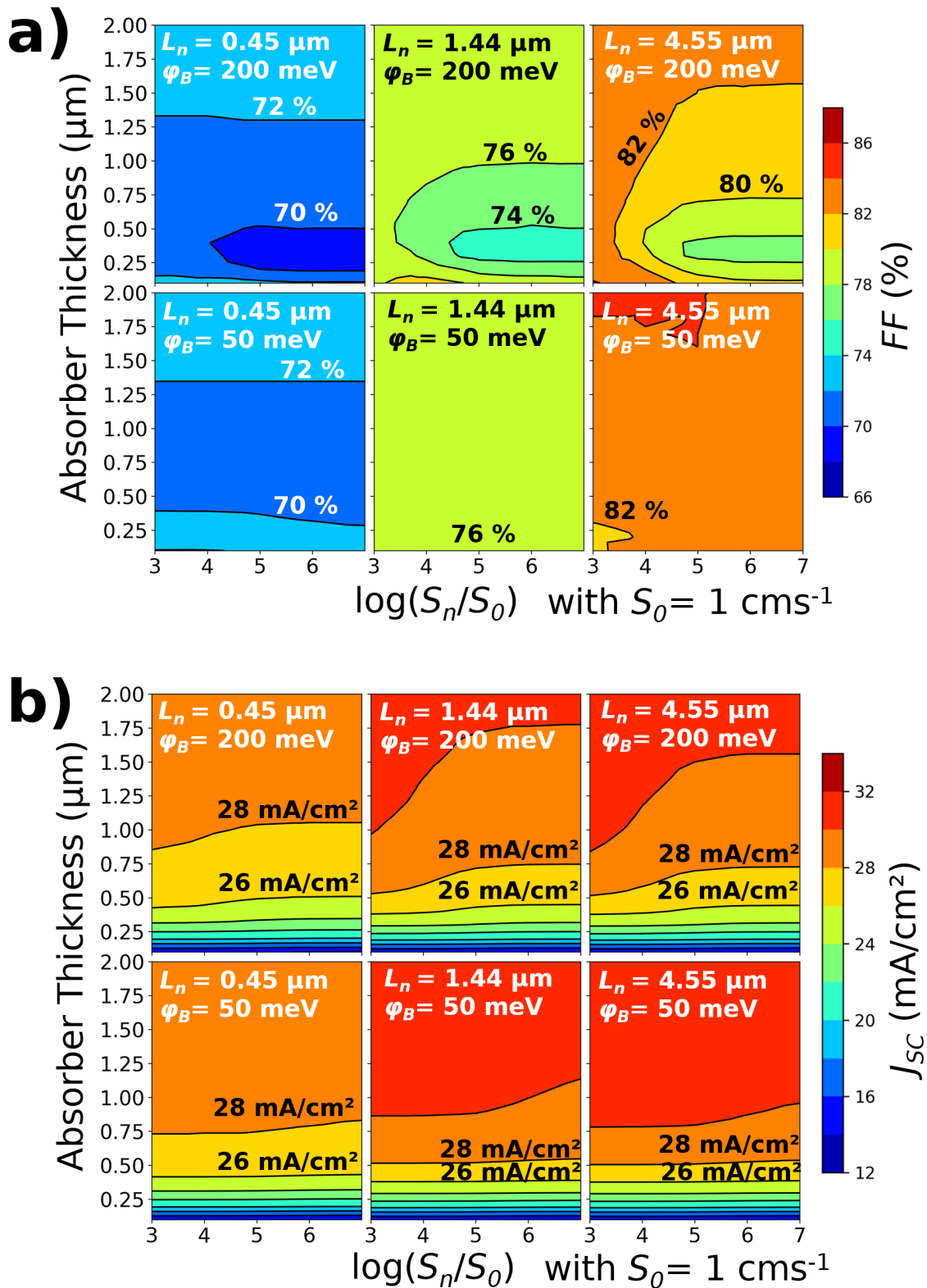Figure 4.27: Color plots displaying FF (a), and J_{SC} (b) as a function of the absorber thickness and back contact recombination velocity, for different minority carrier diffusion lengths and two different barrier heights at the back contact.

4.11 Conclusion

Chapter 4 did analyze the electrical properties of the ITO and Mo back contacts and its relevance for the performance of CIGSe solar cells. Bifacial measurements were used to determine the back contact recombination velocity of the ITO/CIGSe interface. An advanced methodology was developed for this purpose, which takes into account that important properties like the charge carrier mobility are unknown. The back contact recombination velocity of the CIGSe/ITO interface of the employed samples is between $5 \cdot 10^4$ cm/s and $5 \cdot 10^5$ cm/s according to these simulations.

Admittance measurements revealed an absence of the N1 signal for the ITO-based samples. Furthermore, differences of the $V_{OC}(T)$ measurements between the two back contact types and the vanishing of the N1 signal for the thinnest absorber layer sample, all suggest that a hole extraction barrier is present for the Mo back contact. This can be seen as a strong indicator that the N1 signal is related to a back contact barrier. It is the first published result that demonstrated the vanishing of the N1 signal upon the usage of another back contact type. The determined back contact barrier height was found to be within 160 meV and 210 meV according to $V_{OC}(T)$ measurements and between 175 meV and 285 meV according to admittance measurements. The absence of the capacitance step for the ITO-based samples could be related to an absence of a hole extraction barrier or it could hint to a high level of p-type doping close to the ITO interface, which would reduce the height of the capacitance step greatly.

A reduction of J_{SC} was observed with decreasing sample temperature for ITO-based samples. This indicates a temperature dependence of the carrier collection for samples with an ITO back contact. The exact carrier extraction mechanism at the CIGSe/ITO interface is still unknown. A carrier transport via tunneling processes was proposed. It was discussed that a high density of acceptor defects may be present at the ITO/CIGSe interface. The presence of such defects could allow for tunneling transport at this interface, while it would simultaneously strongly reduce the extension of the space charge region at the back contact of the ITO-based solar cells. A small extension of the space charge region at this interface is in accordance with the measured carrier density profiles and it could potentially explain the absence of a capacitance step for the ITO-based samples. Electrical simulations suggest that a 1 nm thick layer with a defect density of about $3 \cdot 10^{20}$ cm^{-3} would allow for a carrier transport via trap assisted tunneling at the ITO/CIGSe interface.

Finally, the influence of the back contact on the solar cell parameters was investigated using simulations. It was found that the V_{OC} difference between the two different back contact types cannot be explained by a different back contact recombination velocity. Only for the 300 nm absorber layer, the differences can partly be explained through the differences in the barrier height, and/or a different back contact recombination velocity. The simulation results suggest that for the expected minority carrier diffusion lengths, a strong impact of the back contact on V_{OC} is mainly limited to the case of a completely depleted absorber layer. It was therefore suggested that the observed differences are rather related to a different quality of the absorber layers grown on the different back contact types. XRD measurements support the thesis that the layer growth was different on the two back contact types.

Chapter 5

Nano structured back contacts

5.1 Introduction

The electrical and optical properties of the Al/ITO back contact were discussed in Chapter 3 and 4. The following chapter presents first results of prototype samples, which combine this highly reflective back contact with an additional scattering element.

First of all, cross sections of complete solar cells will be analyzed, which were prepared on structured substrates (Section 5.2). Based on these data a simple growth model will be presented to compute the growth of each layer (Section 5.3). This model is used to find the characteristic growth parameters of each layer. The performance and J_{SC} gain of several solar cells based on structures created via lithography will be presented (Section 5.5). Afterward, the absorption within those devices is calculated using 3D simulations (Section 5.6). Furthermore, the results of structured solar cells obtained with two additional structuring techniques will be presented which are more viable for industrial production processes (Section 5.7). Finally, a comparison of the calculated absorption in solar cells for two differently positioned SiO_2 nanostructures will be presented (Section 5.8).

Note that the results of this chapter are partly published in:

- **Schneider T**, Tröndle J, Fuhrmann B, Syrowatka F, Sprafke A, Scheer R. 2020 Ultrathin CIGSe Solar Cells with Integrated Structured Back Reflector. *Solar RRL* 4, 2000295 (doi:10.1002/solr.202000295)

5.2 Structure transposition

SiO_2 structures with a fixed pitch of 1.96 μm and different targeted structure heights (100 nm, 200 nm, 300 nm, 400 nm, 500 nm) were prepared to analyze the growth behavior of the different solar cell layers. The structures were prepared using laser interference lithography (LIL) as explained in Section 2.1.2. The complete solar cells consisting of Al(110 nm)/ITO(250 nm)/CIGSe(600 nm)/CdS(45 nm)/ZnO(120 nm)/ITO(240 nm) were deposited on top of those structures in a single CIGSe deposition run. The CIGSe was deposited with a maximum deposition temperature of 480°C, and with 2 nm of NaF PDT.
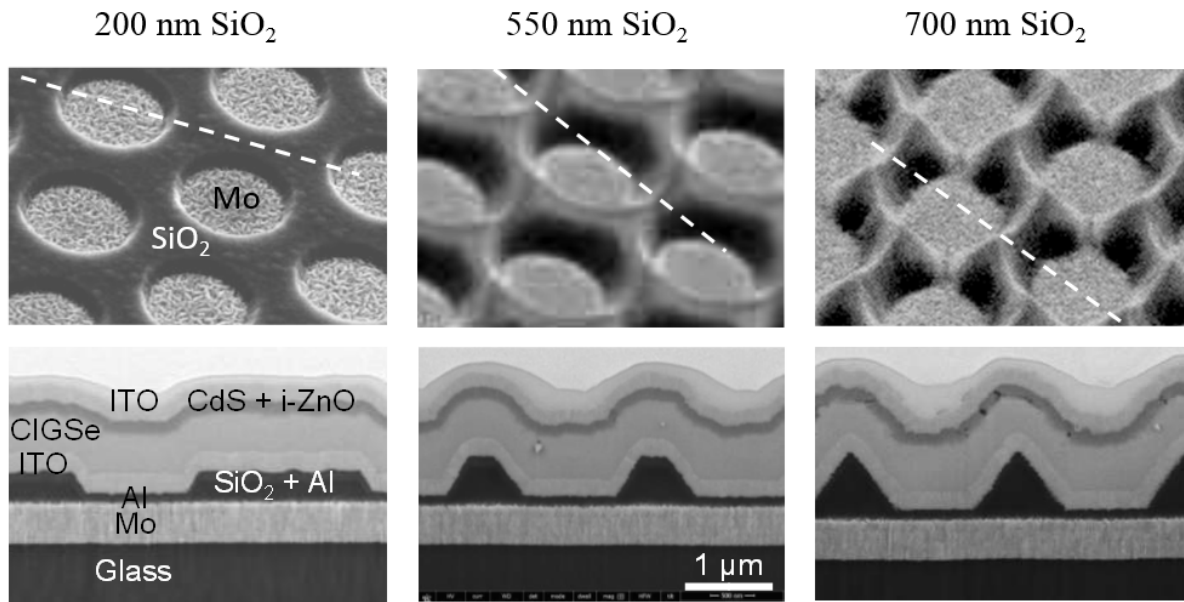
Figure 5.1: SEM pictures of three sample structures with different heights of the deposited SiO$_2$ (200 nm, 550 nm, 700 nm). The upper row shows pictures with a slight tilting, while the lower row shows cross sections alongside the axis defined in the corresponding upper pictures.

The resulting structures were characterized using SEM cross sections prepared by a focused ion beam (FIB). The FIB was used to remove the solar cell layers alongside a well defined line. Several SEM cross section were made at different lateral positions alongside one axis, creating a stack of images at different positions of the structure (similar to the usage of computed tomography scans in medicine).

SEM cross sections are given in Figure 5.1 together with a top view with at a slightly tilted angle. Most of the layers can be distinguished by the material contrast in the SEM cross sections. However, only a small contrast is visible between the SiO$_2$ and Al layer. Furthermore, the CdS layer can not be seen clearly due to its relatively low layer thickness.

The cross sections show that the walls of the holes in the SiO$_2$ structure are inclined with the same angle against the substrate surface. The reason for the inclined walls was explained in Section 2.1.2. The top part of the structures in contrast is flat. This is not true anymore for the 700 nm height structure. As visible from the top perspective in Figure 5.1, a complex structure is found on top of the SiO$_2$ structures for the 700 nm height sample. This structure can be understood from the merging of SiO$_2$ on top of the photoresist pillars, prior to the lift off. The merging of the SiO$_2$ is starting at the direct path between the center of the photoresist pillars. Hence, no SiO$_2$ will reach the substrate at this positions, creating a dent in the final structure. A higher SiO$_2$ structure with the same structuring process would most likely lead to a complete merging of the SiO$_2$ on top of the photoresist pillars and therefore disable the lift-off of the pillars.

The cross sections show that the surface structure is mostly transposed to the upper layers. However, the structure does change slightly with each layer, leading to a less pronounced structure height. The biggest change is visible after the CIGSe deposition. A finer random structure is imposed on top of the desired structure by the roughness of the layers. This effect is also most pronounced after the CIGSe deposition. The next section will try to find a quantitative
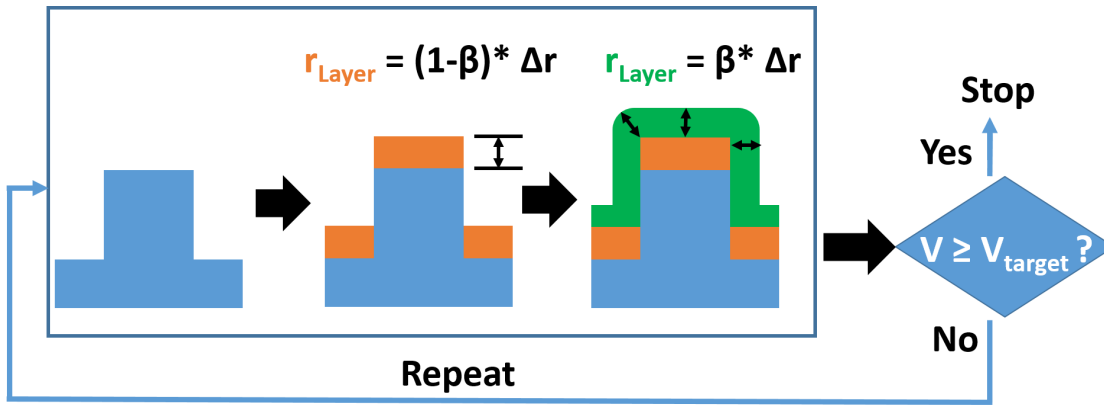
Figure 5.2: Flowchart representing the working principle of the algorithm for the layer growth calculation. V denotes the total volume of the calculated layers. The target volume V_{target} corresponds to the desired total volume of the calculated layers

parameter to describe how well a surface structure below a solar cell layer will be transposed to its top surface.

5.3 Modeling of the layer growth

Next, a simple growth model will be presented, which was implemented in a self-written Fortran program (the developed algorithm can be found in the Appendix H). The chosen approach is similar to the growth model presented by Sever et al. [103]. Two basic growth modes are first defined.

The first growth mode will be called vertical growth hereafter and describes the pure growth in vertical direction (see the orange material in Figure 5.2). This growth would occur if the atoms forming the new layer would arrive from the normal direction in respect to the plane of the unstructured sample and no diffusion of these atoms would occur.

The second growth mode, which will be referenced as conformal growth, describes the growth of the material alongside the surface normal of the former surface shape (see the green material in Figure 5.2). Such a growth behavior can be observed for example with the deposition technique of atomic layer deposition (ALD).

The employed model assumes that the growth process can be expressed by a mixture of the two elementary growth processes (vertical and conformal growth). A certain layer (e.g the CIGSe-layer) is calculated by calculating a series of thinner layers of the material, which will be called sub layers in the following. A new sub layer is calculated on the former, while alternating between both elementary growth processes. The thickness of the newly calculated sub layers is denoted $d_{conformal}$ for the conformal growth and $d_{vertical}$ for the vertical growth. The fraction between these two quantities is defined by $\beta = d_{conformal}/(d_{conformal} + d_{vertical})$. A value of $\beta=0$ corresponds therefore to a growth process which completely conserves the surface structure. A value $\beta>0$ is usually expected due to surface diffusion. Different values of β can be used to tune the layer growth behavior. After the calculations of each sub-layer, the volume of all sub-layers is calculated. The calculation is finished as soon as this volume is equal to the targeted volume.
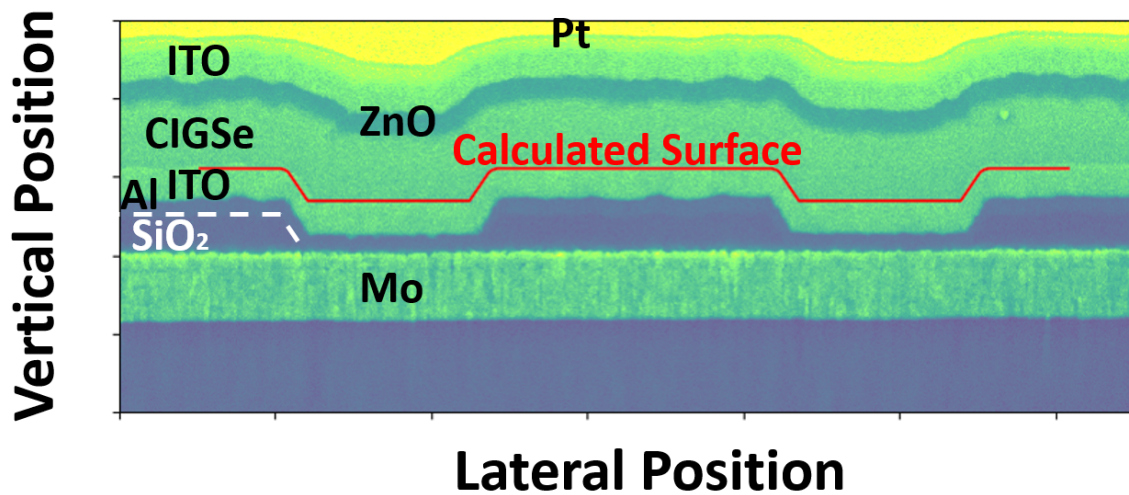
Figure 5.3: Display of the employed method to determine the value of β for each layer. The red line shows the calculated surface of the ITO/CIGSe interface. The plot was created for different values of β, directly plotting the results into the SEM cross sections. Note that the SEM picture is displayed as a color plot.

The cross section pictures were used to determine a value for β for each layer of the solar cell. The volume, that each layer should have for a given sample area was determined from the thicknesses of each layer measured on the unstructured substrate. The growth of the first deposited layer of the solar cell (Al) was calculated for $\beta = 0 \,..\, 1$. A cross section of the calculated 3D surface was then calculated and a projection was plotted directly in the SEM cross section pictures as visible in Figure 5.3 for the rear ITO layer. Using this comparison, the value of β was determined, which represents the closest approximation of the SEM picture. The calculated surface with the best value for β was then used as the new starting point to calculate the subsequent layer, again varying $\beta = 0 \ldots 1$. This process was performed for all available structures.

A value of $\beta = 0.5$ was found for the CIGSe layer using this technique. On the other hand $\beta = 0.3$ was found for the ZnO, both ITO, and the Al layers. The determination of β for Al was especially error-prone due to its small thickness. No value could be extracted for CdS because the layer was difficult to identify in the SEM cross sections. This is causing some uncertainty for the value of β for ZnO and CIGSe, which is however expected to be insignificant. Overall a good representation of the calculated layer surfaces of the SEM cross sections was achieved (see Appendix K). The schematic images of Figure 2.5 were produced from the calculations.

The SEM pictures show that the rear structure is already not completely transposed to the front interface, even with a relatively wide pitch of ~2 μm and an absorber thickness of 500 nm. The strongest change of the interface structure was seen after the deposition of the CIGSe layer. This is however to be expected due to the higher thickness of this layer in comparison to the other layers.

Sever et al. developed a calculation model for the layer growth on structured surfaces and used it for a thin-film Si solar cell [103]. The approach here uses the same idea. Therefore, it is possible to compare the values, although the computational representation of the layers differs from the one used here. In the work of Sever et al. a value of $\beta = 0.2$ was found for the growth of ZnO and a value of $\beta = 0.3$ was found for the growth of amorphous Si, deposited on structured

SnO_2:F.

Kovacic et al. applied the same model to analyze the layer growth of complete CIGSe solar cells, deposited on randomly structured ZnO substrates [42]. A value of $\beta = 0.3$ was found for all analyzed layers (Mo, CIGSe, ZnO, ZnO:Al).

Two remarks have to be made regarding the determined value for the CIGSe in the work presented here. First, the CIGSe top interface has an additional random structure caused by the crystal size which makes it difficult to determine a precise value for β. An absolute error for β of 0.1 is therefore estimated. Secondly, the exact growth of the CIGSe is possibly process dependent, e.g. the process temperature affects atom diffusion and crystal size during the deposition process.

The different value of β for the CIGSe found by Kovacic et al., might be therefore a result of the different absorber deposition temperature (and hence, likely a different crystal size). However, this is purely speculative. Further experiments would be required for such a statement. It is however a good sign, that a similar value for β was found for the growth of the other involved layers.

The layer growth determines up to which structure dimension a structure is still transposed to the front side. Very fine structures will not be transposed to the front interface. The non-structuring of the front interface is not necessary of disadvantage for the structure. The largest gains are obtained, when the light is completely trapped in the absorber layer. If the rear structure does scatter the light at a sufficiently low angle against the front interface of the sample, the light can be reflected back by total reflection. A structuring of the front contact might compromise this process in some cases.

5.4 Chemical composition

Two additional sets of solar cells were prepared to analyze the performance of the solar cells. The two created sample sets will be referred to in the following as set 1 and set 2. Solar cells based on the samples shown in the preceding section exhibited strong shunting problems. As a consequence, no metal grid was deposited on the solar cells of set 1 and set 2. This was necessary because very small solar cell areas of about ~10 mm^2 were used to limit the possibility of shunting problems for those solar cells.

The thickness of the SiO_2 layers was determined using ellipsometry measurements on SiO_2 layers deposited in the same run on Si wafers. The structure heights are 100, 200, 280, 550, and 700 nm for set 1 and 100, 170, 300, and 500 nm for set 2. It must be noted that the sample with the 100 nm structure showed a milky appearance, indicating a problem with the lift off process.

The chemical composition is a GGI of 0.37 for the first set of samples and 0.3 for the second set, while the CGI is 0.84 for both sample sets as determined using EDX measurements. Corresponding GDOES measurements are given in Figure 5.4. The average GGI of sample set 2 is slightly lower than for set 1, with a similar notch depth.

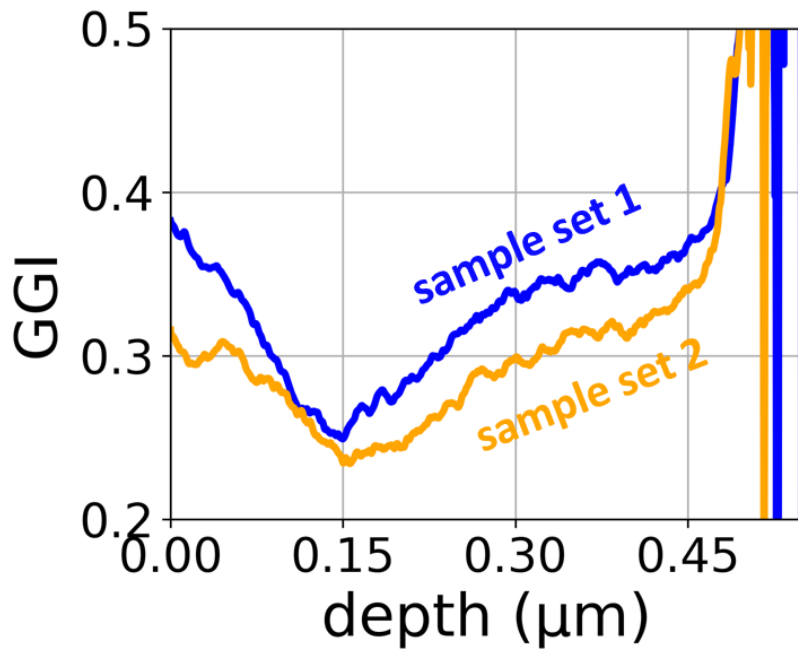Figure 5.4: GGI profiles determined from GDOES measurements on unstructured reference samples.
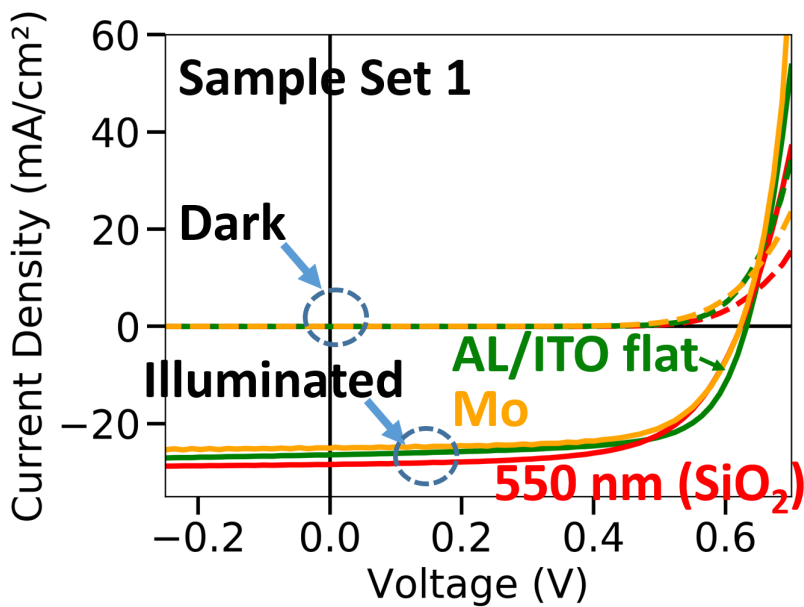

Figure 5.5: Exemplary JV curves measured on the best solar cells with an Mo-back contact (orange), and an Al/ITO back contact on an unstructured (green) and structured back contact with a structure height of 550 nm (red). The full lines are measured with illumination, while the dashed lines are measured in the dark.
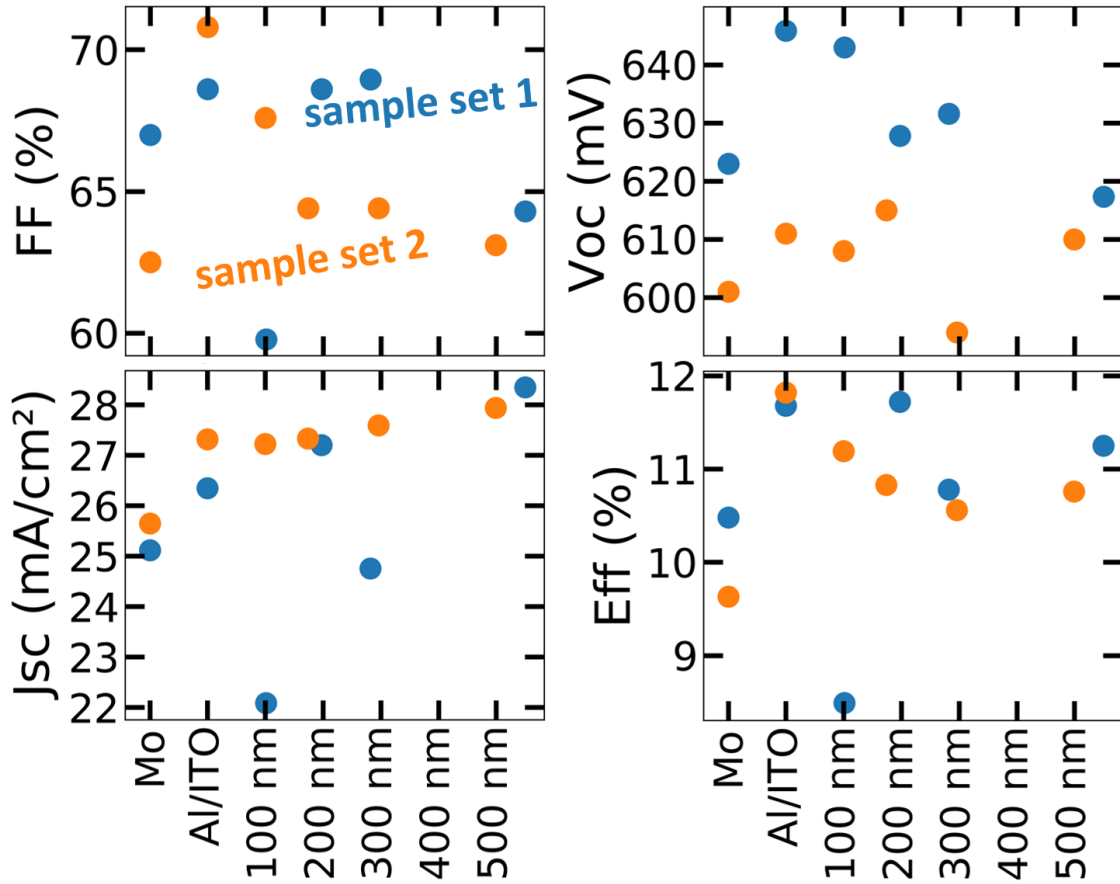
Figure 5.6: Solar cell parameters of reference samples with a Mo back contact, with a flat Al/ITO back contact, and structured back contacts with different SiO_2 layer thicknesses for sample sets 1 and 2.

5.5 Characterization of LIL structured solar cells

Figure 5.5 shows exemplary JV curves of set 1. Solar cells without any apparent shunting were obtained. The only exception is the solar cell based on the 700 nm structure, which was strongly shunted. The determined shunt resistance from dark JV curves was above 20 kΩcm^2 for all solar cells used for the extraction of the solar cell parameters. A relative strong crossover is visible.

The determined solar cell parameter are given in Figure 5.6. Note that the J_{SC} values are calculated from the EQE measurements for an AM1.5G spectra. The FF found in the samples are between 60% and 70%. No systematic trend is visible regarding the FF of the different sample types, except for set 2 where a decrease of the FF is observed with increasing structure height. The V_{OC} values of the Al/ITO-based samples are mostly slightly higher than for the corresponding Mo-references. The average V_{OC} is about 10 - 20 mV higher in set 1 compared to set 2. A decrease of V_{OC} with increasing structure height is visible for set 1.

The short circuit density is increased by 1.2 mA/cm^2 (set 1) and 1.7 mA/cm^2 (set 2), when comparing the flat Al/ITO-based samples with the Mo-references. The additional structuring leads to a total increase of 3.2 mA/cm^2 (set 1) and 2.3 mA/cm^2 (set 2) for the highest structures. The J_{SC} values increase with the structure height (with two exceptions in set 1). The achieved *PCE* is increased from 10.5% (set 1) and 9.6% (set 2) for the Mo-references to 10.7% (set 1) and

11.8% (set 2) with the flat Al/ITO-based samples. The structured samples exhibit all reduced *PCE* values compared to the corresponding flat Al/ITO-samples; the gains in J_{SC} are offset by a reduction of the other parameters.

The CIGSe layer of set 1 possesses a higher GGI value, which could explain the higher V_{OC} values of this set. The absence of an increased *PCE* by the structuring despite the increased J_{SC} values gives a hint that the structuring process could have a negative impact on the other cell parameters. The lift off process can partly fail which means that the photoresist will partly be present before the CIGSe deposition. The photoresist will likely decompose during the CIGSe deposition. This might lead to local defects in the layer systems. The 100 nm height sample from set 1 looked noticeably different from the other samples which is likely caused by an unsuccessful lift-off process. This sample posses a lower *FF* value than the other samples of the set and especially the J_{SC} value is noticeable low. The other structured samples might suffer from the same effect, but on a smaller level. The structured samples were furthermore also subjected to more preparation steps, which could potentially affect the solar cell performance. The structuring could affect the sample performance in various ways. The pn-junction has rather a 3D distribution compared to the simple flat case, which is essentially a 1D problem. It is furthermore unclear if the alkali metals will be distributed evenly, or if a lateral inhomogeneity of the doping density does occur through it. This could increase the general inhomogeneity of the sample, and therefore have a negative impact on the sample performance. However, the structured and unstructured samples of set 2 are mostly on a similar V_{OC} level and a similar observation can be made for the *FF* values of set 1 (especially when the likely faulty 100 nm structure is excluded). The absence of an increased *PCE* compared to the unstructured Al/ITO sample could therefore also be related to the typical scattering of solar cell parameters, typically experienced between different CIGSe solar cells even when they are from the same CIGSe deposition run.

The measured EQE curves are given in Figure 5.7 a) and b) for both sets. A solar cell with Mo back contact and the same window structure, but with a 2.8 μm absorber layer is also given for comparison. The number of curves was reduced to simplify the figure. A full set of curves is given in the Appendix G.

First of all, a distinct peak can be seen at ~900 nm for the unstructured Al/ITO-based samples. A second peak is visible for the flat Al/ITO sample of set 2 at 820 nm. Both peaks disappear with increasing structuring height. Instead, a broader peak is visible at longer wavelengths, which increases the EQE value in this region. The 100 nm and 280 nm (given in the appendix) samples show a decreased EQE over the full spectra. A small increase in the EQE with increasing structure height is also visible for shorter wavelengths around 600 nm. This effect is much more pronounced in set 1.

The best structure reaches about 88% of the J_{SC} value of the 2.8 μm absorber thickness reference. The band gap of the Al/ITO-based solar cells appears to be lower in comparison to the Mo-based samples. This difference can be explained by optical simulations as shown later in the simulations section. The EQE curves of sample set 1 show overall more variation over the whole spectral range. The results of set 2 are therefore probably more representative of the actual influence of the structures on the EQE.

Further structures with a pitch of 1 μm were prepared using LIL. However, those samples exhibited a strong scattering of the JV results, likely due to the occurrence of cracks in the ITO and Al layers as can be seen in the SEM crosssection in Figure 5.8. The corresponding EQE curves are therefore likely not representative for the actual absorption increase by the structures. The experimental results can be found in the Appendix L.
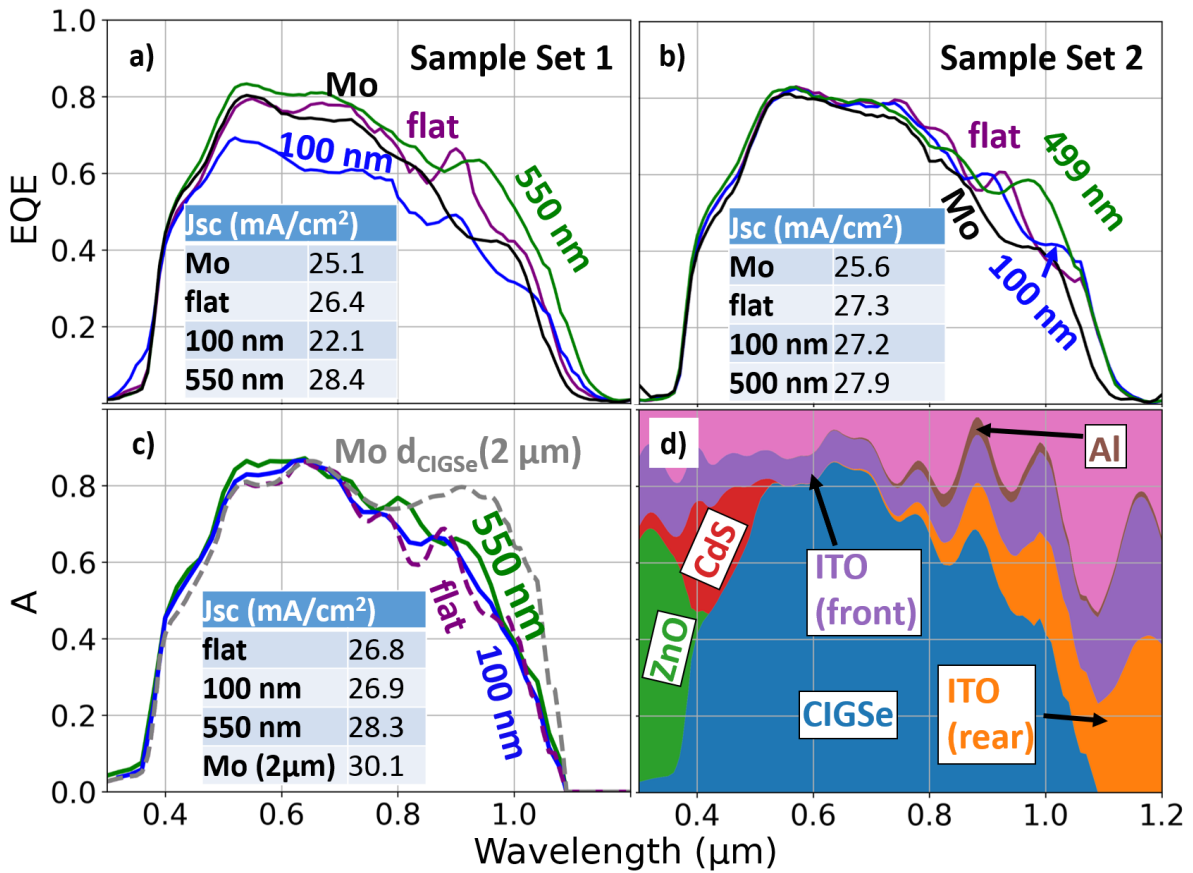
Figure 5.7: External quantum efficiency of solar cells with different back contacts for sample set 1 (a) and sample set 2 (b). An additional CIGSe solar cell with a 2.8 µm absorber and a Mo back contact is shown in both figures for comparison. (c) Calculated absorption within the CIGSe layer of a complete solar cell. The dashed lines are calculated using the transfer-matrix-method for an unstructured sample with an Al/ITO back contact (purple), a Mo back contact (black) and a solar cell with Mo back contact with a 2.8 µm absorber (grey). The other curves are from FDTD calculations for the structural dimensions of sample set 1. (d) Calculated relative absorption within the separate solar cell layers for an unstructured solar cell with Al/ITO back contact. A plot of the complete dataset can be found in the Appendix G.
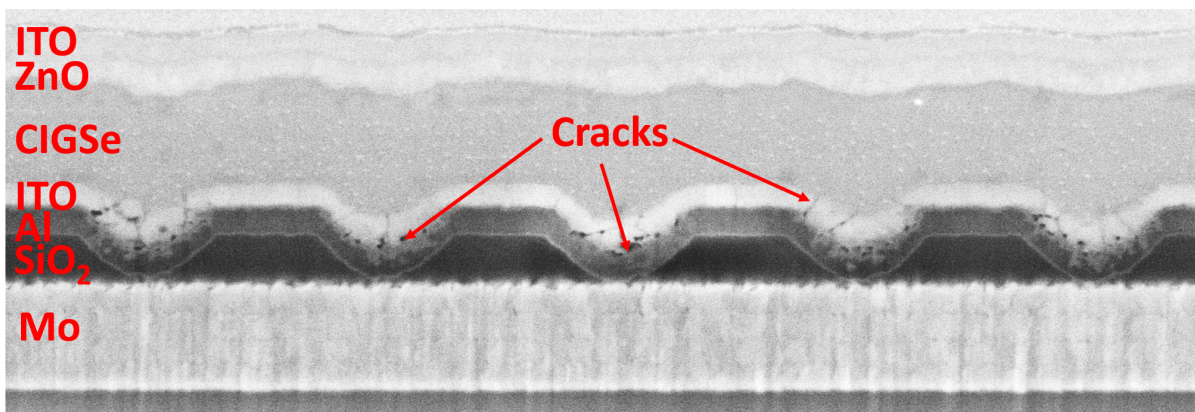
Figure 5.8: Cross section of a LIL structured solar cell from the set 3 created using a FIB cut.
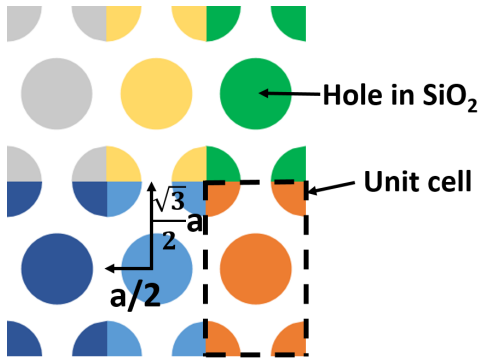
Figure 5.9: Visualization of the implementation of the hexagonal pattern in MEEP with a pitch distance a. Each color represents a different elementary cell. Each point represents a hole in the SiO$_2$ structure.
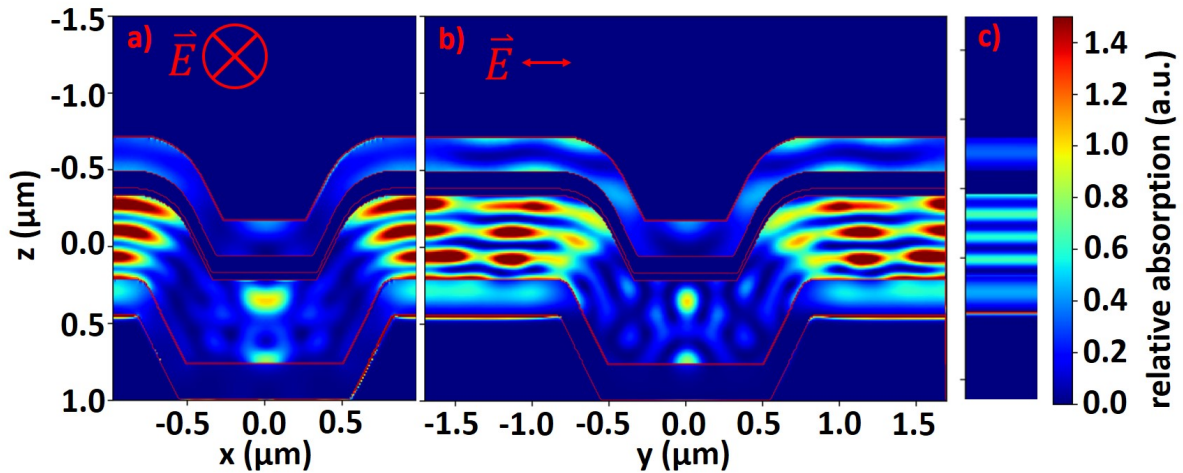
Figure 5.10: (a, b) Calculated local absorption within a solar cell corresponding to the 550 nm structure height sample from sample set 1 for a wavelength of 940 nm. The used axes are shown in Figure 2.5. (c) The same data calculated for a flat solar cell with the same layer thicknesses. All pictures share the same color scale, which shows the local absorption within a volume element in arbitrary units.

5.6 3D optical simulations

3D optical simulations were conducted using FDTD calculations implemented in the software package MEEP. Technical details about the configuration of the FDTD simulations are given in the Appendix I. The layer growth properties determined in Section 5.3 were used to calculate the 3D structures using the layer thicknesses from set 1. The employed software only supports euclidean base vectors. However, the hexagonal pattern can be implemented using euclidean base vectors as visible in Figure 5.9.

A second problem is related to the GGI gradient. The GGI gradient of the sample can only be determined for the unstructured sample using GDOES measurements, while the GGI distribution of the structured sample is not accessible (the distribution may be visible using TEM-EDX measurements). However, an approximation of the GGI using a constant value makes it difficult to compare the experimental data with the simulations, due to deviations expected for the absorption of light at longer wavelengths. As a solution to this problem, the CIGSe layer was

110

calculated as several thinner CIGSe layers of constant GGI stacked on top of each other. The GGI gradient measured on the unstructured sample of set 1 was used to determine the GGI value of each sub layer. This distribution can differ from the GGI distribution of the real structured CIGSe solar cell. The GGI gradient is formed after the second stage of the three-stage-process (and also the third stage) due to the different mobilities of the Ga and In atoms [14]. The surface structure after the first and second stage does consequently affect the GGI distribution of the final CIGSe layer. The differences are however expected to be low for the investigated structural dimensions in relation to the CIGSe layer thickness.

The absorption was calculated for each material of the solar cell by summing up the local absorption at all positions according to Equation 2.9. The calculation was performed for the two polarization directions shown as x- and y-axis in Figure 2.5. Generally, the difference in global absorption in the CIGSe layer for the two polarization was found to be very small (<0.01 %) for all wavelengths. Reference curves were calculated in 1D using TMM calculations for the unstructured solar cells with an Al/ITO back contact as well as for the two solar cells with the Mo back contact having an absorber thickness of 0.6 µm and 2.8 µm.

The results are given in Figure 5.7 c) to allow an easy comparison with the experimental EQE curves. The overall shapes of the calculated absorption curves are in close agreement to the corresponding EQE spectra, with the exception of a peak at 820 nm, which is visible for the 550 nm structure in simulations but does not appear in the experiment. This peak might be visible in the 500 nm structure of sample set 2. The beforehand mentioned apparent difference between the band gaps of samples with Mo back contact in comparison to samples with Al/ITO back contact is also visible in the simulations. This difference can therefore be explained by an increased absorption of light for the Al/ITO-based samples in comparison to the Mo back contact samples.

The peaks are generally more pronounced in the simulations than in the experiment, with EQE values generally lower than the calculated absorption at the peak positions. Additionally, some discrepancies can be seen at around 620 nm with lower EQE values than for the calculated absorption.

The Figures 5.10 a) and b) show the local absorption for a solar cell with a 550 nm structure height at a wavelength of 940 nm, for which the structured solar cell shows a increased absorption within the CIGSe layer compared to the flat sample. The respective plot for the unstructured sample is shown in Figure 5.10 c) for comparison. Locally increased absorption caused by interference is visible in the unstructured case. This local absorption is enhanced for the structured case by additional local maxima in the elevated part of the structure. Contrary to this, the CIGSe layer exhibits a decreased absorption in the valley region. Additionally, a smaller region of increased absorption is found in the center of the valley.

The additional pattern is likely created by the light scattered at the front interfaces over the "hole-region". The shape of the front redirects light away from the "hole-region" of the sample to the outer parts, which explains why the average absorption is decreased in the "hole-region" and increased in the elevated portions. The absorption patterns in the lower portion of the sample can be understood from the reflection on the inclined portion of the Al/ITO interface. The shape of the interface focuses light to the center of the structure. There it overlaps with light, which traverses the center of the structure without redirection. The combination of those waves should be able to create the observed pattern.

The increase of J_{SC} can be understood from this figure. Light scattered at the front interface will traverse the absorber layer twice with an angle regarding to the non inclined portion of

the structure. The effective absorption length is therefore increased. The portion of the front interface which is curved instead of flat is increasing with increasing structure height. Therefore, this scattering effect is more pronounced for higher structures. This explains why the J_{SC} values increase with the structure height.

The inhomogeneous distribution of generated carries could have a negative impact on the cell performance. It causes the solar cell to be effectively under different illumination conditions at different lateral positions. It is however unclear how the inhomogeneous carrier generation translates into an inhomogeneous carrier distribution, when carrier diffusion is considered and to which extend the solar cell parameter are affected.

A quite similar EQE value was measured at around 500 nm, comparing the structured with the unstructured solar cells. This suggests that the structure is not causing a change of the average reflectivity of the sample. This is expected given the fact that usually finer structures are necessary to view the interfaces as an effective media.

Figure 5.7 d) shows the absorption within the different solar cell layers for the unstructured sample. There are two strong absorption losses related to the non-optimized ITO used. Parasitic absorption occurs in the front ITO for a wide wavelength range. In addition, parasitic absorption occurs within the rear ITO at long wavelengths. This limits the possible achievable gain through the structuring and could be mitigated through an optimization of the ITO layers. The relative parasitic absorption of the incoming solar energy within the rear ITO layer, for energies below the band gap of the CIGSe, was calculated to 3.8% in the flat case, 3.8% for the 100 nm structure, and 4.2% for the 550 nm structure.

5.7   Towards industrial applications

The structuring of solar cells using the LIL method is suited to produce a variation of nanostructures in a well controlled fashion. However, an industrial application appears to be difficult, due to limited up-scaling capability of this lithography method. Two alternative structuring techniques were tested.

The first structure is based on a semi-random crater like structure, created in Al doped ZnO layers as can be seen in the sketch of Figure 5.11 a). This structure was provided by the research institute of Jülich. It was originally developed to fabricate structured electrical back contacts for thin film Si solar cells [104]. The structure is created through a chemical etching of a sputtered ZnO:Al layer. Depending on the sputtering conditions, crater of different sizes will occur due to an anisotropic etching of the ZnO:Al layer. The full solar cell stack was then deposited on top of those structures as visible in the cross section provided in Figure 5.11 b).

The second structure was created by laser-structuring of a soda lime glass performed by the institute for nanophotonics Göttingen. Figure 5.11 c) shows a 3D representation of an AFM measurement on the structured glass surface. Figure 5.11 d) shows a height diagram extracted from the AFM measurements. The structure has a height of about 200 nm, with a pitch of about 2 μm.

Samples of both types were processed together with set 2 from Section 5.5. Exemplary JV curves are given in Figure 5.12 a). The solar cell based on the ZnO:Al structure shows a similar
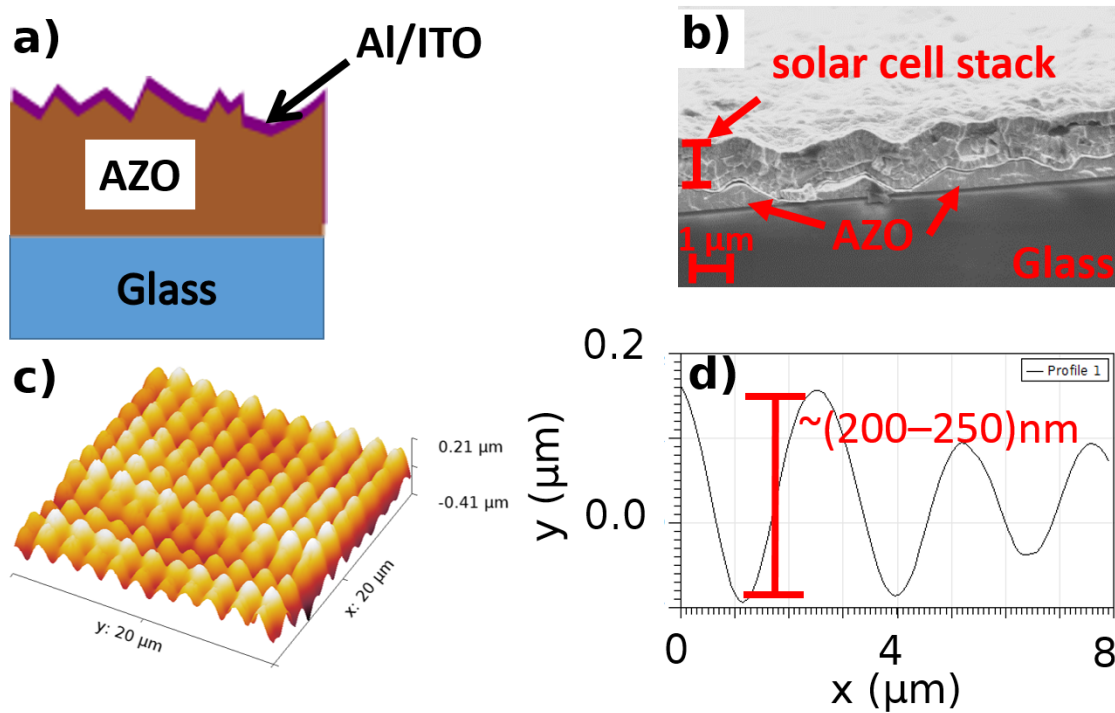
Figure 5.11: a) Sketch of the employed, structured ZnO:Al back contact. b) Cross section SEM-picture of a solar cell based on a structured ZnO:Al back contact. c) 3D representation of an AFM-measurement of the surface of a laser structured glass. d) To c) corresponding height diagram along one axis.
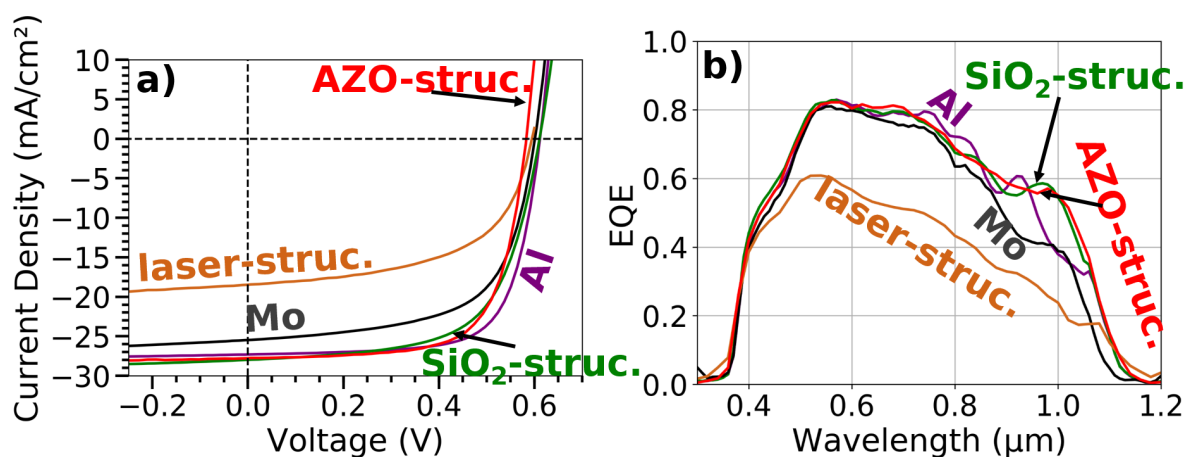
Figure 5.12: a) Exemplary JV curves from set 2. The SiO$_2$-structured sample denotes the 500 nm height sample. b) Corresponding EQE measurements of the same samples as presented in a).

Table 5.1: Extracted solar cell parameters of different back contact structures belonging to set 2. The J_{SC} values have been obtained from EQE measurements, while the FF and the V_{OC} values were obtained from JV measurements

Back contact	V_{OC} (mV)	FF (%)	J_{SC} (mA/cm^2)	PCE (%)
Mo	601	62.5	25.6	9.6
Al/ITO	611	70.8	27.3	11.8
(500 nm SiO$_2$ structure)/Al/ITO	610	63.1	27.9	10.8
(Laser structured SLG)/Al/ITO	595	56.4	18.6	6.2
(Nanostructured ZnO)/Al/ITO	583	69.0	28.0	11.3

JV curve as the best performing sample prepared using the LIL structuring method. The laser structured sample shows in contrast a poor J_{SC} value with some distortion of the JV curve.

The determined solar cell parameters are given in Table 5.1. The sample based on the laser structured solar cell shows a similar V_{OC} value to the unstructured samples, while having the poorest FF in the batch. The biggest effect can be seen however regarding J_{SC}, which is significant lower compared to the other samples.

The sample based on the structured ZnO layer has a reduced V_{OC} value, while having a decent FF in the context of the other samples. While the J_{SC} value is similar to the best J_{SC} value obtained using the LIL structured solar cell of the set, still no increase of the PCE is obtained.

A comparison of the EQE results is visible in Figure 5.12 b). The laser structured sample shows an overall low EQE value, which is constantly further declining for wavelength above 500 nm. The ZnO:Al-based sample shows in contrast a comparable EQE shape to the 500 nm height sample prepared using LIL structuring.

The results on the nanostructured ZnO substrate are promising. A further investigation of such structures with varying structural dimension might lead to higher gains. This process could be potentially easier be scaled up than the LIL structured samples. The results on the laser structured samples have been in contrast unsuccessful. A possible reason could be the presence of debris from the laser structuring, which were not properly removed in the cleaning of the sample. Cracks could be furthermore present in ITO similar to the observations made in Figure 5.8. Furthermore, this sample did not have an alkali metal diffusion barrier. Hence a higher amount of Na might have been present during the absorber preparation.

5.8 Investigation of the placement of SiO$_2$ nanostructures within the solar cell

The growth parameters determined in Section 5.3 allow a systematic prediction of the absorption in further structures. The impact of the pitch distance on the absorption was studied for two different systems. The first system is the same LIL based structure as discussed in the beginning of this chapter. The same SiO$_2$ structure was in contrast put on top of a flat Al/ITO back contact for the second structure type as visible in Figure 5.13 b). The structural dimension of the width of the holes in the SiO$_2$ as measured from the experiments was used. The width of the holes was scaled with the pitch distance. Namely by keeping the ratios a/r_{top} and a/r_{bottom} constant, with the pitch distance a, r_{top} the radius of the hole measured at the top of SiO$_2$ structure, and r_{bottom}

the radius of the hole measured at the bottom of SiO_2 structure. The height of the structures was fixed to 300 nm throughout the simulations. The layer stack of the unstructured solar cell is Al(100 nm)/ITO(100 nm)/CIGSe(500 nm)/CdS(45 nm)/ZnO(100 nm)/ITO(100 nm). The GGI from set 1 of Section 5.4 was used for the CIGSe layer. The resulting EQE curves for the four calculated pitch distances (250 nm, 500 nm, 1000 nm, and 2000 nm) can be seen in Figure 5.13. An unstructured solar cell with a Mo back contact and a 2.8 μm absorber layer is also shown as a reference. Figure 5.14 shows the corresponding J_{SC} values under the assumption of no electrical losses. The highest J_{SC} value is obtained for the 500 nm pitch structure with the SiO_2 on top of the Al/ITO, due to a broad increase of the EQE for a wavelength around 1 μm. In case of the other structures the highest J_{SC} values are obtained for both the 0.5 μm and 1 μm pitch structure. The structure with the SiO_2 underneath the Al/ITO reaches up to 95% of the J_{SC} value of the reference with the thick absorber layer, while the other system reaches up to 99% of this J_{SC} value. The calculated absorption of the latter mentioned system is very close to the absorption of a solar cell with a 2.8 μm absorber layer, which shows that the light is effectively trapped within the solar cell.

Figure 5.15 shows the calculated local absorption at a wavelength of 940 nm and a pitch of 1 μm for both structure types. Both structures show a similar pattern of locally increased absorption in the upper part of the structure. A difference in the absorption distribution can be seen in the lower part of the structures. A stronger local absorption pattern can be seen for the structure with the SiO_2 placed above the Al/ITO layers. The emerging pattern along the x-axis could give a hint, that a waveguide mode might propagate through this structure. The SiO_2 does allow a propagation of the light within it, in contrast to the Al. A propagation of the light parallel to the substrate surface is therefore likely obtainable for wider range of structural dimension with the SiO_2 on top of a flat reflector than for the other structure type, which might be an explanation for the different overall performance of the two structure types.

However, the optical simulation results of Krc et al. and Kovacic et al. showed that effective light trapping can be obtained with highly reflective back contact, deposited on top of a structured sample [4, 42]. A 2D sine like structure showed good results in both publications. The investigated structure might be therefore simply not suited to obtain effective light trapping for the regarded structural dimensions. An inversion of the structure used here (hills instead of holes) could be investigated. This structure is closer to the structures for which Krc et al. and Kovacic et al. already demonstrated good results via simulations.

These results show furthermore that the parasitic absorption within the rear ITO can be sufficiency low for a 100 nm thick ITO layer, and that similar J_{SC} values as for regular thick solar cells are obtainable with this back contact. Higher gains might be also obtainable when different structure heights and more pitch distances would be included in the simulations.

The simulations show that structures with the alternative SiO_2 placement and a pitch of around 1 μm should give much higher gains than the experimentally investigated structures. However, a realization of structures with a 1 μm pitch has already proven difficult using the lift-off method. A different preparation method than the lift-off method should therefore be used to test this structure type. Reactive ion etching could be used for this purpose as shown by Jarzembowski et al. in [36]. The preparation of solar cells with the alternative placement of the SiO_2 was not tested experimentally in this work, because it would have created further experimental questions like the impact of the etching process on the ITO interface.
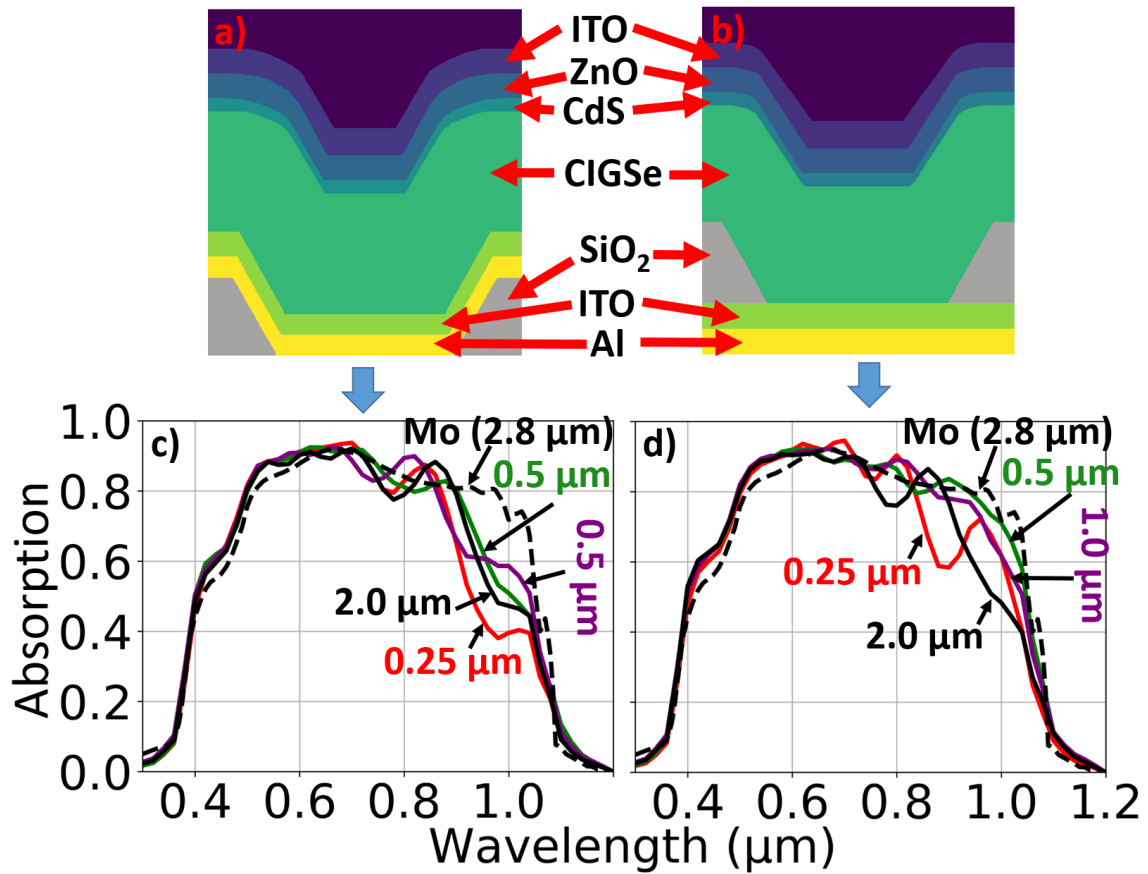
Figure 5.13: a) and b): Schematically cross sections of the simulated structures, with the SiO_2 structure placed under the Al/ITO back contact (a), or on top of it (b). The calculated absorption within the CIGSe layer is shown for the structures shown in a) and b) is given in c) and d) respectively. The full lines give the absorption for the four different pitch distances, while the dashed lines show the same result for a sample with a 2.8 µm absorber layer with a Mo back contact.
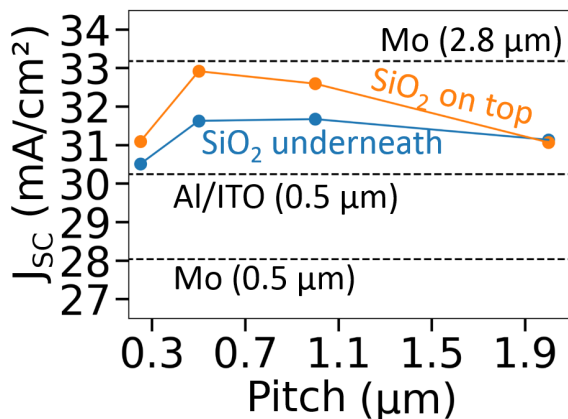
Figure 5.14: Maximum obtainable J_{SC} values with the absorption spectra shown in Figure 5.13. The dashed lines give the J_{SC} values of unstructured solar cells with the same layer thicknesses as the structured samples with the corresponding CIGSe layer thicknesses displayed in the parenthesis.
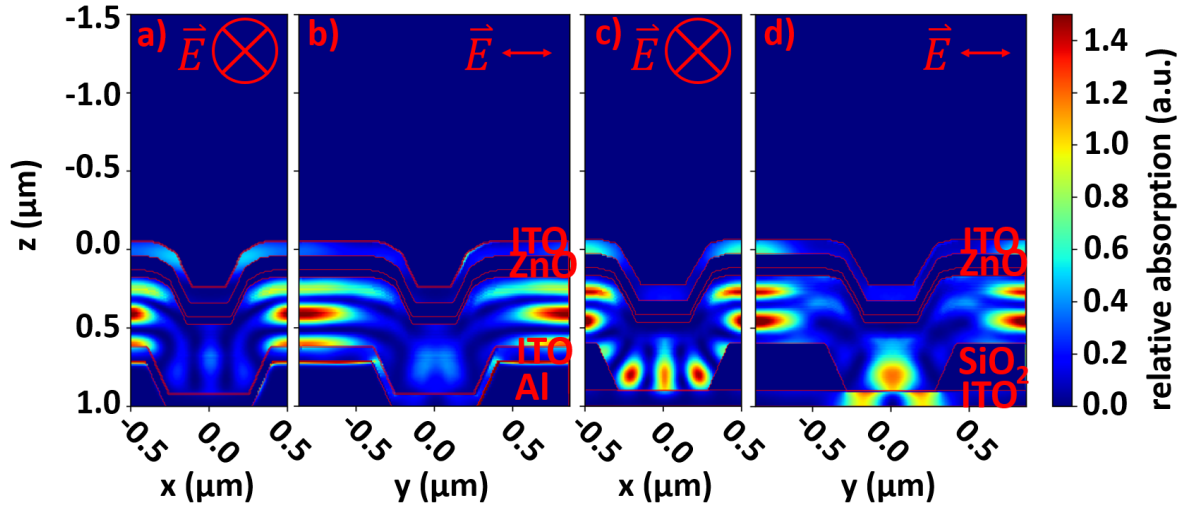
Figure 5.15: Calculated local absorption within two solar cell with a pitch of 1 μm and a structure height of 300 nm for a wavelength of 940 nm. a) and b) correspond to the structure with the SiO$_2$ placed beneath the Al/ITO layers, while the SiO$_2$ are placed above these layers in the cases of c) and d). The used axes are shown in Figure 2.5. All pictures share the same color scale, which shows the local absorption within a volume element in arbitrary units.

5.9 Conclusion

First prototypes of CIGSe solar cells were successfully prepared, which implement a nanostructured, highly reflective and conductive back contact. It are the first experimental results, which combine those three properties for CIGSe based solar cells to the knowledge of the author. A J_{SC} increase of up to 3.2 mA/cm^2 was obtained using the LIL structured solar cells with an Al/ITO back contact compared to the corresponding Mo-reference. The obtained current is about 88% of the measured current of a Mo-based solar cell with a 2.8 μm thick absorber layer but with otherwise the same layer structure.

Despite this increase in J_{SC}, no increase in the *PCE* was obtained, when the structured Al/ITO-based solar cells are compared to the unstructured Al/ITO-based solar cells. The reduction of the *FF* and/or V_{OC} could be related to systematic changes induced by the structures. An inhomogeneous distribution of the carrier generation and inhomogeneous doping density distributions were discussed as possible origins. However, it is difficult to assess the potential influence of these potential problems. The reduced *PCE* could be also entirely related to random effects in the sample preparation process.

A simple growth model was applied to obtain the characteristic growth parameters of the various layers of the solar cells. The characteristic growth parameter β was determined to be 0.3 for ZnO, ITO, Al, and 0.5 for CIGSe. The experimental structure was successfully reproduced using the chosen growth model with the extracted parameters. The calculated structures were then used for 3D optical simulations to calculate the absorption within the CIGSe layer. The obtained absorption spectra mostly resemble the obtained EQE spectra. The local absorption distribution shows that the light is scattered at the front interface to the elevated parts of the CIGSe layer. The resulting absorption distribution is causing an inhomogeneous lateral distribution of the generated charge carriers.

Two additional structures, which were created using other structuring methods were evaluated.

Quite poor performances were obtained for solar cells based on a laser structured glass substrates. The debris from the structuring process and the absence of an alkali barrier were discussed as possible causes for the poor performance. A sample based on a structured ZnO:Al substrate showed in contrast a similar J_{SC} gains like the best LIL based structure. This structuring technique might be viable in an industrial process.

Another positioning of the SiO$_2$ nanostructures within the solar cell stack was investigated using FDTD simulations and compared with the configuration used in the experiments. It was found that significantly higher gains should be obtainable for SiO$_2$ structures prepared on top of a flat Al/ITO back contact. The best structures reached 99% of the J_{SC} value of a solar cell with a 2.8 μm thick absorber layer.

The results demonstrate that the concept of a structured solar cell with an integrated metallic reflector is in principle working. Larger gains are expected upon a further optimization.

Chapter 6

Summary and Outlook

Alternative back contacts for the commonly used Mo back contact were developed in this thesis for CIGSe solar cells to improve the reflectivity at the rear interface to the absorber layer. A reduction of the absorber layer thickness without losses in the power conversion efficiency of the solar cells is the goal of this efforts. Back contacts comprising of a metal layer covered by an ITO layer proved to be promising candidates to archive this goal. The electrical properties of the CIGSe/ITO interface was consequently investigated. An Al/ITO back contact was furthermore successfully combined with a structuring of the substrate.

Various metal/TCO combinations were tested as alternative back contact for CIGSe solar cells. Both an Al/ITO and an Au/ITO back contact were successfully integrated into solar cells. Both back contacts allow a reduction of the CIGSe absorber thickness by 35% without losses in J_{SC}, taking a CIGSe solar cell with a 2 μm thick absorber layer and a Mo back contact as a reference. Almost no additional gain is obtained for the unstructured sample, if the Al is replaced by the more reflective Au, Ag or Cu in this configuration. Au has only a value in academic research, but not as an industrial application due to the high associated cost.

Other metal/TCO combinations suffered from strong shunting issues. Diffusion of Cu was observed for an ITO-based back contact, which leads to the formation of large quantities of $CuSe_2$ during the absorber layer deposition. It was shown that this problem can be strongly reduced by the film preparation parameters of the TCO layer. Shunt free solar cells were demonstrated for small area solar cells (~1 mm^2) with a Cu/ITO and with a Cu/ZnO back contact. Local shunts lead to a shunting of solar cells with a larger area, which are likely caused by a local failure of the diffusion barrier. The exact reasons for this local failures were not found. Different reasons have been discussed including the incorporation of dirt particles in between the deposition steps and local inhomogeneities of the TCO layer.

The most promising candidate proved to be the Al/ITO back contact. Solar cells were successfully processed for process temperatures up to 600 °C. This is in contrast to most literature results with a TCO/CIGSe interface at the back contact, where usually poor performances are obtained at elevated deposition temperatures. High process temperatures might be interesting for the industrial application, where usually shorter processing times are required. This indicates that it is possible to obtain CIGSe solar cells with reasonable FF on TCO-based back contacts, without the usage of an additional layer between the TCO and the CIGSe (like the usage of a thin $MoSe_2$ layer employed in various publications [38, 55, 57]).

Different ITO thicknesses were tested for the Al/ITO back contact. An increase of J_{SC} by 2.2% was obtained when comparing a sample with a 100 nm thick ITO layer to a sample with a

400 nm thick ITO layer. A reduction to a thickness of 50 nm resulted in a strong reduction of J_{SC} indication a problem with the charge carrier collection. This problem is likely caused at the ITO/CIGSe interface. Further experiments are required to understand this issue. The lateral conductivity of the ITO is not required in this configuration due to the superior metal conductivity of the Al. A reduction of the ITO thickness is therefore desirable to reduce parasitic absorption.

TEM measurements showed that no Ga_2O_3 was detectable on the back contact interface for a deposition temperature of 480 °C, while a thin layer of Ga_2O_3 was found for a deposition temperature of 600 °C. A possible reason for the rather good results at elevated deposition temperatures could lie in a high thermal stability of the ITO layer, which could depend on the sputtering deposition condition. Another likely explanation is the avoidance of Na during the absorber deposition by the usage of an alkali diffusion barrier. Literature results suggest that Na can lead to an enhanced formation of Ga_2O_3 [10, 11].

Further research is required to understand the carrier extraction at the CIGSe/ITO interface at all. The presence of a highly defective region with a high p-type doping in the CIGSe layer close to the ITO interface was suggested. JV curves were successfully simulated for a bifacial solar cell with such a layer close to the back contact. A 1 nm layer with a defect density larger than $3 \cdot 10^{20}$ cm^{-3} was found to be sufficient to enable carrier transport between the CIGSe layer and the rear ITO layer. A current transport via direct tunneling was found for defect densities above $8 \cdot 10^{20}$ cm^{-3}. The compensation of Se vacancies by oxygen was brought forward as a possible explanation for such a highly doped layer. Without the presence of such an highly doped layer, differences in the determined charge carrier densities would be expected when a Mo-based sample is compared to a ITO-based sample for an ultrathin absorber layer, due to the extension of the rear pn-junction.

An interesting finding is the absence of the N1 signal for the ITO-based samples, as well as for the Mo-based solar cell with an ultrathin absorber layer. This is the first report of those experimental findings to the knowledge of the author. It was shown this observation is a strong indication that the signal which was debated for decades is caused by a barrier at the back contact.

A methodology was developed to determine the back contact recombination velocity at the ITO/CIGSe interface through the combination of bifacial JV and EQE measurements. This methodology attempts to reduce the number of assumptions for material properties of the CIGSe absorber layer, which are difficult to determine (like the charge carrier mobilities). A value between $5 \cdot 10^4$ cm/s and $5 \cdot 10^5$ cm/s was determined for S_n at the ITO/CIGSe interface.

Higher V_{OC} values were observed for solar cells with an ITO-based back contact compared to samples with a Mo back contact. This effect is increased with a decrease of the absorber layer thickness. Electrical simulations were used to understand this issue. The simulation results suggest that these V_{OC} differences are likely related to higher carrier diffusion lengths in the CIGSe absorber layer grown on the ITO-based back contact instead of a direct contribution of the back contact recombination. The results suggest further that the back contact recombination velocity has significant effects on V_{OC}, mainly when the absorber layer is completely depleted for moderated diffusion lengths.

Solar cells based on the Al/ITO back contact have been successfully prepared on structured substrates, combining a highly reflective back contact with a scattering element. The best structure has reached about 88% of the short circuit current density of a solar cell with a 2.8 μm thick absorber and a Mo back contact. An increase of the *PCE* was not reached due to a reduction of

the other parameters. The results were used furthermore to find the characteristic growth parameters in a simple growth model. FDTD simulations were used to model the absorption within the CIGSe absorber layer of structured solar cells. The obtained absorption spectra match the obtained EQE spectra. The increase in absorption is likely caused by a scattering of the light at the structured front interface.

First attempts of scalable structuring processes were tested. Promising results were obtained using a chemical etched ZnO:Al layer as substrate. Larger gains are likely obtainable through a systematic variation of the structural parameters. Overall, different structures could be tested regarding their absorption enhancement, reliability in the processing, and the industrial applicability.

Several relevant problems could not be touched in this work. Industrial produced CIGSe solar cells usually use monolithically inter-connected structures, the implementation of such structures needs to be evaluated with the Al/ITO-based back contacts. Another important topic is the influence of alkali elements for ultrathin solar cells with the alternative back contact. The NaF PDT used in this work was not optimized in any way. Furthermore, heavier alkali elements could also be studied, which likely would enable higher efficiencies.

Appendix

Appendix A

Determination of optical constants from UV-VIS measurements

The following section will explain how the optical constants (refractive index n, extinction coefficient k) were extracted for the ITO layers from UV-VIS measurements.

The UV-VIS measurements provide the wavelength dependent transmission and reflectance of the sample (glass/ITO). Unfortunately, different combinations of n and k can lead to the same transmission and reflectivity of the sample, even when the thickness of the investigated layer is precisely known. The TMM was employed to determine possible values for n and k for the investigated layer. The reflectivity and transmission of the layer stacks were calculated for varying values for n and k of the ITO layer. The absolute deviation D of the calculated values from the measured values which will be defined by

$$D = |T_{Exp} - T_{Cal}| + |R_{Exp} - R_{Cal}|, \tag{A.1}$$

was calculated for each combination of n and k, with the transmittance T and the reflectivity R. T_{Exp}, and R_{Exp} describe the experimental values, while T_{Cal}, and R_{Cal} give the calculated values from the TMM.

Figure A.1 a) shows the lowest calculated absolute deviation for a specific value of n (with the k value obtaining the lowest deviation D). Figure A.1 b) shows the same representation for k. Some uncertainty can be seen for the determination of n at a wavelength of ~900 nm, due to a broad minimum. This problem is however less pronounced for shorter or longer wavelengths. The values for n in this region were obtained by drawing a continuous line between the results for longer wavelength and the results at shorter wavelengths. As a result, some uncertainty for the correct determination of n has to be assumed, especially for wavelengths around 900 nm.
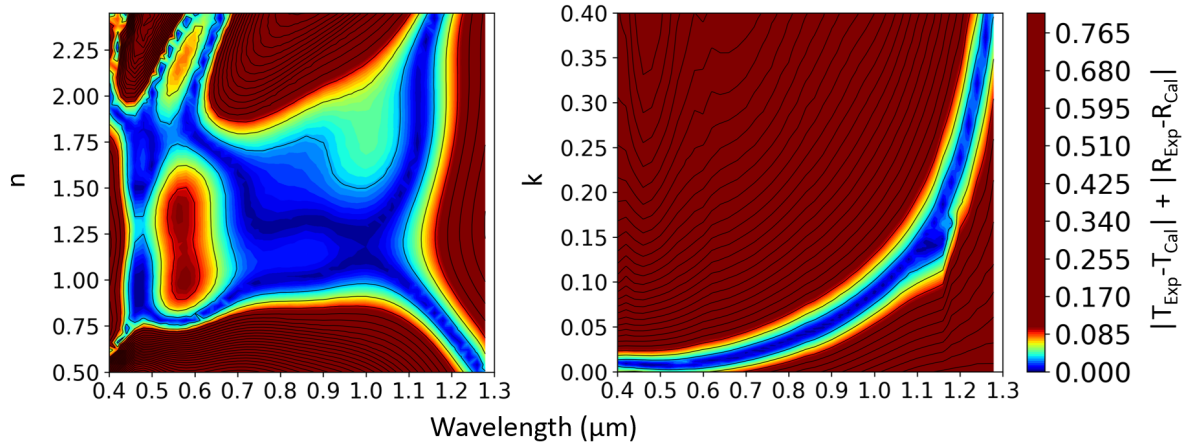
Figure A.1: Color plot showing the determined deviation D for varying values of n and k. Both n, and k have been varied in both graphs, the combination of n and k yielding the lowest value for D is used for the color axis.

These problems are much less pronounced for the determination of k, where a clear minimum can be seen for almost all wavelengths.

Measurements of higher precision might be obtainable through ellipsometry measurements. This method has additionally the information of the effect of the sample on the polarization of the incoming light. However, the determination of optical parameters from ellipsometry does rely the usage of a optical model describing the interaction of the media with the light. The correct determination of such a model can be challenging for an absorptive medium.

Appendix B

N1 signal derivation

The temperature dependence of the prefactor in the Arrhenius plot can be derived as follows. The admittance of the equivalent circuit of two diodes in series is given by

$$\frac{1}{Y_{total}} = \frac{1}{G_J + i\omega C_J} + \frac{1}{G_C + i\omega C_C}, \tag{B.1}$$

with the total admittance Y_{total}, the measurement frequency $\omega = 2\pi f$, the conductivity G, and the capacitance C. Quantities with the subscript C refer to the back contact diode while variables with J are associated with the junction diode at the front. The admittance of the sample is evaluated using an equivalent circuit comprised of a capacitor and resistor in parallel:

$$Y_{total} = G_{total} + i\omega C_{total} \tag{B.2}$$

The measured value C_{total} can be linked to Equation B.1 using a comparison of the imaginary part of both equations for Y. This leads to the following expression:

$$C_{total} = \frac{C_C G_J^2 + C_J G_C^2 + \omega^2 C_C C_J (C_C + C_J)}{(G_C + G_J)^2 + \omega^2 (C_C + C_J)^2} \tag{B.3}$$

The admittance measurements are evaluated by a calculation of the critical frequency ω_0, which is defined as

$$\omega_0 = max\left(-\omega \frac{dC}{d\omega}\right). \tag{B.4}$$

Applying Equation B.4 to Equation B.3 leads to

$$\omega_0 = \frac{G_J + G_C}{C_J + C_C}, \tag{B.5}$$

which is the essential equation to obtain the barrier height ϕ_B because of the temperature dependence of $G_C \sim exp(\frac{q\phi_B}{kT})$. Therefore ϕ_B can be determined from an Arrhenius plot. The equation can be further simplified using the condition $G_J \ll G_C$, which is usually applicable if the JV curve is not limited by the conductivity of the back contact, leading to

$$\omega_0 = \frac{G_C}{C_J + C_C}. \tag{B.6}$$

The Arrhenius plot requires the determination of the temperature dependence of G_J, C_C and C_J. An expression for G_C can be obtained from the current of the Schottky diode J_C using

$$G_C = \frac{dJ_C}{dV_C}, \tag{B.7}$$

where V_C denotes the voltage drop across the back contact. Several expression can be found in the literature to describe J_C, which are based on different assumptions about the limiting factor for the current transport through the Schottky diode. Herein, the expression of the so-called diffusion theory is employed, which is given by

$$J_C = q\mu_p E_{max} N_V exp\left(\frac{-q\phi_B}{kT}\right)\left[exp\left(\frac{qV_C}{kT}\right) - 1\right], \tag{B.8}$$

with the majority carrier mobility μ_p, the maximum of the electric field close to the Schottky diode denoted as E_{max} and N_V the effective density of states in the valence band. E_{max} can be expressed as

$$E_{max} = \sqrt{\frac{2q(\phi_i - V_C)N_A}{\varepsilon_s \varepsilon_0}}, \qquad (B.9)$$

containing the built-in voltage ϕ_i of the Schottky diode. Therefore G_J can be derived as

$$G_J = q\mu_p N_V exp(\frac{-q\phi_B}{kT})(\frac{d}{dV_C}[E_{max}][exp(\frac{qV_C}{kT}) - 1] + E_{max}\frac{d}{dV_C}[exp(\frac{qV_C}{kT}) - 1]), \qquad (B.10)$$

with

$$\frac{d}{dV_C}[E_{max}][exp(\frac{qV_C}{kT}) - 1] = \frac{-2qN_A}{\varepsilon_s \varepsilon_0}(\frac{2q(\phi_i - V_C)N_A}{\varepsilon_s \varepsilon_0})^{-1/2}[exp(\frac{qV_C}{kT}) - 1] = \frac{-2qN_A}{\varepsilon_s \varepsilon_0 E_{max}}[exp(\frac{qV_C}{kT}) - 1]$$
$$(B.11)$$

$$E_{max}\frac{d}{dV_C}[exp(\frac{qV_C}{kT}) - 1] = E_{max}\frac{q}{kT}exp(\frac{qV_C}{kT}). \qquad (B.12)$$

Equation B.10 can be further simplified under the assumption

$$\frac{2qN_A}{\varepsilon_s \varepsilon_0 E_{max}}[exp(\frac{qV_C}{kT}) - 1] \ll E_{max}\frac{q}{kT}exp(\frac{qV_C}{kT}). \qquad (B.13)$$

or equivalently

$$\frac{2N_A kT}{\varepsilon_s \varepsilon_0 E_{max}^2}[exp(\frac{qV_C}{kT}) - 1]/exp(\frac{qV_C}{kT}) \ll 1. \qquad (B.14)$$

Under the assumption $G_J \ll G_C$ only a small portion of the applied bias voltage will drop over the back contact. Inserting typical values ($N_A = 10^{16} \, cm^{-3}, T = 200 \, K, \phi_i = 0.2 \, V, V_C = 0.01 \, V, \varepsilon_s = 13.6$) leads to 0.04 for the left-hand side of Equation B.13, which is much smaller than 1. Hence it appears reasonable to neglect the contribution of $\frac{d}{dV_C}[E_{max}][exp(\frac{qV_C}{kT}) - 1]$ in Equation B.10 leading to the following expression for G_J:

$$G_J = q\mu_p N_V exp(\frac{-q\phi_B}{kT})E_{max}\frac{q}{kT}exp(\frac{qV_C}{kT}). \qquad (B.15)$$

The temperature dependence of the prefactor of the Arrhenius plot can be discussed using Equation B.6. The effective density of states is proportional to $T^{1.5}$. The temperature dependence of μ_p will depend on the specific sample and measurement temperature. C_C, C_J and E_{max} posses all some temperature dependence. However, the temperature dependence of those quantities is generally very small, as will be confirmed later by simulations. The temperature dependence of ω_0 can be expressed eventually as:

$$\omega_0 = \xi(T)exp(\frac{q(V_C - \phi_B)}{kT}) \, with \, \xi(T) = const \cdot \mu_p(T) \cdot T^{0.5}. \qquad (B.16)$$
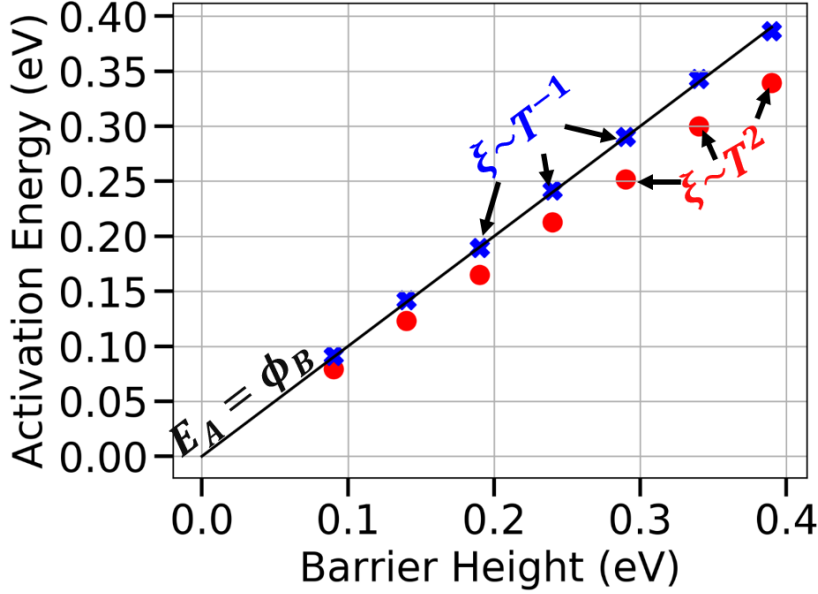
Figure B.1: Determined activation energy E_a of solar cells with different Schottky barrier heights ϕ_B. The activation energies were obtained using an Arrhenius plot according to Equation B.16 from calculated capacitance-frequency curves. The crosses were calculated using a temperature-dependent prefactor of $\xi(T) = const * T^{-1}$ while the points are calculated using a prefactor of $\xi(T) = const * T^2$. The black line is plotted as a visual guide.

Were $\mu_p(T)$ represents the temperature dependence of the majority carrier mobility. In total the barrier height can be obtained by linear fitting of a $ln(\omega_0 T / \mu_p(T))$ vs. T^{-1} plot. The voltage drop on the back contact can be neglected as long as $G_J \ll G_C$ is valid. The derived expression was tested by calculating temperature-dependent capacity-frequency curves using AFORS-HET. These curves were evaluated using an Arrhenius plot with the temperature dependence of Equation B.16. The effective carrier densities N_{eff} and mobilities μ have been adapted for each temperature using $N_{eff} = N_{eff}(300\,\mathrm{K}) \cdot T^{1.5}$ and $\mu = \mu(300\,\mathrm{K}) \cdot T^{-1.5}$ for both carrier types. The temperature dependence of the mobilities represents the case that the mobilities are limited by acoustic deformation potential scattering. The results are given in Figure B.1 as a function of the Schottky barrier height. The maximum deviation between the actual and determined barrier height is 1% and therefore the derived prefactor appears to be valid and the temperature dependence of C_C, C_J and E_{max} can indeed be neglected. Despite originating from different effects, the analysis of defect contributions to the admittance spectra is quite similar to the analysis for the determination of the back contact barrier height. The Arrhenius plot is constructed in the same way, with the only difference that the prefactor is $\xi(T) = const \cdot T^2$. This factor is quite often used in the analysis of admittance spectra. Hence this temperature dependence was also added to Figure 10 in order to point out how much difference in the determined activation energy is obtained by using this prefactor. The relative deviation of the determined activation energy using this prefactor in relation to the barrier height is about 13%.
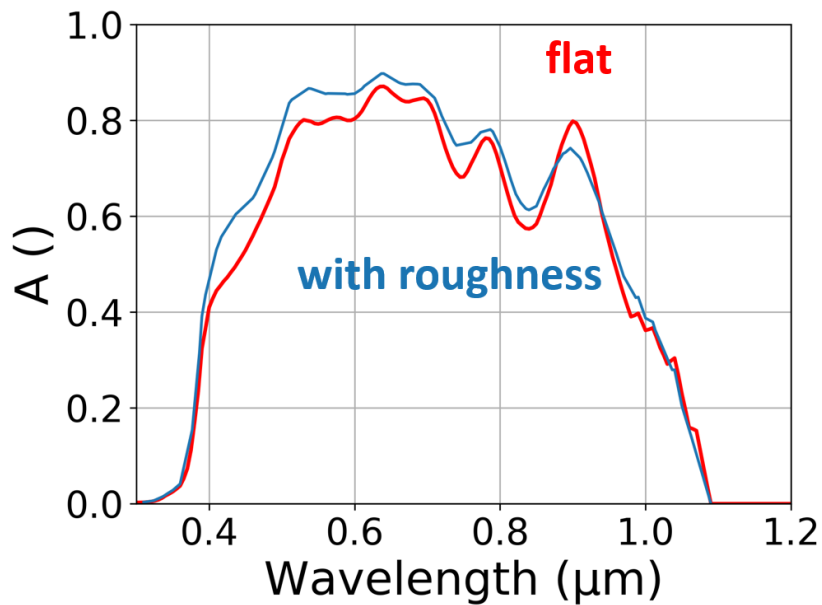
Figure C.1: Comparison of the calculated absorption within the CIGSe layer for a cell with and without the interface roughness. The calculations have been performed using 2D FDTD calculation using layer dimension as found in the experiment but with a constant GGI of 0.37.

Appendix C

Effect of the surface roughness on the solar cell reflectivity

The effect of the surface roughness was evaluated using 2D simulations using the software MEEP. A SEM cross section of the unstructured reference of set 1 (Section 5.5) was used as an input for the calculations. The absorption within the CIGSe was calculated and compared with the result for a completely flat solar cell with the same thickness. The GGI was set to a constant value of 0.37 for simplicity.

The absorption within the CIGSe is overall increased for the rough sample due to a reduction of the reflectivity of the sample. The absorption peak are furthermore reduced for the rough sample.
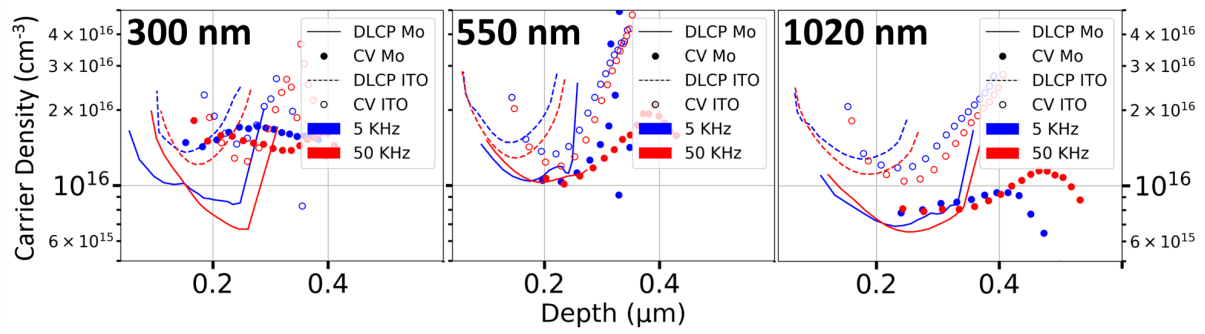
Figure D.1: Charge carrier densities determined for the different sample types from CV and DLCP measurements at frequencies of 5 kHz and 50 kHz.

Appendix D

Determination of the charge carrier density

Figure D shows in comparison to Figure 4.11, additional the results for at a measurements frequency of 5 KHz. The shapes of the curves remain quite similar between the two measurement frequencies are obtained with the higher measurement frequency. Slightly higher carrier densities are obtained at the lower frequency.

Appendix E

Further admittance measurements on ITO-based samples

Figure E shows the results of further admittance measurements on ITO-based samples. No N1 signal is visible in both samples. Figure E a) displays admittance measurements of the sample with a 50 nm ITO diffusion barrier from Section 3.4. The curves are decaying with increasing frequencies for all temperatures. Comparing the curves with the other results, this signal might be identical to the signal U2. The other sample has ITO as electrical back contact, with the CIGSe deposited at 480 °C and an absorber thickness of 1.1 µm. This sample shows the U1 signal and the apparent decrease of capacity at higher frequencies associated with the series resistance.

Appendix F

Summary of employed simulation parameters

Table F.1 gives the model parameters used for the simulation in Figure 4.17.

The simulation parameters used for the tunneling current between the CIGSe and the ITO in Section 4.9 can be found in Table F.2.

Figure E.1: Capacity frequency measurements of: a) The 50 nm ITO diffusion barrier sample from Section 3.4. b) An ITO-based sample with an absorber thickness 1.1 μm of deposited at 480 °C.

Table F.1: Model parameters for each solar cell layer used in the AC simulations displayed in Figure 4.17.
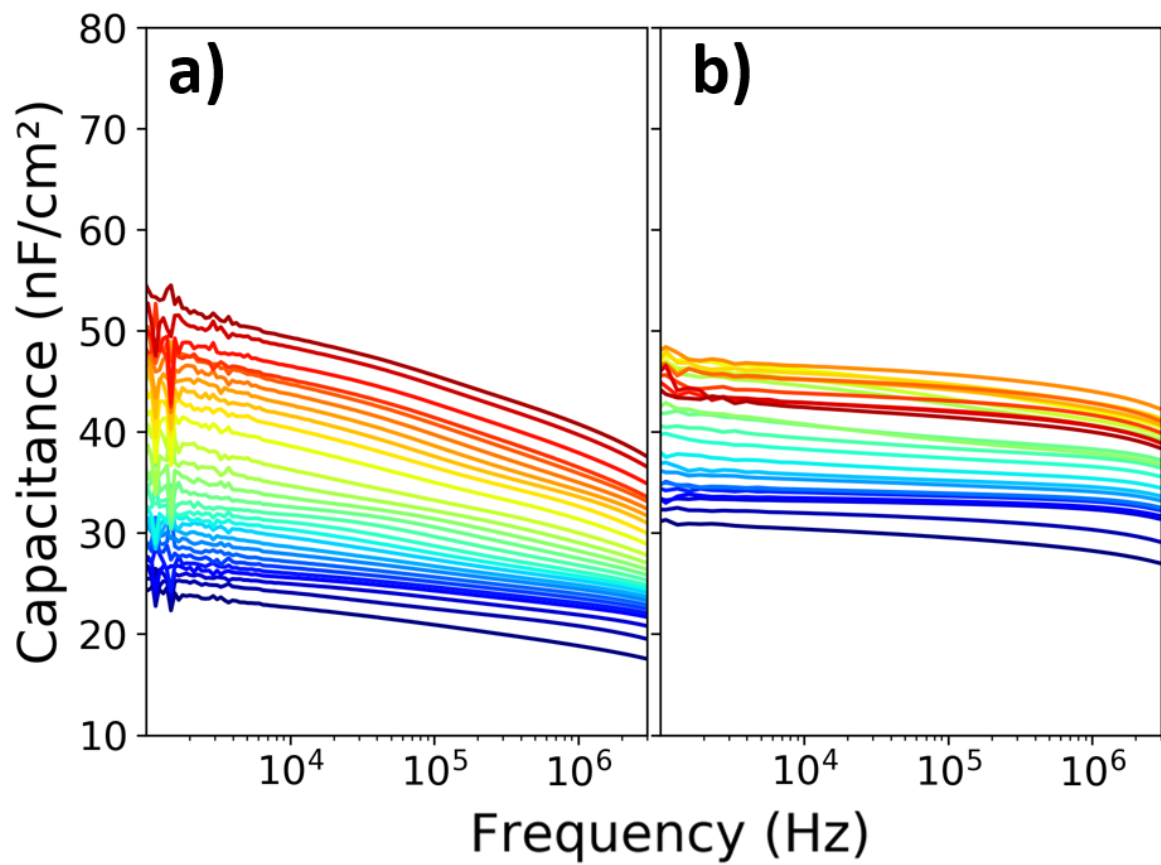
	ITO (Front)	ZnO	CdS	CIGSe
d (nm)	200	100	45	300
ε ()	9	9	10	13.6
χ (eV)	4.1	4.1	4	4.122
E_g (eV)	4	3.3	2.4	1.218
N_C (cm^{-3})	$2.2 \cdot 10^{18}$	$2.2 \cdot 10^{18}$	$2.2 \cdot 10^{18}$	$2.2 \cdot 10^{18}$
N_V (cm^{-3})	$1.8 \cdot 10^{19}$	$1.8 \cdot 10^{19}$	$1.8 \cdot 10^{19}$	$1.8 \cdot 10^{19}$
μ_n (cm^2/(Vs))	100	100	100	40
μ_p (cm^2/(Vs))	100	100	100	1
N_a (cm^{-3})	0	0	0	$2 \cdot 10^{16}$
N_d (cm^{-3})	10^{19}	10^{18}	10^{17}	0
v_e (cm/s)	10^7	10^7	10^7	10^7
v_h (cm/s)	10^7	10^7	10^7	10^7
Defect				
Type	acceptor	-	-	donor
E_d-E_v (eV)	1.7	-	-	midgap
Density (cm^{-3})	10^{14}	-	-	10^{13}
c_n (cm^2)	10^{-14}	-	-	$2 \cdot 10^{-11}$
c_p (cm^2)	10^{-14}	-	-	10^{-12}

Table F.2: Model parameters employed for the current transport within a ITO-based solar cell.

	ITO (Front)	ZnO	CdS	CIGSe	p++ layer	ITO (Rear)
d (nm)	200	200	45	300	1	200
ε ()	9	9	10	13.6	13.6	9
χ (eV)	4.1	4.1	4	4.122	4.122	4.5
E_g (eV)	4	3.3	2.4	1.218	1.218	4
N_C (cm^{-3})	$2.2 \cdot 10^{18}$	$2.2 \cdot 10^{18}$	$2.2 \cdot 10^{18}$	$2.2 \cdot 10^{18}$	$2.2 \cdot 10^{18}$	$2.2 \cdot 10^{18}$
N_V (cm^{-3})	$1.8 \cdot 10^{19}$	$1.8 \cdot 10^{19}$	$1.8 \cdot 10^{19}$	$1.8 \cdot 10^{19}$	$1.8 \cdot 10^{19}$	$1.8 \cdot 10^{19}$
μ_n (cm^2/(Vs))	100	100	100	60	60	100
μ_p (cm^2/(Vs))	100	100	100	1	1	100
N_a (cm^{-3})	0	0	0	$1 \cdot 10^{16}$	$1 \cdot 10^{16}$	0
N_d (cm^{-3})	10^{20}	10^{16}	10^{17}	0	0	10^{20}
v_e (cm/s)	10^7	10^7	10^7	10^7	10^7	10^7
v_h (cm/s)	10^7	10^7	10^7	10^7	10^7	10^7
Defect						
Type	acceptor	-	-	donor	don./acc. (Gauss dis.)	acceptor
E_d-E_v (eV)	1.7	-	-	midgap	midgap/ 0.3($\sigma = 0.1$)	1.7
Density (cm^{-3})	10^{14}	-	-	10^{13}	10^{13}/varied	10^{14}
c_n (cm^2)	10^{-14}	-	-	$2 \cdot 10^{-11}$	$2 \cdot 10^{-11}$/10^{-9}	10^{-14}
c_p (cm^2)	10^{-14}	-	-	10^{-12}	10^{-12}/10^{-9}	10^{-14}

Appendix G

Complete EQE sets of LIL based structures

Figure G.1 shows the complete data set of the samples presented in Section 5.5.

Appendix H

Details about the layer growth calculations

A schematic explanation of the layer growth calculation algorithm was already given in Section 5.3. The developed algorithm for the calculations will be explained in the following. The height profile of the structure was chosen to be represented by a 2D array of the structure height at a certain position $H(x_n, y_m)$, where x_n and y_m define the lateral position on a Cartesian axis system (n and m are the integer position within the array). Such a representation is capable to represent arbitrary surface structures, as long as the structure does not possess any overhang or similar features. Two different growth modes had to be implemented.

The implementation of the vertical growth mode is trivial. The new surface height after a sub layer growth H_{new} is given by $H_{new}(x_n, y_m) = H(x_n, y_m) + d$ for all positions of the array.

The implementation of the normal growth mode is more challenging. A Minkowski addition was used for this purpose. The Minkowski addition will be explained in the following with the help of Figure H.1, which shows the addition of a circle (A) and a triangle (B). The new object (displayed in green) is obtained by a "stamping" of object A at each position of B. The same result can be obtained when object B is "stamped" at each position, which is part of A. This geometrical operation gives the desired behavior as can be seen in the example. The Minkowski addition of the surface structure with a sphere is rather straightforward for an array representation of the structure.
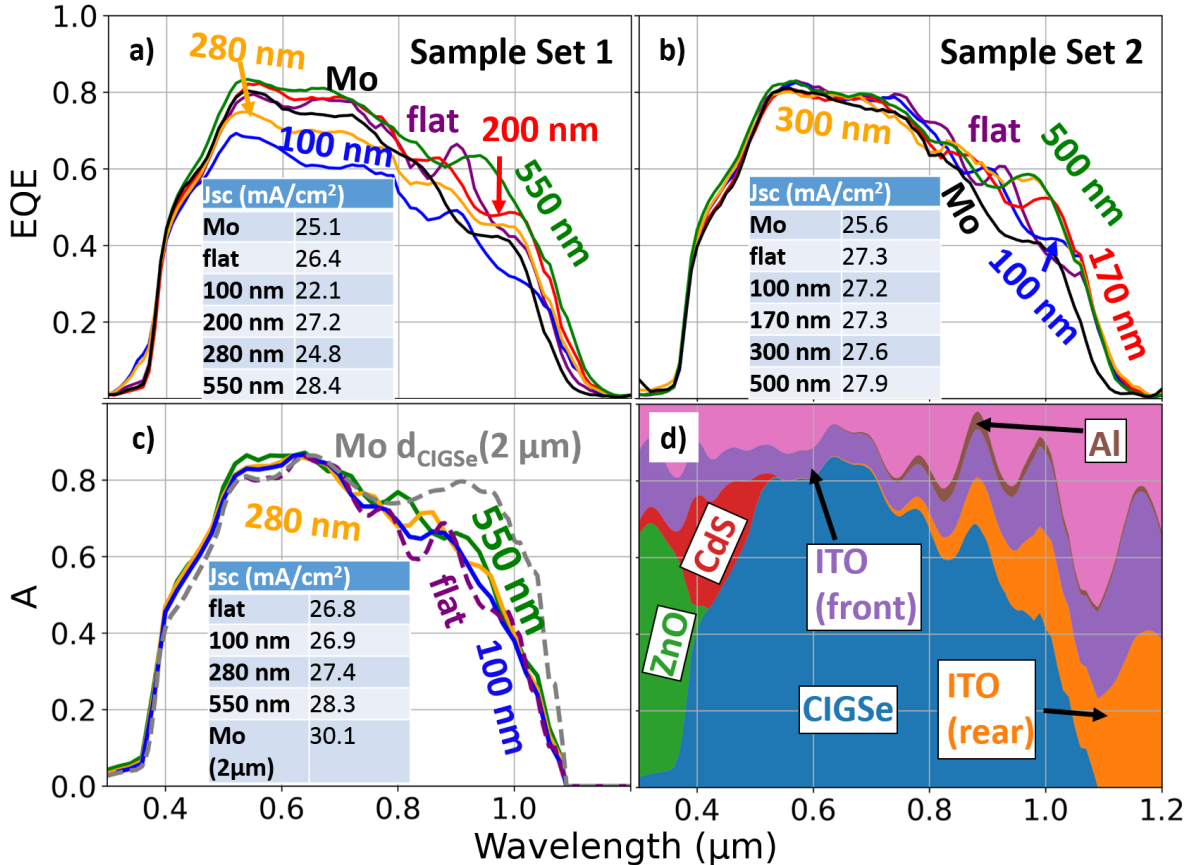
Figure G.1: External quantum efficiency of solar cells with different back contacts for sample set 1 (a) and sample set 2 (b). An additional CIGSe solar cell with a 2.8 µm absorber and a Mo back contact is shown in both figures for comparison. (c) Calculated absorption within the CIGSe layer of a complete solar cell. The dashed lines are calculated using the transfer-matrix-method for an unstructured sample with an Al/ITO back contact (purple), a Mo back contact (black) and a solar cell with Mo back contact with a 2.8 µm absorber (grey). The other curves are from FDTD calculations for the structural dimensions of sample set 1. (d) Calculated relative absorption within the separate solar cell layers for an unstructured solar cell with Al/ITO back contact.

Figure H.1: Minkowski sum (green) of a circle (orange) and a triangle (blue).

The projection of spheres has to be calculated from all adjacent positions of the structure for the Minkowski addition. The algorithm is iterating over all array elements and saves the newly calculated height for each point in a new array. The projection of a sphere origination from an arbitrary position $H(x_k, y_l)$ is given by

$$H_{new}(x_n, y_m) = H(x_k, y_l) + \sqrt{d} - (n-k)^2 \Delta x - (m-l)^2 \Delta x, \tag{H.1}$$

where k and l denote the array index of the other position, and with Δx being the spatial resolution of the array elements. Equation H.1 is only valid when the lateral distance between the two regarded positions is less than d (otherwise the sphere cannot reach the position). The projection is calculated for all position, which fulfill this condition. The highest calculated value is then saved in the new array $H_{new}(x_n, y_m)$.

The calculated area was chosen to be slightly larger than the size of an elementary element of the periodic structure. Artifacts at the border of the calculated area can be avoided this way.

Appendix I

Technical details of the FDTD simulations

FDTD simulations have been performed with the software package MEEP. The spatial resolution was set to 5 nm. A plane wave was positioned at a distance of 1 μm in front of the structure. A perfectly matched layer (PML) with a thickness of 1 μm was employed at the edges of the simulation area in forward and backward direction to avoid reflections at the borders. Periodic conditions have been used along the other four directions. The convergence of the system was tested prior to the simulations by the calculation of the absorbance within the separate layers after different simulation times. An appropriate time according to this testing was then used for all simulations.

Appendix J

Overview of the highest PCE solar cells obtained with the Al/ITO back contact

This section gives a summary on the solar cells with the highest obtained *PCE* values with Al/ITO-based solar cells, for three different absorber thicknesses. The CIGSe was deposited with a maximum deposition temperature of 480 °C and 2 nm of NaF PDT for all samples. The layer thicknesses and process conditions are similar to the ones used in Section 3.4, while an ITO barrier layer thickness of 200 nm was used for the Al/ITO-based samples.

The JV and EQE curves of the sample set can be seen in Figure J.1, while the extracted parameters are given in Table J.1. The V_{OC} values of the Al/ITO-based samples are on a similar level for all samples, while a reduction of the V_{OC} values can be seen for the Mo-based samples with decreasing absorber thickness. The *FF* are overall on a similar level, the difference observable
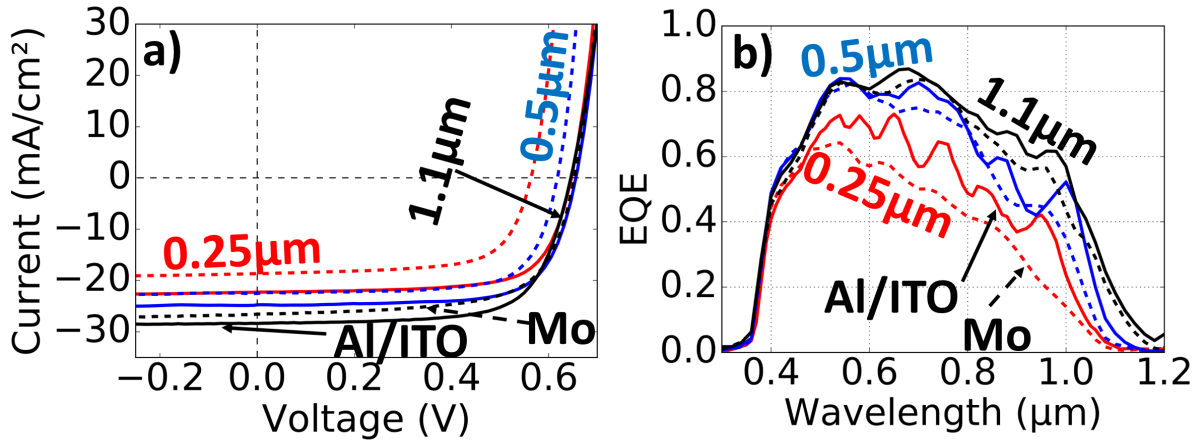
Figure J.1: a) Illuminated JV curves of solar cells with a Mo back contact (full lines) or an Al/ITO back contact (dashed lines) for solar cells with a 0.25 μm (red), 0.5 μm (blue), 1.1 μm (black) absorber layer thickness. b) Corresponding EQE curves to a).

Table J.1: Extracted solar cell parameters for the measurements presented in Figure J.1.

d_{CIGSe} (μm)	BC	V_{OC} (mV)	J_{SC} (mA/cm^2)	J_{SC} (EQE) (mA/cm^2)	FF (%)	PCE (%)	PCE (EQE) (%)
0.25	Mo	564	18.7	18	68.2	7.1	6.9
	Al/ITO	647	22.3	23.5	70.9	10.2	10.7
0.5	Mo	618	22.5	25.3	71.4	10.0	11.2
	Al/ITO	656	24.8	26.9	71.7	11.6	12.6
1.1	Mo	653	26.6	27.8	66.7	11.6	12.1
	Al/ITO	646	28.3	29.6	69.0	12.7	13.1

are likely explainable by process scattering. The J_{SC} values decrease with the absorber thickness. The Al-based samples show higher J_{SC} values for all samples. The relative difference between the two sample types is increasing with decreasing absorber layer thickness.

The influence of the increased reflectivity at the (ITO/Al)/CIGSe interfaces in comparison to the Mo/CIGSe interface can be clearly seen in the EQE curves. A larger number of peaks is visible for the Al-based samples, especially for the thinnest absorber layer thickness.

Appendix K

Comparison of the calculated 3D structure with the experimental structure

Figure K.1 shows the surface lines of all calculated layers inside the corresponding SEM cross section for the 1.96 μm pitch structure with a structure height of 200 nm.
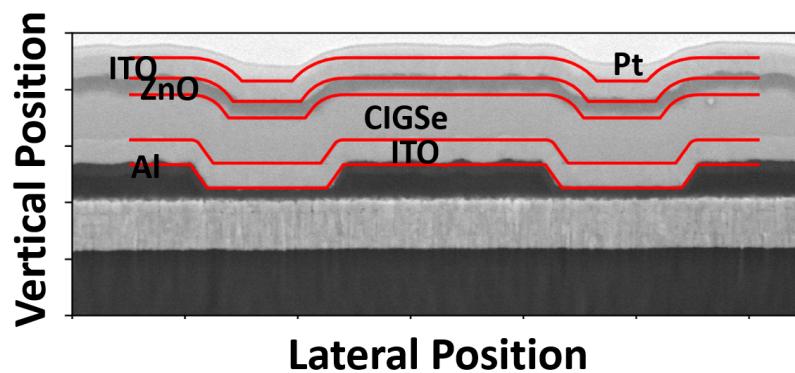

Figure K.1: Projection of the calculated 3D structure (red lines) inside the cross section for the 1.96 μm pitch structure with a structure height of 200 nm.
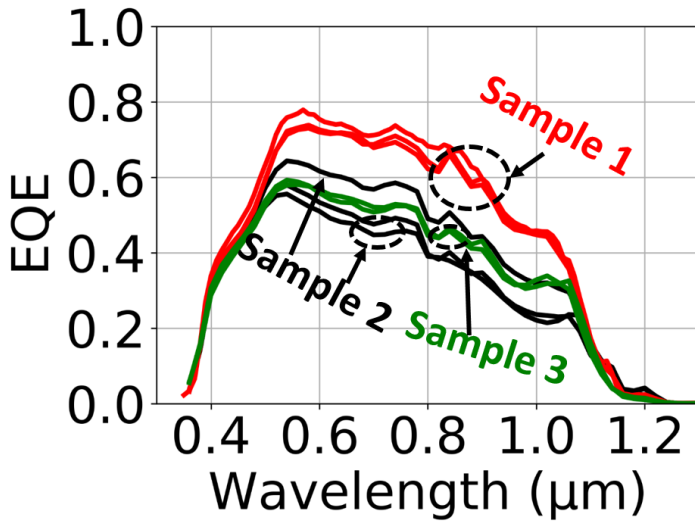
Figure L.1: Measured EQE curves of three different samples from sample set 3. Each color represents EQE curves belonging to the same sample.

Appendix L

Preparation of further LIL-based structures.

Additional samples with a structured back contact were prepared using the LIL method. Two batches, which will be referred as set 3 and set 4 will be presented in the following. The pitch was reduced to 1 μm, with a structure height of 300 nm. The thickness of both the front and rear ITO layer was reduced to approximately 100 nm. The other process parameters were identical to the samples shown in Section 5.2. Also, no metal grid was applied to those samples due to the usage of very small sample areas. All displayed solar cells possess a parallel resistance well above 10 kΩ.

The structured solar cells exhibited a strong scattering of the EQE curves (and J_{SC} values), between different solar cells on the same sample, and another scattering between samples processed in the same deposition run. This can be seen in Figure L.1, which shows several EQE curves on different solar cells distributed over three samples, which were processed simultaneously. A lot of the EQE curves show a quite poor performance, with the EQE curve reduced over almost the full spectral range. The EQE curves appear to be systematically different between the three samples. The losses appear to be larger at longer wavelengths. A similar EQE

Table L.1: Extracted solar cell parameters for set 3 and set 4. The J_{SC} values were obtained from EQE measurements, while the FF and V_{OC} was obtained from JV measurements.

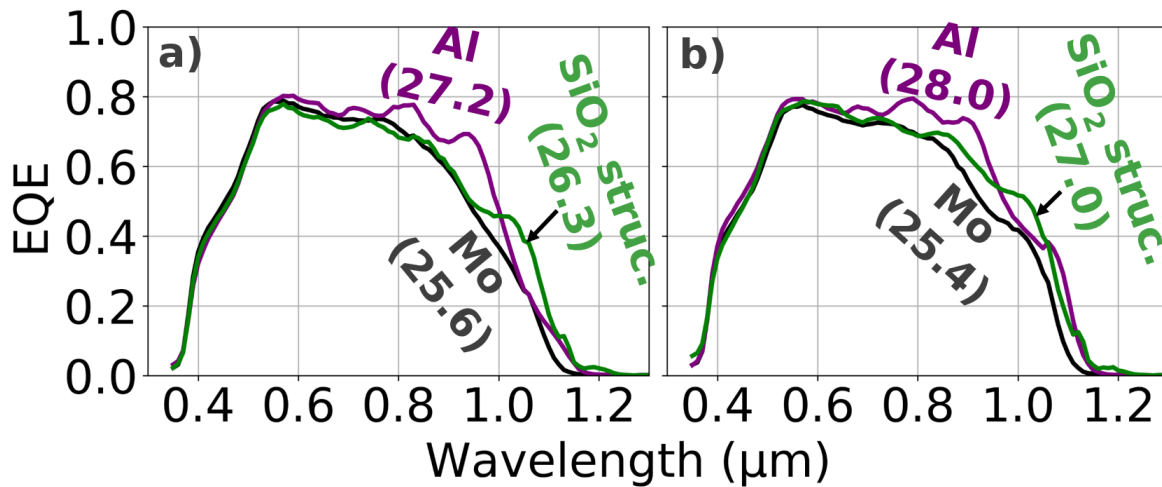| Back contact	V_{OC} (mV)	FF (%)	J_{SC} (mA/cm^2)	PCE (%)
Set 3				
Mo	600	69.3	25.6	10.6
Al/ITO	587	62.8	27.2	10.0
(SiO$_2$ structure)/Al/ITO	529	61.1	26.3	8.5
Set 4				
Mo	590	67.8	25.4	10.2
Al/ITO	561	58.5	28.0	9.2
(SiO$_2$ structure)/Al/ITO	501	50.1	27.0	6.8

Figure L.2: Measured EQE curves of sample set 3 (a)) and set 4 (b)). The values in the brackets give the calculated J_{SC} values in units of mA/cm^2.

value is visible at a wavelength of 500 nm, while the lowest EQE at 1000 nm is roughly only half of the highest EQE value at this wavelength.

Solar cell parameters of the best solar cells obtained in the two batches are given in Table L.1. The Mo references show V_{OC} values around 600 mV, which is a similar value to the comparable samples in this work. The corresponding FF values are slightly below 70% for both Mo reference samples. The J_{SC} value of the unstructured Al/ITO-based samples are by 1.6 mA/cm^2 (set 3) and by 2.6 mA/cm^2 (set 4) higher than for the corresponding Mo-reference. However, both the FF and the V_{OC} values are considerably reduced, especially in set 4. This effect is even more pronounced for the structured solar cell, with very poor V_{OC} values and a very low FF for set 4. The short circuit density of the structured solar cells are lower than the corresponding unstructured Al/ITO samples. The PCE values are decreased for the Al/ITO-based samples, compared to the Mo-references, due to poor FF and V_{OC} values.

Corresponding EQE curves can be seen in Figure L.2. The EQE of the flat samples with the Al/ITO back contact is higher than the EQE of the Mo references for wavelengths above ~700 nm. The structured solar cells surpass the EQE of the unstructured solar cells with the Al/ITO back contact only in a small region around 1 µm. The EQE of the structured solar cells is

considerably lower than the EQE of the unstructured reference outside this region.

FIB measurements were conducted on structured solar cells, as can be seen in Figure 5.8. Cracks can clearly be seen, located mostly in the rear ITO layer, but to some extent also in the Al layer. The cracks are all located in the inclined region of the structure. It makes sense that those cracks are mostly visible in the hole region/inclined portion of the structure. The mechanical stress induced by different thermal expansion coefficients of the materials is assumed to be highest in this region.

The presence of this cracks could explain the strong scattering of the results. Cracks can lead to a local diffusion of the Al in the absorber layer and/or lead to a selenization of the Al. It might also affect the structure of the ITO, which might lead to the formation of more Ga_2O_3. The clear visibility of cracks in combination with the strong scattering in Figure L.1, raises the question if the best EQE results in Figure L.2 are still affected by carrier collection problems. The results obtained with the unstructured Al/ITO back contact are also rather poor. This indicated that the Al/ITO-based solar cells did have already some systematic problems. Hence the experiment would have to be repeated, maybe with thicker ITO layers, to test if the observed problems are related to the reduced ITO thickness at the back contact.

Bibliography

[1] "Paris Agreement" 2015, United Nations Treaty Collection, Chapter XXVII 7. d. Tech. rep., Paris.

[2] Kost C, Shammugan S, Fluri V, Peper D, Memar A, Schlegl T. 2021 Levelized Cost of Electricity: Renewable Energy Technologies. Tech. rep., Fraunhofer Institute for Solar Energy Systems ISE, Freiburg. (doi:10.13140/RG.2.2.22457.08800).

[3] Birant G, de Wild J, Meuris M, Poortmans J, Vermang B. 2019 Dielectric-based rear surface passivation approaches for Cu(In,Ga)Se 2 solar cells-A review. *Applied Sciences (Switzerland)* **9**, 4. (doi:10.3390/app9040677).

[4] Krc J, Sever M, Campa A, Lokar Z, Lipovsek B, Topic M. 2017 Optical confinement in chalcopyrite based solar cells. *Thin Solid Films* **633**, 193–201. (doi:10.1016/j.tsf.2016. 08.056).

[5] Nakada T, Hirabayashi Y, Tokado T, Ohmori D, Mise T. 2004 Novel device structure for Cu(In,Ga)Se2 thin film solar cells using transparent conducting oxide back and front contacts. *Solar Energy* **77**, 6, 739–747. (doi:10.1016/j.solener.2004.08.010).

[6] Nakada T. 2005 Microstructural and diffusion properties of CIGS thin film solar cells fabricated using transparent conducting oxide back contacts. *Thin Solid Films* **480-481**, 419–425. (doi:10.1016/j.tsf.2004.11.142).

[7] Mollica F, Jubault M, Donsanti F, Loubat A, Bouttemy M, Etcheberry A, Naghavi N. 2017 Light absorption enhancement in ultra-thin Cu(In,Ga)Se2 solar cells by substituting the back-contact with a transparent conducting oxide based reflector. *Thin Solid Films* **633**, 202–207. (doi:10.1016/j.tsf.2016.10.006).

[8] Keller J, Shariati Nilsson N, Aijaz A, Riekehr L, Kubart T, Edoff M, Törndahl T. 2018 Using hydrogen-doped In2O3 films as a transparent back contact in (Ag,Cu)(In,Ga)Se2 solar cells. *Progress in Photovoltaics: Research and Applications* **26**, 3, 159–170. (doi: 10.1002/pip.2977).

[9] Keller J, Chen WC, Riekehr L, Kubart T, Törndahl T, Edoff M. 2018 Bifacial Cu(In,Ga)Se2 solar cells using hydrogen-doped In2O3 films as a transparent back contact. *Progress in Photovoltaics: Research and Applications* **26**, 10, 846–858. (doi: 10.1002/pip.3025).

[10] Gouillart L, Cattoni A, Goffard J, Donsanti F, Patriarche G, Jubault M, Naghavi N, Collin S. 2019 Development of reflective back contacts for high-efficiency ultrathin Cu(In,Ga)Se 2 solar cells. *Thin Solid Films* **672**, January 2019, 1–6. (doi:10.1016/j. tsf.2018.12.041).

[11] Gouillart L, Cattoni A, Chen WC, Goffard J, Riekehr L, Keller J, Jubault M, Naghavi N, Edoff M, Collin S. 2021 Interface engineering of ultrathin Cu(In,Ga)Se2 solar cells on reflective back contacts. *Progress in Photovoltaics: Research and Applications* **29**, 2, 212–221. (doi:10.1002/pip.3359).

[12] Würfel P. 2005 *Physics of Solar Cells*. Weinheim, Germany: Wiley, 1 ed. (doi:10.1002/9783527618545).

[13] Jarzembowski E, Syrowatka F, Kaufmann K, Fränzel W, Hölscher T, Scheer R. 2015 The influence of sodium on the molybdenum/Cu(In,Ga)Se2 interface recombination velocity, determined by time resolved photoluminescence. *Applied Physics Letters* **107**, 5. (doi:10.1063/1.4928187).

[14] Scheer R, Schock HW. 2011 *Chalcogenide Photovoltaics*. June. Weinheim, Germany: Wiley-VCH Verlag GmbH & Co. KGaA. (doi:10.1002/9783527633708).

[15] Guillemoles JF, Kirchartz T, Cahen D, Rau U. 2019 Solar Energy Conversion and the Shockley-Queisser Model, a Guide for the Perplexed , Table 1, 1–16.

[16] "Unit cell of the CIGSe chalcopyrite structure" from https://en.wikipedia.org/wiki/Copper_indium_gallium_selenide_solar_cell (23.11.2022).

[17] Abou-Ras D, Nikolaeva A, Caicedo Dávila S, Krause M, Guthrey H, Al-Jassim M, Morawski M, Scheer R. 2019 No Evidence for Passivation Effects of Na and K at Grain Boundaries in Polycrystalline Cu(In,Ga)Se2 Thin Films for Solar Cells. *Solar RRL* **3**, 8, 1–7. (doi:10.1002/solr.201900095).

[18] Zhang L, He Q, Jiang WL, Liu FF, Li CJ, Sun Y. 2009 Effects of substrate temperature on the structural and electrical properties of Cu(In,Ga)Se2 thin films. *Solar Energy Materials and Solar Cells* **93**, 1, 114–118. (doi:10.1016/j.solmat.2008.09.002).

[19] Jung S, Ahn SJ, Yun JH, Gwak J, Kim D, Yoon K. 2010 Effects of Ga contents on properties of CIGS thin films and solar cells fabricated by co-evaporation technique. *Current Applied Physics* **10**, 4, 990–996. (doi:10.1016/j.cap.2009.11.082).

[20] Yin G, Manley P, Schmid M. 2014 Influence of substrate and its temperature on the optical constants of CuIn1-xGaxSe2 thin films. *Journal of Physics D: Applied Physics* **47**, 13. (doi:10.1088/0022-3727/47/13/135101).

[21] Jehl Z, Erfurth F, Lombez L, Gerard I, Bouttemy M, Tran-Van P, Etcheberry A, Voorwinden G, Dimmler B, Wischmann W, *et al.* 2010 INFLUENCE OF THE SURFACE ROUGHNESS ON CIGS-BASED SOLAR CELL PARAMETERS Z. *International Institute for Environment and Development* **07/80**, 2, 125.

[22] Orgassa K. 2004 *Coherent optical analysis Of the Zno/Cds/Cu(In,Ga)Se2 thin film solar cell*. Aachen: Shaker Verlag.

[23] Guanchao Y. 2015 *Preparation of Ultra-thin CuIn 1-x Ga x Se 2 Solar Cells and Their Light Absorption Enhancement*. Ph.D. thesis, Technical University Berlin.

[24] Vermang B, Watjen JT, Frisk C, Fjallstrom V, Rostvall F, Edoff M, Salome P, Borme J, Nicoara N, Sadewasser S. 2014 Introduction of Si PERC rear contacting design to boost efficiency of Cu(In,Ga)Se2solar cells. *IEEE Journal of Photovoltaics* **4**, 6, 1644–1649. (doi:10.1109/JPHOTOV.2014.2350696).

[25] Dingemans G, Terlinden NM, Pierreux D, Profijt HB, Van De Sanden MC, Kessels WM. 2011 Influence of the oxidant on the chemical and field-effect passivation of Si by ALD Al2O3. *Electrochemical and Solid-State Letters* **14**, 1, 10–14. (doi:10.1149/1.3501970).

[26] Dingemans G, Einsele F, Beyer W, Van De Sanden MC, Kessels WM. 2012 Influence of annealing and Al2O3 properties on the hydrogen-induced passivation of the Si/SiO2 interface. *Journal of Applied Physics* **111**, 9. (doi:10.1063/1.4709729).

[27] Hoex B, Gielis JJ, Van De Sanden MC, Kessels WM. 2008 On the c-Si surface passivation mechanism by the negative-charge-dielectric Al2O3. *Journal of Applied Physics* **104**, 11. (doi:10.1063/1.3021091).

[28] Werner F, Stals W, Görtzen R, Veith B, Brendel R, Schmidt J. 2011 High-rate atomic layer deposition of Al2O3 for the surface passivation of Si solar cells. *Energy Procedia* **8**, April, 301–306. (doi:10.1016/j.egypro.2011.06.140).

[29] Vermang B, Wätjen JT, Fjällström V, Rostvall F, Edoff M, Gunnarsson R, Pilch I, Helmersson U, Kotipalli R, Henry F, *et al.* 2015 Highly reflective rear surface passivation design for ultra-thin Cu(In,Ga)Se2 solar cells. *Thin Solid Films* **582**, 300–303. (doi:10.1016/j.tsf.2014.10.050).

[30] Vermang B, Fjallström V, Gao X, Edoff M. 2014 Improved rear surface passivation of Cu(In,Ga)Se2 solar cells: A combination of an Al2O3 rear surface passivation layer and nanosized local rear point contacts. *IEEE Journal of Photovoltaics* **4**, 1, 486–492. (doi: 10.1109/JPHOTOV.2013.2287769).

[31] Vermang B, Fjällström V, Pettersson J, Salomé P, Edoff M. 2013 Development of rear surface passivated Cu(In,Ga)Se2 thin film solar cells with nano-sized local rear point contacts. *Solar Energy Materials and Solar Cells* **117**, 505–511. (doi:10.1016/j.solmat.2013.07.025).

[32] Kotipalli R, Vermang B, Joel J, Rajkumar R, Edoff M, Flandre D. 2015 Investigating the electronic properties of Al2O3/Cu(In,Ga)Se2 interface. *AIP Advances* **5**, 10. (doi: 10.1063/1.4932512).

[33] Salomé PM, Vermang B, Ribeiro-Andrade R, Teixeira JP, Cunha JM, Mendes MJ, Haque S, Borme J, Águas H, Fortunato E, *et al.* 2018 Passivation of Interfaces in Thin Film Solar Cells: Understanding the Effects of a Nanostructured Rear Point Contact Layer. *Advanced Materials Interfaces* **5**, 2, 1–10. (doi:10.1002/admi.201701101).

[34] Van Lare C, Lenzmann F, Verschuuren MA, Polman A. 2015 Dielectric Scattering Patterns for Efficient Light Trapping in Thin-Film Solar Cells. *Nano Letters* **15**, 8, 4846–4852. (doi:10.1021/nl5045583).

[35] Vermang B, Wätjen JT, Fjällström V, Rostvall F, Edoff M, Kotipalli R, Henry F, Flandre D. 2014 Employing Si solar cell technology to increase efficiency of ultrathin Cu(In,Ga)Se 2 solar cells. *Progress in Photovoltaics: Research and Applications* **22**, 10, 1023–1029. (doi:10.1002/pip.2527).

[36] Jarzembowski E, Fuhrmann B, Leipner H, Fränzel W, Scheer R. 2017 Ultrathin Cu(In,Ga)Se2 solar cells with point-like back contact in experiment and simulation. *Thin Solid Films* **633**, 61–65. (doi:10.1016/j.tsf.2016.11.003).

[37] Heinemann MD, Ruske F, Greiner D, Jeong AR, Rusu M, Rech B, Schlatmann R, Kaufmann CA. 2016 Advantageous light management in Cu(In,Ga)Se2 superstrate solar cells. *Solar Energy Materials and Solar Cells* **150**, 76–81. (doi:10.1016/j.solmat.2016.02.005).

[38] Bissig B, Carron R, Greuter L, Nishiwaki S, Avancini E, Andres C, Feurer T, Buecheler S, Tiwari AN. 2018 Novel back contact reflector for high efficiency and double-graded Cu(In,Ga)Se2 thin-film solar cells. *Progress in Photovoltaics: Research and Applications* **26**, 11, 894–900. (doi:10.1002/pip.3029).

[39] Sim JK, Kang S, Nandi R, Jo JY, Jeong KU, Lee CR. 2018 Implementation of graphene as hole transport electrode in flexible CIGS solar cells fabricated on Cu foil. *Solar Energy* **162**, January, 357–363. (doi:10.1016/j.solener.2018.01.053).

[40] Yin G, Knight MW, van Lare MC, Solà Garcia MM, Polman A, Schmid M. 2017 Optoelectronic Enhancement of Ultrathin CuInGaSe2 Solar Cells by Nanophotonic Contacts. *Advanced Optical Materials* **5**, 5. (doi:10.1002/adom.201600637).

[41] Heinemann MD, Efimova V, Klenk R, Hoepfner B, Wollgarten M, Unold T, Schock HW, Kaufmann CA. 2015 Cu(In,Ga)Se 2 superstrate solar cells: prospects and limitations. *Progress in Photovoltaics: Research and Applications* **23**, 10, 1228–1237. (doi:10.1002/pip.2536).

[42] Kovacic M, Krc J, Lipovsek B, Chen WC, Edoff M, Bolt PJ, van Deelen J, Zhukova M, Lontchi J, Flandre D, *et al.* 2019 Light management design in ultra-thin chalcopyrite photovoltaic devices by employing optical modelling. *Solar Energy Materials and Solar Cells* **200**, April. (doi:10.1016/j.solmat.2019.109933).

[43] Byrnes J. 2021. Multilayer optical calculations (arXiv:1603.02720).

[44] McPeak KM, Jayanti SV, Kress SJ, Meyer S, Iotti S, Rossinelli A, Norris DJ. 2015 Plasmonic films can easily be better: Rules and recipes. *ACS Photonics* **2**, 3, 326–333. (doi:10.1021/ph5004237).

[45] "Illustration of how the finite-difference time-domain method in computational electromagnetism discretizes the space" from https://de.wikipedia.org/wiki/Finite_Difference_Time_Domain (23.11.2022).

[46] Yee K. 1966 Numerical solution of initial boundary value problems involving maxwell's equations in isotropic media. *IEEE Transactions on Antennas and Propagation* **14**, 3, 302–307. (doi:10.1109/TAP.1966.1138693).

[47] Oskooi AF, Roundy D, Ibanescu M, Bermel P, Joannopoulos JD, Johnson SG. 2010 Meep: A flexible free-software package for electromagnetic simulations by the FDTD method. *Computer Physics Communications* **181**, 3, 687–702. (doi:10.1016/j.cpc.2009.11.008).

[48] Varache R, Leendertz C, Gueunier-Farret ME, Haschke J, Muñoz D, Korte L. 2015 Investigation of selective junctions using a newly developed tunnel current model for solar cell applications. *Solar Energy Materials and Solar Cells* **141**, 14–23. (doi:10.1016/j.solmat.2015.05.014).

[49] Liu Y, Sun Y, Rockett A. 2012 A new simulation software of solar cells - WxAMPS. *Solar Energy Materials and Solar Cells* **98**, 124–128. (doi:10.1016/j.solmat.2011.10.010).

[50] Liu CM, Liu WL, Chen WJ, Hsieh SH, Tsai TK, Yang LC. 2005 ITO as a Diffusion Barrier Between Si and Cu. *Journal of The Electrochemical Society* **152**, 3, G234. (doi: 10.1149/1.1860511).

[51] Wada T, Kohara N, Nishiwaki S, Negami T. 2001 Characterization of the Cu(In,Ga)Se2/Mo interface in CIGS solar cells. *Thin Solid Films* **387**, 1-2, 118–122. (doi:10.1016/S0040-6090(00)01846-0).

[52] Wuerz R, Eicke A, Kessler F, Rogin P, Yazdani-Assl O. 2011 Alternative sodium sources for Cu(In,Ga)Se2 thin-film solar cells on flexible substrates. *Thin Solid Films* **519**, 21, 7268–7271. (doi:10.1016/j.tsf.2011.01.399).

[53] Yoon JH, Kim JH, Kim WM, Park JK, Baik YJ, Seong TY, Jeong Jh. 2014 Electrical properties of CIGS/Mo junctions as a function of MoSe2 orientation and Na doping. *Progress in Photovoltaics: Research and Applications* **22**, 1, 90–96. (doi:10.1002/pip. 2377).

[54] Mirhosseini H, Kiss J, Roma G, Felser C. 2016 Reducing the Schottky barrier height at the MoSe2/Mo(110) interface in thin-film solar cells: Insights from first-principles calculations. *Thin Solid Films* **606**, 143–147. (doi:10.1016/j.tsf.2016.03.053).

[55] Abou-Ras D, Kostorz G, Bremaud D, Kälin M, Kurdesau FV, Tiwari AN, Döbeli M. 2005 Formation and characterisation of MoSe2 for Cu(In,Ga)Se 2 based solar cells. *Thin Solid Films* **480-481**, 433–438. (doi:10.1016/j.tsf.2004.11.098).

[56] Hong J, Lee S, Lee S, Han H, Mahata C, Yeon HW, Koo B, Kim SI, Nam T, Byun K, *et al.* 2014 Graphene as an atomically thin barrier to Cu diffusion into Si. *Nanoscale* **6**, 13, 7503–7511. (doi:10.1039/c3nr06771h).

[57] Rostan PJ, Mattheis J, Bilger G, Rau U, Werner JH. 2005 Formation of transparent and ohmic ZnO:Al/MoSe2 contacts for bifacial Cu(In,Ga)Se2 solar cells and tandem structures. *Thin Solid Films* **480-481**, 67–70. (doi:10.1016/j.tsf.2004.11.001).

[58] Brewer SH, Franzen S. 2004 Calculation of the electronic and optical properties of indium tin oxide by density functional theory. *Chemical Physics* **300**, 1-3, 285–293. (doi: 10.1016/j.chemphys.2003.11.039).

[59] Maiberg M, Hölscher T, Zahedi-Azad S, Scheer R. 2015 Theoretical study of time-resolved luminescence in semiconductors. III. Trap states in the band gap. *Journal of Applied Physics* **118**, 10, 1–10. (doi:10.1063/1.4929877).

[60] Kotipalli R, Poncelet O, Li G, Zeng Y, Francis LA, Vermang B, Flandre D. 2017 Addressing the impact of rear surface passivation mechanisms on ultra-thin Cu(In,Ga)Se2 solar cell performances using SCAPS 1-D model. *Solar Energy* **157**, 603–613. (doi: 10.1016/j.solener.2017.08.055).

[61] Dinca SA, Schiff EA, Egaas B, Noufi R, Young DL, Shafarman WN. 2009 Hole drift mobility measurements in polycrystalline CuIn 1-xGaxSe2. *Physical Review B - Condensed Matter and Materials Physics* **80**, 23, 1–12. (doi:10.1103/PhysRevB.80.235201).

[62] Dinca SA, Schiff EA, Shafarman WN, Egaas B, Noufi R, Young DL. 2012 Electron drift-mobility measurements in polycrystalline CuInGaSe2 solar cells. *Appl. Phys. Lett.* **100**, 110, 103901–61906.

[63] Lee J, Cohen JD, Shafarman WN. 2005 The determination of carrier mobilities in CIGS photovoltaic devices using high-frequency admittance measurements. *Thin Solid Films* **480-481**, 336–340. (doi:10.1016/j.tsf.2004.11.087).

[64] Umehara T, Iinuma S, Sadono A, Kurokawa Y, Yamada A. 2015 Electrical characterization of Cu(In,Ga)Se2 thin films peeled off from Mo-coated soda-lime glass substrate by AC Hall measurement. *Japanese Journal of Applied Physics* **54**, 1, 018001. (doi:10.7567/JJAP.54.018001).

[65] Werner F, Bertram T, Mengozzi J, Siebentritt S. 2017 What is the dopant concentration in polycrystalline thin-film Cu(In,Ga)Se2? *Thin Solid Films* **633**, 222–226. (doi:10.1016/j.tsf.2016.09.038).

[66] Neugebohrn N, Hammer MS, Neerken J, Parisi J, Riedel I. 2015 Analysis of the back contact properties of Cu(In,Ga)Se2solar cells employing the thermionic emission model. *Thin Solid Films* **582**, 332–335. (doi:10.1016/j.tsf.2014.10.073).

[67] Hsiao KJ, Liu JD, Hsieh HH, Jiang TS. 2013 Electrical impact of MoSe2 on CIGS thin-film solar cells. *Physical Chemistry Chemical Physics* **15**, 41, 18174–18178. (doi:10.1039/c3cp53310g).

[68] Eisenbarth T, Unold T, Caballero R, Kaufmann CA, Schock HW. 2010 Interpretation of admittance, capacitance-voltage, and current-voltage signatures in Cu(In,Ga)Se2 thin film solar cells. *Journal of Applied Physics* **107**, 3. (doi:10.1063/1.3277043).

[69] Ott T, Schönberger F, Walter T, Hariskos D, Kiowski O, Salomon O, Schäffler R. 2015 Verification of phototransistor model for Cu(In,Ga)Se2solar cells. *Thin Solid Films* **582**, 392–396. (doi:10.1016/j.tsf.2014.09.025).

[70] Villanueva-Tovar A, Kodalle T, Kaufmann CA, Schlatmann R, Klenk R. 2020 Limitation of Current Transport across the Heterojunction in Cu(In,Ga)Se2 Solar Cells Prepared with Alkali Fluoride Postdeposition Treatment. *Solar RRL* **4**, 4, 1–7. (doi:10.1002/solr.201900560).

[71] Cwil M, Igalson M, Zabierowski P, Siebentritt S. 2008 Charge and doping distributions by capacitance profiling in Cu(In,Ga)Se2 solar cells. *Journal of Applied Physics* **103**, 6, 1–9. (doi:10.1063/1.2884708).

[72] Sozzi G, Lazzarini M, Menozzi R, Carron R, Avancini E, Bissig B, Buecheler S, Tiwari AN. 2017 A numerical study of the use of C-V characteristics to extract the doping density of CIGS absorbers. *2017 IEEE 44th Photovoltaic Specialist Conference, PVSC 2017*, 1, 966–969. (doi:10.1109/PVSC.2017.8366521).

[73] Cadel E, Barreau N, Kessler J, Pareige P. 2010 Atom probe study of sodium distribution in polycrystalline Cu(In,Ga)Se2 thin film. *Acta Materialia* **58**, 7, 2634–2637. (doi:10.1016/j.actamat.2009.12.049).

[74] Werner F, Wolter MH, Siebentritt S, Sozzi G, Di Napoli S, Menozzi R, Jackson P, Witte W, Carron R, Avancini E, *et al.* 2018 Alkali treatments of Cu(In,Ga)Se2 thin-film absorbers and their impact on transport barriers. *Progress in Photovoltaics: Research and Applications* **26**, 11, 911–923. (doi:10.1002/pip.3032).

[75] Herberholz R, Igalson M, Schock HW. 1998 Distinction between bulk and interface states in CuInSe2/CdS/ZnO by space charge spectroscopy. *Journal of Applied Physics* **83**, 1, 318–325. (doi:10.1063/1.366686).

[76] Rau U, Braunger D, Herberholz R, Schock HW, Guillemoles JF, Kronik L, Cahen D. 1999 Oxygenation and air-annealing effects on the electronic properties of Cu(In,Ga)Se2 films and devices. *Journal of Applied Physics* **86**, 1, 497–505. (doi:10.1063/1.370758).

[77] Heath JT, Cohen JD, Shafarman WN. 2004 Bulk and metastable defects in CuIn1-xGaxSe2 thin films using drive-level capacitance profiling. *Journal of Applied Physics* **95**, 3, 1000–1010. (doi:10.1063/1.1633982).

[78] Igalson M, Urbaniak A, Edoff M. 2009 Reinterpretation of defect levels derived from capacitance spectroscopy of CIGSe solar cells. *Thin Solid Films* **517**, 7, 2153–2157. (doi:10.1016/j.tsf.2008.10.092).

[79] Walter T, Herberholz R, Müller C, Schock HW. 1996 Determination of defect distributions from admittance measurements and application to Cu(In,Ga)Se2 based heterojunctions. *Journal of Applied Physics* **80**, 8, 4411–4420. (doi:10.1063/1.363401).

[80] Eisenbarth T, Caballero R, Nichterwitz M, Kaufmann CA, Schock HW, Unold T. 2011 Characterization of metastabilities in Cu(In,Ga)Se2 thin-film solar cells by capacitance and current-voltage spectroscopy. *Journal of Applied Physics* **110**, 9. (doi:10.1063/1.3656453).

[81] Werner F, Babbe F, Elanzeery H, Siebentritt S. 2019 Can we see defects in capacitance measurements of thin-film solar cells? *Progress in Photovoltaics: Research and Applications* **27**, 11, 1045–1058. (doi:10.1002/pip.3196).

[82] Hölscher T, Schneider T, Maiberg M, Scheer R. 2018 Impact of air-light exposure on the electrical properties of Cu(In,Ga)Se2 solar cells. *Progress in Photovoltaics: Research and Applications* **26**, 11, 934–941. (doi:10.1002/pip.3041).

[83] Hölscher T, Walter T, Schneider T, Maiberg M, Scheer R. 2019 Device simulation of Cu(In,Ga)Se2 solar cells by means of voltage dependent admittance spectroscopy. *Thin Solid Films* **669**, July 2018, 345–350. (doi:10.1016/j.tsf.2018.11.022).

[84] Nicollian EH, Brews JR. 2003 *MOS (Metal Oxide Semiconductor) Physics and Technology*.

[85] Abou-Ras D, Mukherji D, Kostorz G, Brémaud D, Kälin M, Rudmann D, Döbeli M, Tiwari AN. 2005 Dependence of the MoSe2 formation on the Mo orientation and the Na concentration for Cu(In,Ga)Se2 thin-film solar cells. *Materials Research Society Symposium Proceedings* **865**, January, 287–292. (doi:10.1557/proc-865-f8.1).

[86] Hölscher T, Förster S, Schneider T, Maiberg M, Widdra W, Scheer R. 2017 Light induced degradation of Cu(In,Ga)Se2 thin film surfaces . *Applied Physics Letters* **111**, 1, 011604. (doi:10.1063/1.4992116).

[87] Hurkx GA, Klaassen DB, Knuvers MP. 1992 A New Recombination Model for Device Simulation Including Tunneling. *IEEE Transactions on Electron Devices* **39**, 2, 331–338. (doi:10.1109/16.121690).

[88] Liu Y, Ahmadpour M, Adam J, Kjelstrup-Hansen J, Rubahn HG, Madsen M. 2018 Modeling Multijunction Solar Cells by Nonlocal Tunneling and Subcell Analysis. *IEEE Journal of Photovoltaics* **8**, 5, 1363–1369. (doi:10.1109/JPHOTOV.2018.2851308).

[89] Cahen D, Noufi R. 1989 Defect chemical explanation for the effect of air anneal on CdS/CuInSe2 solar cell performance. *Applied Physics Letters* **54**, 6, 558–560. (doi: 10.1063/1.100930).

[90] Kim H, Horwitz JS, Kushto G, Piqué A, Kafafi ZH, Gilmore CM, Chrisey DB. 2000 Effect of film thickness on the properties of indium tin oxide thin films. *Journal of Applied Physics* **88**, 10, 6021–6025. (doi:10.1063/1.1318368).

[91] Sugiyama K, Ishii H, Ouchi Y, Seki K. 2000 Dependence of indium-tin-oxide work function on surface cleaning method as studied by ultraviolet and x-ray photoemission spectroscopies. *Journal of Applied Physics* **87**, 1, 295–298. (doi:10.1063/1.371859).

[92] Bose S, Cunha JM, Suresh S, De Wild J, Lopes TS, Barbosa JR, Silva R, Borme J, Fernandes PA, Vermang B, *et al.* 2018 Optical Lithography Patterning of SiO2 Layers for Interface Passivation of Thin Film Solar Cells. *Solar RRL* **2**, 12, 1–6. (doi:10.1002/solr.201800212).

[93] Van Lare C, Yin G, Polman A, Schmid M. 2015 Light Coupling and Trapping in Ultrathin Cu(In,Ga)Se2 Solar Cells Using Dielectric Scattering Patterns. *ACS Nano* **9**, 10, 9603–9613. (doi:10.1021/acsnano.5b04091).

[94] Choi S, Kamikawa Y, Nishinaga J, Yamada A, Shibata H, Niki S. 2018 Lithographic fabrication of point contact with Al2O3 rear-surface-passivated and ultra-thin Cu(In,Ga)Se2 solar cells. *Thin Solid Films* **665**, August, 91–95. (doi:10.1016/j.tsf.2018.08.044).

[95] Yin G, Song M, Duan S, Manley P, Greiner D, Kaufmann CA, Schmid M. 2016 Well-controlled dielectric nanomeshes by colloidal nanosphere lithography for optoelectronic enhancement of ultrathin Cu(In,Ga)Se2 solar cells. *ACS Applied Materials and Interfaces* **8**, 46, 31646–31652. (doi:10.1021/acsami.6b10135).

[96] Mansfield LM, Kanevce A, Harvey SP, Bowers K, Beall C, Glynn S, Repins IL. 2018 Efficiency increased to 15.2% for ultra-thin Cu(In,Ga)Se2 solar cells. *Progress in Photovoltaics: Research and Applications* **26**, 11, 949–954. (doi:10.1002/pip.3033).

[97] Roussillon Y, Karpov VG, Shvydka D, Drayton J, Compaan AD. 2004 Back contact and reach-through diode effects in thin-film photovoltaics. *Journal of Applied Physics* **96**, 12, 7283–7288. (doi:10.1063/1.1808902).

[98] Jehl Z, Gallium I, Cigse Ds. 2012 Realization of ultrathin Copper Indium Gallium Diselenide (CIGSe) solar cells To cite this version : HAL Id : tel-00697615 Zacharie Jehl Li Kao Elaboration of ultrathin Copper Indium Gallium Di-Selenide based Solar Cells .

[99] Jehl Z, Erfurth F, Naghavi N, Lombez L, Gerard I, Bouttemy M, Tran-Van P, Etcheberry A, Voorwinden G, Dimmler B, *et al.* 2011 Thinning of CIGS solar cells: Part II: Cell characterizations. *Thin Solid Films* **519**, 21, 7212–7215. (doi:10.1016/j.tsf.2010.12.224).

[100] Li-Kao ZJ, Naghavi N, Erfurth F, Guillemoles JF, Gérard I, Etcheberry A, Pelouard JL, Collin S, Voorwinden G, Lincot D. 2012 Towards ultrathin copper indium gallium diselenide solar cells: proof of concept study by chemical etching and gold back contact engineering. *Progress in Photovoltaics: Research and Applications* **20**, 5, 582–587. (doi:10.1002/pip.2162).

[101] Yang S, Zhong J, Sun B, Zeng X, Luo W, Zhao X, Shu Y, Chen J, He J. 2019 Influence of base pressure on property of sputtering deposited ITO film. *Journal of Materials Science: Materials in Electronics* **30**, 14, 13005–13012. (doi:10.1007/s10854-019-01662-w).

[102] Ledinek D, Salomé P, Hägglund C, Zimmermann U, Edoff M. 2018 Rear Contact Passivation for High Bandgap Cu(In, Ga)Se2 Solar Cells with a Flat Ga profile. *IEEE Journal of Photovoltaics* **8**, 3, 864–870. (doi:10.1109/JPHOTOV.2018.2813259).

[103] Sever M, Lipovšek B, Krč J, Čampa A, Sánchez Plaza G, Haug FJ, Duchamp M, Soppe W, Topič M. 2013 Combined model of non-conformal layer growth for accurate optical simulation of thin-film silicon solar cells. *Solar Energy Materials and Solar Cells* **119**, 59–66. (doi:10.1016/j.solmat.2013.05.016).

[104] Hüpkes J, Owen JI, Pust SE, Unteâ. 2012 Chemical etching of zinc oxide for thin-film silicon solar cells. *ChemPhysChem* **13**, 1, 66–73. (doi:10.1002/cphc.201100738).

Publications

- **Schneider T**, Dethloff C, Hölscher T, Kempa H, Scheer R. 2021 Comparison of Mo and ITO back contacts in CIGSe solar cells: Vanishing of the main capacitance step. *Progress in Photovoltaics: Research and Applications* 2021;30(2):191-202 (doi:10.1002/pip.3476)

- **Schneider T**, Hölscher T, Kempa H, Scheer R. 2020 Determination of the back contact recombination velocity of a $Cu(In,Ga)Se_2$/ITO interface using bifacial solar cells. *37th European Photovoltaic Solar Energy Conference* 621-626 (doi:10.4229/EUPVSEC20202020-3CO.7.6)

- **Schneider T**, Tröndle J, Fuhrmann B, Syrowatka F, Sprafke A, Scheer R. 2020 Ultrathin CIGSe Solar Cells with Integrated Structured Back Reflector. *Solar RRL* 4, 2000295 (doi:10.1002/solr.202000295)

- **Schneider T**, Scheer R. 2019 Aluminum Based Back Reflectors for Ultrathin $Cu(In,Ga)Se_2$ Solar Cells with ITO Diffusion Barrier. *36th European Photovoltaic Solar Energy Conference and Exhibition* 684-688 (doi:10.4229/EUPVSEC20192019-3BV.1.44)

- Mahmoudi B, Caddeo F, Lindenberg T. **Schneider T**, Hölscher T, Scheer R, Maijenburg W. 2020 Photoelectrochemical properties of Cu-Ga-Se photocathodes with compositions ranging from $CuGaSe_2$ to $CuGa_3Se_5$. *Electrochimica Acta* 367, 137183 (doi:10.1016/j.electacta.2020.137183)

- Hölscher T, Walter T, **Schneider T**, Maiberg M, Scheer R. 2019 Device simulation of Cu(In,Ga)Se2 solar cells by means of voltage dependent admittance spectroscopy. *Thin Solid Films* 669, 345-350 (doi:10.1016/j.tsf.2018.11.022)

- Hölscher T, **Schneider T**, Maiberg M, Scheer R. 2018 Critical role of air-light exposure on co-evaporated $Cu(In,Ga)Se_2$ solar cells. *36th Japanese Journal of Applied Physics* 57, 08RC07 (doi:10.7567/Jjap.57.08rc07)

- Hölscher T, **Schneider T**, Maiberg M, Scheer R. 2018 Impact of air-light exposure on the electrical properties of $Cu(In,Ga)Se_2$ solar cells. *Progress in Photovoltaics: Research and Applications* 26, 934-941 (doi:10.1002/pip.3041)

- Hölscher T, Förster S, **Schneider T**, Maiberg M, Widdra W, Scheer R. 2017 Light induced degradation of Cu(In,Ga)Se2 thin film surfaces Applied. *Physics Letters* 111, 011604 (doi:10.1063/1.4992116)

Danksagung

Zunächst möchte ich mich herzlich bei Prof. Dr. Roland Scheer bedanken, welcher mir die Forschung an diesem interessanten Thema ermöglicht hat und mir viele Freiheiten in meiner arbeitsweise gelassen hat.

Des Weiteren möchte ich den Gutachtern danken, welche sich Zeit genommen haben, diese Arbeit zu begutachten.

Dr. Wolfgang Fränzel und Dr. Heiko Kempa danke ich führ ihre Unterstützung beim Lösen von technischen Problemen als auch für ihren Einsatz bei der Organisation innerhalb der Fachgruppe.

Weiter Danke ich den Mitarbeitern des IZM Dr. Bodo Fuhrman, Sven Schlenker, Frank Heyroth und Dr. Bodo Fuhrmann, welche stets eine große Hilfe sind und viele Sachen erst ermöglicht haben. Insbesondere möchte ich hier Dr. Bodo Fuhrman dafür danken, dass er viel Arbeit bei der Betreuung von Masterstudenten abgenommen hat.

Bedanken möchte ich mich auch bei Dr. Jürgen Hüpkes für die Bereitstellung der stukturierten ZnO-Schicht als auch bei den Mitarbeitern des Institus für Nanophotonik Göttingen für die Laserstrukturierung von Glas.

Die Masterstudenten Arrigo Facchini, Johanna Tröndle und Borui Sun möchte für ihre Unterstützung bei der Anfertigung von nanostrukturierten Proben danken.

Bei Ulrich Fahnert, Thomas Richter und Dr. Torsten Hölscher möchte ich mich für die zahlreichen spaßigen Stunden in unserem Büro bedanken sowie für die ebenso zahlreiche Unterstützung bei technischen Problemen.

Dr. Alexander Sprafke danke ich für die ausführlichen Diskussionen zu optischen Simulationen.

Weiterhin möchte ich den anderen Mitgliedern der Fachgruppe Photovoltaik danken, welche mich über die Jahre begleitet haben.

Meinen Eltern möchte ich an dieser Stelle danken, dass sich mich stets unterstützt haben. Weiterhin möchte ich mich bei meiner guten Freundin Ronja bedanken, die teile dieser Arbeit für mich gegengelesen hat. Schließlich möchte ich mich bei meiner Partnerin Viola bedanken, welche jeden Tag für mich da ist.

Angaben zur Person und zum Bildungsgang

Persönliche Daten

Name	Thomas Schneider
E-Mail-Adresse	thomasschneider1988@googlemail.com
Geburtsdatum	08.06.1988, Halle (Saale)

Akademischer Werdegang

Seit 11/15	Promotionsstudium Physik Forschungsthema: „Integration hochreflektiver Rückkontakte in nanostrukturierte Cu(In, Ga)Se$_2$ Solarzellen" Martin-Luther-Universität Halle-Wittenberg
10/12 - 07/15	Masterstudium Physik Masterarbeit: „Elektrische Charakterisierung von Al$_2$O$_3$/ZnO- und Al$_2$O$_3$/TiO$_2$-Schichtsystemen zur Passivierung von Silizium" Martin-Luther-Universität Halle-Wittenberg
10/08 - 09/12	Bachelorstudium Physik Bachelorarbeit: „ALD-Prozessoptimierung von Al$_2$O$_3$ Schichten zur Passivierung von schwarzem Si" Martin-Luther-Universität Halle-Wittenberg
07/07	Abitur Schwerpunkt: Elektrotechnik Gutjahrschule, Halle

Selbstständigkeitserklärung

Hiermit versichere ich, dass ich die vorliegende Dissertation mit dem Titel:

"Integration of highly reflective back contacts in microstructured Cu(In, Ga)Se2 solar cells"

selbstständig und nur unter Verwendung der angegebenen Quellen und Hilfsmittel angefertigt habe. Die aus fremden Quellen direkt oder indirekt übernommenen Stellen sind als solche kenntlich gemacht. Die Arbeit wurde bisher in gleicher oder ähnlicher Form keiner anderen Prüfungsbehörde vorgelegt und auch nicht veröffentlicht.

Halle, den 26.10.2023